

UCLA

UCLA Electronic Theses and Dissertations

Title

Engineering Al-based Thin Film Materials for Power Devices and Energy Storage Applications

Permalink

<https://escholarship.org/uc/item/9dw399n1>

Author

Perng, Ya-Chuan

Publication Date

2012

Peer reviewed|Thesis/dissertation

UNIVERSITY OF CALIFORNIA

Los Angeles

Engineering Al-based Thin Film Materials for Power Devices and Energy Storage Applications

A dissertation submitted in partial satisfaction of the
requirements for the degree Doctor of Philosophy
in Chemical Engineering

by

Ya-Chuan Perng

2012

ABSTRACT OF THE DISSERTATION

Engineering Al-based Thin Film Materials for Power Devices and Energy Storage Applications

by

Ya-Chuan Perng

Doctor of Philosophy in Chemical Engineering

University of California, Los Angeles, 2012

Professor Jane P. Chang, Chair

Al-based materials, specifically aluminum oxide (Al_2O_3), aluminum nitride (AlN) and lithium aluminosilicate ($\text{Li}_x\text{Al}_y\text{Si}_z\text{O}$) were synthesized via atomic layer deposition (ALD) and investigated for their applications in power electronics and miniaturized Li-ion batteries.

Al_2O_3 and AlN films were deposited on two substrates, silicon carbide (SiC) and gallium nitride (GaN) based heterostructures, AlGaN/GaN, to compare their electrical performances as alternative dielectrics for wide bandgap semiconductor based power devices. Amorphous Al_2O_3 was deposited at 195-200 °C at a rate of 0.75-1 Å/cycle. The film exhibited a dielectric constant of 9 and a leakage current density of 10^{-3} A/cm² at 8 MV/cm on SiC. When it was applied on AlGaN/GaN, the Al_2O_3 passivation resulted in an increased sheet carrier density but a decrease in the mobility compared to those of a clean AlGaN/GaN substrate. Crystalline AlN was deposited at 540 °C at a rate of 1.5 Å/cycle. The AlN film demonstrated a dielectric constant of 8.3 and a leakage current density of 10^{-3} A/cm² at 4.3 MV/cm on SiC. When AlN was applied on

AlGaIn/GaN, an increased carrier density was observed while the electron mobility was at 1130 cm²/V-s, similar to that of a clean AlGaIn/GaN substrate. The electrical properties of synthesized AlN were promising and comparable to those of MBE or sputtered AlN, confirming the promise of ALD for synthesizing AlN. Due to their material properties, Al₂O₃ is the preferred choice for preventing gate leakage current on SiC, whereas AlN demonstrated superior capability of passivating AlGaIn/GaN.

Stoichiometric LiAlSiO₄ was realized at 290 °C with a rate of ~23 Å/global cycle, in which one global cycle sequence represented 10(Al-O)-6(Li-O)-4(Si-O) ALD cycles. As-deposited films were amorphous, pin-hole free, as confirmed by electrochemical testing in ferrocene, and conformal over 3D nanowires (NW). The ionic conductivity of Li_xAl_ySi_zO films was 10⁻⁹-10⁻⁷ S/cm and the activation energy was 0.34-0.98 eV, both correlated to cation contents in the films. After rapid thermal annealing (RTA) at 900 °C, the as-deposited LiAlSiO₄ films crystallized into epitaxial β-LiAlSiO₄ on Si (001) with a relationship of β-LiAlSiO₄ (1 $\bar{2}$ 10) || Si (100) and β-LiAlSiO₄ (10 $\bar{1}$ 0) || Si (001). The application of the LiAlSiO₄ film on tin dioxide (SnO₂) NWs showed that the film possessed a high ionic conductivity, which suppressed the formation of metallic Sn particles, showing the capability of Li_xAl_ySi_zO films to serve as electrolytes and surface modification layers in 3D Li-ion microbatteries.

The dissertation of Ya-Chuan Perng is approved.

Mark S. Goorsky

Robert F. Hicks

Tatiana Segura

Michael Wojtowicz

Jane P. Chang, Committee Chair

University of California, Los Angeles

2012

TABLE OF CONTENTS

CHAPTER 1: INTRODUCTION	1
1.1 Motivation.....	2
1.2 Al-based Materials	3
1.3 Wide Bandgap Semiconductor Based High-Power Devices	5
1.4 On-Chip Energy Storage Application.....	29
1.5 Scope and Organization	53
CHAPTER 2: EXPERIMENTAL SETUP	54
2.1 Thin-Film Deposition Reactors.....	54
2.2 Material Characterization.....	70
2.3 MOS-CAP Fabrication.....	86
2.4 Band Alignment	90
2.5 Hall Measurement.....	92
2.6 Electrolyte Characterization.....	95
CHAPTER 3: BINARY Al-BASED MATERIALS FOR HIGH-POWER DEVICES.....	103
3.1 Al ₂ O ₃ on SiC	104
3.2 Al ₂ O ₃ on AlGaN/GaN.....	107
3.3 ALD of AlN	115
3.4 AlN on 4H-SiC	124
3.5 AlN on AlGaN/GaN	129
3.6 Summary	131
CHAPTER 4: IONIC CONDUCTIVE LiAlSiO ₄ FILMS FOR ELECTROLYTES	133
4.1 ALD of LiAlSiO ₄	133
4.2 Conformality of Li _x Al _y Si _z O Coating	136
4.3 Electrochemistry Characteristic	138
4.4 Ionic Conductivity	140
4.5 Controlled Crystallization of LiAlSiO ₄	143
4.6 Effect on SnO ₂ NW Electrode	148
4.7 Summary	150
CHAPTER 5: SUMMARY AND FUTURE WORK	152
APPENDICES	156
BIBLIOGRAPHY.....	190

LIST OF FIGURES

Figure 1.1. Structures and conductivities of Al-based materials, Al_2O_3 , AlN and LiAlSiO_4 , as elements are introduced into Al. (Horn 1967; Winter and Ghose 1979; Ishizawa, Miyata et al. 1980; Gil 1998; Sartbaeva, Redfern et al. 2004)	4
Figure 1.2. Illustrations of an intrinsic AlGaN/GaN heterostructure: (a) net charges at the interface, resulted from the net spontaneous polarization and piezoelectric polarization between i-AlGaN and i-GaN, and (b) energy diagram illustrating the opposite dipoles electrically balancing the net charges due to polarization. (Mishra, Parikh et al. 2002).....	9
Figure 1.3. Energy band diagrams of an n-AlGaN/i-GaN HEMT at (a) equilibrium and (b) the onset of threshold. (Sze and Ng 2007) The ψ_p is the potential variation, ϕ_{Bn} is the barrier height, t is the thickness of AlGaN film and V_T is the threshold voltage.....	9
Figure 1.4. Illustrations of current collapse and dispersion issues for AlGaN/GaN HEMTs. (a) Drain current collapse refers to the actual $I_{D,max}$ (solid) being lower than the theoretical value (dash). (Hasegawa, Inagaki et al. 2003) (b) Current dispersion refers to the difference between a large-signal AC and DC pulse on the gate. (Mishra, Shen et al. 2008)	12
Figure 1.5. Schematic diagrams of (a) a passivated AlGaN/GaN HEMT to eliminate the current collapse issue and (b) a MIS-HEMT structure with a dielectric layer serving as the surface passivation and gate dielectric layer. (c) The corresponding band diagram of (b).....	13
Figure 1.6. Bulk structures of common crystalline Al_2O_3 polymorphs: (a) hexagonal (α -phase) (Ishizawa, Miyata et al. 1980), (b) orthorhombic (κ -phase) (Ollivier, Retoux et al. 1997), (c) cubic (γ -phase) (Zhou and Snyder 1991) and (d) monoclinic (θ -phase) (Husson and Repelin 1996).	15
Figure 1.7. Crystal structures of AlN: (a) wurtzite and (b) zinc-blende, and their corresponding atomic arrangement and stacking sequences along [0001] and [111] directions, respectively. (Gil 1998)	18
Figure 1.8. The experimental values of bandgap and dielectric constant of various dielectrics. The theoretical values were used for compounds in parenthesis, adapted from (Wallace and Wilk 2003; Gila, Ren et al. 2004).	22
Figure 1.9. Diagrams of band alignments for high-k dielectrics on (a) GaN and AlGaN ($\text{Al}_{0.3}\text{Ga}_{0.7}\text{N}$) and (b) SiC. (Singh and Hefner 2004; Robertson and Falabretti 2006; Maeda, Hiroki et al. 2007)	23
Figure 1.10. Illustrations of (a) AlN and (b) $\gamma\text{-Al}_2\text{O}_3$ on 4H-SiC to demonstrate that a sharp interface with less dangling bonds can be formed by AlN due to its similar atomic arrangement and lattice constant to those of 4H-SiC.....	24
Figure 1.11. Energy diagrams of germanium (Ge) surface bonded TMA reacting with (a) NH_3 and (b) H_2O , adapted from (Xu, Chen et al. 2011).	28
Figure 1.12. A schematic diagram of a discharging battery (electrochemical cell) and the electrode reactions divided from the cell reaction, adapted from (Kiehne 2003). $S(N)_{red}$ and $S(P)_{ox}$ are the components of the negative and positive electrodes, respectively.	30

Figure 1.13. The energy diagram of a fluid electrolyte relative to the potentials of the solid electrodes, including the anode (reductant during battery discharge) and the cathode (oxidant during battery discharge), of a galvanic cell, adapted from (Kiehne 2003).	31
Figure 1.14. Comparisons of different battery systems in terms of (a) specific power and specific energy (Cairns 2004) and (b) energy density and specific energy, adapted from (Tarascon and Armand 2001).	33
Figure 1.15. A schematic diagram of charging/discharging of Li-ion batteries. (Kiehne 2003)..	34
Figure 1.16. Examples of three-dimension battery layouts: (a) arrays of cathodes and anodes, (b) arrays of anodes coated with a thin layer of electrolyte and with remaining space filled with the cathode material, (c) “sponge” architectures and (d) substrate trenches, adapted from (Long, Dunn et al. 2004; Notten, Roozeboom et al. 2007).	37
Figure 1.17. Schematic diagrams of (a) 2D parallel-plate and (b) 3D anode array (HCP) batteries.	38
Figure 1.18. (a) The surface area of electrodes as a function of electrode diameter and pitch. (b) The surface area of electrodes as a function of electrode height and diameter. D is 5 nm and L is 1 mm.	39
Figure 1.19. Theoretical areal capacity of LiCoO ₂ and graphite half-cells as a function of aspect ratio and pitch of the 3D graphite anode features (d is 700 nm, t is 15 nm, D is 750 nm and L is 1 mm). Solid symbols are for graphite and shallow symbols are for LiCoO ₂	41
Figure 1.20. Phase diagram of the Li ₂ O-Al ₂ O ₃ -SiO ₂ system, adapted from (Roy and Osborn 1949).	46
Figure 1.21. Crystal structures of LiAlSiO ₄ : (a) α-eucryptite (Hesse 1985), (b) β-eucryptite (Pillars and Peacor 1973) and (c) γ-eucryptite (Norby 1990).	47
Figure 1.22. The crystal structure and the corresponding atomic projection on the (0001) plane of (a) β-quartz and (b) β-LiAlSiO ₄ . (Nagel and Bohm 1982; Kihara 1990)	48
Figure 1.23. The ionic conductivity of LiAlSiO ₄ as a function of (a) temperature and (b) Li content, adapted from (Nagel and Bohm 1982).	50
Figure 1.24. The calculated activation energy of Li ion diffusion in glass Li _x Al _{1-x} Si _{0.5} O ₄ as a function of Al/Li ratio, adapted from (Li and Garofalini 2004).	51
Figure 2.1. Schematic diagrams of (a) the high-vacuum ALD chamber and (b) the integration of this chamber with a high-vacuum cluster system for XPS analysis.	55
Figure 2.2. The design of the sample stage in the high-vacuum ALD chamber, composed of a receiver fork, standoffs and a heating station with a linear manipulator to bring the heater in contact with the molybdenum sample holder.	57
Figure 2.3. The mechanism for transferring a molybdenum sample holder between the high-vacuum ALD reactor and the cluster system.	58
Figure 2.4. A schematic diagram of the vacuum ALD chamber and the layout of gas delivery systems.	59
Figure 2.5. A schematic diagram of the layout of gas delivery systems to the high-vacuum ALD reactor.	60

Figure 2.6. An illustration of one chemical pulsing sequence for ALD of Al_2O_3	61
Figure 2.7. An illustration of one chemical pulsing sequence for ALD of AlN	62
Figure 2.8. Illustrations of (a) one chemical pulsing sequence for ALD of Li_2O , Al_2O_3 and SiO_2 , and (b) the global sequence combining a, b and c as local cycle numbers of Li_2O , Al_2O_3 and SiO_2 ALD growths, respectively, for ALD of $\text{Li}_x\text{Al}_y\text{Si}_z\text{O}$	64
Figure 2.9. An AFM image of a clean 4H-SiC (0001) surface. The RMS roughness was 2.83 Å.....	65
Figure 2.10. XPS spectra of 275Å $\text{AlGaN}/5000\text{Å}$ GaN samples with different surface treatments: (a) as-received without any surface treatment, (b) cleaned by $\text{NH}_4\text{OH}:\text{H}_2\text{O}_2:\text{DI}$ (1:1:5) solution (70 °C) followed by $\text{HCl}:\text{H}_2\text{O}$ (1:1) and (c) cleaned in acetone, followed by isopropyl and NH_4OH (50 °C).....	67
Figure 2.11. (a) SEM and (b) TEM images of Si nanowires synthesized by chemical vapor deposition on a Si substrate.....	68
Figure 2.12. A Nyquist plot showing the real and imaginary parts of the impedance measured from an ITO/quartz substrate over a frequency range of 20 to 10^6 Hz.....	69
Figure 2.13. An <i>in-situ</i> HRTEM image and SAED patterns of a single crystalline SnO_2 nanowire at the reaction front during the lithiation process. (Zhang, Liu et al. 2012).....	69
Figure 2.14. A schematic diagram of the <i>in-situ</i> RHEED setup on the high-vacuum ALD chamber.....	71
Figure 2.15. (a) The Ewald sphere and Laue circles for the RHEED analysis. (Braun 1999) (b) The RHEED pattern of a clean 4H-SiC (0001) surface along $[\bar{1}2\bar{1}0]$ azimuth.....	72
Figure 2.16. <i>In-situ</i> XPS spectra of a 250 Å AlN film on 4H-SiC: (a) survey and (b) N 1s.....	75
Figure 2.17. Comparison of photoemission spectra of Li_2O on Si taken by (a) XPS with Al $K\alpha$ source (photon energy of 1486.6 eV) and (b) UPS with synchrotron (photon energy of 140 eV). The Li_2O film was grown by 10 ALD cycles.....	76
Figure 2.18. Ellipsometric measurement of a ~345 Å AlN film on 4H-SiC: (a) experimental ψ and Δ compared to the Cauchy model (dashed lines) and (b) the dispersion of fitted index of refraction.....	78
Figure 2.19. A schematic illustration of the synchrotron XRD setup with a four-circle diffractometer and the spectra for Si and LiAlSiO_4 on Si: (a) specular scan, (b) in-plane scan and (c) phi scan. The Si peaks are not completed for preventing the detector from saturation. (d) The angular position and d-spacing are compared with the JCPDS database. (e) A crystal model showing the interfacial epitaxial relationship of LiAlSiO_4 on Si.....	81
Figure 2.20. (a) An HRTEM image of ~10 nm LiAlSiO_4 over a Au/ SiO_2 core-shell nanoparticle and (b) the corresponding EDX data to confirm the Si and Al presence.....	83
Figure 2.21. (a) An HRTEM cross-section image of AlGaN and (b) the corresponding SEAD pattern showing the out-plane (0001) and in-plane ($20\bar{2}0$) diffractions.....	84
Figure 2.22. AFM images of (a) a clean 4H-SiC with an RMS roughness of 2.83 Å and (b) a 130 Å AlN film on 4H-SiC with an RMS roughness of 7.64 Å.....	86

Figure 2.23. A process flow of the MOS capacitor device fabrication for characterizing the electrical performance of synthesized Al ₂ O ₃ and AlN films on 4H-SiC.....	87
Figure 2.24. Normalized C-V characteristic measured from a 1000 Å Pt/100 Å Ti/268 Å Al ₂ O ₃ /n-type 4H-SiC MOS capacitor with 1000 Å Al as the back-side contact.....	88
Figure 2.25. Leakage current density as a function of electric field across a 260 Å γ -Al ₂ O ₃ film measured from an Al/260 Å γ -Al ₂ O ₃ /4H-SiC MOS capacitor. The dotted lines indicate that the leakage current density reached 10 ⁻³ A/cm ² at 2.6 MV/cm.....	90
Figure 2.26. Schematic for determining the valance band offset at a dielectric/SiC interface by XPS spectra. (Waldrop and Grant 1996)	91
Figure 2.27. XPS spectra of (a) 4H-SiC, (b) a 200 Å Al ₂ O ₃ film, and (c) a 25 Å Al ₂ O ₃ film on 4H-SiC.....	92
Figure 2.28. Schematic diagrams of the Hall measurement for determining the sheet resistance, carrier density and mobility of 2DEG in the AlGa _N /Ga _N heterojunction with surface passivated by ALD films: (a) the orientations of applied magnetic field, current and the induced Hall voltage (Solymar and Walsh 2004) and (b) the sample setup.....	94
Figure 2.29. (a) Setup of the cyclic voltammetry measurement. (b) Characteristic IV curve measured on a clean ITO/quartz substrate in a solution of 1 mM Fc and 100 mM TBATFB in PC.....	98
Figure 2.30. Nyquist plots of calculated impedance from various circuit models.....	100
Figure 2.31. A schematic diagram of the setup for impedance measurements.....	101
Figure 2.32. (a) Impedance data from a 10 nm Li _x Al _y O film on ITO/quartz at various temperatures. The data were fitted (line) by the circuit shown in the inset. (b) Ionic conductivity as a function of temperature, as determined by the data in (a).	102
Figure 3.1. A schematic diagram of band alignment at the amorphous Al ₂ O ₃ /4H-SiC interface determined by XPS analysis.....	104
Figure 3.2. XRD spectra of γ -Al ₂ O ₃ on 4H-SiC measured with a four-circle diffractometer: (a) specular scan of a 20 nm Al ₂ O ₃ film and (b) in-plane phi scans on γ -Al ₂ O ₃ films with two thicknesses in comparison with that of the substrate 4H-SiC. (Tanner, Toney et al. 2007).....	105
Figure 3.3. (a) Normalized current-voltage characteristic of MOS capacitors made from 260 Å as-deposited Al ₂ O ₃ on epitaxial 4H-SiC with 1×10 ⁻⁴ cm ² Al gate (solid line) in comparison with a calculated ideal curve (dash line). (b) Comparison of current leakage using crystalline and amorphous Al ₂ O ₃ films as the gate dielectric. (Tanner, Perng et al. 2007)	106
Figure 3.4. (a) Thickness of Al ₂ O ₃ films as a function of ALD cycle at 195 °C on clean AlGa _N /Ga _N with the deposition rate determined by the slope. (b) An HRTEM cross-section image of 3.36 nm Al ₂ O ₃ grown via 45 ALD cycles on AlGa _N to confirm the thickness calculated via XPS spectra.....	108
Figure 3.5. <i>Ex-situ</i> XPS spectra of 35 Å Al ₂ O ₃ on AlGa _N /Ga _N : (a) survey in comparison with that of a clean AlGa _N /Ga _N substrate, (b) Al2p and (c) O1s.....	109
Figure 3.6. <i>In-situ</i> HREED patterns of Al ₂ O ₃ /AlGa _N /Ga _N after 0, 3, 9, 11 and 45 ALD cycles at 195 °C.....	109

Figure 3.7. <i>Ex-situ</i> RHEED images of 34 Å, 81 Å and 105 Å Al ₂ O ₃ films on AlGa _{0.34} N/GaN after RTA in N ₂ at 1000 °C for 1 min.	110
Figure 3.8. XRD spectra of a 34 Å γ -Al ₂ O ₃ film on 275 Å Al _{0.34} Ga _{0.66} N/5000Å GaN/AlN nucleation/sapphire: (a) specular scan and (b) phi scan on the γ -Al ₂ O ₃ (4 $\bar{4}$ 0) in-plane reflection in comparison with the off-peak phi scan, showing no measurable offset. The substrate peaks are incomplete because the scan was not performed over the peak to prevent the detector saturation. (c) In-plane radial scan on γ -Al ₂ O ₃ (4 $\bar{4}$ 0) reflection of a 105 Å film in comparison with the off-peak scan at phi=20°, showing a measurable offset. (d) Phi scans on γ -Al ₂ O ₃ (4 $\bar{4}$ 0) in-plane reflection of films with various thicknesses in comparison with that of the substrate AlGa _{0.34} N (20 $\bar{2}$ 0) reflection.....	112
Figure 3.9. (a) An HRTEM image of a ~130 Å γ -Al ₂ O ₃ film on Al _{0.34} Ga _{0.66} N/5000Å GaN/AlN/sapphire. The corresponding diffraction patterns generated from fast Fourier transformation (FFT) of (b) the γ -Al ₂ O ₃ film and (c) AlGa _{0.34} N substrate. (d) Atomic arrangements on AlGa _{0.34} N (0001) and γ -Al ₂ O ₃ (111) planes and a schematic showing the interface epitaxial alignment of γ -Al ₂ O ₃ (111) AlGa _{0.34} N (0001) and γ -Al ₂ O ₃ (1 $\bar{1}$ 0) AlGa _{0.34} N (11 $\bar{2}$ 0).	113
Figure 3.10. The effect of amorphous Al ₂ O ₃ thickness on passivating the AlGa _{0.34} N/GaN heterostructure: (a) sheet carrier density, and (b) carrier mobility (-○-) and sheet resistance (-■-).	115
Figure 3.11. Identification of N in AlN on Si and SiC via XPS analysis as a function of deposition temperature. The films were grown at (a) 350, (b) 360 and (c) 380 °C using TMA and 99.99% NH ₃ of 30 ALD cycles in a vacuum hot-wall reactor.....	116
Figure 3.12. <i>Ex-situ</i> XPS spectra of AlN grown on Si using TMA and N radicals at substrate temperatures of (a) 200 °C and (b) 25 °C in a vacuum reactor.	117
Figure 3.13. Composition of AlN on 4H-SiC, as determined by <i>ex-situ</i> XPS analysis, as a function of substrate and reactor wall temperatures using TMA and 99.99% NH ₃ under high-vacuum.	119
Figure 3.14. (a) Illustrations of deposition cycle sequences with different NH ₃ pulse time under various operation pressure ranges and (b) corresponding N atomic percentage in the deposited films on 4H-SiC, as determined by <i>ex-situ</i> XPS analysis, via 100 deposition cycles using TMA and 99.99% NH ₃ at a substrate temperature of 500 °C.	120
Figure 3.15. Composition of AlN on 4H-SiC, as determined by <i>in-situ</i> XPS analysis, as a function of ALD cycle using TMA and 99.99% NH ₃ at a substrate temperature of 540 °C under high vacuum.	121
Figure 3.16. Composition of ~250 Å AlN on 4H-SiC, as determined by <i>in-situ</i> XPS analysis, as a function of NH ₃ purity. The films were grown at a substrate temperature of 540 °C under high vacuum using TMA and (1) 99.99% NH ₃ , (2) 99.99994% NH ₃ (blue grade) or (3) blue grade NH ₃ with moisture removal.	122
Figure 3.17. (a) AlN growth rate (Å/cycle) on 4H-SiC as a function of substrate temperature using TMA and blue grade NH ₃ , the latter with (●) and without (○) moisture removal. (b) Normalized integrated absorbance of C-H ₃ stretching vibrations versus annealing temperature after a saturation TMA exposure at room temperature, adapted by (Dillon, Ott et al. 1995).....	123

Figure 3.18. Composition of AlN on 4H-SiC, as determined by <i>ex-situ</i> XPS analysis, as a function of substrate temperature using TMA and blue grade NH ₃ , the latter (a) with and (b) without moisture removal.	124
Figure 3.19. The thickness of AlN films on 4H-SiC measured via spectroscopic ellipsometry as a function of ALD deposition cycle using TMA and anhydrous NH ₃ at a substrate temperature of 540 °C.....	125
Figure 3.20. <i>In-situ</i> XPS spectra of 250 Å AlN on 4H-SiC, deposited using TMA and anhydrous NH ₃ at a substrate temperature of 540 °C: (a) survey and (b) N 1s.	126
Figure 3.21. <i>In-situ</i> RHEED images of (a) 4H-SiC (0001) substrate, (b) 150 Å AlN on 4H-SiC (0001) and (c) 150 Å AlN on 8° off-axis epi-SiC (0001). The films were grown using TMA and anhydrous NH ₃ at a substrate temperature of 540 °C.	127
Figure 3.22. An AFM image (1.9 μm × 1.9 μm) of 672 Å AlN on 4H-SiC, deposited using TMA and anhydrous NH ₃ at a substrate temperature of 540 °C, with an RMS roughness of 7.67 Å. .	127
Figure 3.23. Electrical performance of MIS capacitors made from 130 Å as-deposited AlN on n-type 8° off-axis epitaxial 4H-SiC (0001) with 9.62×10 ⁻⁴ cm ² Pt/Ti gate: (a) normalized current-voltage characteristic and (b) leakage current density as a function of applied electrical field in comparison with that of 1900 Å PVD AlN (Wolborski, Rosen et al. 2006) and 327 Å MBE AlN (Onojima, Suda et al. 2002) on SiC. The dotted lines indicate that the leakage current density reached 10 ⁻³ A/cm ² at 4.3 MV/cm.	128
Figure 3.24. <i>Ex-situ</i> XPS survey spectrum of a 150 Å AlN film on AlGaN/GaN, deposited using TMA and anhydrous NH ₃ at a substrate temperature of 540 °C.	129
Figure 3.25. The effect of as-deposited AlN thickness on passivating the AlGaN/GaN heterostructure: (a) sheet carrier density, and (b) carrier mobility (-○-) and sheet resistance (-■-).	131
Figure 4.1. The thickness of Li ₂ O (-□-), Al ₂ O ₃ (-▲-) and SiO ₂ (-●-) films grown on Si at 290 °C as a function of ALD deposition cycle. The thickness of Li ₂ O was calculated from Si signal attenuation from XPS spectra while the thicknesses of Al ₂ O ₃ and SiO ₂ were determined via spectroscopic ellipsometry.....	134
Figure 4.2. The thickness of LiAlSiO ₄ films grown on SiO ₂ /Au nanoparticles at 290 °C as a function of global cycle which composed of 10(Al-O)-6(Li-O)-4(Si-O). The film thickness was determined by HRTEM imaging.	135
Figure 4.3. (a) UPS spectra of Li _x Al _y Si _z O on Ge deposited via 5 global cycles of b(Al-O)-a(Li-O)-c(Si-O). (b) Calculated Li contents from the UPS spectra as a function of (Li-O) deposition cycle fraction (a/(a+b+c)).	136
Figure 4.4. HRTEM images of conformal ~8 nm LASO coatings, deposited via the 2(Al-O)-2(Li-O)-2(Si-O) deposition sequence, over (a) SiGe and (b) Si nanowires. (c) A scanning TEM (STEM) image of the coated Si nanowires in (b) and the corresponding EDX analysis along the cross-section, confirming the presence of Si, Al and O in the coating.	137
Figure 4.5. (a) An SEM image of a clean CVD synthesized Si NWs on Si substrate. (b) An HRTEM image of one of the Si NWs after LASO deposition of 6 global cycles of the 10(Al-O)-	

6(Li-O)-4(Si-O) sequence. (c) The corresponding EDX data confirmed the Si and Al presence and (d) the corresponding ICP-MS data confirmed the Li presence.	138
Figure 4.6. Cyclic voltammetry characteristics of a clean ITO (dash line) and 6 nm LiAlSiO ₄ coated ITO (solid line) in a solution of 1 mM ferrocene and 100 mM TBATFB in anhydrous PC.	139
Figure 4.7. (a) Nyquist plots of impedance data (symbols) of as-deposited LASO films prepared via 5 global cycles of b(Al-O)-a(Li-O)-c(Si-O), where b:a:c=2:16:2 (▲), 10:6:4 (○) and 16:2:2 (●), and the fittings (lines) for interpreting the ionic conductivity. (b) The corresponding ionic conductivity as a function of Li content.	140
Figure 4.8. Ionic conductivity as a function of film thicknesses with the films prepared via the 10(Al-O)-6(Li-O)-4(Si-O) sequence.....	141
Figure 4.9. Ion conductivity of LASO and LAO films prepared via 5 cycles of the 10(Al-O)-6(Li-O)-4(Si-O) (-●-) and 10(Al-O)-6(Li-O)-4(Al-O) (-▲-) sequences, respectively, as a function of temperature in comparison with data reported in literature of single crystal β-LiAlSiO ₄ (⊥c) (-Δ-) (Nagel and Bohm 1982), β-LiAlSiO ₄ (//c) (◇) (Nagel and Bohm 1982), LiAlSiO ₄ (-▼-) (Thangadurai and Weppner 2002) and Li _{4.4} Al _{0.4} Si _{0.6} O ₄ (-□-) (Thangadurai and Weppner 2002).....	143
Figure 4.10. (a) A deposition cycle map of LASO films on Si prepared by 5 global cycles of b(Al-O)-a(Li-O)-c(Si-O). (b) The corresponding compositional map, as determined by synchrotron UPS analysis, showing the cation contents varied with <i>in-situ</i> annealing temperatures: as-deposited (●), 500 °C (○), and 900 °C (●).....	144
Figure 4.11. XRD spectra of 10 nm LiAlSiO ₄ on Si (001) after post-deposition RTA at various temperatures, (1) as-deposited, (2) 500 °C and (3) 900 °C, for 90 seconds in N ₂ : (a) specular scans, (b) in-plane scans and (c) phi scan of 900 °C annealed film. (d) The corresponding UPS spectra to confirm the presence of cations, especially Li. Thin films were prepared using the 10(Al-O)-6(Li-O)-4(Si-O) sequence.....	146
Figure 4.12. XRD spectra of LASO on Si (001) after post-deposition RTA at 900 °C: (a) specular scan and (b) in-plane scan. The films were grown by 5 global cycles of b(Al-O)-a(Li-O)-c(Si-O), where b:a:c = (1) 12:4:4, (2) 7:11:2, (3) 5:9:6 and (4) 10:6:4.	147
Figure 4.13. Crystal models showing the interfacial epitaxial relationship of β-LiAlSiO ₄ on a Si (001) substrate: (a) side-view and (b) top-view.....	148
Figure 4.14. <i>In-situ</i> HRTEM cross-section images of a 6nm amorphous LiAlSiO ₄ coated SnO ₂ nanowire: (a) before and (b) during the lithiation process. SEAD patterns of the nanowire during the lithiation process: (c) unreacted site showing diffractions of SnO ₂ and (d) lithium incorporated site showing diffractions of Li ₁₃ Sn ₅ . (Zhang, Liu et al. 2012)	150

LIST OF TABLES

Table 1.1. Physical properties of promising wide bandgap semiconductors and Al-based gate dielectrics, in comparison with Si and GaAs. (Strite and Morkoc 1992; Yoder 1996; Kemerley, Wallace et al. 2002; Morkoc 2008).....	6
Table 1.2. Comparison of the electrical performances of various dielectric materials used in 4H-SiC MISFETs.....	14
Table 1.3. Comparison of the electrical performances of various dielectric materials (thickness t) used in passivated AlGaIn/GaN HEMTs or MIS-HEMTs. The values were compared with clean AlGaIn/GaN HEMTs prior to the coating of dielectrics and were shown in percentage (\uparrow representing an increase and \downarrow representing a decrease).	14
Table 1.4. Structural parameters and physical properties of various phases of alumina. (Lee, Cho et al. 2007; Lizarraga, Holmstroem et al. 2011)	16
Table 1.5. Structural parameters and physical properties of AlN polytypes. (Strite and Morkoc 1992; Morkoc, Strite et al. 1994; Willander, Friesel et al. 2006; Morkoc 2008)	19
Table 1.6. Gibbs free energies at various temperatures of possible interfacial reactions between the binary Al-based materials, Al ₂ O ₃ and AlN, and AlGaIn or SiC substrate.	25
Table 1.7. Comparison of various thin film deposition techniques for AlN and the corresponding material properties. (Stevens, Kinniburgh et al. 1995; Adam, Kolodzey et al. 2001; Engelmark, Iriarte et al. 2001; Onojima, Suda et al. 2002; Kakanakova-Georgieva, Persson et al. 2004; Onojima, Kaido et al. 2005; Wolborski, Rosen et al. 2006; Xi, Chen et al. 2006; Claudel, Blanquet et al. 2009)	27
Table 1.8. Electrode materials for Li-ion batteries and their capacities. (Tarascon and Armand 2001; Kiehne 2003; Needham, Wang et al. 2007; Chan, Peng et al. 2008; Chan, Zhang et al. 2008; Uchiyama, Hosono et al. 2008)	35
Table 1.9. Chemical reactions of electrodes during the charge and discharge of the graphite/LiCoO ₂ battery system with an equilibrium voltage of 3.9 V. (Kiehne 2003).....	35
Table 1.10. Calculated battery areal capacity and areal energy of three LIB systems in 3D layouts with an electrolyte thickness of 15 nm and voltage of 3.5V (assumption), showing that the energy density of the cell given a foot-print area of 1mm ² can be optimized to achieve the requirement (1J/mm ²) as an on-chip power source.....	42
Table 1.11. A list of Li ionic conductors with their ionic conductivities and corresponding activation energies (E_a). (Thangadurai and Weppner 2002).....	44
Table 1.12. Structural parameters and physical properties of LASO. (Li 1968; Johnson, Biefeld et al. 1976; Sartbaeva, Redfern et al. 2004).....	47
Table 1.13. The lattice point basis of a β -LiAlSiO ₄ unit cell. (Pillars and Peacor 1973)	49
Table 1.14. Comparison of deposition techniques for LiAlSiO ₄ and the corresponding material properties. (Johnson, Biefeld et al. 1976; Shin-ichi, Satoshi et al. 2004).....	52
Table 2.1. List of chemical precursors and process gases used in this work.	63

Table 2.2. A list of the spin orbit splitting energies and atomic sensitivity factors used in this work. (Briggs and Seah 1990)	74
Table 2.3. A list of fitting parameters for the Cauchy dispersion model used to describe optical properties of synthesized materials.	78
Table 2.4. A set of data measured from 150 Å AlN thin-film passivated AlGaIn/GaN via the Hall measurement with an input DC current and a magnetic field of 91 μA and 0.315 T, respectively.	95
Table 2.5. Basic electrical elements and their impedance.	99
Table 3.1. Dielectric/wide bandgap semiconductor material systems studied in this work for high-power device applications.	104
Table 3.2. Electrical results of ALD Al ₂ O ₃ and AlN films on two wide bandgap semiconductors, SiC and AlGaIn/GaN, in comparison with the results reported in literature. (Onojima, Suda et al. 2002; Chen, Chen et al. 2008; Basu, Singh et al. 2010; Liu, Yang et al. 2011)	132

ACKNOWLEDGEMENTS

I would like to thank all the collaborators and people who guided, supported and helped me on completing this thesis work. First and foremost, I want to thank my advisor, Professor Chang, for her instructions, comments and support on my research. Her dedication to teaching, research and work ethic is always an inspiration to me and drives me to challenge myself. Her communication and writing skills always impressed and inspired me to improve my skills. I would also like to thank the members of my thesis committee, including Professor Mark Goorsky, Professor Robert Hicks, Professor Tatiana Segura and Dr. Michael Wojtowicz at Northrop Grumman, for their advice and comments on my thesis work. I would also like to thank Dr. Vincent Gambin and Randy Hsing at Northrop Grumman for providing III-V semiconductor wafers and the help on material characterization that were critical to my study on III-V materials. I also owe thanks to Professor Stephen Sadow of the University of South Florida for growing the SiC epitaxial layers that were important to my device fabrication. I would like to thank Professor Bruce Dunn, Nick Cirigliano and Daniel Membreno as well for their assistance on the battery project, especially the knowledge of battery technology and material characterizations. I also want to thank Mike Toney, Steven Sun and the technicians at the Stanford Synchrotron Radiation Laboratory for their assistance with synchrotron x-ray scattering and ultraviolet photoemission spectroscopy measurements, which proved to be critical to the analysis of epitaxial LiAlSiO_4 films. I would like to thank the Center for Integrated Nanotechnologies (CINT) for the collaboration on nanowire battery measurements; Dr. Tom Picraux at Los Alamos National Laboratory and Professor Yu Huang for providing nano-featured materials. I am also grateful for the funding support of the National Science Foundation (NSF)

and Defense Advanced Research Projects Agency (DARPA) Integrated Micro/Nano-Electromechanical Transducers (iMINT) Center for my research at UCLA.

Integral as well to the success in my research are my labmates. I appreciate all the support and help from the Chang lab members: my mentor Carey Tanner for teaching me data analysis, device fabrication and operation of high-vacuum ALD reactor; senior students Monica Sawkar-Mathur, Ryan Martin and John Hoang for their patient guidance on high-vacuum parts, passing down the lab responsibilities and encouragement; my fellow labmate James Dorman for taking TEM images, trying to help me on research and having him by my side from the first day we met in class, prelims, conferences, commencement and thesis writing; coffee and thesis buddy Nathan Marchack for his company while I had to stay late or spent the night in lab working on my thesis writing; Vladan Jankovic for his impressive scientific thinking and providing useful suggestions; the students who entered the lab later, including Calvin, Jea, Diana and Jack, for taking over the lab responsibilities and doing tedious or menial tasks that we senior students felt were unworthy of our time and the postdocs, including Dr. Jiurong Liu, Dr. Yuanbing Mao, Dr. Jerry Hsu, Dr. Feng Zhang and Dr. Ju Choi, for their help with my project and useful instructions on doing research. I want to thank Dr. Wilson Lin for the resources from the Nanolab and suggestions on job searching and all the Nanolab staff members. I would also like to thank the staff of the Machine Shop and Tool Crib for their help which minimized the downtime of my reactor, specifically when we moved the lab.

Last, I want to thank my friends and family members for their support. The list of individuals I should thank could go on for pages and pages, and I sincerely apologize if any individuals were left out.

VITA

2006 B.S., Chemical Engineering
National Taiwan University, Taipei, Taiwan

June 2011 AVS Graduate Student Award
11th International Conference on Atomic Layer Deposition

PUBLICATIONS AND PRESENTATIONS

L. Q. Zhang, X. H. Liu, Y.-C. Perng, J. Cho, J. P. Chang, S. X. Mao, Z. Z. Ye and J. Y. Huang, "Direct observation of Sn crystal growth during the lithiation and delithiation processes of SnO₂ nanowires," *Micron*. (2012).

H. Zhou, J. A. Dorman, Y.-C. Perng, J. P. Chang and J. Liu, "Temperature-dependent electron transport in highly ordered Co/Al₂O₃ core-shell nanocrystal memory synthesized with di-block co-polymers," *App. Phys. Lett.* **111**, 064505 (2012).

F. Zhang, Y.-C. Perng, J. H. Choi, T. Wu, T.-K. Chung, G. P. Carman, C. Locke, S. Thomas, S. E. Saddow and J. P. Chang, "Atomic layer deposition of Pb(Zr, Ti)O_x on 4H-SiC for metal-ferroelectric-insulator-semiconductor diodes," *J. Appl. Phys.* **109**, 124109 (2011).

H. Zhou, J. A. Dorman, Y.-C. Perng, S. Gachot, J. -G. Zheng, J. P. Chang and J. Liu, "Memory Characteristics of ordered Co/Al₂O₃ core-shell nanocrystal arrays assembled by diblock copolymer process," *App. Phys. Lett.* **98**, 192107 (2011).

H. Zhou, J. A. Dorman, Y.-C. Perng, S. Gachot, J. Huang, Y. Mao, J. P. Chang and J. Liu, "Co/HfO₂ Core-Shell Nanocrystal Memory," *Material Research Society Symposium Proceedings*. **1250** (2010).

M. Sawkar-Mathur, Y.-C. Perng, J. Lu, H.-O. Blom, J. Bargar, and J. P. Chang, "The effect of aluminum oxide incorporation on the material and electrical properties of hafnium oxide on Ge," *App. Phys. Lett.* **93**, 233501 (2008).

C. M. Tanner, Y.-C. Perng, C. Frewin, S. E. Saddow and J. P. Chang, "Electrical performance of Al₂O₃ gate dielectric films deposited by atomic layer deposition on 4H-SiC," *App. Phys. Lett.* **91**, 203510 (2007).

Y.-C. Perng, and J. P. Chang, presentation on "Engineering AlN Thin Films by Atomic Layer Deposition on Wide Bandgap Semiconductors as Gate Dielectric," *AVS 57th International Symposium & Exhibition*, Nashville, TN, November, 2011.

Y.-C. Perng, J. Cho, D. Membreno, N. Cirigliano, B. Dunn and J. P. Chang, presentation on "Engineering Li_xAl_ySi_zO Ion Conducting Thin Films by Atomic Layer Deposition for Lithium-ion Battery Applications," *AVS 57th International Symposium & Exhibition*, Nashville, TN, November, 2011.

Y.-C. Perng, and J. P. Chang, presentation on "Engineering AlN Thin Films by Atomic Layer Deposition on Wide Bandgap Semiconductors as Gate Dielectric," *2011 AIChE Annual Meeting*, Minneapolis, MN, October, 2011.

Y.-C. Perng, J. Cho, D. Membreno, N. Cirigliano, B. Dunn and J. P. Chang, presentation on "Engineering Li_xAl_ySi_zO Ion Conducting Thin Films by Atomic Layer Deposition for Lithium-ion Battery Applications," *2011 AIChE Annual Meeting*, Minneapolis, MN, October, 2011.

Y.-C. Perng, J. Cho, D. Membreno, N. Cirigliano, M. F. Toney, B. Dunn and J. P. Chang, presentation on “Engineering $\text{Li}_x\text{Al}_y\text{Si}_z\text{O}$ Thin Films as a Solid Electrolyte for 3D Microbatteries,” *11th International Conference on Atomic Layer Deposition*, Cambridge, MA, June, 2011.

Y.-C. Perng, F. Zhang, J. H. Choi and J. P. Chang, poster on “Engineering AlN and PZT Thin Films by Atomic Layer Deposition on Wide Bandgap Semiconductors,” *11th International Conference on Atomic Layer Deposition*, Cambridge, MA, June, 2011.

Y.-C. Perng, J. Cho, D. Membreno, M. F. Toney, B. Dunn and J. P. Chang, poster on “Engineering $\text{Li}_x\text{Al}_y\text{Si}_z\text{O}$ Thin Films as a Solid Electrolyte for 3D Microbatteries,” *2011 MRS Spring Meeting*, San Francisco, CA, April, 2011.

Y.-C. Perng, and J. P. Chang, poster on “Engineering Epitaxial AlN Thin Films by Atomic Layer Deposition on Wide Bandgap Semiconductors,” *2011 MRS Spring Meeting*, San Francisco, CA, April, 2011.

Y.-C. Perng, J. Cho, V. Jankovic, M. F. Toney, D. Membreno, B. S. Dunn and J. P. Chang, presentation on “Synthesis of LiAlSiO_4 Electrolyte Layers for Applications in 3-D Micro-Batteries,” *2010 AIChE Annual Meeting*, Salt Lake City, UT, November, 2010.

Y.-C. Perng, J. Cho, D. Membreno, B. S. Dunn and J. P. Chang, presentation on “Engineering $\text{Li}_x\text{Al}_y\text{Si}_z\text{O}$ Thin Films as a Solid Electrolyte for 3D Microbatteries,” *AVS 57th International Symposium & Exhibition*, Albuquerque, NM, October, 2010.

F. Zhang, T. E. Quicquel, Y.-C. Perng, T. Wu, G. P. Carman, S. Tolbert and J. P. Chang, presentation on “Atomic Layer Deposited $\text{Pb}(\text{Zr,Ti})\text{O}_x$ Films Composited as Ferroelectric and Multiferroic Materials with CoFe_2O_4 .” *AVS 57th International Symposium & Exhibition*, Albuquerque, NM, October, 2010.

Y.-C. Perng and J. P. Chang, presentation on “Engineering Epitaxial AlN Thin Films on 4H-SiC,” *2010 MRS Spring Meeting*, San Francisco, CA, April, 2010.

Y.-C. Perng, J. Cho, C. Eisler, N. Cirigliano, D. Membreno, B. S. Dunn and J. P. Chang, presentation on “Engineering LiAlSiO_4 via Atomic Layer Deposition for the Electrolyte Material in Lithium Micro-batteries,” *2010 MRS Spring Meeting*, San Francisco, CA, April, 2010.

F. Zhang, Y.-C. Perng and J. P. Chang, presentation on “Atomic Layer Deposition of $\text{Pb}(\text{Zr,Ti})\text{O}_x/\text{Al}_2\text{O}_3$ Ultrathin Films on 4H-SiC” *MRS Spring Meeting*, San Francisco, CA, April, 2010.

H. Zhou, J. Huang, J. Liu, J. A. Dorman, Y. Mao, Y.-C. Perng, S. Gachot and J. P. Chang, presentation on “Co/HfO₂ (Al₂O₃) Core Shell Nanocrystal Memory,” *MRS Spring Meeting*, San Francisco, CA, April, 2010.

Y.-C. Perng and J. P. Chang, presentation on “The Growth of AlN Thin Films on Wide Bandgap Semiconductors,” *AVS 56th International Symposium & Exhibition*, San Jose, CA, November, 2009.

Y.-C. Perng and J. P. Chang, presentation on “The Growth of AlN Thin Films on Wide Bandgap Semiconductors,” *2009 AIChE Annual Meeting*, Nashville, TN, November, 2009.

CHAPTER 1: INTRODUCTION

Further miniaturization of portable power electronics can be seen as limited by dielectrics on wide bandgap (WBG) semiconductors and the integration of on-chip energy storage sources to support the device operation with optimum performance. In both power devices and energy storage applications, high quality electrical insulating layers synthesized at low temperatures with surface conformality and precise thickness controls at atomic scales are important. WBG semiconductors, silicon carbide (SiC) and gallium nitride (GaN), are promising semiconductor materials for building high-power devices, such as SiC metal-insulator-semiconductor field-effect-transistors (MISFET) and AlGaN/GaN based MIS-high electron mobility transistors (HEMT). However, these devices are not primarily used in consumer industry due to the lack of reliable gate dielectric layers. For on-chip energy sources, incorporating three-dimensional (3D) battery structures by fabricating the electrodes into non-planer high aspect ratio features is a potential approach to build microbatteries with the required power density. To make a 3D lithium-ion (Li-ion) microbattery, the challenge is to synthesize a conformal, pin-hole free and ionic conductive but electrical insulating thin-film material over the high aspect ratio electrodes as the electrolyte layer. Aluminum-based materials Al_2O_3 and AlN possess properties suitable for gate dielectric materials in WBG-based power electronic devices while LiAlSiO_4 with 1D Li-ion channels and high thermal stability is an attractive electrolyte material in Li-ion batteries. Among thin-film synthesis techniques, atomic layer deposition (ALD) is chosen in this work to synthesize these Al-based thin film materials for power devices and battery applications.

1.1 Motivation

Semiconductor electronic devices like radio frequency (RF) electronics that operate at high-power and high-temperature conditions have broad applications in aerospace, automotive, defense industries and even personal communication equipments. (Kemerley, Wallace et al. 2002; Mishra, Parikh et al. 2002) WBG semiconductors silicon carbide (SiC) and gallium nitride (GaN) are potential substrate materials for high-power communication devices because their physical properties are superior to those of Si or GaAs, a convention material for the application. (Morkoc, Strite et al. 1994; Yoder 1996) However, the MISFET or MIS-HEMT devices using these WBG materials have not yet been primarily used in consumer industry due to the lack of reliable gate dielectric layers. (Ostling, Ghandi et al. 2011) In these applications, dielectrics must have enough band offsets and high quality interfaces to the substrate for providing adequate barrier heights and eliminating the leakage current.

To reduce the portable equipment sizes, these electronics have entered into nano-scale fabrication, making it possible to consider the integration of miniaturized batteries as on-chip energy sources to enable autonomous operation of these electronic devices. Li-ion batteries are known of their energy storage capability, possessing a higher energy density compared to other batteries, making them attractive for powering portable devices. However, the current layout with two-dimensional (2D) plane electrodes cannot provide sufficient power with a reduced footprint for the on-chip usage. Through incorporating 3D structures into the battery design via fabricating the electrodes into non-planar geometries, the power and energy density of the cell with a given footprint area can be optimized simultaneously to meet the requirement as an on-chip energy source. (Long, Dunn et al. 2004) However, the challenge remains to engineer a conformal and pin-hole free electrolyte layer over the high aspect ratio electrodes. Since liquid

electrolytes fail to provide uniform coatings as the scale reaches their compressibility, synthesizing conformal and ultra-thin solid-state ionic conductive films on electrode surfaces to compensate their intrinsically lower ionic conductivity compared to liquid-phase electrolytes is a critical issue for the 3D micro-battery fabrication.

This thesis investigates alternative aluminum-based thin film materials for WBG (SiC/GaN) based power devices and Li-ion batteries.

1.2 Al-based Materials

Aluminum (Al) is the third most abundant element after silicon (Si) and oxygen (O) and the most abundant metal in the earth crust so it can be easily accessed. (Horn 1967) Metallic Al is a soft, lightweight and easily machined material, making it and its alloys important as structural components in various areas, such as aerospace industry and transportation. Due to its strong affinity to oxygen, Al is rarely found in the elemental state but in oxides or silicates, widely existing in minerals and ceramics. (Horn 1967) When Al forms compounds with other elements, its face-centered cubic (FCC) structure (Horn 1967) as well as intrinsic material properties change as function of the type and concentration of incorporated elements. Therefore, a variety of Al-based materials with desired material properties can be synthesized by introducing specific elements for different applications. For instance, semiconductors or ionic conductors can be formed from metallic Al by introducing elements such as nitrogen (N) or lithium (Li), as shown in Figure 1.1.

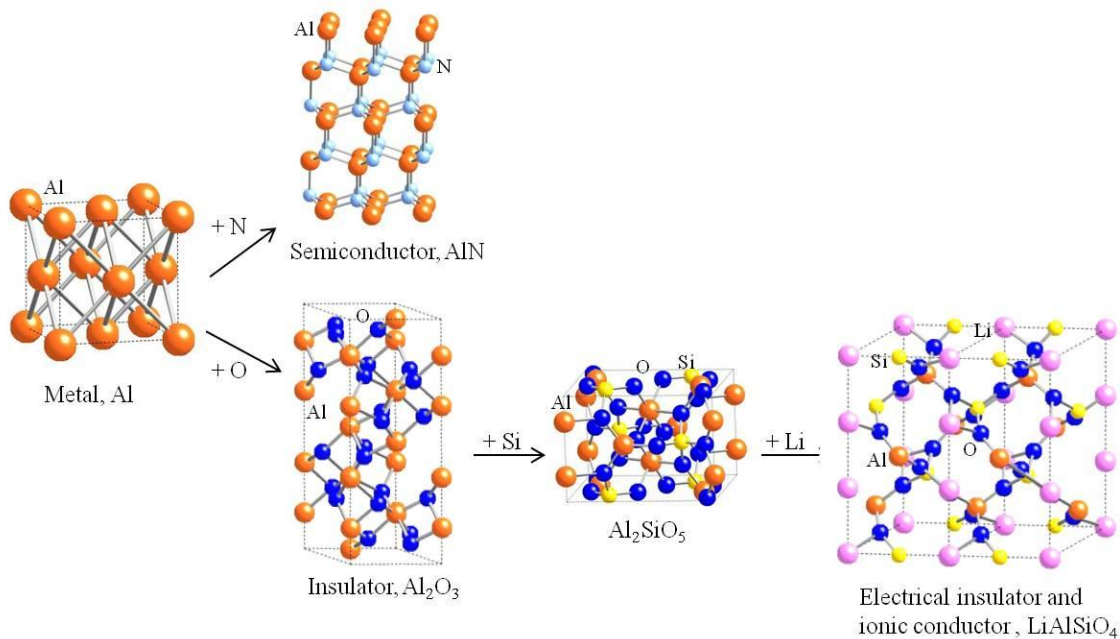


Figure 1.1. Structures and conductivities of Al-based materials, Al_2O_3 , AlN and LiAlSiO_4 , as elements are introduced into Al. (Horn 1967; Winter and Ghose 1979; Ishizawa, Miyata et al. 1980; Gil 1998; Sartbaeva, Redfern et al. 2004)

When either O or N atoms are incorporated into metallic Al (coordination number is 8), electrical conductivity of the material changes into insulating Al_2O_3 or semi-conducting AlN . Al_2O_3 is known as a high dielectric constant material and has been widely used for surface passivation or as dielectrics in semiconductor electronic devices. AlN , possessing similar material properties to those of Al_2O_3 , can potentially be used as gate dielectrics or surface passivation layers in electronic power devices as well, as discussed in Section 1.3. Other than electrical conductivity, ionic conductivity of an Al-based material can also be adjusted by incorporating cations such as mobile Li ions. For instance, LiAlSiO_4 , a composite of $\text{Li}_2\text{O}-\text{Al}_2\text{O}_3-2\text{SiO}_2$, is known as an ionic conductor which can work at high temperatures. Its special crystal structure of the β -eucryptite phase possesses one dimensional (1D) Li-ion channels,

making it a promising electrolyte material for solid-state Li-ion batteries (Johnson, Morosin et al. 1975), as discussed in Section 1.4.

The following sections describe the criteria for making reliable WBG semiconductor based devices and engineering rechargeable 3D Li-ion microbatteries. The requirements for dielectric and electrolyte materials for these applications are also discussed to demonstrate how Al-based materials play a role on enhancing the reliability and enable the autonomous operation of on-chip high-power communication devices.

1.3 Wide Bandgap Semiconductor Based High-Power Devices

Wide bandgap (WBG) semiconductors with bandgaps larger than ~ 2.2 eV, such as SiC and GaN, are suitable for power devices because of their inherent material properties. Table 1.1 summarizes the material and electrical properties of SiC and GaN in comparison with those of Si and gallium arsenide (GaAs), conventional materials for power devices, and those of AlN and Al₂O₃, potential gate dielectric materials. The saturation electron velocities (v_{sat}) in both 4H-SiC and GaN are approximately twice as large as that in either Si or GaAs, thus proving faster device speeds under high operating electric fields (Taur and Ning 1998), without being affected by the heat generated during the operation due to their higher breakdown fields and larger bandgaps. (Weitzel, Palmour et al. 1996) Therefore, 4H-SiC and GaN are superior than Si and GaAs for high-power device applications, such as radio frequency (RF) electronics, primarily used in radar, communication electronics, aerospace and automotive industry. (Strite and Morkoc 1992)

Table 1.1. Physical properties of promising wide bandgap semiconductors and Al-based gate dielectrics, in comparison with Si and GaAs. (Strite and Morkoc 1992; Yoder 1996; Kemerley, Wallace et al. 2002; Morkoc 2008)

Property	Silicon	GaAs	4H SiC	w-GaN	w-AlN	Al ₂ O ₃
Lattice constant (Å)	5.43	5.65	3.07 10.05	3.19 5.19	3.11 4.98	
Density (g/cm ³)	2.328		3.211	6.095	3.255	
Bandgap (eV)	1.1	1.43	3.26	3.45	6.2	7.0
Saturated electron Velocity (cm/s)	1.0×10 ⁻⁷	1.0×10 ⁻⁷	2.0×10 ⁻⁷	2.2×10 ⁻⁷	1.4×10 ⁻⁷	
Electron mobility (cm ² /V-s)	1500	8500	1140	1250		
Hole mobility (cm ² /V-s)	600	400	50	850		
Breakdown (10 ⁵ V/cm)	3	6	30	>10	12-18	135
Dielectric constant	11.8	12.5	9.6/10	9	8.5	9.0
Resistivity (Ω-cm)	1000	10 ⁸	>10 ¹²	>10 ¹⁰	>10 ¹³	
Thermal Conductivity (W/cm-K)	1.5	0.46	4.9	1.3	2.0	0.5
Hardness (kg/mm ²)	1000	600	2130		1200	
Heterostructure	SiGe/Si	AlGaAs/GaAs InGaAs/GaAs	-	AlGaN/GaN InGaN/GaN	AlN/GaN	

1.3.1 SiC MISFET and AlGaN/GaN HEMT

Using SiC for operation at high temperatures, high powers and high frequencies can be applied to build power devices with various structures. (Willander, Friesel et al. 2006) MISFET structure is known as one device layout for high-power applications because of their high speed and low power loss. (Morkoc, Strite et al. 1994) Besides, its ability of forming native oxide on the surface was considered as an advantage for developing MIS-based SiC power devices. (Singh

2006) However, physics-based issues which degrade the device reliability, such as high interface state density, have found in SiO₂/SiC junctions. The interface states can be interface traps due to the existence of carbon clusters or dangling bonds on the SiC surface, which may trap electrons and result in high mobile electron scattering and low electron mobility in the channel region. (Singh 2006) The trapped electrons at the interface states may serve as the source of Fowler-Nordheim tunneling current into the dielectric which lowers the device reliability. Therefore, finding alternative dielectrics is required for enhanced reliability of SiC-based MISFETs for high-power device applications.

Other WBG semiconductors, such as GaN, possess breakdown field and thermal conductivity poorer than SiC so they find limited application in MISFETs but are more desirable in HEMTs. HEMTs are also known as the modulation-doped field-effect transistors (MODFET), heterojunction field-effect transistors (HFET), two-dimensional electron-gas field-effect transistors (TEGFET), and selectively doped heterojunction transistors (SDHT). In HEMTs, heterojunctions have to be formed by two semiconductors with a small lattice mismatch to minimize interface traps, interface defects or dislocations from the interface bonding. Wurtzite AlN ($E_g \sim 6.2$ eV) and GaN ($E_g \sim 3.45$ eV) have considerably different band gaps but similar lattice constants (in a), 3.11 Å and 3.19 Å, respectively, thus Al_xGa_{1-x}N alloy is a suitable material to form a heterojunction with GaN. By varying the Al content, the bandgap of Al_xGa_{1-x}N can be further adjusted from 3.4 eV to 6.2 eV. The most commonly used heterojunction in a GaN-based HEMT is Al_{0.3}Ga_{0.7}N ($E_g \sim 4.1$ eV, $\kappa \sim 9$) on GaN, with one of them n-type doped or both intrinsic. What differentiates a HEMT from a conventional FET is that the channel is formed by a heterojunction, across which carriers can move without being scattered by doping impurities upon an applied gate voltage thus achieving a higher mobility. (Sze and Ng 2007)

The working principle of such an AlGaN/GaN heterostructure in a device is based on the two-dimensional electron gas (2DEG) accumulated at the heterojunction due to the band offset between AlGaN and GaN. Without doping, the HEMT structure functions with carriers induced by the polarization field at the heterojunction due to the polarization from material themselves and the strain between AlGaN and GaN. Positive charges (+Q) can be induced at the $\text{Al}_x\text{Ga}_{1-x}\text{N}/\text{GaN}$ interface with negative charges (-Q) induced on the surface, as shown in Figure 1.2 (a). Due to the polarization dipole $\pm Q$, an opposing dipole composed of a positive charged surface donor (density as N_D^+) and a 2DEG at the interface (density as n_s) form to neutralize the charges, as shown in Figure 1.2 (b). (Mishra, Parikh et al. 2002) On the other hand, the carriers are primarily from the intentional doping when doped AlGaN is used. Energy band diagrams of a metal/n-AlGaN/i-GaN device are shown in Figure 1.3, in which the band alignment between AlGaN and GaN is assumed to be symmetric. Due to the higher conduction band energy of the AlGaN layer, electrons in this layer tend to move towards the interface with GaN at equilibrium while some holes may be induced in GaN at small concentrations. When a negative gate voltage is applied on the metal, the conduction band of GaN near the interface bends towards the Fermi energy with high concentration electrons accumulated, and the heterojunction acts as a quantum well to confine the electrons, known as 2DEG. When the voltage exceeds the threshold voltage, the device is on, thus termed the enhancement mode device. As the applied gate voltage increases, more electrons accumulate within the interface, increasing the electron density (n_s) in the 2DEG as well as the source and drain current. Similar to other FETs, the conductivity of this layer or channel is controlled by the voltage applied to the gate.

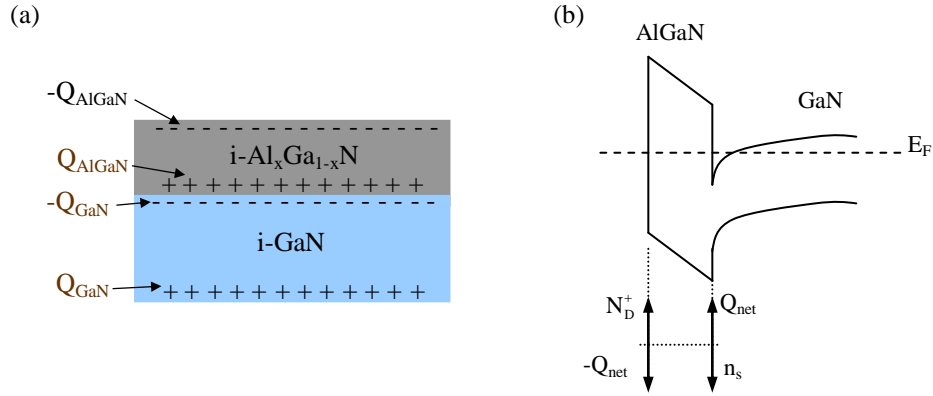


Figure 1.2. Illustrations of an intrinsic AlGaN/GaN heterostructure: (a) net charges at the interface, resulted from the net spontaneous polarization and piezoelectric polarization between i-AlGaN and i-GaN, and (b) energy diagram illustrating the opposite dipoles electrically balancing the net charges due to polarization. (Mishra, Parikh et al. 2002)

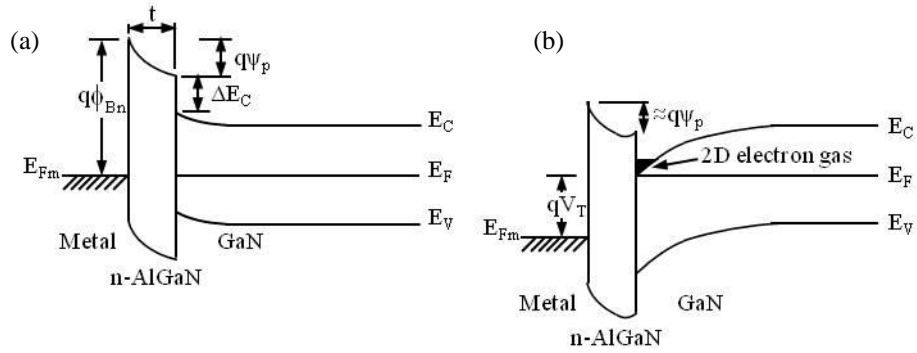


Figure 1.3. Energy band diagrams of an n-AlGaN/i-GaN HEMT at (a) equilibrium and (b) the onset of threshold. (Sze and Ng 2007) The ψ_p is the potential variation, ϕ_{Bn} is the barrier height, t is the thickness of AlGaN film and V_T is the threshold voltage.

In general, the density of 2DEG (n_s) is a function of the modulation doping and the polarization field between the AlGaN/GaN heterostructure. The induced polarization field varies with the Al mole fraction (x) due to the different spontaneous polarization and piezoelectric constants (e , usually with subscript indicating the orientations) of the two materials, w-AlN ($e_{31}=-0.6$ and $e_{33}=1.46$ C/m²) and w-GaN, ($e_{31}=-0.49$ and $e_{33}=0.73$ C/m²) and the strains from

lattice mismatch. The polar natures of $\text{Al}_x\text{Ga}_{1-x}\text{N}$ and GaN provide a net spontaneous polarization:

$$P_{sp} = P_{sp}^{\text{AlGa}} - P_{sp}^{\text{GaN}} = [x(P_{sp}^{\text{AlN}}) + (1-x)P_{sp}^{\text{GaN}}] - P_{sp}^{\text{GaN}} \quad (1.1)$$

where $P_{sp}^{\text{AlN}} = -0.081$ and $P_{sp}^{\text{GaN}} = -0.029 \text{ C/m}^2$. (Singh 2003) The tensile strain caused by the lattice difference between AlGa and GaN results in a piezoelectric polarization:

$$P_{pz} = e_{33}\varepsilon_{zz} + e_{31}(\varepsilon_{xx} + \varepsilon_{yy}) \quad (1.2)$$

where ε is the strain between the two materials. (Singh 2003) Since the values of these parameters can be found or calculated, the net polarization (P) within the AlGa/GaN heterojunction can be written as a function of Al mole fraction (x):

$$P(x) = P_{pz} + P_{sp} = [-(3.2x - 1.9x^2) - 5.2x] 10^{-6} \text{ C/cm}^2 \quad (1.3)$$

From equation (1.3), the net polarization as well as n_s increases with increasing Al contents. (Mishra, Parikh et al. 2002) In the absence of modulation doping, the induced polarization field yields a n_s value: $n_s = P(x)/e = \sim(5x) 10^{13} \text{ cm}^{-2}$. (Luo, Johnson et al. 2002) Unlike n_s which increases with increasing Al contents, electron mobility (μ_s) has a maximum value when the Al content is between 27%~35%. (Lu, Kumar et al. 2003) (Derluyn, Boeykens et al. 2005) The maximum of μ_s is due to the competition between two effects. When n_s is small, mobility increases with the density; once n_s is larger than a certain value, the scattering among electrons become important resulting a decrease in the mobility. Therefore, $\text{Al}_x\text{Ga}_{1-x}\text{N}$ with an Al mole fraction of 30% is usually used for optimized mobility at the 2DEG channel. The n_s for this composition is $\sim 1.5 \times 10^{13} \text{ cm}^{-2}$, about 5-10 times higher than that of typical GaAs or InP HEMTs. (Morkoc, Cingolani et al. 1999)

1.3.2 Criteria for Dielectrics in HEMT

Although the AlGaIn/GaN heterostructure in an HEMT offers improved carrier mobility compared to a MISFET, it failed to provide required performance for high-power applications due to issues related to drain current collapse, I-V dispersion, gate- and drain-lag, large gate leakage. “Current collapse”, as shown in Figure 1.4 (a), indicates decreases of the drain current (I_D) compared to theoretical values. (Hasegawa, Inagaki et al. 2003) I-V dispersion, also known as gate-lag, illustrates I_D of AC is less than the value of DC and with an increase in V_{knee} , shown in Figure 1.4 (b). (Luo, Mehandru et al. 2002) The maximum saturated output power of the device can be estimated as: $P_{sat} = \Delta I \times \Delta V / 8$, where $\Delta V = 2(V_D - V_{knee})$ and $\Delta I = I_{D,max}$ (mA/mm). (Green, Chu et al. 2000) Therefore, the reduced $I_{D,max}$ and increased V_{knee} from current collapse or current dispersion lead to a lower output power than the expected value as well as a reduced efficiency ($Eff = P_{out}/Gain$) of the devices. These two problems are generally due to the presence of surface states between the gate and drain of the devices or trapping centers in the resistive buffer underlying the active channel. (Luo, Mehandru et al. 2002; Horio, Takayanagi et al. 2006) It has been found that these two issues can be mitigated with dielectrics deposited on the AlGaIn surface to serve as a passivation layer, as shown in Figure 1.5 (a). (Binari, Ikossi et al. 2001; Kim, Thompson et al. 2003; Derluyn, Boeykens et al. 2005)

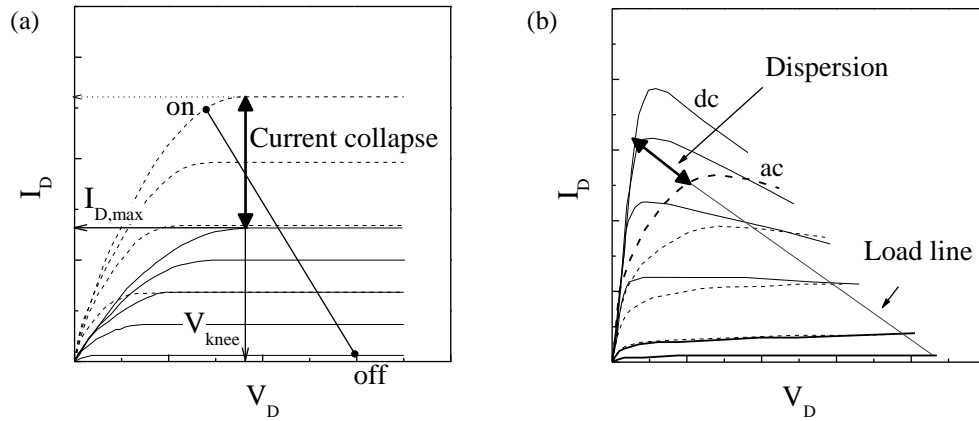


Figure 1.4. Illustrations of current collapse and dispersion issues for AlGaIn/GaN HEMTs. (a) Drain current collapse refers to the actual $I_{D,max}$ (solid) being lower than the theoretical value (dash). (Hasegawa, Inagaki et al. 2003) (b) Current dispersion refers to the difference between a large-signal AC and DC pulse on the gate. (Mishra, Shen et al. 2008)

In addition, the relatively high leakage current from the Schottky metal gate, known as gate leakage current (I_g), is another major issue of the device. By incorporating a gate dielectric layer into device fabrication for MIS-HEMTs, as shown in Figure 1.5 (b), the gate leakage issue can be depressed by the increased barrier height, as shown in Figure 1.5 (c). In the layout, dielectrics are used to not only substitute the Schottky contact between the gate and AlGaIn for increasing the resistance (or barrier heights) to reduce the leakage current but also serve as passivation layers on the surface. It combines the advantages of a MISFET and a HEMT as less leakage current and high mobility channels provided by the 2DEG, respectively.

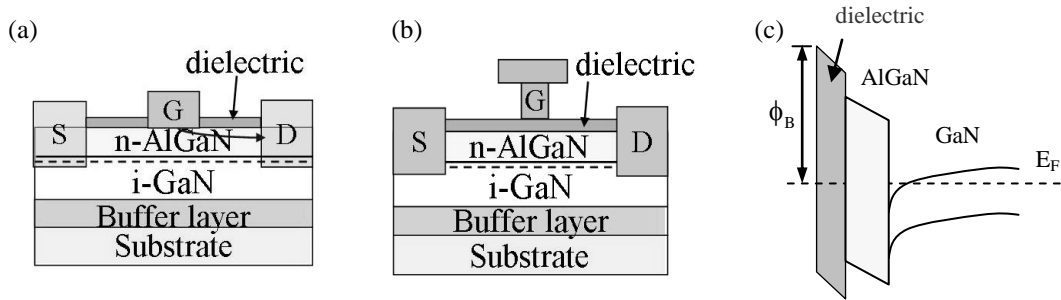


Figure 1.5. Schematic diagrams of (a) a passivated AlGaIn/GaN HEMT to eliminate the current collapse issue and (b) a MIS-HEMT structure with a dielectric layer serving as the surface passivation and gate dielectric layer. (c) The corresponding band diagram of (b).

Engineering dielectric materials with properties incompatible with the substrate material may change the electrical performance of devices in both cases of SiC and AlGaIn/GaN. Since both of them are for high-temperature and high-power applications, the criteria for choosing gate dielectrics are similar. In general, advantageous properties of alternative dielectrics for improving performance and reliability of SiC and AlGaIn/GaN MIS-based power devices include high dielectric constant (κ), high dielectric breakdown strength, large valence and conduction band offsets, low interface state density and stable interface. (Singh 2006) High- k dielectrics, such as SiO_2 , Si_3N_4 , SiON , Sc_2O_3 , ZrO_2 , HfO_2 , and Al_2O_3 , with thicknesses of 10-80 nm have been implemented on either 4H-SiC for MISFETs (Mahapatra, Chakraborty et al. 2007; Tanner, Perng et al. 2007; Posadas, Walker et al. 2008) or AlGaIn/GaN for MIS-HEMTs with enhanced maximum drain current densities (Mehandru, Luo et al. 2003; Balachander, Arulkumaran et al. 2005; Liu, Chor et al. 2007; Chao, Xingzhao et al. 2011). Table 1.2 and Table 1.3 summarizes the device performance of SiC MISFETs and AlGaIn/GaN MISHEMTs using various dielectric films, respectively. For AlGaIn/GaN HEMTs, the 2DEG properties may vary with the processing and surface treatment used for the device fabrication so the effect of each dielectric material on the AlGaIn/GaN HEMTs cannot be judged by directly comparing their 2DEG

properties. Therefore, Table 1.3 lists not only the electrical performance of dielectric passivated HEMTs or MIS-HEMTs but also the increase or decrease in percentage using the electrical performance of clean HEMTs (prior to the dielectric growth) reported in each work.

Table 1.2. Comparison of the electrical performances of various dielectric materials used in 4H-SiC MISFETs.

Materials	Thickness (Å)	D_{it} (10^{11} $\text{cm}^{-2}\text{eV}^{-1}$)	E (MV/cm) at $J_{\text{leak}}=10^{-3}$ A/ cm^2)	Reference
Al ₂ O ₃	40	-	8	(Liu, Yang et al. 2011)
AlN	2000	7-40	-	(Onojima, Kaido et al. 2005)
	327 / 357	-	1.3 / 3	(Onojima, Suda et al. 2002)
HfO ₂	450	50	5.3	(Taube, Gieraltowska et al. 2011)
SiO ₂	500	-	5	(Usman, Hallen et al. 2011)
HfO ₂ /SiO ₂	250/60	7	5.7	(Mahapatra, Chakraborty et al. 2007)

Table 1.3. Comparison of the electrical performances of various dielectric materials (thickness t) used in passivated AlGaIn/GaN HEMTs or MIS-HEMTs. The values were compared with clean AlGaIn/GaN HEMTs prior to the coating of dielectrics and were shown in percentage (↑ representing an increase and ↓ representing a decrease).

	t (Å)	n_s (10^{12} cm^{-2})	μ_s (10^3 cm^2/Vs)	$I_{D \text{ max}}$ (mA/mm)	Reference
Al ₂ O ₃	250	14 (9%↑)	0.84 (5%↓)	350 (4%↑)	(Basu, Singh et al. 2010)
AlN	30	-	-	327 (16%↑)	(Cho, Shimizu et al. 2002)
	1200	11 (29%↑)	1.3 (15%↑)	-	(Chen, Chen et al. 2008)
	40	7 (19%↑)	-	530 (46%↑)	(Stoklas, Gregusova et al. 2011)
Si ₃ N ₄	800	6.9 (3%↑)	-	805 (5%↑)	(Jeon and Lee 2005)
	1200	12 (41%↑)	1.2 (5 %↑)	-	(Chen, Chen et al. 2008)
SiO ₂	370	-	-	856 (71%↑)	(Arulkumaran, Egawa et al. 2005)
	100	9 (30%↑)	1.7 (10%↓)	960 (25%↑)	(Marso, Heidelberg et al. 2006)
HfO ₂	200	11 (31%↑)	1.0 (11%↓)	587 (17%↑)	(Liu, Chor et al. 2007)

The enhancements in HEMTs are due to the increased 2DEG density (n_s) from surface passivation. Because of the increased electron scattering, decreases in the mobility were found in most of these cases. (Liu, Chor et al. 2007) Materials with tensile stress, such as Si₃N₄,

nevertheless, are shown to have the ability to increase both carrier concentration and mobility of the device as surface passivation layers. (Chen, Chen et al. 2008) Since AlN is a piezoelectric material and Al_2O_3 has a large E_g , they are examined in this work to study their effects of surface passivation.

1.3.3 Aluminum Oxide (Al_2O_3) and Aluminum Nitride (AlN)

Al_2O_3 , also known as alumina, is a native oxide of metallic Al and an important ceramic material, which is widely used as cutting tool coatings, catalysis, dielectrics in electronic devices and corrosion-resistant coatings. (Thomas, Vivier et al. 1997; Belonoshko, Ahuja et al. 2000; Nie, Meletis et al. 2002) Due to the strong reactivity of metallic Al with atmospheric oxidant (H_2O or O_2), a thin layer of Al_2O_3 on the order of several nanometers is usually formed on the surface and passivates the surface from further oxidation. Therefore, the material is also known as a diffusion barrier or passivation layer. (Groner, George et al. 2006)

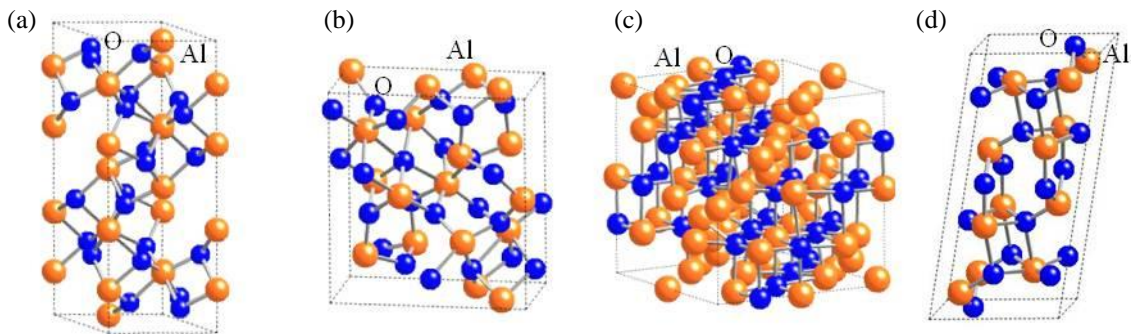


Figure 1.6. Bulk structures of common crystalline Al_2O_3 polymorphs: (a) hexagonal (α -phase) (Ishizawa, Miyata et al. 1980), (b) orthorhombic (κ -phase) (Ollivier, Retoux et al. 1997), (c) cubic (γ -phase) (Zhou and Snyder 1991) and (d) monoclinic (θ -phase) (Husson and Repelin 1996).

Crystalline Al_2O_3 possesses different meta-stable polymorphs, including γ , δ , η , θ , κ , β , χ alumina and the thermodynamically stable α - Al_2O_3 phase, also known as corundum. (Paglia, Rohl et al. 2005) The polymorphs are categorized by the stacking sequence of oxygen and the distribution of Al at tetrahedral or octahedral interstitial sites. Due to the hardness, resistance and thermal stability at temperatures above 1000°C , α - Al_2O_3 is the favored crystalline phase for most applications. Oxygen atoms in α - Al_2O_3 are stacked as hexagonal-close-pack (HCP) with Al occupying octahedral sites, while oxygen in κ , γ , δ , η , θ phases form face-centered cubic lattice with various percentage of octahedral sites occupied by Al. (Lee, Cho et al. 2007) Figure 1.6 shows the unit cells of common alumina phases (α , κ , γ and θ). A comparison of common Al_2O_3 phases in lattice parameters, oxygen packing arrangements and their computed physical properties is shown in Table 1.4. The aluminum coordination numbers in the material are represented by Al_{IV} and Al_{VI} as four-fold and six-fold, respectively. It shows that the percentage of Al_{VI} decreases with smaller densities and less stable crystal structures of the polymorphs. (Lizarraga, Holmstroem et al. 2011)

Table 1.4. Structural parameters and physical properties of various phases of alumina. (Lee, Cho et al. 2007; Lizarraga, Holmstroem et al. 2011)

Phase of Al_2O_3	α	κ	γ	θ
Density (g/cm^3)	3.98	3.77	3.60	3.61
Lattice parameters: a (\AA)	4.76	4.83	7.94	11.80
b (\AA)	4.76	8.31	7.94	2.91
c (\AA)	12.99	8.94	7.86	5.62
Oxygen packing	AB	ABAC	ABC	ABC
Al_{IV} (%), Al_{VI} (%)	0, 100	25, 75	25, 75	50, 50
Bandgap (eV)	6.72	5.49		5.04
Dielectric constant	9.72	10.99		8.52

Other than α - Al_2O_3 , another stable state of Al_2O_3 is amorphous, which can be grown by thin film deposition techniques due to its high crystallization temperature of $\sim 800^\circ\text{C}$ (Wallace

and Wilk 2003) and used as gate dielectrics in semiconductor devices. Although crystalline phase can be obtained through post-deposition thermal processing or depositions at temperatures $>800^{\circ}\text{C}$, grain boundaries may form in the film if the material is not single crystalline. A grain boundary in a film provides a potential path for current leakage and also serves as a diffusion path which may cause the formation of undesired materials at the interface or shifts in the flat band voltage and the threshold voltage of electronic devices. Moreover, any change in grain sizes or orientations in a poly-crystalline can result in uncontrolled change in dielectric constant, making reproducibility a difficult task. (Wallace and Wilk 2003) As a result, amorphous phase of Al_2O_3 is widely used as thin films for surface passivation and gate dielectric layers in electronic devices. Amorphous Al_2O_3 thin films are used not only in electronic devices but also in optical devices, catalysis, luminescence, manufacture tools for well-defined crystalline materials and most recently Li-ion batteries. (Jung, Cavanagh et al. 2010; Lizarraga, Holmstroem et al. 2011)

AlN , another binary Al-based material, is a wide bandgap semiconductor and has drawn attentions in various fields, especially electronic and optical devices. Unlike Al_2O_3 , it only possesses two polytypes like other group III nitrides (III-N), wurtzite and zinc-blende, as shown in Figure 1.7. The lattice constants and material properties are listed in Table 1.5. The wurtzite structure has a hexagonal unit cell and can be viewed as two interpenetrating hexagonal close-packed (HCP) lattices formed by Al and N atoms, whereas the zinc-blende structure has a cubic unit cell and can be viewed as two interpenetrating FCC lattices. (Gil 1998) In a wurtzite structure, the stacking sequence along the c-axis, $[0001]$ direction, is ABABA so wurtzite AlN (w- AlN) is also known as 2H- AlN . For a zinc-blende structure, the arrangement is ABCABC along the $[111]$ direction so zinc-blende AlN (z- AlN) is also known as 3C- AlN . (Gil 1998)

Similar to other III-N, AlN are always grown heteroepitaxially on substrates like sapphire, SiC and Si. (Cimalla, Pezoldt et al. 2007)

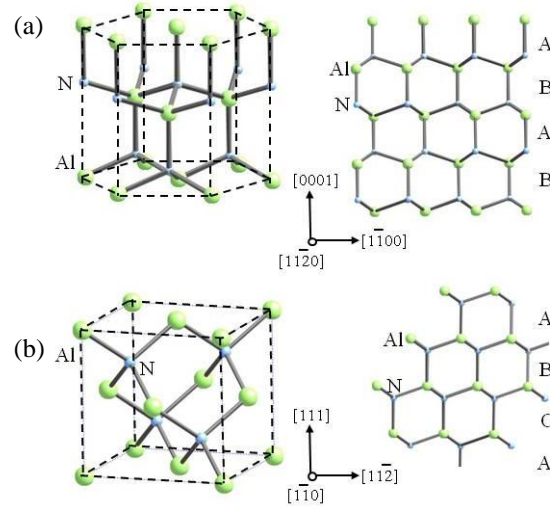


Figure 1.7. Crystal structures of AlN: (a) wurtzite and (b) zinc-blende, and their corresponding atomic arrangement and stacking sequences along $[0001]$ and $[111]$ directions, respectively. (Gil 1998)

In reality, the Al and N sublattices in unstrained w-AlN are arranged in such a way that there is relative movement from the ideal wurtzite position, resulting in a shift of charge from one atom to another in the basis and producing a spontaneous polarization in the crystal. (Singh 2003) Unlike w-AlN, the Al and N sublattices in unstrained z-AlN are arranged in such a way that there is no shift of charge from one atom to another. Therefore, there is no net spontaneous polarization in z-AlN. (Singh 2003) Other than the spontaneous polarization, the charge shift for polarization in AlN can arise due to piezoelectric effect when the material is under strain. (Singh 2003) During w-AlN growths along $[0001]$ direction on another nitride material to form a nitride heterostructure, a coherent strain may be formed at the interface due to the small bulk lattice mismatch between the two materials (Poisson effect), resulting in a piezoelectric polarization,

which can be described by equation (1.2). This piezoelectric polarization effect can also be found in z-AlN when the strain tensor is off-diagonal, as described by the equation: (Singh 2003)

$$[P_x, P_y, P_z] = [e_{14}\varepsilon_{yz}, e_{14}\varepsilon_{zx}, e_{14}\varepsilon_{xy}] \quad (1.4)$$

where e_{14} is the piezoelectric constant. For z-AlN growths along [001] direction, the strain tensor is diagonal where $\varepsilon_{xy}=\varepsilon_{yz}=\varepsilon_{zx}=0$, so there is no piezoelectric effect. For other orientation growths, especially [111], there is a strong piezoelectric effect.

Table 1.5. Structural parameters and physical properties of AlN polytypes. (Strite and Morkoc 1992; Morkoc, Strite et al. 1994; Willander, Friesel et al. 2006; Morkoc 2008)

Phase of AlN	wurtzite (2H)	zinc-blende (3C)
Density (g/cm ³)	3.255	
Lattice parameters: a (Å)	3.11	4.38
b (Å)	3.11	4.38
c (Å)	4.98	4.38
Nitrogen packing	AB	ABC
Al _{IV} (%), Al _{VI} (%)	100, 0	100, 0
Bandgap (eV)	6.2 (direct)	6.0 (indirect)
Dielectric constant	8.5	9.56

Because wurtzite structure is the stable polytype of AlN in the bulk form, (Saib, Bouarissa et al. 2008) most applications and studies are of w-AlN. W-AlN possesses a wide direct bandgap of 6.2 eV, making it suitable for sharp cut-off ultraviolet (UV) photon detectors and UV light emitting diodes. Furthermore, it can be alloyed with other wurtzite III-Ns, like InN and GaN, which have smaller direct bandgaps (1.89 and 3.45 eV, respectively) and be used for emitting diodes in broadened energy range of visible to UV light. (Yoder 1996) In addition to the wide bandgap, AlN has a high thermal stability, thermal conductivity, thermal expansion coefficient and piezoelectric property, allowing it to be used in electronic devices as well. For instance, alloy with GaN or itself can be used with GaN to form heterojunctions in HEMTs.

(Morkoc, Strite et al. 1994; Morkoc, Cingolani et al. 1999) Due to its small lattice mismatch (1.3%) and similar thermal expansion coefficient to SiC, AlN has served as a buffer layer for high quality epitaxial GaN to be grown on top of SiC. It has also been considered as a gate dielectric on Si (111) and shown an interface charge of $8 \times 10^{11} \text{ cm}^{-2}$ when molecular beam epitaxy (MBE) was used for the synthesis. (Stevens, Kinniburgh et al. 1995) Recently, it is considered as gate dielectric and surface passivation material for wide bandgap (WBG) semiconductor devices, such as SiC-based metal-insulator-semiconductor field-effect transistors (MISFETs) and AlGaIn/GaN MIS-HEMTs, for high-temperature and high-power applications. (Wolborski, Rosen et al. 2006; Chen, Chen et al. 2008)

1.3.4 Al₂O₃ and AlN for WBG Power Devices

The reliability of MIS-based devices is usually dependent on the leakage current resulted from carrier transferring directly from the substrate into dielectrics. For SiC and GaN- based devices, the most common conduction mechanism for the leakage current is the Fowler-Nordheim (F-N) tunneling (Hashizume, Ootomo et al. 2003; Singh 2006). The tunneling emission current density (J_{FN}) is a function of the electric field in the dielectric (E_d) and can be described by the formula: (Agarwal, Seshadri et al. 1997)

$$J_{\text{FN}} = A E_d^2 \exp(-B/E_d) \quad (1.5)$$

where $A = (q^3 / 8\pi\hbar)(m_s / m_d)(1/\phi_b)$, $B = 8\pi(2m_d)^{1/2}\phi_b^{3/2} / 3\hbar q$, q is the electron charge, m_s and m_d are the effective electron masses in the semiconductor substrate and dielectric, respectively, h is the Plank's constant and ϕ_b is the dielectric/semiconductor barrier height. Therefore, for power devices to operate under high electric fields, it is important to minimize the electric field

in the dielectric and increase the barrier height to lower the potential leakage from F-N tunneling. Based on Gauss' Law ($\nabla \cdot \epsilon E = 0$), the electric field is correlated to the dielectric constant ($\kappa = \epsilon / \epsilon_0$, ϵ_0 is a constant) of a material and the value of ϵE is a constant at the interface of two materials. Thus, the effective electric fields in the dielectric and semiconductor are inversely proportional to their dielectric constants (κ). If a low- κ dielectric, such as SiO_2 ($\kappa=3.9$) is used in the device, the effective electric field in it is higher than that in the substrate GaN ($\kappa=9$) or SiC ($\kappa=10$), potentially resulting in a higher leakage. It suggests the use of an insulator with a dielectric constant similar to or greater than that of the substrates as an alternative way to address this issue. Besides, a higher dielectric constant also results in a lower inversion channel resistance or on-resistance (R_{ch}) for MISFETs at a given voltage because of the relationship as

$$R_{\text{ch}} \propto \frac{t}{\kappa} \quad (1.6)$$

where t is dielectric thickness and κ is the dielectric constant. Therefore, with a higher dielectric constant the film thickness can be thicker. (Singh 2006) Even though the electric field in the dielectric can be reduced if a high- κ material is used, the electric field still has to be lower than its breakdown field. Therefore, high breakdown field strength of the dielectric material is also important. The dielectric constant of Al_2O_3 and AlN are 9 and 8.5, respectively and their high breakdown field strength of 13.5 and 1.5 MV/cm, respectively, making them potential materials using on these WBG materials for high-power devices.

On the other hand, it is equally important to assure adequate band offset (barrier height) between the dielectric layer and the semiconductor to prevent the unintended transport of carriers from the semiconductor into the conduction/valence bands of the dielectric, contributing to gate leakage. To provide sufficient barrier and inhibit leakage, the values of band offsets for both conduction and valence bands have to be over 1 eV. (Robertson and Falabretti 2006) Since the

substrates are WBG semiconductors, the bandgap of the dielectrics has to be even larger. Figure 1.8 summarizes bandgaps and dielectric constants of potential gate dielectrics. Although several dielectrics, such as TiO_2 and La_2O_3 , possess higher dielectric constant values, they lack of wide bandgap to provide sufficient barrier heights. Therefore, the practical κ for potential gate dielectric is actually limited.

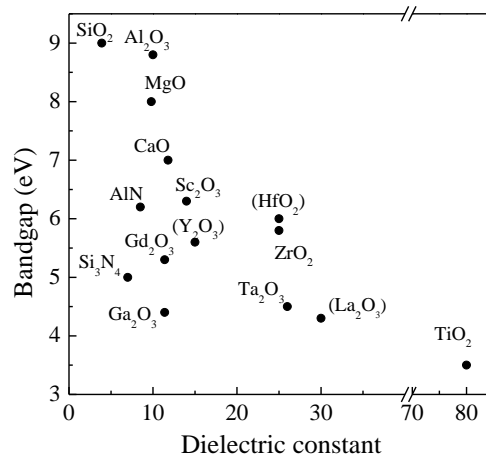


Figure 1.8. The experimental values of bandgap and dielectric constant of various dielectrics. The theoretical values were used for compounds in parenthesis, adapted from (Wallace and Wilk 2003; Gila, Ren et al. 2004).

The band offsets of dielectrics to AlGaN/GaN and SiC determined using the charge neutrality level (CNL) calculation method and experimental data are shown in Figure 1.9. Al_2O_3 and AlN have band offsets to SiC higher than 1 eV, making them viable gate dielectric alternatives for SiC MISFETs.

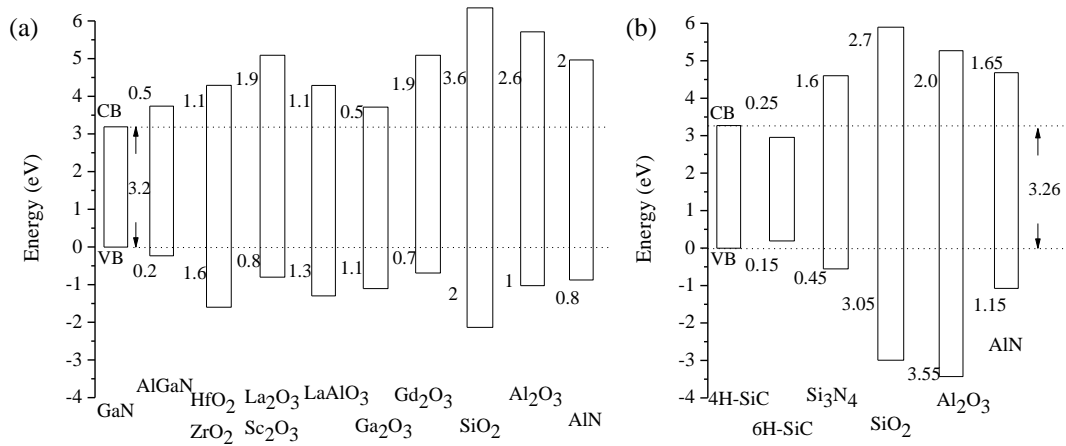


Figure 1.9. Diagrams of band alignments for high-k dielectrics on (a) GaN and AlGaN ($\text{Al}_{0.3}\text{Ga}_{0.7}\text{N}$) and (b) SiC. (Singh and Hefner 2004; Robertson and Falabretti 2006; Maeda, Hiroki et al. 2007)

Although AlN has a conduction band offset to AlGaN smaller than 1 eV, which might result in a higher leakage current than Al_2O_3 , the material has other properties superior to Al_2O_3 for serving as dielectric layers on the WBG substrates, such as a similar atomic arrangements to those of SiC and GaN and a higher thermal stability with no potential chemical reactions occurring at the interface. The quality of oxide/semiconductor interface is crucial since any energy traps or defects near the interface, known as interface states, may result in a leakage current and degrade the device performance. Therefore, a relatively low interface state density (D_{it}) at the dielectric/substrate interface is necessary. Due to the carbon cluster at the interface, SiC possesses a high midgap D_{it} of $\sim 10^{12} \text{ cm}^{-2}\text{eV}^{-1}$ to its native oxide, SiO_2 . (Afanas'ev, Stesmans et al. 2003) In order to lower the value, additional surface treatments, such as annealing in NO or N_2O , which reduced the SiO_2/SiC interface state densities to $< 10^{11} \text{ cm}^{-2}\text{eV}^{-1}$ are required. (Afanas'ev, Stesmans et al. 2003; Mahapatra, Chakraborty et al. 2007) For GaN or AlGaN, there is no high quality native oxide so depositing a dielectric film with low D_{it} seems to be a viable option. Considering the high electric field required for SiC and GaN to work at their optimum

performance, it makes the high- κ material more attractive for these WBG power devices. As a result, it is desirable to achieve a $D_{it} < 10^{11} \text{ cm}^{-2}\text{eV}^{-1}$ for high- κ SiC-based MIS or AlGaN/GaN MIS-HEMT devices. In order to form a high quality interface with small D_{it} , the lattice mismatch of a dielectric layer to the substrate has to be minimized to reduce the amount of dangling bonds at the interface. AlN has a similar atomic arrangement and a small lattice mismatch to SiC (1.3%) and GaN (2.6%), enabling it to form an epitaxial interface. A material like Al_2O_3 possessing good electrical properties but larger lattice mismatches or different atomic arrangements at the interface to SiC or AlGaN/GaN may induce more interface states. As a result, instead of applying the crystalline films, amorphous films is the way to solve the difficulty. Based on the crystal structure and epitaxial relationship reported in literature, the interfaces of AlN on 4H-SiC and $\gamma\text{-Al}_2\text{O}_3$ on 4H-SiC are shown in Figure 1.10. It shows that AlN can generate a sharp interface on SiC and provide a better interface quality compared to Al_2O_3 , suggesting that AlN is a potential material for gate dielectrics or interfacial layers to engineer an epitaxial gate dielectric stack on SiC.

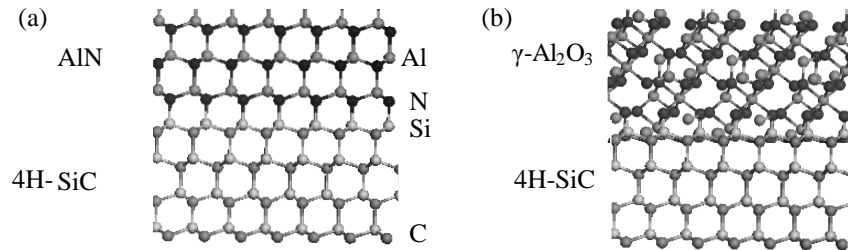


Figure 1.10. Illustrations of (a) AlN and (b) $\gamma\text{-Al}_2\text{O}_3$ on 4H-SiC to demonstrate that a sharp interface with less dangling bonds can be formed by AlN due to its similar atomic arrangement and lattice constant to those of 4H-SiC.

On the other hand, candidates for the gate dielectric also have to exhibit thermal stability during post-deposition processing such as rapid thermal annealing and for the device to function

at high temperatures. In order to have a high quality interface at elevated temperatures, it is important that no chemical reactions occur between the dielectric and semiconductor at the interface. Reactions result in substrate oxidation or formation of compound may decrease the interface quality as well as device performance. Therefore, Gibbs free energy of possible interface reactions of Al_2O_3 or AlN on the WBG substrates is calculated for assessing the thermal stability of these binary Al-based materials, (Barin, Knacke et al. 1973) shown in Table 1.6. Most of the interfacial reactions have energy values larger than 4.5 eV, suggesting those interfaces are stable. However, reaction (A1) for Al_2O_3 on AlGaN has a Gibbs free energy value smaller than 2 eV and has the highest probability of happening, producing Ga_2O_3 and AlN at the interface. As a result, AlN appears to be superior to Al_2O_3 in this case.

Table 1.6. Gibbs free energies at various temperatures of possible interfacial reactions between the binary Al-based materials, Al_2O_3 and AlN , and AlGaN or SiC substrate.

ΔG (eV) / Temperature (K)		298	500	700	900	1100
A1	$\text{Al}_2\text{O}_3 + 2\text{GaN} \rightarrow \text{Ga}_2\text{O}_3 + 2\text{AlN}$	1.71	1.65	1.63	1.59	1.57
A2	$\text{Al}_2\text{O}_3 + 2\text{GaN} \rightarrow \text{Ga}_2\text{O}_3 + 2\text{Al} + \text{N}_2$	7.67	7.15	6.68	6.20	5.81
A3	$\text{Al}_2\text{O}_3 + \text{GaN} \rightarrow \text{Ga} + \text{NO} + \text{Al}_2\text{O}_2$	13.88	12.88	12.01	11.10	10.23
A4	$2\text{Al}_2\text{O}_3 + \text{GaN} \rightarrow \text{Ga} + \text{NO}_2 + 4\text{AlO}$	36.77	34.56	32.56	30.48	28.36
A5	$\text{Al}_2\text{O}_3 + \text{AlN} \rightarrow \text{Al} + \text{NO} + \text{Al}_2\text{O}_2$	16.04	15.09	14.27	13.35	12.57
A6	$\text{Al}_2\text{O}_3 + \text{AlN} \rightarrow 3\text{Al} + \text{NO} + \text{O}_2$	20.25	19.30	18.43	17.47	16.74
A7	$\text{Al}_2\text{O}_3 + \text{AlN} \rightarrow 3\text{Al} + \text{NO}_3$	20.60	19.95	19.47	18.86	14.61
A8	$\text{Al}_2\text{O}_3 + 2\text{AlN} \rightarrow \text{Al} + \text{N}_2 + 3\text{AlO}$	24.32	22.63	21.16	19.56	17.99
A9	$3\text{Al}_2\text{O}_3 + 2\text{AlN} \rightarrow \text{N}_2\text{O}_5 + 2\text{Al}_2\text{O}_2 + 4\text{Al}$	47.91	46.09	44.62	42.88	41.50
B1	$2\text{Al}_2\text{O}_3 + 3\text{SiC} \rightarrow 3\text{SiO}_2 + \text{Al}_4\text{C}_3$	6.29	6.11	5.94	5.64	5.59
B2	$\text{Al}_2\text{O}_3 + \text{SiC} \rightarrow \text{C} + \text{SiO} + \text{Al}_2\text{O}_2$	11.62	10.67	9.89	9.11	8.28
B3	$2\text{Al}_2\text{O}_3 + \text{SiC} \rightarrow \text{CO}_2 + \text{SiO}_2 + \text{Al}_2\text{O}_2 + 2\text{Al}$	16.35	15.31	14.44	13.44	12.66
B4	$\text{Al}_2\text{O}_3 + \text{SiC} \rightarrow \text{C} + \text{SiO} + 2\text{AlO}$	17.17	15.87	14.74	13.62	12.40
C1	$4\text{AlN} + 3\text{SiC} \rightarrow \text{Si}_3\text{N}_4 + \text{Al}_4\text{C}_3$	5.38	5.16	4.94	4.73	4.55
C2	$4\text{AlN} + 3\text{SiC} \rightarrow 3\text{C} + \text{Si}_3\text{N}_4 + 4\text{Al}$	7.46	7.11	6.85	6.63	6.42

In conclusion, both Al_2O_3 and AlN are promising gate dielectric candidates for 4H-SiC and AlGaN/GaN because of their high breakdown field, high dielectric constants and large band offsets. AlN has a similar atomic arrangement and small lattice mismatch to both 4H-SiC and AlGaN (-2.4 %), making it possible to form a higher quality interface with these substrates, providing lower interface densities (D_{it}). (Onojima, Kaido et al. 2005) For the application on AlGaN/GaN , AlN can serve as a superior passivation layer to Al_2O_3 because of its piezoelectric properties, spontaneous polarization and thermal stability. (Cros, Garro et al. 2007)

1.3.5 Synthesis of Al_2O_3 and AlN

Various methods have been studied and used to grow Al-based materials. Metal-organic chemical vapor deposition (MOCVD) with precursor gases introduced simultaneously into the reactor forms the solid film via vapor phase chemical reactions. MOCVD deposits films with a poor surface uniformity and morphology and usually requires high deposition temperatures. (Messier and Wong 1971) Sputtering and pulse laser deposition (PLD) by physical vapor deposition (PVD) using high energy ions and high-power laser, respectively, to evaporate the source material to grow the film via condensation usually involves substrate surface modifications or damages and induced undesired interface states. Molecular beam epitaxy (MBE), widely used in growing epitaxial films (Morkoc, Strite et al. 1994), provides slow growth rates and requires a larger reactor space and complicated setup. More recently, atomic layer deposition (ALD) is used to synthesize thin films for atomic-scaled control and large wafer processing capability at lower deposition temperatures. (Ott, Klaus et al. 1997) Al_2O_3 growth using trimethylaluminum (TMA) and water (H_2O) are known as an ideal model for ALD to synthesize high quality films. (George 2010)

For AlN films, the most conventional methods are MOCVD and MBE. (Morkoc, Strite et al. 1994) In MOCVD, TMA or other Al-source precursors reacts with NH₃ in vapor phase and grow AlN on substrates, which require a high substrate temperature to thermally dissociate NH₃. After the growth, cooling may induce strain and defects in the film due to the thermal mismatch between the AlN film and the substrate, preventing the formation of a high quality film. In MBE, aluminum is evaporated (>1200 °C) from a standard effusion cell while nitrogen is decomposed using an electron cyclotron resonance (ECR) plasma. Thus, a high substrate temperature is not required. However, the reactor requires a large footprint and uses plasma, making it difficult for larger-size wafer processing. Other techniques, such as sublimation, reactive sputtering, PVD and ALD have also demonstrated the capability for AlN. Table 1.7 summarized techniques used for AlN thin film depositions and the properties of synthesized films.

Table 1.7. Comparison of various thin film deposition techniques for AlN and the corresponding material properties. (Stevens, Kinniburgh et al. 1995; Adam, Kolodzey et al. 2001; Engelmark, Iriarte et al. 2001; Onojima, Suda et al. 2002; Kakanakova-Georgieva, Persson et al. 2004; Onojima, Kaido et al. 2005; Wolborski, Rosen et al. 2006; Xi, Chen et al. 2006; Claudel, Blanquet et al. 2009)

Method	Crystallinity	Deposition temperature (°C)	Surface RMS roughness on SiC (Å)	Dielectric constant	Bandgap (eV)
MOCVD	epitaxial	800-1215	200-350	8.4	6.10
MBE	epitaxial	600-1000	3-14	9.4	
Sublimation	epitaxial	1900			
Sputtering	epitaxial	350-500		4-11	5.20
PVD	polycrystalline	<250		8.8	
ALD	amorphous/ polycrystalline	400-600	(the objective of this work)		

TMA and ammonia (NH₃), widely employed precursors for AlN MOCVD growth, have been studied and demonstrated for possible ALD growth at a lower deposition temperature of

~423 °C. (Mayer, Rogers et al. 1991; Liu, Bertolet et al. 1995) It was found that TMA decomposed at temperatures >350 °C while temperatures >280 °C is required for NH₃ to react with -CH₃ ligands of TMA that are bonded on the surface to form AlN, making it critical to perform the growth within an optimum temperature window. Besides, one major challenge for synthesizing high-purity AlN using chemically based method, such as an ALD process, is the oxygen incorporation in the film due to the residual moisture in reactors and gas lines. Xu et al. showed that a higher energy is required for NH₃ to complete the half reaction with TMA to form AlN compared to that of H₂O reacting with TMA, as shown in Figure 1.11, confirming the existence of moisture would lead to the growth of Al₂O₃ or AlO_xN_y, instead of AlN. (Xu, Chen et al. 2011) Besides, due to the stronger bond between Al-O than that of Al-N, AlN surface tends to oxidize upon exposure to air, which contains moisture. In this work, ALD process using the TMA and NH₃ chemistry for AlN growths is studied to synthesize thin films with precise control in thickness and conformality and with a lower growth temperature. (Cleveland, Banerjee et al. 2010; George 2010)

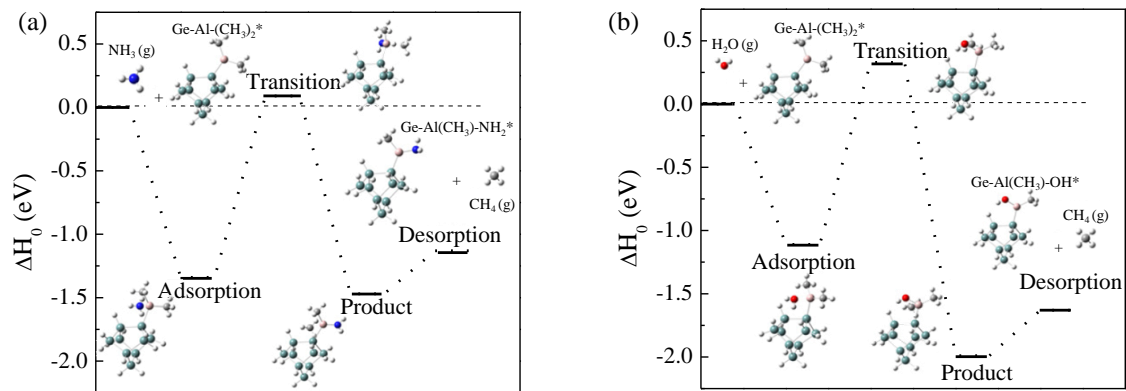


Figure 1.11. Energy diagrams of germanium (Ge) surface bonded TMA reacting with (a) NH₃ and (b) H₂O, adapted from (Xu, Chen et al. 2011).

1.4 On-Chip Energy Storage Application

Batteries are devices which store energy by chemical compounds. During discharge, a chemical process occurs that generates energy which can be drawn as electric current at a given voltage. Based on the chemical process, batteries can be categorized into two types: primary and secondary batteries. If the chemical process is irreversible, the type of batteries is known as primary batteries. The other type, the electrical energy converted and restored into the two electrodes as chemical compounds by the reverse chemical reactions during battery charge, is known as secondary (rechargeable) batteries. (Kiehne 2003) In an electrochemical cell, chemical compounds of higher energy are converted by the cell reaction into compounds of lower energy with energy released. In a battery, one type of electrochemical cell, the cell reaction is divided into two electrode reactions at the negative and positive electrodes. The reaction at the negative electrode is the oxidation of the electrode compound, $S(N)_{\text{red}}$, which releases electrons:



Since the reaction is anodic, the negative electrode is the anode. The other reaction at the positive electrode is the reduction of the electrode compound, $S(P)_{\text{ox}}$, which accepts electrons:



Due to the cathodic reaction, the positive electrode is the cathode. The flow of electrons from one electrode to the other forms a current flow (I) that can be drawn from the battery, as shown in Figure 1.12. Therefore, the generation or consumption of energy related to the cell reaction is converted into an electric current directly.

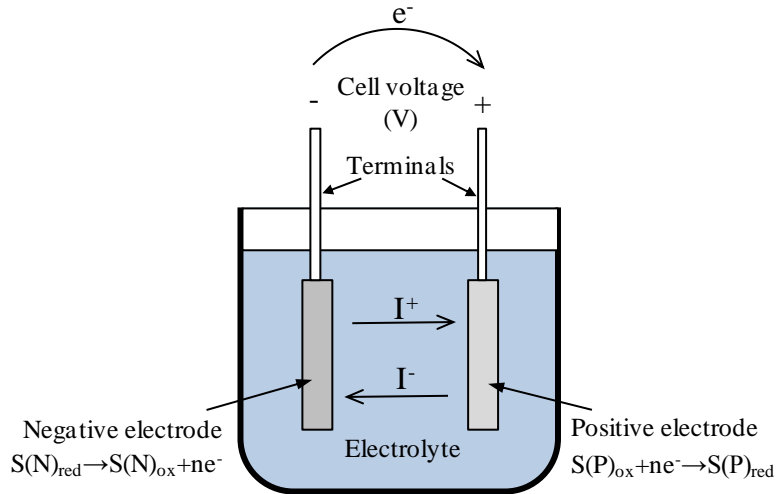


Figure 1.12. A schematic diagram of a discharging battery (electrochemical cell) and the electrode reactions divided from the cell reaction, adapted from (Kiehne 2003). $S(N)_{red}$ and $S(P)_{ox}$ are the components of the negative and positive electrodes, respectively.

The overall cell reaction of a battery can be written as:



When the battery is secondary, this reaction is reversible and a corresponding amount of energy has to be supplied to the cell during the charge. In this case, the negative electrode becomes the cathode and the positive electrode becomes the anode.

The other critical component of batteries is the electrolyte. In some cases, it is only the medium for electrode reactions and ionic conductivity and does not appear in the cell reaction. Therefore, the oxidation potential, potential of lowest unoccupied molecular orbital (LUMO), of the electrolyte has to be higher than the potential of the anode (or than the Fermi energy of the anode material) whereas the reduction potential, potential of highest occupied molecular orbital (HOMO), has to be lower than the corresponding potential of the cathode (Fermi edge of the cathode), as shown in Figure 1.13. (Kiehne 2003)

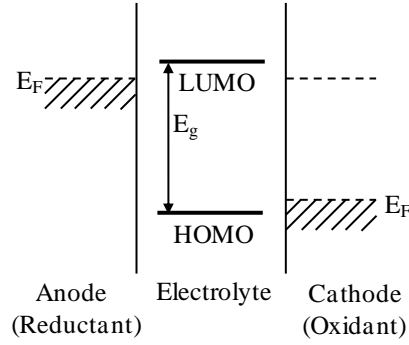


Figure 1.13. The energy diagram of a fluid electrolyte relative to the potentials of the solid electrodes, including the anode (reductant during battery discharge) and the cathode (oxidant during battery discharge), of a galvanic cell, adapted from (Kiehne 2003).

The discharging/charging behavior of a battery depends on a variety of parameters, like voltage, capacity, specific energy and specific power. In a reversible system, the battery cell voltage (V) can potentially be derived from the thermodynamic data of the chemical reactions for equilibrium by the relation: (Kiehne 2003)

$$V = -\Delta G / (nF) \quad (1.10)$$

where ΔG is the change of Gibbs free energy for the chemical reaction in a cell, which describing the (maximum) amount of chemical energy that can be converted into electrical energy, n is number of exchanged electronic charges, F is the Faraday constant (=96485 C/mole). However, the equilibrium voltage cannot exactly be measured if the reaction at electrodes is not reversible or there are secondary reactions causing a slight deviation. The capacity of a battery (C_{Ah}) is defined as the total electrical charge (Q) in unit of Amp-hour (Ah) that can be drawn from the battery to deliver a discharge current (I) over the time (Δt) for a complete discharge of the chemical energy, given by the relation: (Kiehne 2003; Goodenough and Youngsik 2011)

$$C_{Ah} = \int_0^t I(t) dt = \int_0^Q dq \quad (1.11)$$

For system comparison, it is common to normalize the energy content by the battery weight (M), volume (V_{battery} for battery, V_{anode} for anode and V_{cathode} for cathode) or footprint (ℓ^2) as specific capacity (C_{Ah}/M), capacity density ($C_{\text{Ah}}/V_{\text{anode (cathode)}}$) or areal capacity (C_{Ah}/ℓ^2), respectively. The energy content (E) of a battery in unit of Watt-hour (Wh) or Joule (J) that describes the energy can be drawn from the battery is represented by (Kiehne 2003)

$$E = \int_0^t V(t)I(t)dt = \int_0^Q V(q)dq \quad (1.12)$$

Because capacity measurements are usually performed at a constant current load, the energy output of a cell can be calculated by multiplying the measured capacity with the discharge voltage. (Kiehne 2003) The power output (P_{out}) of a battery, in unit of W, that describes how fast that the stored energy can be drawn from the battery can be defined as: (Goodenough and Youngsik 2011)

$$P_{\text{out}} = IV \quad (1.13)$$

Similar to the capacity, the energy content and the power output can be normalized by the battery weight, volume or footprint. Figure 1.14 shows comparisons of battery systems in terms of their specific power (P_{out}/M) and specific energy (E/M) and in terms of their energy density (E/V_{battery}) and specific energy. It shows that Li-ion batteries possess higher specific energy with the value independent to discharging time and higher energy density compared to other battery technologies, enabling the batteries to provide the same amount of energy with lighter weights and smaller sizes. In addition to their other outstanding features, such as high voltage, low self-discharging rate and wide operation temperature range (Nishi 2001), Li-ion batteries are widely used nowadays and have been improved dramatically in size reduction and attainable energy density for portable electronics. Therefore, Li-ion batteries were chosen in this work to be further minimized for on-chip energy storage application.

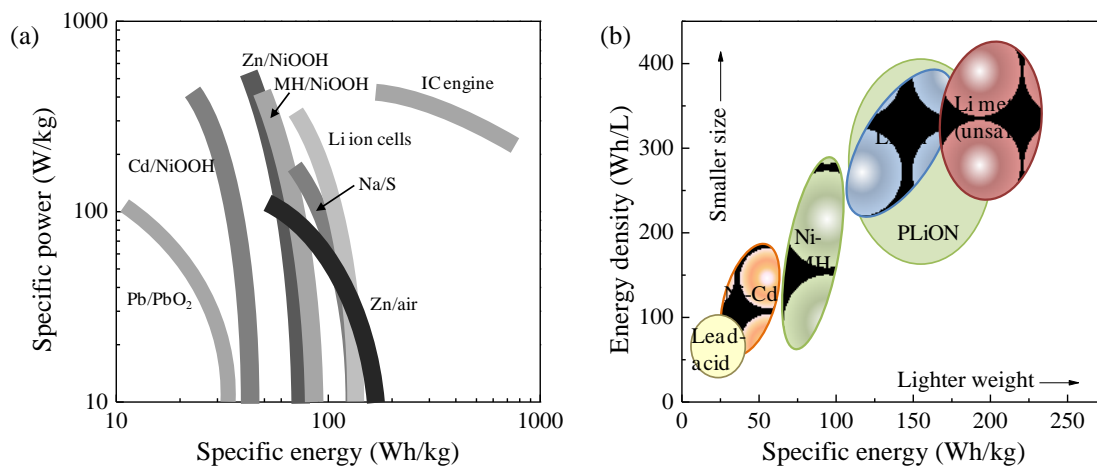


Figure 1.14. Comparisons of different battery systems in terms of (a) specific power and specific energy (Cairns 2004) and (b) energy density and specific energy, adapted from (Tarascon and Armand 2001).

1.4.1 Li-ion Battery Operation

Li-ion batteries (LIB), a type of secondary batteries, operate with “host lattices” for both negative and positive electrodes, between which Li ions are exchanged during discharge and charge. The back and forth reactions of the Li ions is named “rocking chair” or “swing” principle, as shown in Figure 1.15.

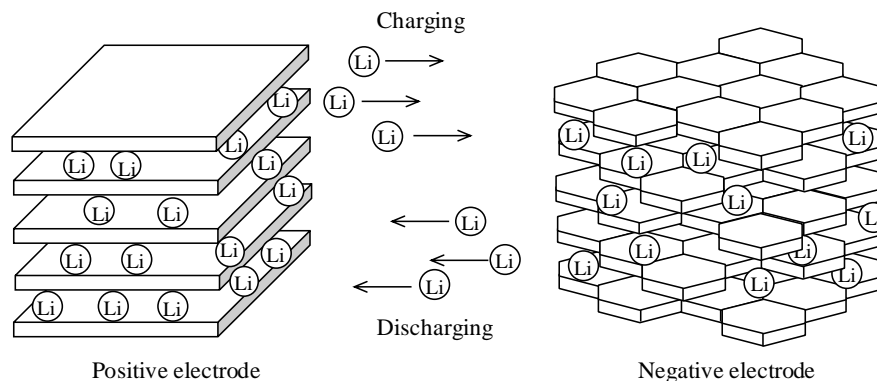


Figure 1.15. A schematic diagram of charging/discharging of Li-ion batteries. (Kiehne 2003)

The electrode materials for LIBs should possess electrical conductivity and ability to incorporate lithium. Table 1.8 lists electrode materials for LIBs and their capacities. Negative electrode compounds, like graphite and Si, should be able to accommodate large amount of lithiums in the charge state and provide them to the positive electrode during discharge. Positive electrode compounds in LIBs should be able to intercalate Li-ions at a high positive potential and possess high mobility for Li ions and electrons within the cathodic lattice. Transition metal oxides, like LiNiO_2 and LiCoO_2 , have layered structures which can intercalate Li ions into the space between the layers to serve as cathodic materials during discharge. The other host structure for positive electrode materials is spinel, like Mn_2O_4 . (Kiehne 2003) The cell voltage of LIBs is ~ 3.5 V with slight variation depending on the electrodes. (Tarascon and Armand 2001)

Table 1.8. Electrode materials for Li-ion batteries and their capacities. (Tarascon and Armand 2001; Kiehne 2003; Needham, Wang et al. 2007; Chan, Peng et al. 2008; Chan, Zhang et al. 2008; Uchiyama, Hosono et al. 2008)

Negative electrode	Specific capacity (mAh/g)	Positive electrode	Specific capacity (mAh/g)
Graphite	372	LiCoO ₂	274
SnO ₂	783	LiNiO ₂	190
Carbons	~600	Li _x Mn ₂ O ₄	-
3D-Metal oxides	~800		
Nitrides LiM _y N ₂	~900		
Germanium	1624		
Si	~4200		

For the graphite/lithium cobalt oxide (LiCoO₂) electrode system, carbons in the graphite accommodate lithiums and provide them to the cobalt oxide (CoO₂) during discharge to form LiCoO₂ as a formula of maximum amount of lithium intercalation. (Kiehne 2003) During cycling of the battery system, Li ions move between the two host lattices of C_x and CoO₂. Table 1.9 lists the chemical reactions of both electrodes in the charge and discharge states to show the concept. (Kiehne 2003)

Table 1.9. Chemical reactions of electrodes during the charge and discharge of the graphite/LiCoO₂ battery system with an equilibrium voltage of 3.9 V. (Kiehne 2003)

	Discharge state	Charge state
Negative	LiC ₆ → C ₆ + Li ⁺ + e ⁻	LiCoO ₂ → CoO ₂ + Li ⁺ + e ⁻
Positive	CoO ₂ + Li ⁺ + e ⁻ → LiCoO ₂	C ₆ + Li ⁺ + e ⁻ → LiC ₆
Cell	LiC ₆ + CoO ₂ → C ₆ + LiCoO ₂	C ₆ + LiCoO ₂ → LiC ₆ + CoO ₂

For battery electrolytes, chemical and electrochemical stabilities are required for high energy density LIBs. Electrolytes currently used are mixtures of lithium salts, such as LiClO₄, LiBF₄ and LiPF₆, and organic solvents, which must have a high dielectric constant and a low viscosity to facilitate faster ion transport. (Kiehne 2003) The higher the dielectric constant of a solvent, the easier the electrolyte salt can be dissolved and dissociated. (Kiehne 2003) Cyclic

esters, including propylene carbonate (PC) and ethylene carbonate (EC), are promising solvents due to their high dielectric constants. However, their polarity results in high solution viscosity. Therefore, their mixtures with low viscous straight alkyl carbonates, such as dimethyl carbonate (DMC) and diethyl carbonate (DC), are usually used for faster ion transport. (Kiehne 2003) Solid electrolytes possess lower ionic conductivity than fluids in general, resulting in a higher internal resistance unless the thickness decreases significantly. Therefore, the battery using solid electrolytes can only allow low loads. An electrolyte material must be stable and possess a high ionic conductivity and a low electrical conductivity. One example of the electrolytes is mixture of lithium iodide with Al_2O_3 or SiO_2 . (Kiehne 2003) Other solid electrolyte alternatives are discussed in Section 1.4.3.

1.4.2 Three-Dimensional Li-ion Microbatteries

The development of rechargeable LIBs has been driven by the demands for portable electronics over the last two decades. As the electronics industry entered into nano-scale device fabrications, such as Smart Dust sensors (Warneke and Pister 2004), the autonomous operation of these devices relied on fabrication of a miniaturized on-chip power source. The layout in current battery technology composed of planar electrodes and liquid-based electrolytes fails to meet the power delivery requirement for this application. This is because that the energy content (proportional to the battery volume) and output power (proportional to the surface area of electrodes) decreases with a reduced battery foot print. Three-dimensional (3D) structures, fabricating the electrodes into non-planer geometries, as shown in Figure 1.16, were proposed to increase the electrode surface areas and electrode volumes within a given and reduced footprint while maintaining the distance between the two electrodes (Long, Dunn et al. 2004). First, the

anodes and cathodes are arrays of rods separated by a continuous electrolyte phase (Figure 1.16 (a)). Second, a concentric rod array arrangement of one of the electrode materials are coated by an ionic conductive dielectric (electrolyte) layer, with the counter electrode material filling the remaining spaces (Figure 1.16 (b)). Third is the “sponge” approach where the electrolyte layer is formed around a random 3D network of electrode material (Figure 1.16 (c)). Fourth, trenches are used as the substrate to serve as a 3D feature template for conformal anode, electrolyte and cathode films to be deposited on top (Figure 1.16 (d)).

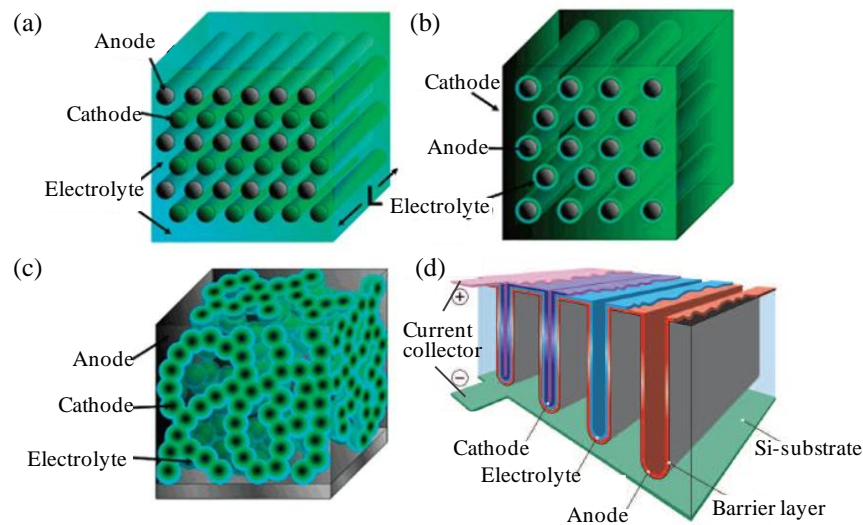


Figure 1.16. Examples of three-dimension battery layouts: (a) arrays of cathodes and anodes, (b) arrays of anodes coated with a thin layer of electrolyte and with remaining space filled with the cathode material, (c) “sponge” architectures and (d) substrate trenches, adapted from (Long, Dunn et al. 2004; Notten, Roozeboom et al. 2007).

With the second type of design, the large surface area enhancement can be obtained in a relatively simple process and the performance can be potentially assessed by characterizing a single rod or nanowire battery thus this work focuses on coating the electrodes with a conformal and thermally stable electrolyte material. Figure 1.17 compares 2D and 3D battery electrode layouts, with parameter defined for determining the effect of aspect ratios on the electrode

surface area (a factor of power density) and the energy density of a 3D battery. The negative electrode (anode) pillars are arranged in a hexagonal close pack (HCP) with the notation d for the electrode diameter, P for the distance between the centers of two neighbor pillars, also known as the pitch, H for the height of the anode pillars and D for the distance between the closest electrode pillars to the edge.

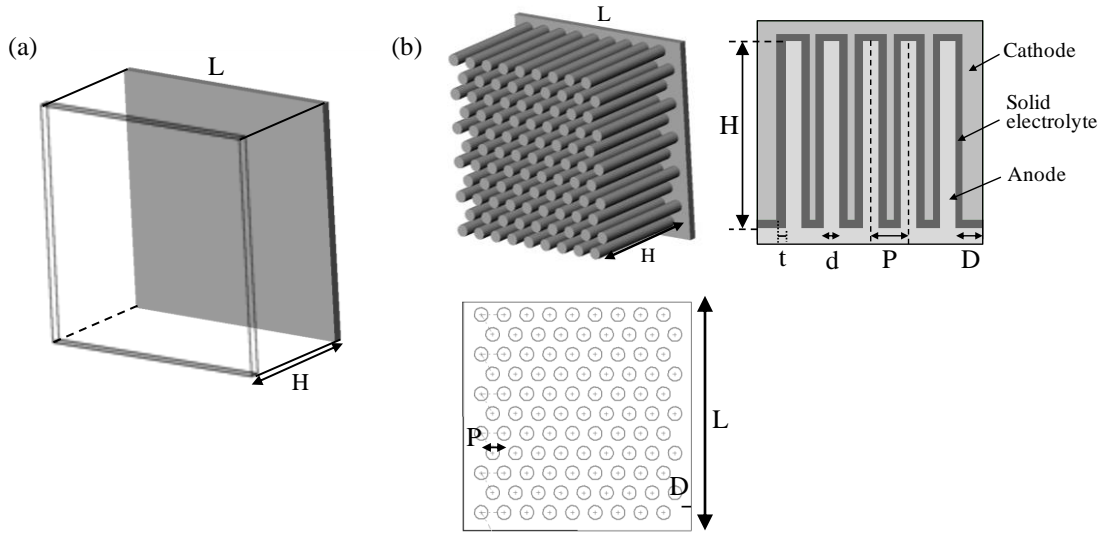


Figure 1.17. Schematic diagrams of (a) 2D parallel-plate and (b) 3D anode array (HCP) batteries.

When the 3D battery design is incorporated, the 1D ion transport distance, which is the distance between the cathode and the anode in planar battery design, is maintained or reduced while the surface area can be enhanced by the increasing the aspect ratio (AR, H/d) and heights (H) of the anode pillars. With a hexagonal close-packed (HCP) arrangement, as shown in Figure 1.17 (b), and a battery footprint of L^2 , the number of the anode pillars (N_{anode}) can be estimated as:

$$N_{\text{anode}} = \left[\frac{L - 2 * D}{P} \right] * \left[\frac{L - 2 * D}{(\sqrt{3} / 2) * P} \right] \quad (1.14)$$

The surface area of the 3D anode (SA_{3D}) is:

$$SA_{3D} = L^2 + \pi d * H * N_{\text{anode}} = SA_{2D} + \pi d^2 * AR * N_{\text{anode}} \quad (1.15)$$

where SA_{2D} is the surface area of a 2D planar anode. According to the two equations, the SA_{3D} can be shown as a function of d , P and H when D and L are fixed (Figure 1.18).

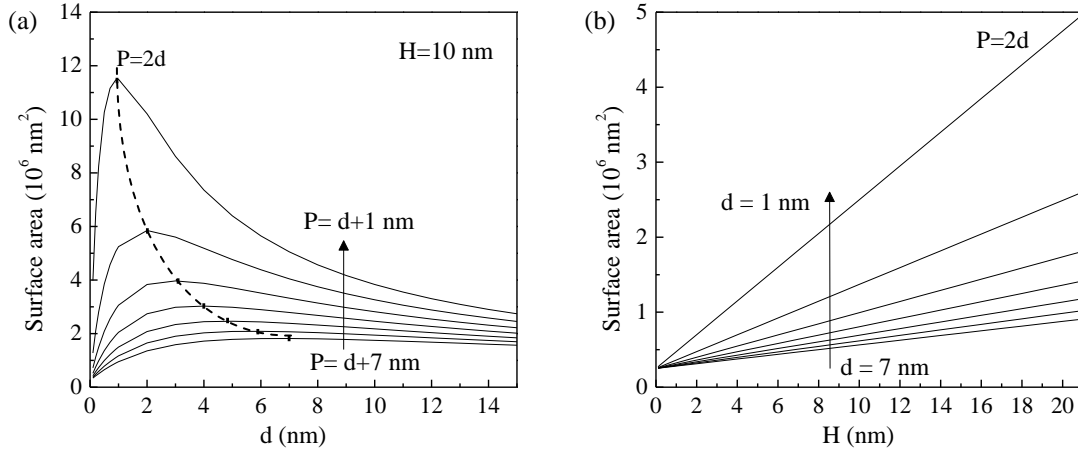


Figure 1.18. (a) The surface area of electrodes as a function of electrode diameter and pitch. (b) The surface area of electrodes as a function of electrode height and diameter. D is 5 nm and L is 1 nm.

The calculation suggested that the rising H and decreasing d , also known as increasing AR , SA_{3D} as the electrode reaction sites can be increased for a higher current and an improved power density. Based on equation (1.10) and equation (1.11), the energy content of a battery is proportional to the battery capacity which is a function of the electrode material and volume.

The volumes of anode and cathode with the 3D layout can be defined as:

$$V_{\text{anode}} = \pi \left(\frac{d}{2}\right)^2 * H * N_{\text{anode}} = \pi \left(\frac{d^3}{4}\right) * AR * N_{\text{anode}} \quad (1.16)$$

$$\begin{aligned} V_{\text{cathode}} &= L^2 * H - \pi \left(\frac{d+t}{2}\right)^2 * H * N_{\text{anode}} \\ &= \left[L^2 - \pi \left(\frac{d+t}{2}\right)^2 * N_{\text{anode}} \right] * d * AR \end{aligned} \quad (1.17)$$

where t is the thickness of the electrolyte. The areal capacity of electrodes (anode or cathode) for half-cells can then be calculated based on the theoretical specific capacity, the volume and the density (ρ) of electrodes with the relation:

$$\frac{C_{\text{Ah,electrode}}}{\ell^2} = \frac{C_{\text{Ah,electrode}}}{M} \frac{\rho_{\text{electrode}} V_{\text{electrode}}}{\ell^2} \quad (1.18)$$

The equations show that the areal capacity of anode and cathode is proportional to H or AR (when d is fixed). One of the state-of-art Li-ion thin film battery, consisting of graphite and LiCoO_2 , with a battery thickness of $15 \mu\text{m}$ provides an energy density of 2 J/mm^3 , referring a areal energy of $\sim 1 \times 10^{-2} \text{ J/mm}^2$ (Bates, Dudney et al. 2000). The value is two orders of magnitude lower than the requirement for powering on-chip devices (1 J/mm^2) (Warneke, Last et al. 2001). By building a 3D microbattery with a size of 1 mm^3 , the height of the cell increased from micrometers to millimeters, may potentially allow the areal energy to meet the requirement of 1 J/mm^2 .

However, only considering increasing the aspect ratio of one electrode may not be practical for determining the parameters of a 3D battery layout since the energy content or the capacity of a battery is related to both electrodes. For a graphite/ LiCoO_2 battery system, the areal capacity of the two electrode half-cells are calculated and shown as a function of the aspect ratio of anode pillars in Figure 1.19 when d , t are fixed and the densities of for graphite and LiCoO_2 are 2.23 g/cm^3 (Uchiyama, Hosono et al. 2008) and 5.06 g/cm^3 (Wartena, Curtright et al. 2004), respectively. The calculation shows that the areal capacity of half-cells increases with rising aspect ratio but there is a large areal capacity difference between the graphite and LiCoO_2 half-cells when a pitch of 180 or 200 nm is used. Because the capacity of a battery cell is determined by the lower value between that of the anode and cathode, large amount of the cathode compound may be wasted in this case. When P is decreased to 168 nm, the capacity of

two materials matches with each other and the capacity for the battery system reaches the maximum value. Therefore, in order to use the electrode material efficiently, the theoretical capacity of both cathode and anode materials need to be considered in designing the 3D layout.

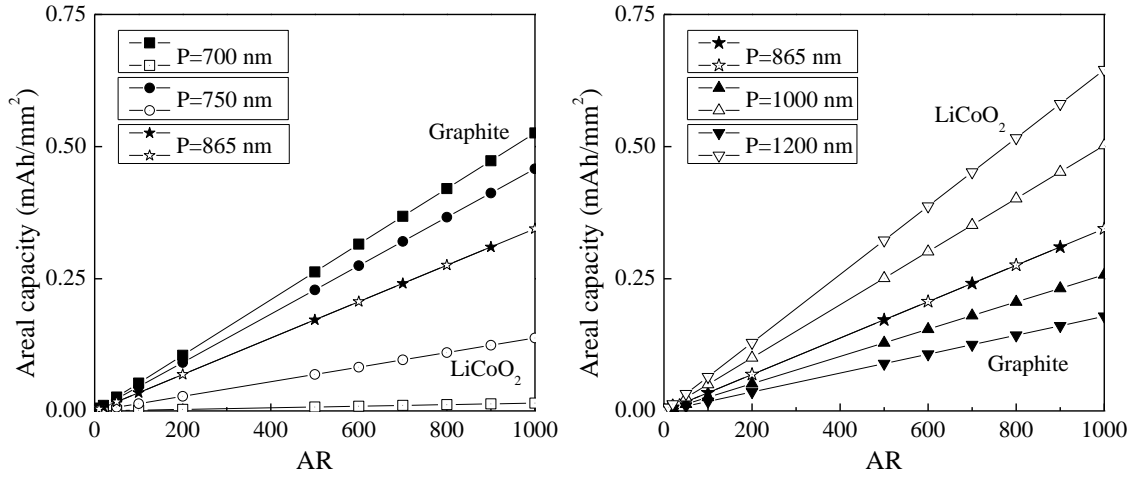


Figure 1.19. Theoretical areal capacity of LiCoO₂ and graphite half-cells as a function of aspect ratio and pitch of the 3D graphite anode features (d is 700 nm, t is 15 nm, D is 750 nm and L is 1 mm). Solid symbols are for graphite and shallow symbols are for LiCoO₂.

Three dimensional LIB systems composed of negative electrode materials, including graphite, tin dioxide (SnO₂) and germanium (Ge), and positive electrode LiCoO₂ are studied to show that a theoretical areal energy of 1 J/mm² can be achieved, as listed in Table 1.10, with a battery footprint of 1 mm×1mm and a cell voltage of 3.5 V. The calculation was performed using 6.95 g/cm³ (Uchiyama, Hosono et al. 2008) and 5.32 g/cm³ (Chan, Zhang et al. 2008) as the density of SnO₂ and Ge, respectively. The calculation suggests that the areal energy of the cell can be optimized by increasing the AR to achieve the requirement as an on-chip power source if the 3D design can be realized and fabricated using suitable materials and 3D feature parameters.

Table 1.10. Calculated battery areal capacity and areal energy of three LIB systems in 3D layouts with an electrolyte thickness of 15 nm and voltage of 3.5V (assumption), showing that the energy density of the cell given a foot-print area of 1mm² can be optimized to achieve the requirement (1J/mm²) as an on-chip power source.

Cathode/ Anode capacity density	Heights H (μm)	Diameter d (nm)	AR	Pitch P (nm)	Areal Capacity (mAh/mm ²)	Areal Energy (J/mm ²)
LiCoO ₂ / Graphite 1386 / 829.6 (mAh/cm ³)	500	700	714	865	0.246	3.10
	500	1400	357	1705	0.252	3.18
	1000	1400	714	1705	0.505	6.36
LiCoO ₂ / SnO ₂ 1386/5421 (mAh/cm ³)	500	700	714	1490	0.542	6.83
	500	1400	357	2963	0.547	6.89
	1000	1400	714	2963	1.094	13.79
LiCoO ₂ / Ge 1386/ 8645 (mAh/cm ³)	500	700	714	1803	0.590	7.43
	500	1400	357	3590	0.594	7.48
	1000	1400	714	3590	1.188	14.96

The high aspect ratio 3D nanowire array of negative electrodes for LIBs could be engineered by different methods, such as vapor-liquid-solid (VLS), wet chemistry synthesis (Sierra-Sastre, Choi et al. 2008), chemical vapor deposition (CVD) and electron beam lithography. In order to assess the performance of the electrode arrays, nanowires (NW) of high capacity negative electrode materials, such as Si, Ge and SnO₂, are attractive. During charge of these negative electrode materials, the Li intercalation results in severe volumetric expansion and sometimes cracks in the materials. When the size was reduced from bulk to NWs, this issue may be less so the cycling performance of these high capacity materials has been studied by building a half NW cell. (Chan, Peng et al. 2008; Huang, Zhong et al. 2010) However, there are still issues of using these anode materials for building a NW battery. For example, one issue for using SnO₂ as the negative electrode in LIBs is the formation of metallic Sn particles during battery cycling, resulting possible short-circuit failure and Sn-catalyzed electrolyte decomposition. (Huang, Zhong et al. 2010) The phenomena can be described based on two reactions: (Huang, Zhong et al. 2010)



In a normal charge (lithiation) process, Sn NPs generated in the first step are consumed in the second step, which is a reversible reaction. However, the second step may not occur if the cycling speed is fast, resulting in large Sn NP generation. (Huang, Zhong et al. 2010; Zhang, Liu et al. 2012) In order to prevent the formation of large Sn NPs, higher Li transport speed is required for the second reaction, equation (1.19), to happen and form Li-Sn alloys. Therefore, applying a layer of high Li ionic conductive coating over the NWs may be a way to provide sufficient Li ions to consume Sn within a short time and prevent the failure of SnO₂ electrode. According to the studies of NW LIBs done by Ruzmetov et al., it is found that a high quality electrolyte film is required to prevent the self-discharge of the battery with an ultra-thin thickness for building 3D microbatteries. (Ruzmetov, Oleshko et al. 2012)

1.4.3 The Need for Solid Electrolytes

Various phases of electrolytes, including liquid (Ohta, Koshina et al. 1995), organic gel (Park, Hyun et al. 2008; Ren, Sun et al. 2009) and solid oxides (Bates, Dudney et al. 2000) have been studied in an attempt to meet the requirements for battery miniaturization. The ionic conductivities (σ_{ion}) of these Li ionic conductors are listed in Table 1.11.

Table 1.11. A list of Li ionic conductors with their ionic conductivities and corresponding activation energies (E_a). (Thangadurai and Weppner 2002)

Compound	Phase	σ_{ion} at RT (S/cm)	E_a (eV)
LiPF ₆ -PC-DMC	Liquid	4.9×10^{-3}	
LiPF ₆ , EC-DMC	Liquid	8.8×10^{-3}	
LiClO ₄ , PC-DMC	Liquid	3.9×10^{-3}	
Li-(C ₂ H ₂ F ₂) _n -C ₃ F ₆	Organic gel	2.3×10^{-3}	0.27
LiBF ₄	Polymer	6.0×10^{-4}	
La _{0.55} Li _{0.36} TiO ₃	Solid	1.5×10^{-3}	0.33
Li _{1.3} Al _{0.3} Ti _{1.7} (PO ₄) ₃	Solid	7.0×10^{-4}	0.20
Li ₃ N	Solid	4.0×10^{-4}	0.30
Li β -alumina	Solid	1.3×10^{-4}	0.27
β -LiAlSiO ₄	Solid	4.7×10^{-5}	0.95
LiI (40 mol. % Al ₂ O ₃)	Solid	1.0×10^{-5}	
LiTi ₂ (PO ₄) ₃	Solid	2.0×10^{-6}	0.30
0.2Li ₂ O-0.55SiO ₂ -0.25P ₂ O ₅	Solid	8.0×10^{-7}	0.42
LiI	Solid	1.0×10^{-7}	0.43
PEO-LiClO ₄	Solid	1.0×10^{-7}	0.31

Even though liquid and gel electrolytes possess higher ionic conductivities than the non-liquid alternatives, difficulties are found to coat them uniformly without pin-holes for electrical leakages over high aspect ratio micro-scale features. (Thokchom and Kumar 2010) Moreover, there are other issues of using liquid electrolyte, such as pollution, discharge, solid electrolyte interface (SEI) formation and unfavorable side reactions. (Wakihara 2001; Shi, Lu et al. 2003) Therefore, solid oxides with mobile Li-ions have become viable as they can achieve the requirements of an electrolyte and be easily deposited. Besides, the intrinsically lower ionic conductivities can potentially be compensated if a conformal, pin-hole free and ultra-thin SSIC is used to shorten the distance between the electrodes for ion transport. For all solid-state ionic conductors (SSICs), the ionic conduction is a thermally activated process and the conductivity can be described by the Arrhenius equation: (Johnson, Biefeld et al. 1976; Thangadurai and Weppner 2002)

$$\sigma_{\text{ion}} = \sigma_o \exp(-E_a / kT) \quad (1.21)$$

or

$$\sigma_{\text{ion}} T = \sigma_T \exp(-E_a / kT) \quad (1.22)$$

where σ_o and σ_T represent the pre-exponential factor, E_a represents activation energy of the ion conduction, k is the Boltzmann's constant and T is the absolute temperature. The mechanism for Li conduction in SSICs is ion hopping from site to site through the structure and therefore partial occupancy of energetically equivalent or near-equivalent sites are required. (Bruce 1995) Without thermal activation, mobile ions in the material are located in a particular site, undergoing thermal vibrations, for most of the time. Occasionally, these mobile ions escaped from the site and hop into an adjacent site since the conduction pathway can be considered as a series of potential barriers with the barrier energy known as the activation energy, which is directly related to the crystal structure. (Bruce 1995) In densely packed crystal structures, like most SSICs, there are no well-defined conduction pathways for the ion hopping to happen so that the activation energies for the ionic conduction are larger, usually 1 eV or more, and the conductivities are low. (Bruce 1995)

1.4.4 Lithium Aluminosilicate (LiAlSiO₄)

Lithium aluminosilicate (LASO), $(\text{Li}_2\text{O})_x-(\text{Al}_2\text{O}_3)_y-(\text{SiO}_2)_z$, is known as ionic conductors which work at high temperatures for electrolyte applications. Its crystal structure is a function of compositions of the three constituent oxides and can be found on the phase equilibrium diagram shown in Figure 1.20.

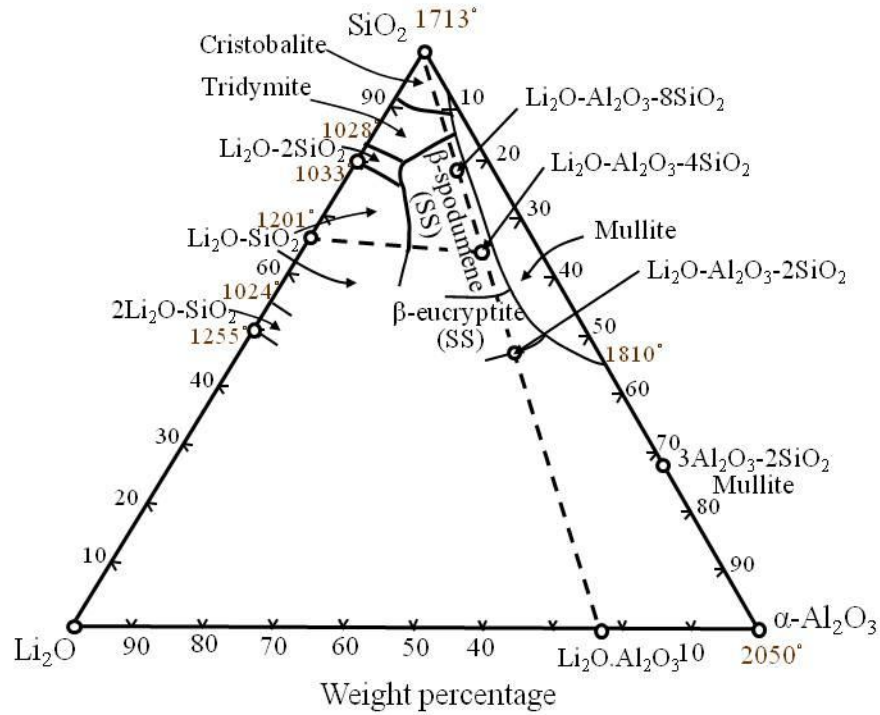


Figure 1.20. Phase diagram of the $\text{Li}_2\text{O}-\text{Al}_2\text{O}_3-\text{SiO}_2$ system, adapted from (Roy and Osborn 1949).

Lattice constants and material properties of common structures, eucryptite (LiAlSiO_4), spodumene ($\text{LiAlSi}_2\text{O}_6$) and petalite ($\text{LiAlSi}_4\text{O}_{10}$) (London and Burt 1982), are summarized in Table 1.12. Among them, LiAlSiO_4 , also known as eucryptite, is considered in this work as the electrolyte material for on-chip battery applications due to its β -eucryptite structure, as shown in Figure 1.21, which has the potential to enable Li-ions to shuffle directly between the cathode and anode through 1D Li channels.

Table 1.12. Structural parameters and physical properties of LASO. (Li 1968; Johnson, Biefeld et al. 1976; Sartbaeva, Redfern et al. 2004)

Phase of LASO	α -eucryptite	β -eucryptite	γ -eucryptite	Spodumene	Petalite
Density (g/cm^3)	2.66	2.351	2.56	3.18	2.40
Composition	LiAlSiO_4	LiAlSiO_4	LiAlSiO_4	$\text{LiAlSi}_2\text{O}_6$	$\text{LiAlSi}_4\text{O}_{10}$
Crystal system	Rhombohedral	Hexagonal	Monoclinic	Monoclinic	Monoclinic
Space group	R3	$P6_422$	$P1a1$	$C12c1$	$P1a1$
Lattice parameters:	13.48	5.24	8.23	9.45	11.75
a (\AA)/b (\AA)/c (\AA)	13.48	5.24	5.03	8.39	5.14
E_a (eV)	9	5.59	8.27	5.22	7.63
	-	1.05	-	0.87	-

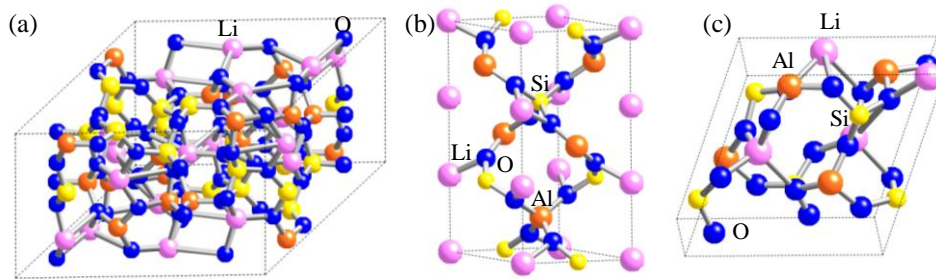


Figure 1.21. Crystal structures of LiAlSiO_4 : (a) α -eucryptite (Hesse 1985), (b) β -eucryptite (Pillars and Peacor 1973) and (c) γ -eucryptite (Norby 1990).

The β -eucryptite structure can be seen as a framework of β -quartz (pure SiO_2), as shown in Figure 1.22 (a), with element Li and Al incorporated. β -quartz belonging to the hexagonal system (space group $P6_221$ or $P6_421$) is formed by building blocks of SiO_4 tetrahedron with each corner O atom bonded to two tetrahedra, also referred to bridging oxygen (BO). When Li_2O was added to form lithium containing silicate glasses $(\text{Li}_2\text{O})_x(\text{SiO}_2)_{1-x}$, the incorporation of alkali attributes to the disruption of the SiO_4 tetrahedra network and the formation of non-bridging oxygen (NBO) sites. (Lammert, Kunow et al. 2003; Soltay and Henderson 2005) The NBOs provide relatively weak connections between one tetrahedral cation (Si) and one or more Li^+ . (Stebbins and Xu 1997) Therefore, the composites are ionic conductive due to jumps or diffusive transport of Li-ion but the effectiveness of these ion transport mechanisms decrease by

correlated forward and backward motions. (Lammert, Kunow et al. 2003) When pure quartz is doped by Al_2O_3 , Al atoms replace Si atoms in the lattice sites due to their comparable atomic sizes. If there are alkali ions, like Li^+ , to balance the charge, the quartz structure can be maintained. In this way, the quartz structure changed from SiO_4 tetrahedra and BOs to SiO_4 and AlO_4 tetrahedra and BOs with Li-ions occupying interstitial sites. (Stebbins and Xu 1997) The material, which can be represented by $\text{Li}_x\text{Al}_x\text{Si}_{1-x}\text{O}_2$ ($0 < x < 1$) based on the composition, possesses high thermal stability because of the stable quartz structure and ionic conductivity due to the transport of mobile Li-ions. Ideally, more Li ions are desired for a higher ionic conductivity of the material, hence incorporation of more Al atoms is needed. However, the oxygen bridge between two Al-ions is unstable due to the Pauling electrostatic valence rule, suggesting no more than 50% of the Si atoms in tetrahedra can be replaced by Al atoms. (Loewenstein 1954) $\beta\text{-LiAlSiO}_4$, as shown in Figure 1.22 (b), has 50% Si atoms substituted by Al atoms, forming a quartz-like framework of alternating SiO_4 and AlO_4 tetrahedra with Li-ions in the interstitial sites forming 1D channels parallel to the c-axis.

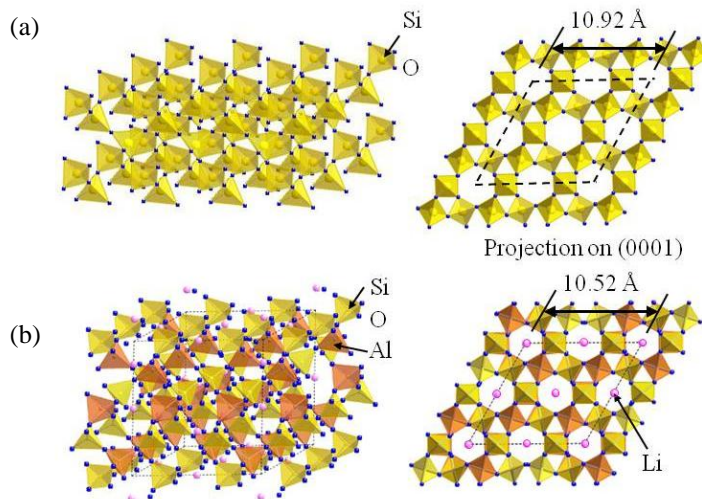


Figure 1.22. The crystal structure and the corresponding atomic projection on the (0001) plane of (a) β -quartz and (b) $\beta\text{-LiAlSiO}_4$. (Nagel and Bohm 1982; Kihara 1990)

Therefore, for β -LiAlSiO₄ single crystal, the ionic conductivity along the c-axis is higher than in other directions (Nagel and Bohm 1982) and the structure is stable at high temperatures because of BOs, making it attractive as battery electrolytes. Same as the β -quartz, β -LiAlSiO₄ has a hexagonal crystal structure with space group of P6₄22 or P6₂22, with a basis of three Si atoms, three Al atoms, three Li atoms and twelve O atoms, as listed in Table 1.13.

Table 1.13. The lattice point basis of a β -LiAlSiO₄ unit cell. (Pillars and Peacor 1973)

Atom	Number	Oxidation state	Site	h	k	l
Li	3	+1	3 a	0	0	0
Al	3	+3	3 d	0.5	0	0.5
Si	3	+4	3 c	0.5	0	0
O	12	-2	12 k	0.21	0.40	0.75

1.4.5 LiAlSiO₄ for 3D Micro-battery

Among the SSICs listed in Table 1.11, β -LiAlSiO₄ is the only 1D ionic conductor, in which the quartz-like framework forming 1D channels for Li transportation, as discussed in Section 1.4.4. It suggests that if an ultra-thin and conformal β -LiAlSiO₄ layer is synthesized on 3D electrodes with the ionic conducting channels connecting the cathode and anode, the lower intrinsic ionic conductivity can be compensated. Furthermore, the material has the highest activation energy, implying the ionic conductivity can be easily enhanced by increased temperatures, as shown in Figure 1.23 (a). Besides, LiAlSiO₄ possesses high thermal stability at elevated temperatures (to 1000 °C) and small thermal expansion, preventing the material from cracking, making it a promising ionic conductor for high temperature electrolyte applications. (Hummel 1951; Johnson, Biefeld et al. 1976) Since both Al₂O₃ and SiO₂ are widely used as gate dielectrics in semiconductor devices, the Li₂O-Al₂O₃-SiO₂ composites with Li transport to

provide ionic conductivity and $\text{Al}_2\text{O}_3\text{-SiO}_2$ to provide electrical insulation is promising for 3D micro-battery applications.

In addition to single crystalline $\beta\text{-LiAlSiO}_4$, amorphous (glass) and poly-crystalline (glass-ceramic) LiAlSiO_4 are also found to be ionic conductive but with lower activation energies of 0.68 eV and 0.78 eV, respectively. (Johnson, Biefeld et al. 1976; Biefeld, Pike et al. 1977) It confirms that the energy barrier for Li ionic conduction is correlated to the crystallinity at a given stoichiometry. $\text{Li}_2\text{O-Al}_2\text{O}_3\text{-SiO}_2$ compositions of other compositions are found to be ionic conductive with different activation energies. The ionic conductivity of the composites prepared by mixing LiAlSiO_4 and SiO_2 has shown to be correlated to the Li-ion content, as shown in Figure 1.23 (b). (Johnson, Biefeld et al. 1976; Nagel and Bohm 1982) Although the ionic conductivity of $\text{Li}_2\text{O-Al}_2\text{O}_3\text{-SiO}_2$ ternary composites is not fully studied, the reported results seem to follow a similar trend. The ionic conductivity increases with rising Li contents but reaches a maximum and then decreases.

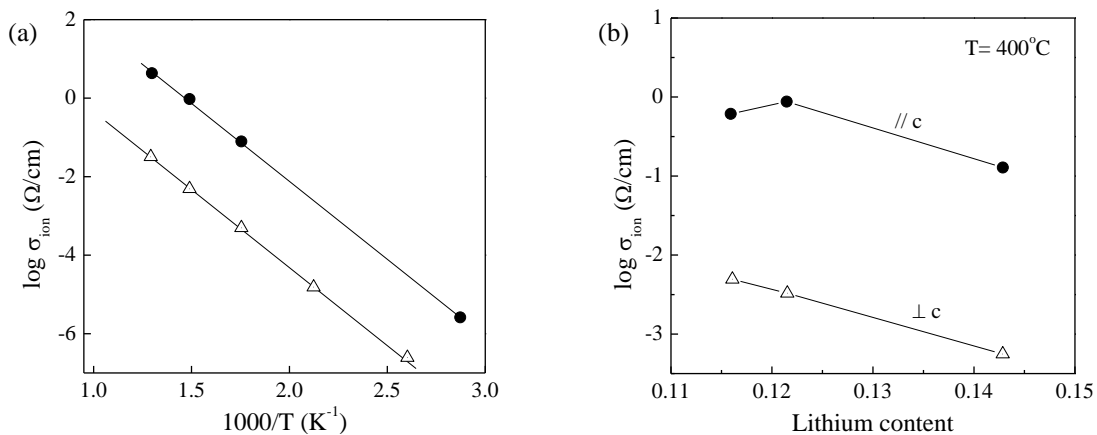


Figure 1.23. The ionic conductivity of LiAlSiO_4 as a function of (a) temperature and (b) Li content, adapted from (Nagel and Bohm 1982).

Besides the crystalline structure, the activation energy of the composites is also related to the cation composition due to the change in crystal structure and bonding which affect the energy

barrier for Li ions to hop from sites to sites inside the material. The ionic conductivity of Li-Al₂O₃ and Li₂SiO₃ can be seen as extreme examples of the composites. Without SiO₂, Li-Al₂O₃ is stacked as layers with ionic conduction path defined, proving 2D ionic conductivity with a lower activation energy of 0.24 eV. (Briant and Farrington 1981) The weaker bond strength of Li-O in the material provides a small barrier height for Li ion hopping, making the diffusion of Li ions less correlated to temperature. Li₂SiO₃, depending on the temperature range and film thickness, possesses an activation energy in a range of 0.44-1.27 eV. (Raistrick, Ho et al. 1976; Furusawa, Kamiyama et al. 2008) The correlation between the activation energy of Li ion diffusion and the Al/Li ratio in Li_xAl_{1-x}Si_{0.5}O₄ has been simulated by Li et al., as shown in Figure 1.24, confirming the activation energy is highly related to the composition as well as the crystal structure.

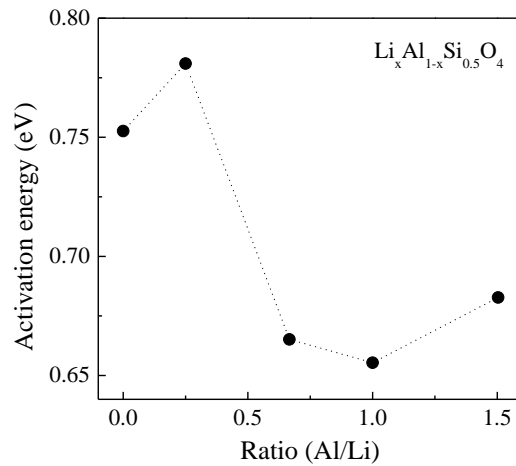


Figure 1.24. The calculated activation energy of Li ion diffusion in glass Li_xAl_{1-x}Si_{0.5}O₄ as a function of Al/Li ratio, adapted from (Li and Garofalini 2004).

Therefore, composition control is an important issue for tuning the ionic conductivity of the composites. The β-eucryptite phase has a 1D Li channels and has been reported to have the highest ionic conductivity among eucryptites. (Johnson, Morosin et al. 1975) Thus, if a β-

LiAlSiO₄ thin film can be synthesized with 1D channels oriented properly, the Li-ions can shuffle between cathode and anode, providing fast ion transportation. Furthermore, the stable aluminum silicate framework can provide electrical insulation between the electrodes and a long-term stability of the battery.

1.4.6 Synthesis of LiAlSiO₄

Prior studies on LiAlSiO₄ were mainly focused on bulk crystals by sintering Al₂O₃, SiO₂ and Li₂CO₃ powders (1:2:1) at high temperatures. (Johnson, Biefeld et al. 1976; Raistrick, Ho et al. 1976) Recently, LiAlSiO₄ thin films are studied using pulsed laser deposition (PLD) with thicknesses in a range of 7.5-1200 nm. (Shin-ichi, Satoshi et al. 2004) For PLD, post-deposition annealing is required for the amorphous film to crystallize into crystalline β- LiAlSiO₄. Table 1.14 details these synthesis techniques for LiAlSiO₄.

Table 1.14. Comparison of deposition techniques for LiAlSiO₄ and the corresponding material properties. (Johnson, Biefeld et al. 1976; Shin-ichi, Satoshi et al. 2004)

Method	Synthesis temperature (°C)	Crystallinity	State	Activation energy (eV)
Sintering	1050-1600	polycrystalline	powder	0.68-1.05
PLD	annealed at 800	polycrystalline	thin-film	0.69-1.02

In this work, LiAlSiO₄ is synthesized by ALD. The thickness and composition controllability of ALD can minimize the ion transport distance and enable the study of the correlation between the cation compositions and the ionic conductivity.

1.5 Scope and Organization

This thesis studies the material and electronic properties of Al-based materials, Al_2O_3 , AlN and LiAlSiO_4 , synthesized via ALD for wide bandgap electronic devices and 3D Li-ion micro-battery applications. Chapter 2 describes the experimental setup used to synthesize and characterize the materials. Chapter 3 summarizes the growth of Al_2O_3 and AlN films on wide bandgap semiconductors, SiC and AlGaIn/GaN . Due to the differences in material properties, Al_2O_3 shows superior in preventing gate leakage current and enhancing 2DEG density, whereas AlN demonstrates the capability of maintaining the mobility of 2DEG. Chapter 4 discusses the ALD growth of ionic conductive LiAlSiO_4 thin films, demonstrating well-controlled growth with high conformality over 3D NWs. The ionic conductivity and activation energy of the material are shown to be comparable to those of bulk LiAlSiO_4 . Chapter 5 concludes this work and provides suggestions for future research.

CHAPTER 2: EXPERIMENTAL SETUP

Two reactors were used to deposit the Al-based thin films via thermal atomic layer deposition (ALD). A high-vacuum chamber with substrate heating was used to grow Al_2O_3 and AlN films on 4H-SiC or AlGaIn/GaN substrates for power device applications. A hot-wall vacuum reactor was used to grow ionic conductor LiAlSiO_4 (Li_2O - Al_2O_3 - SiO_2 composites) films on Si, Ge or ITO substrates for battery applications. Metal-organic precursors, lithium t-butoxide (LTB), tri-methyl aluminum (TMA), and tetraethyl orthosilane (TEOS), were used for Li_2O , Al_2O_3 and SiO_2 , respectively. The oxidant used was water vapor while ammonia was used as a source of nitrogen. Material properties of the synthesized films were characterized via different techniques, such as spectroscopic ellipsometry for film thickness measurements, x-ray photoelectron spectroscopy (XPS) for the surface composition, x-ray/electron diffraction for the crystalline structure and transmission electron microscopy (TEM) for cross-sectional imaging. Electrical properties of the synthesized dielectrics were studied by capacitance-voltage, leakage-voltage and Hall measurements while the ionic conductive films were studied by electrochemistry and impedance measurements.

2.1 Thin-Film Deposition Reactors

Al-based films were deposited using two different reactors due to the precursor chemistry and the film quality required for their applications. In this section, details of the reactor design, precursors and processing gases used are discussed.

A high-vacuum reactor with a base pressure of 2×10^{-8} Torr maintained by a 330 L/s turbomolecular pump backed by a mechanical pump was designed to deposit Al_2O_3 and AlN thin

films via ALD, as shown in Figure 2.1 (a). The chamber pressure was monitored with both a cold cathode gauge and a Pirani gauge. *In-situ* analysis of films grown by the reactor was provided via reflection high-energy electron diffraction (RHEED) and x-ray photoelectron spectroscopy (XPS). The RHEED system composed of an electron gun and screen was installed on the reactor whereas the XPS system was integrated with the reactor via a cluster system of vacuum chambers, as shown Figure 2.1 (b). Samples were loaded into the cluster through the load-lock chamber and transferred among the load-lock, ALD and XPS chambers by a motorized sample stage inside the tube, which has a base pressure of 5×10^{-8} Torr maintained by a cryogenic pump and a turbo pump, and transfer arms with forks that extend into the attached chambers.

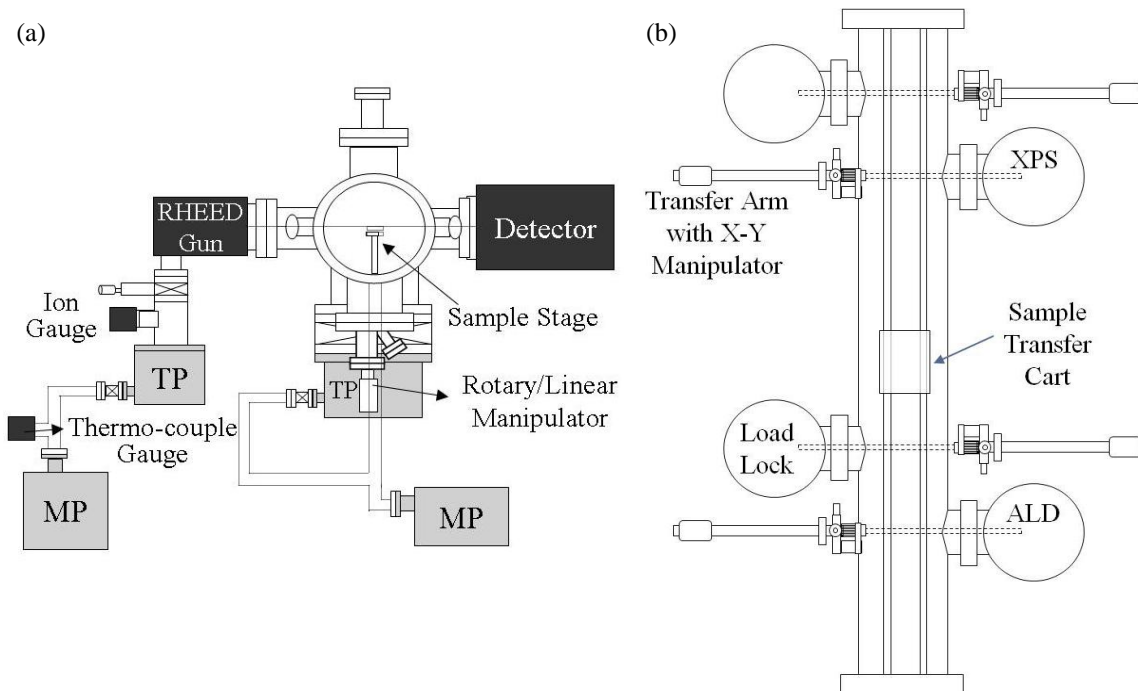


Figure 2.1. Schematic diagrams of (a) the high-vacuum ALD chamber and (b) the integration of this chamber with a high-vacuum cluster system for XPS analysis.

In the high-vacuum ALD chamber, a sample stage composed of a heating station and a receiver fork with standoffs mounted on the bottom flange of the reactor was installed, as shown

in Figure 2.2. Samples were mounted on the top of a sample holder with the same design of the MDC sample holder (MDC 665026) but made of molybdenum (Mo) to enhance thermal conduction since the room temperature thermal conductivity of Mo is 138 W/m-K, about ten times greater than that of stainless steel (16 W/m-K). Sample heating in the chamber was via conduction by a 1-in diameter ceramic heater (GE Advanced Ceramics HT-03) mounted on the heating station. Power connections to the heater were made through vacuum feedthroughs mounted on the flange that supported the heating station manipulator. The heater operates on AC power with a maximum current of 10 Amps, which was controlled by a transformer. Substrate temperatures were monitored using a k-type thermocouple (Omega) mounted on the heater with a screw. Temperature calibration was performed by measuring the temperature of the holder surface (where the sample is), T_{holder} , with the same type of thermocouple mounted on the sample holder via a screw while tracking the heater temperature, T_{station} , and determining the relationship of the two temperatures, which was $T_{\text{holder}} = a T_{\text{station}} + b$ ($^{\circ}\text{C}$) where a and b are constants determined from the calibration and they usually change over time due to the heater degrading. The stage design and calibration details are described in Appendix A.

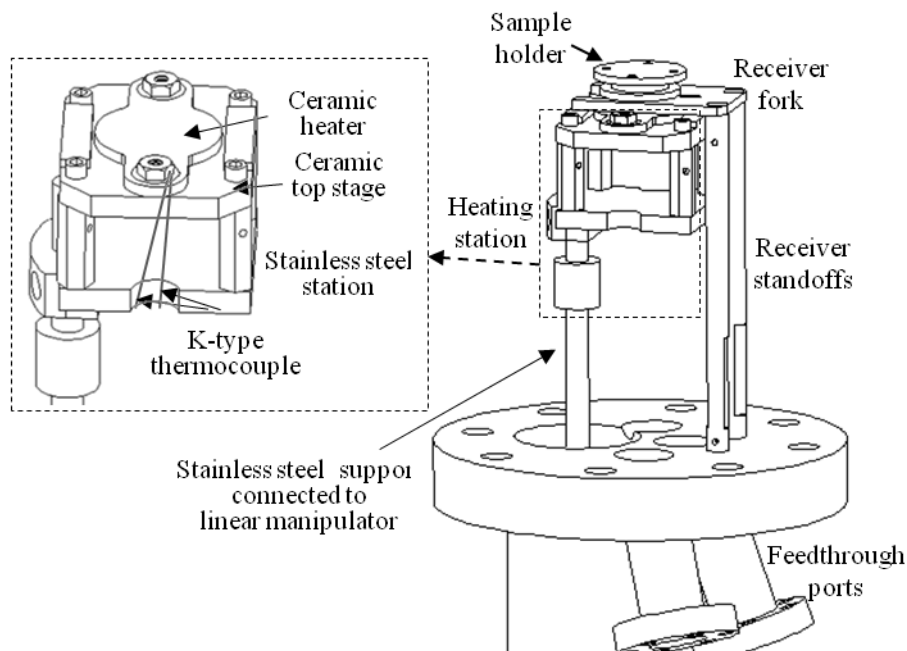


Figure 2.2. The design of the sample stage in the high-vacuum ALD chamber, composed of a receiver fork, standoffs and a heating station with a linear manipulator to bring the heater in contact with the molybdenum sample holder.

The transfer mechanism existing among the chambers and the motorized cart was accomplished by a pin, which fitted to the hole on the bottom of the sample holder, and a transfer arm with a fork, which was used to pick up the holder by coupling with the machined slots around the sample holder. The sample transfer setup inside the reactor was accomplished by the receiver fork and transfer arm, as shown in Figure 2.3. The fork attached onto the transfer arm was used to pick up the holder on the cart in the tube by coupling with the top slot. The arm length was then extended to move the holder into the ALD reactor, followed by the receiving fork coupling with the bottom slot on the holder from the other side. The height of the transfer arm was adjusted to move up the holder into the cutout pocket on the receiving fork. With the linear manipulator, the heating station was moved up to make contact with the sample holder. The last step was to retract the transfer arm to complete the transfer.

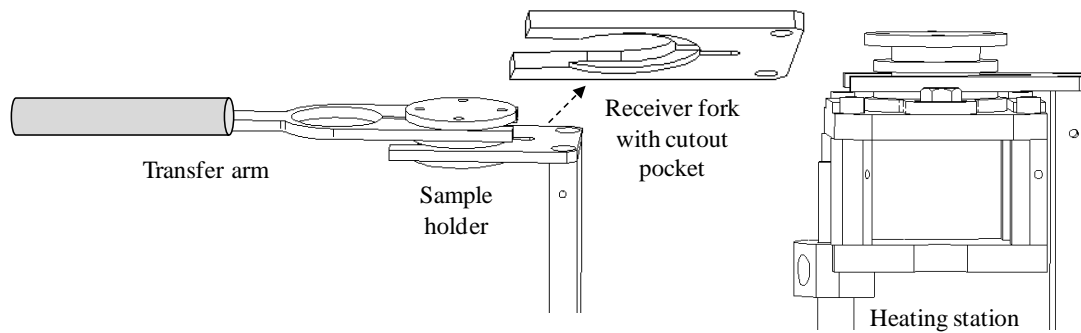


Figure 2.3. The mechanism for transferring a molybdenum sample holder between the high-vacuum ALD reactor and the cluster system.

A hot-wall vacuum reactor was designed to deposit LiAlSiO_4 thin films via ALD with a mechanical pump to maintain the base pressure at 6×10^{-2} Torr, as shown in Figure 2.4. The chamber pressure was monitored by a thermocouple gauge. A manual valve with one side connected to the chamber and the other side to ambient was used for chamber venting. Samples were mounted on a stainless steel plate on a larger mesh which could be conveniently slid in or out from the chamber through the loading door. The sample heating was via radiation from the chamber wall, which was heated by a high-temperature heat rope wrapped around the reactor, to work as a furnace. The temperature of the wall was monitored by a k-type thermal couple (Omega CN 9000A) which is attached to the outside of the reactor wall via Kapton tapes and controlled by a temperature controller (Omega CN9000A), which provided AC current pulse to the heat rope to ensure that the temperature reaches and maintains at the set point. Details of the chamber and heating system designs are in Appendix B.

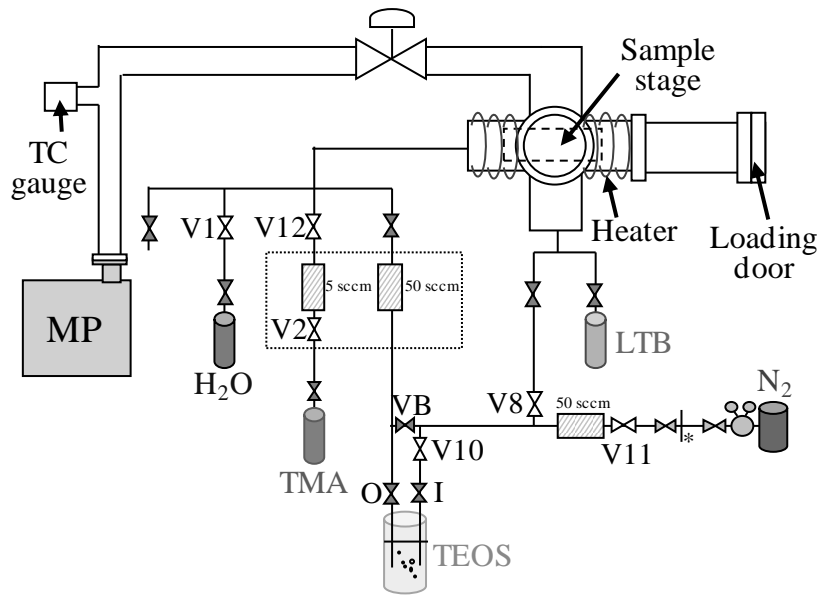


Figure 2.4. A schematic diagram of the vacuum ALD chamber and the layout of gas delivery systems.

2.1.1 Chemistry for ALD Growths and Deposition Sequences

For high-quality Al₂O₃ and AlN thin film growths, an ultra high purity liquid metal-organic precursor of aluminum, trimethylaluminum (TMA), was used and stored in a stainless steel bubbler (Gelest). Water vapor supplied by a deionized water reservoir was used as the oxygen source while ammonia was used as the nitrogen source. Processing gases including oxygen, nitrogen and argon were available on the system. A schematic of the gas line layout is shown in Figure 2.5 with the details of precursors and processing gases listed in Table 2.1. Pneumatic valves were controlled by a solenoid array mounted on an air manifold. Close to both NH₃ cylinders, the lines were connected to the high-purity N₂ line with manual valves for gas line purges. An NH₃ purifier (60-80% MnO₂, Entegris 35KF) was installed in the NH₃ line close to the inlet valve to remove any moisture. The flows of all the process gases were regulated by mass flow controllers (MFC) to maintain operating pressures $< 2 \times 10^{-4}$ Torr. The

vapor pressure of TMA is 8.7 Torr at 25 °C and 70 Torr at 65 °C and therefore a carrier gas is not necessary. The gas lines of TMA and water were heated to 60 °C during the growth to prevent precursor condensation inside the gas line walls during vapor delivery.

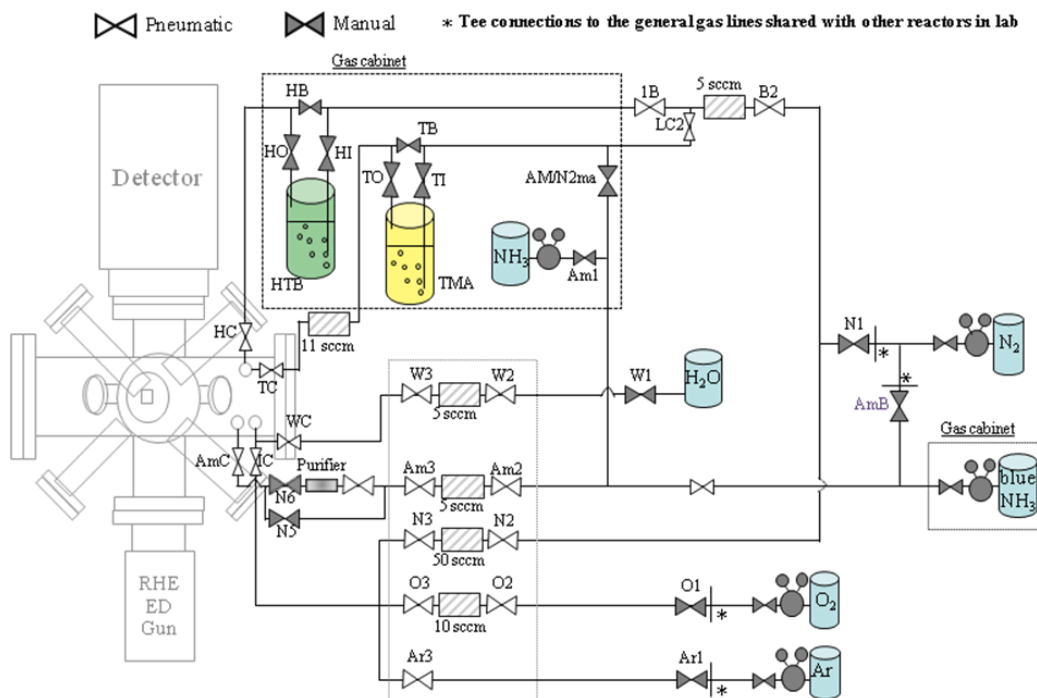
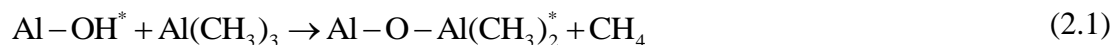


Figure 2.5. A schematic diagram of the layout of gas delivery systems to the high-vacuum ALD reactor.

ALD Al_2O_3 films were grown via TMA and water (H_2O) based on two half reactions: (Gosset, Damlencourt et al. 2002)



where * represents the species which was attached on the surface reaction sites. (Gosset, Damlencourt et al. 2002) Figure 2.6 illustrates the sequence of one Al_2O_3 growth cycle used in this work.

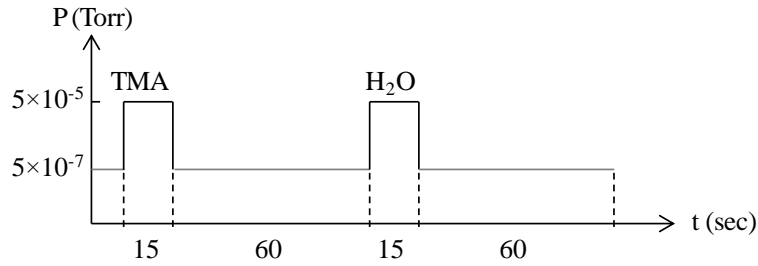
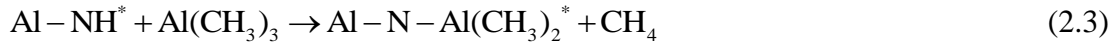


Figure 2.6. An illustration of one chemical pulsing sequence for ALD of Al_2O_3 .

ALD AlN growths were realized using TMA and NH_3 as precursors based on the two chemical reactions listed below:



The growths were performed by alternating a pulse of TMA and a pulse of NH_3 separated by pump-down steps and N_2 purges to avoid vapor-phase reactions. The operating pressure during each chemical pulse was 5×10^{-5} Torr and the pressure reached 5×10^{-7} Torr during the pump-down period. Figure 2.7 illustrates one deposition sequence for ALD of AlN. Details of the operating procedure are in Appendix C. In order to confirm that high deposition temperatures are required to dissociate NH_3 for N incorporation in the synthesized film, a nitrogen radical beam was also used to perform the two half reactions under low-vacuum. The nitrogen atom was provided by a coaxial waveguide microwave radical beam source at 30 W forward power/5W reflected power, provided by a 2.46-KHz Astex microwave power supply, and with a N_2 of 99.999% purity feed gas flow rate of 1 sccm. (Van and Chang 2005)

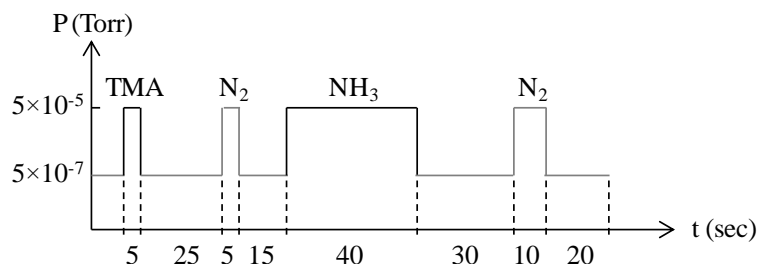


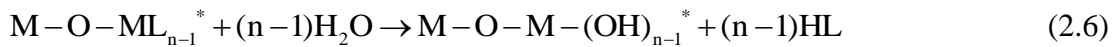
Figure 2.7. An illustration of one chemical pulsing sequence for ALD of AlN.

For LiAlSiO_4 thin film growths, solid metal-organic precursor lithium t-butoxide (LTB) and liquid metal-organic precursors, TMA and tetraethyl orthosilane (TEOS), were used as the source for lithium, aluminum and silicon, respectively. Water vapor supplied by a deionized water reservoir was used as the oxidant. TMA was stored in a stainless container while TEOS was stored in a stainless bubbler (Sigma-Aldrich) using N_2 as a carrier gas. The flows of TMA and TEOS gases were regulated by mass flow controllers (MFC) to maintain operating pressures $< 2 \times 10^{-1}$ Torr. The details of precursors and gases are listed in Table 2.1. LTB is a solid precursor, thus the precursor host and the gas line were heated to 160°C during the growth to ensure sufficient flux for the reaction. The gas lines of TMA, TEOS and water were heated to 60°C to prevent precursor condensation.

Table 2.1. List of chemical precursors and process gases used in this work.

Precursor/Gas	Phase	Chemical formula	Purity (%)	Vendor
LTB	Solid	LiOC(CH ₃) ₃	98	Strem Chemicals
TMA	Liquid	Al(CH ₃) ₃	97	Sigma-Aldrich
			99.99999	Sigma-Aldrich
TEOS	Liquid	Si(OC ₂ H ₅) ₄	99.999	Sigma-Aldrich
Deionized water	Liquid	H ₂ O		
Ammonia	Gas	NH ₃	99.99	Matheson Tri-Gas
			99.99994	Airgas
Oxygen	Gas	O ₂	99.999	Airgas
Nitrogen	Gas	N ₂	99.999	Airgas
Argon	Gas	Ar	99.999	Airgas

The complex oxide Li_xAl_ySi_zO (LASO) was synthesized by alternating ALD growths of Li₂O, Al₂O₃ and SiO₂ with a global deposition sequence designated as b(Al-O)-a(Li-O)-c(Si-O), representing b cycles of Al₂O₃, a cycles of Li₂O and c cycles of SiO₂. The deposition sequence began with Al₂O₃ because it has been shown to provide adequate adhesion to silicon and other chemically inert surfaces, like graphene. (Lee, Park et al. 2008) The half reactions for ALD growths of the three metal oxides can be described by the formulas below:



where M represents the cations (Li, Al or Si), L represents the organic ligands of the metallic precursors (ML_n) and n represents the ligand numbers. Illustrations of deposition cycles for the three oxides and LASO growths are shown in Figure 2.8. Detailed operating procedures of the growths are in Appendix D.

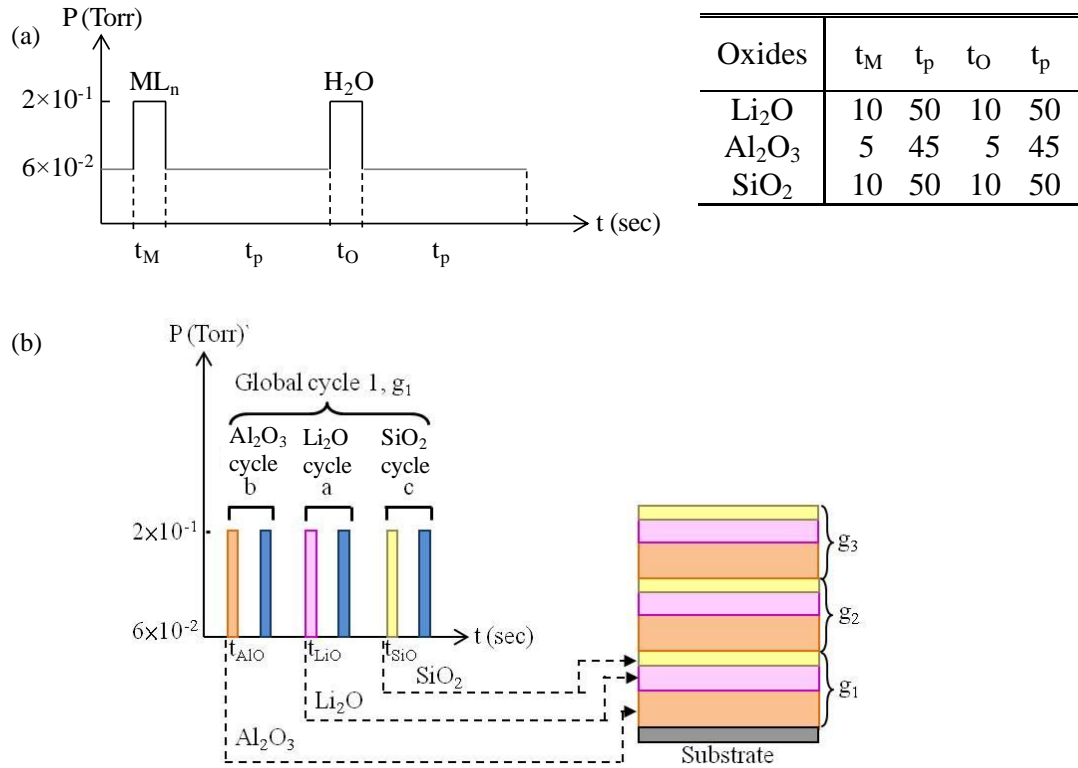


Figure 2.8. Illustrations of (a) one chemical pulsing sequence for ALD of Li_2O , Al_2O_3 and SiO_2 , and (b) the global sequence combining a, b and c as local cycle numbers of Li_2O , Al_2O_3 and SiO_2 ALD growths, respectively, for ALD of $\text{Li}_x\text{Al}_y\text{Si}_z\text{O}$.

In order to study crystallization properties, synthesized films were annealed *ex-situ* in 760 Torr N_2 (99.999%) by rapid thermal annealing (RTA) using RTP 610 (Modular Process Technology Corp.), in which tungsten-halogen lamps serve as the heating source. Annealing temperatures of 900, 1000 and 1100 °C for 60 seconds were used for Al_2O_3 films, whereas temperatures of 500 and 900 °C for 90 seconds were used for LASO films.

2.1.2 Substrate Preparation and Characterization

Chemical mechanical polished (CMP) Si-faced 4H-SiC (0001) wafers (on-axis, nitrogen doping with resistivity of 0.266 $\Omega\text{-cm}$, Cree Inc.) were diced into 1cm^2 pieces as substrates for

growing Al_2O_3 and AlN films. Prior to each deposition, the substrate was cleaned by diluted hydrofluoric acid (HF) (1:20) and followed by DI water rinse to remove the native oxide. An AFM image of a clean 4H-SiC substrate is shown in Figure 2.9 with an RMS roughness of 2.83 Å. For studying electrical properties of deposited films, an epitaxial n-type 4H-SiC ($8\mu\text{m}$ and 10^{15} cm^{-3} nitrogen doping) was grown on an 8° off-axis n-type 4H-SiC (0001) wafer (Cree, Inc) to serve as the substrate. Before the epitaxial SiC (epi-SiC) growth, hydrogen (H_2) etching was used to prepare the samples for subsequent homoepitaxial growth. The epitaxial growth was performed in a horizontal hot-wall chemical vapor deposition (CVD) reactor which heated a graphite susceptor through 10 KHz RF induction. (Myers, Shishkin et al. 2005)

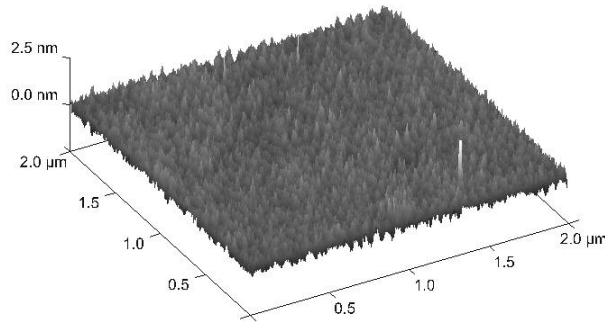


Figure 2.9. An AFM image of a clean 4H-SiC (0001) surface. The RMS roughness was 2.83 Å.

Pieces cut from a wafer of MBE synthesized $\text{AlGaIn}/\text{GaIn}$ on sapphire, with an AlIn nucleation layer serving as a buffer layer, were used as the heterostructure substrates. The GaIn thickness is nominally 5000 Å while the AlGaIn layer is 180 Å . Prior to depositions, 2DEG properties of clean substrates were measured at four edges and the center of the wafer by the Hall measurement discussed in Section 2.5 to obtain the average value for serving as the reference to study the effect of dielectrics on surface passivation. The average values of the carrier density and mobility were found to be $-7.49\pm 0.07 \times 10^{12}\text{ cm}^{-2}$ and $1125.4\pm 7.04\text{ cm}^2/\text{V}\cdot\text{s}$, respectively.

Substrates were then cleaned separately by two different surface treatments to find out a superior process for sample cleaning. X-ray photoelectron spectroscopy was applied to study the surface composition of those cleaned samples, as shown in Figure 2.10. Before the cleaning, the surface was found to have 24.3% C and 15.1% O. After cleaning the sample in $\text{NH}_4\text{OH}:\text{H}_2\text{O}_2:\text{DI}$ (1:1:5), followed by $\text{HCl}:\text{H}_2\text{O}$ (1:1) solutions to remove the surface C and O contents via a digital etching process (Buttari, Heikman et al. 2002), the C content slightly decreased to 23.3% with O content increasing to 16.5%. The increase in O content may be due to surface oxidation. During the first step, the surface was oxidized by the solution. During the second step, only part of the surface oxide was etched, resulting in an increase in the O content. The other treatment was to clean the sample in acetone, followed by isopropyl (IPA) and NH_4OH (50 °C) (Hashizume, Ootomo et al. 2001). The composition analysis showed increases in Ga, Al, and N contents but decreases in C (12.7%) and O contents (9.26%), suggesting the surface treatment by acetone, IPA, and NH_4OH treatment was more effective in cleaning the surface. Therefore, the AlGaN/GaN substrate was cleaned by this treatment prior to each deposition.

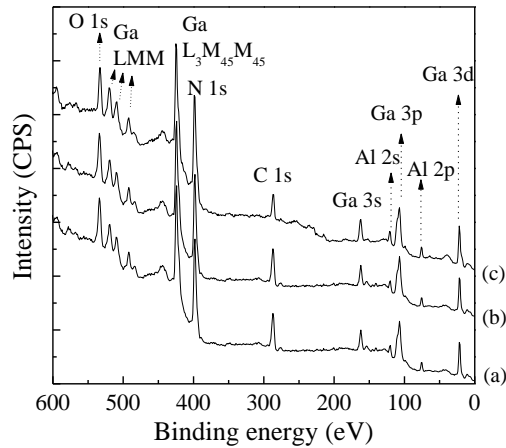


Figure 2.10. XPS spectra of 275 Å AlGaIn/5000 Å GaN samples with different surface treatments: (a) as-received without any surface treatment, (b) cleaned by $\text{NH}_4\text{OH}:\text{H}_2\text{O}_2:\text{DI}$ (1:1:5) solution (70 °C) followed by $\text{HCl}:\text{H}_2\text{O}$ (1:1) and (c) cleaned in acetone, followed by isopropyl and NH_4OH (50 °C).

For LASO thin-film growths, commercial p-type Si (001) and Ge (001) wafer pieces with resistivity of 1-5 $\Omega\text{-cm}$ were used for material characterizations. The conformality study of LASO thin-film coatings on 3D features were performed on wet chemistry synthesized SiO_2/Au core-shell nanoparticles (NP) and SiGe NWs and chemical vapor deposition (CVD) synthesized Si NWs. The SiO_2/Au NPs and SiGe NWs were placed on Si substrates by DI water drop for the LASO deposition and therefore the arrangement of these 3D features was random. The Si NWs were grown on Si substrates vertically with an aspect ratio of 600, as shown in Figure 2.11. The materials for these 3D features were chosen because Si, Ge and their alloy are promising anode materials in Li-ion battery due to their high capacities. (Chan, Peng et al. 2008; Chan, Zhang et al. 2008; Hwang, Lim et al. 2011)

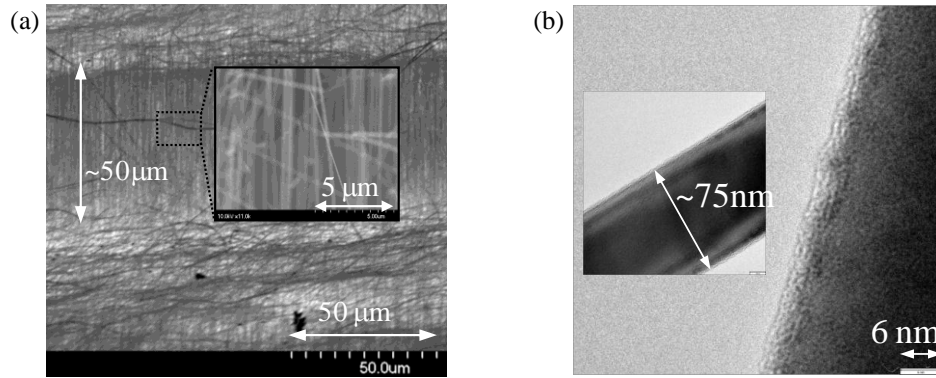


Figure 2.11. (a) SEM and (b) TEM images of Si nanowires synthesized by chemical vapor deposition on a Si substrate.

For studying the electrical performance of synthesized LASO films, pieces of 1 mm-thick indium tin oxide (ITO) coated (sheet resistivity of $20 \pm 5 \text{ } \Omega/\text{sq.}$) on polished quartz glass from Praezisions Glas & Optik GmbH were used as substrates. Before ALD growths, ITO substrates were cleaned using acetone, isopropanol, and DI water. The substrate was used due to its electrical conductivity which served as a backside contact of the deposited LASO films for electrical characterizations. Figure 2.12 shows a Nyquist plot of the impedance response from an ITO/quartz substrate over a frequency range of 20 to 10^6 Hz. The detail of this measurement and other characterization techniques are discussed in the following sections.

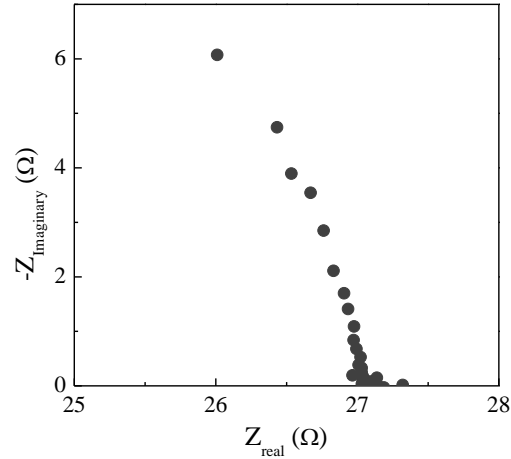


Figure 2.12. A Nyquist plot showing the real and imaginary parts of the impedance measured from an ITO/quartz substrate over a frequency range of 20 to 10^6 Hz.

Finally, the LASO film was applied on SnO_2 NWs prepared by CVD (Zhang, Liu et al. 2012) on Si substrate to study their effect on SnO_2 based NW battery, especially the effect on preventing the formation of Sn NPs during the charging process (lithiation). Figure 2.13 shows the formation of Sn NPs during intentionally Li insertion of a clean SnO_2 NW with an onset current of ~ 15 nA (a current density of $\sim 20 \text{ A/cm}^2$), studied by *in-situ* high resolution transmission electron microscopy imaging (HRTEM).

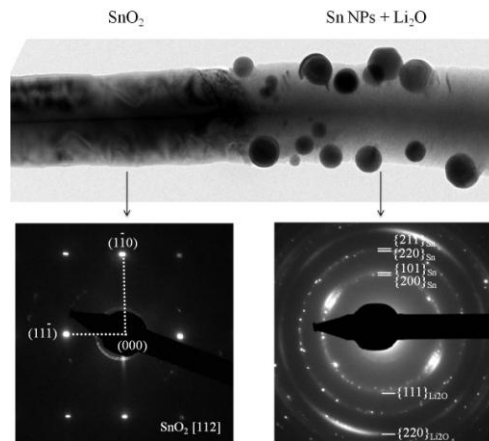


Figure 2.13. An *in-situ* HRTEM image and SAED patterns of a single crystalline SnO_2 nanowire at the reaction front during the lithiation process. (Zhang, Liu et al. 2012)

2.2 Material Characterization

2.2.1 Reflection High-Energy Electron Diffraction

RHEED is a technique providing real-time surface structures without interfering with the growth process. Furthermore, the small incident angle, 1-3 degrees, of the electron beam enables this technique to have high surface sensitivity. Therefore, it is widely used to monitor thin-film growth processes, such as MBE and other methods, for *in-situ* diagnosis. (Ponce, Krusor et al. 1995; Guha, Bojarczuk et al. 2002; Chang, Lee et al. 2007)

In-situ RHEED performed by electron beam energy of 15 keV (Staib Instruments) was used to study changes in the sample surface crystallinity during Al₂O₃ and AlN growths. An electron gun was mounted on one side of the high vacuum ALD chamber with a fluorescent screen on the opposite side for diffraction image projections, as shown in Figure 2.14. Diffraction images on the screen were captured via a charge-coupled device (CCD) camera, mounted outside of vacuum, at a rate of 60 frames/sec and displayed through a PC interface via a PCI-based PXD1000 frame-grabber card and the kSA-400 analytical software. During the operation, the pressure of the electron gun must be $<5 \times 10^{-6}$ Torr to avoid filament damages. The chamber pressure rose to $>10^{-4}$ Torr during chemical pulses while depositions were performed, and therefore, the electron gun was differentially pumped by a 230 L/s turbomolecular pump with an ion gauge monitoring the pressure. To prevent the gun being operated at higher pressures, an interlock was used to lock the electron gun power supply with a pressure set point of 5×10^{-6} Torr. In order to provide a shallow incidence angle, the sample holder surface was positioned with an offset from the center of the flanges by 0.3-inch in the x-direction. With the x-deflection setting to control the angle of the beam leaving the electron gun and the rocking

setting to adjust the beam trajectory via magnets, the incident angle was controlled in the range of 0.2° - 3.6° . During each measurement, the x- and y-deflection parameters were first used to obtain a visible pattern on the phosphor screen for a rough alignment. Then, the deflection parameters and the rocking settings could be slightly adjusted to get better images. The grid and focus parameters provided the adjustment of the intensity and focus of the beam.

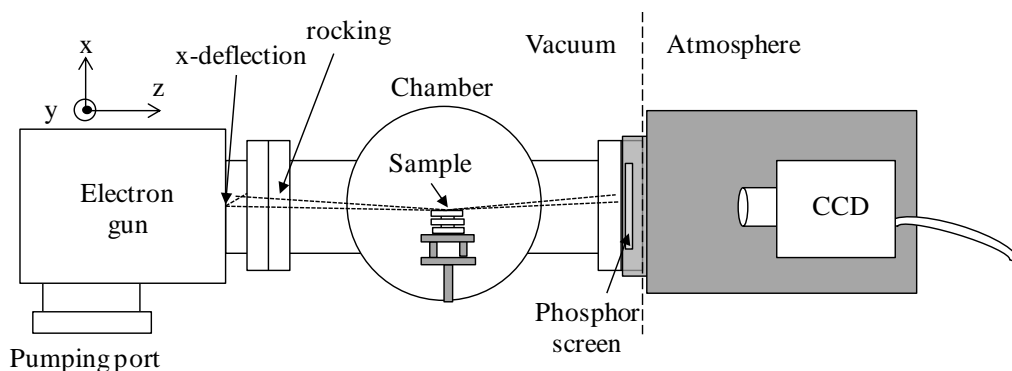


Figure 2.14. A schematic diagram of the *in-situ* RHEED setup on the high-vacuum ALD chamber.

Since the diffraction patterns are generated from constructive interference between electron beams scattered from the measured sample, there is no interference along the direction perpendicular to the sample surface due to the grazing incident angle used in RHEED. The reciprocal lattice, lattice patterns shown by constructive interference, of a surface can be viewed as a set of infinite rods along the dimension perpendicular to the sample surface. The diffraction conditions are satisfied where the rods of reciprocal lattice intersect the Ewald sphere, centered on the sample surface with a radius equal to $2\pi/\lambda$ (electron incident wave length), as shown in Figure 2.15 (a). The intersections from an identical row of the reciprocal rods form concentric circles, known as Laue circles. Since the electron beams only hit one side of the sample, spots shown in the RHEED pattern are arranged at the perimeters of half Laue circles. (Braun 1999)

the kinetic energy (KE) and number of photoelectrons ejected from the material. Only the electrons emitted from the near surface of a sample can escape and be detected since electrons may be scattered by other electrons. (Feldman and Mayer 1986) Therefore, XPS and UPS are surface sensitive technique which usually measure electrons that escaped from the top ~10 nm and ~2nm of the material being analyzed, respectively.

XPS measurements performed with a Mg K α (1253.6 eV) source and a VG100AX hemispherical analyzer provided *in-situ* analysis on the grown AlN films. Samples were measured with the surface oriented normally to the analyzer for an electron takeoff angle of 90°. The measurement of each sample was first performed by a survey scan from 1000 to 0 eV with a step size of 1eV and a pass energy of 100 eV to identify the elements. Then, high resolution scans using a step size of 0.1 eV and a pass energy of 20 eV were performed at selected energy ranges to provide detailed spectra for each element of interest. Since the energy of the x-ray source was known, the electron binding energy (BE) of the atomic orbital, from which electrons emitted, could be determined via an equation listed below:

$$BE = E_{h\nu} - KE - \Phi \quad (2.7)$$

where $E_{h\nu}$ is the x-ray energy, KE is the kinetic energy of emitted electrons and Φ is the spectrometer work function (varies by instrument). (Briggs and Seah 1990) The work function of the instrument used in this work was 4.3 eV. Because the binding energy of each orbital in an element is different, the element and orbital of each peak detected in XPS spectra can be identified according to the binding energy. (Briggs and Seah 1990) Besides, a peak of an element may be deconvoluted into various sub-peaks to assess the chemical environment from the binding energy shift resulted from the surrounding elements. In order to correct surface charges, XPS spectra measured *in-situ* were shifted using the O 1s reference for O-Al-N at 530.4

eV (Rosenberger, Baird et al. 2008). When XPS scans were proceeded *ex-situ*, aliphatic C 1s peak at 284.6 eV was used as the reference. For analyzing ESCA data, the spin orbit splitting (SOS), which is the energy difference between electrons due to coupling between the spin and orbital angular momentum of an electron (Briggs 1977), was also considered. For composition analysis, peaks were fitted by XPSPEAK Software with integrated background (Shirley) subtraction to obtain the integrated intensity (I). The atomic concentration x_i of species i , can be calculated by:

$$x_i = \frac{\frac{I_i}{ASF_i}}{\sum \frac{I_i}{ASF_i}} \times 100\% \quad (2.8)$$

where ASF_i is the atomic sensitivity factor. For UPS, cross-sections of each spectral peak were served as the atomic sensitivity factor for normalized the peak area. Table 2.2 summarizes important parameters used in the work for analyzing ESCA data.

Table 2.2. A list of the spin orbit splitting energies and atomic sensitivity factors used in this work. (Briggs and Seah 1990)

Element	Level	SOS (eV)	ASF _{XPS}	ASF _{UPS}
Ga	3d	0.45	1.3	6.286
Li	1s	-	0.057	0.700
Al	2p	0.41	0.65	4.404
Si	2p	0.60	1.2	4.820
C	1s	-	1.0	-
N	1s	-	1.8	-
O	1s	-	2.2	-

A survey spectrum of a 250 Å AlN film on 4H-SiC is shown in Figure 2.16 (a). To correct surface charge, the entire spectrum was shifted corresponding to the reference O 1s peak

at 530.4 eV. Peaks corresponding to aluminum, nitrogen, oxygen and carbon are detected. Detailed scans of these elements are performed and their atomic percentage was calculated. As show in Figure 2.16 (b), the N 1s peak is deconvoluted into two sub-peaks at binding energies of 395.6 and 397 eV, which are corresponding to N-Al and possibly N-Al-O, respectively.

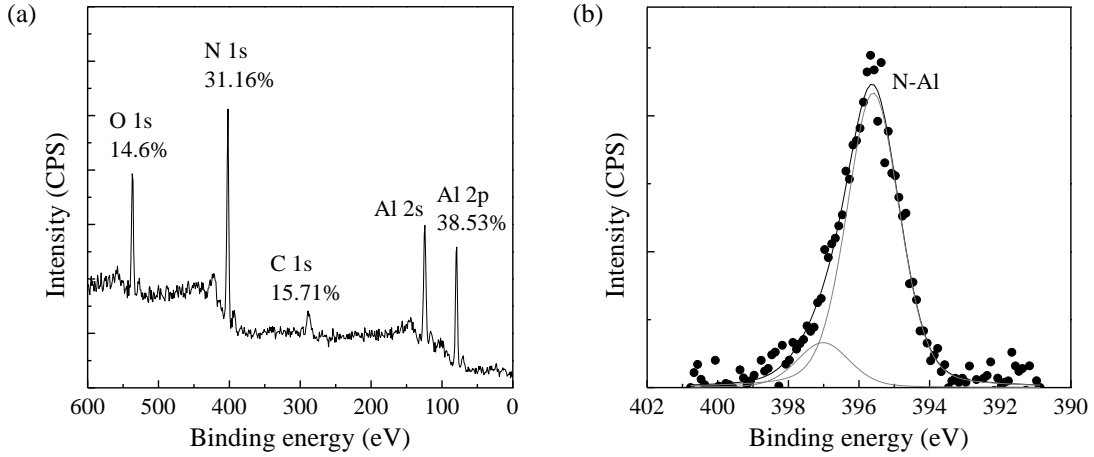


Figure 2.16. *In-situ* XPS spectra of a 250 Å AlN film on 4H-SiC: (a) survey and (b) N 1s.

The thickness of a film can also be determined by the integrated areas of peaks detected from the substrate and film with the following equation: (Hill, Royce et al. 1976)

$$t = \lambda_o \sin \theta \cdot \ln \left[\frac{I_o}{I_s} \frac{ASF_s}{ASF_o} \frac{C_s}{C_o} \frac{\lambda_s}{\lambda_o} + 1 \right] \quad (2.9)$$

where I_s , I_o , C_s , C_o , λ_s and λ_o are the integrated intensity, concentration, and attenuation lengths of the substrate and film, respectively, and θ is the take-off angle which is measured with respect to the surface. For Al_2O_3 grown on AlGaN, the equation shown above was used to calculate the thickness of Al_2O_3 , where $C_{s,\text{Al}}=1/3C_{\text{AlGaN}}=1.50 \times 10^{22}$ atoms/cm³, $C_{o,\text{Al}}=2/5C_{\text{Al}_2\text{O}_3}=6.61 \times 10^{21}$ atoms/cm³, $\lambda_{\text{AlGaN},\text{Al}}=19$ Å (King, Carlson et al. 1999) and $\lambda_{\text{Al}_2\text{O}_3,\text{Al}}=16.7$ Å (Battye, Jenkin et al. 1974). For calculating the thickness of Li_2O deposited on

Si, the used values included $C_{\text{Si}}=4.99 \times 10^{22}$ atoms/cm³, $C_{\text{Li}}=2/3C_{\text{Li}_2\text{O}}=2.70 \times 10^{22}$ atoms/cm³, $\lambda_{\text{Si}}=27$ Å (Bechstedt and Hubner 1981) and $\lambda_{\text{Li}_2\text{O,Li}}=36.1$ Å from NIST electron effective attenuation lengths database. (Powell, Jablonski et al. 2005)

In order to study the cation composition in synthesized $\text{Li}_x\text{Al}_y\text{Si}_z\text{O}$ films on Ge as a function of local ALD cycles a, b and c, UPS spectra taken with a photon energy of 140 eV were used for higher sensitivity on Li elements compared to XPS. At this photon energy, the cross-section of Li 1s is ~1000 times larger (0.7 Mbarns) compared to XPS, thus providing a higher sensitivity. (Yeh and Lindau 1985) For example, Figure 2.17 shows spectra of one sample, 10 ALD cycles of Li_2O grown on an as-received Si wafer piece, measured by XPS (monochromated Al K α , 1486.6 eV) and UPS (synchrotron, 140 eV). The peak-to-noise ratio of Li 1s in the XPS spectrum is small and makes it questionable on defining the peak area.

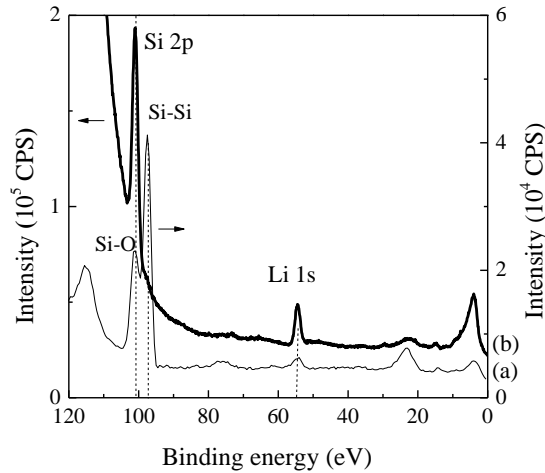


Figure 2.17. Comparison of photoemission spectra of Li_2O on Si taken by (a) XPS with Al K α source (photon energy of 1486.6 eV) and (b) UPS with synchrotron (photon energy of 140 eV). The Li_2O film was grown by 10 ALD cycles.

The synchrotron UPS chamber, possessing the capability of *in-situ* heating, was used to study the surface cation composition of as-deposited LASO films and the change in cation

compositions as a function of annealing temperature.

2.2.3 Spectroscopic Ellipsometry

Ellipsometry is a technique used to measure deposited film or surface layer thickness by measuring the polarization changes between the incident polarized light and the reflection. (Lee, Namkoong et al. 2007) The change in polarization (p) can be considered as two parts, an amplitude ratio (ψ) and a phase difference (Δ), and is commonly written as:

$$p = \tan(\psi) e^{i\Delta} \quad (2.10)$$

The change in polarization is from the interaction between the incident light and the sample materials so it depends on optical properties and thickness of the measured material on a sample. The optical properties can be described by two values which define the interaction between lights and materials, index (n) and extinction coefficient (k). They are both functions of the incident light wavelength (λ) and can be represented by a complex number \tilde{n} as $\tilde{n} = n + ik$. Since the optical properties are defined for a specified material, the measured phase difference and amplitude ratio can be used to determine the layer thickness.

Ex-situ spectroscopy ellipsometry was used to measure the thicknesses of synthesized films by a J.A. Woollam M-88 rotating analyzer spectroscopic ellipsometer (RAE) over a wavelength range of 280-766nm. The measured data were fitted by the WVASE 32 software with a Cauchy dispersion model describing optical properties of the measured material based on the following relationship:

$$n(\lambda) = A + \frac{B}{\lambda^2} + \frac{C}{\lambda^4} \quad (2.11)$$

where A, B, and C are the fitting parameters for the model. Values of the fitting parameters used in this work for different synthesized materials are listed in Table 2.3. Knowing the thicknesses of films deposited by various ALD cycles, the deposition rate, also known as growth per cycle (GPC), can be determined in a unit of angstrom per cycle ($\text{\AA}/\text{cycle}$). An example of spectroscopic ellipsometry plot of ψ and Δ for a $\sim 345 \text{ \AA}$ AlN film on 4H-SiC is shown in Figure 2.18 with a Cauchy model fitting shown in dash lines. The refractive index dispersion shown in Figure 2.18 (b) is comparable to literature. (Bass 1994)

Table 2.3. A list of fitting parameters for the Cauchy dispersion model used to describe optical properties of synthesized materials.

	A	B	C
AlN	2.09	-0.00125	9.93×10^{-4}
Al ₂ O ₃	1.75	0.00773	-2.07×10^{-4}
SiO ₂	1.45	0.00376	5.13×10^{-6}

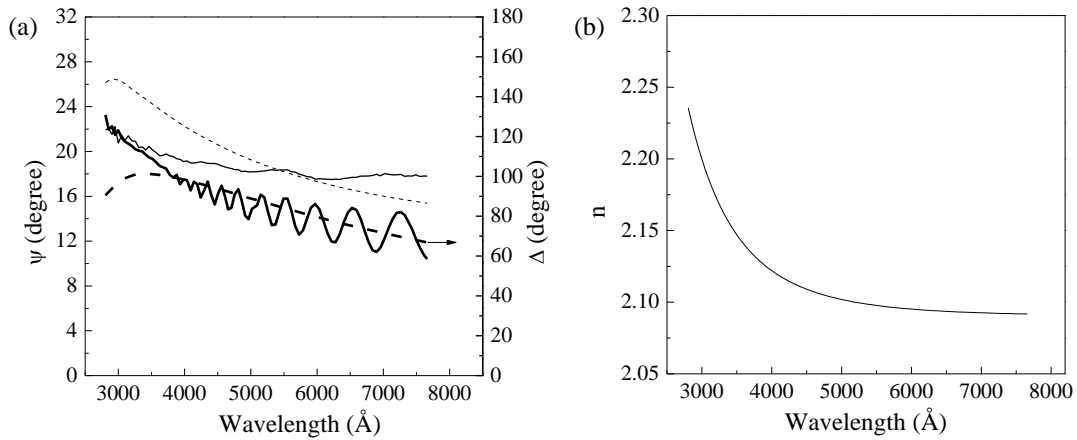


Figure 2.18. Ellipsometric measurement of a $\sim 345 \text{ \AA}$ AlN film on 4H-SiC: (a) experimental ψ and Δ compared to the Cauchy model (dashed lines) and (b) the dispersion of fitted index of refraction.

2.2.4 X-ray Diffraction

X-ray diffraction (XRD) is a technique used to define crystal structures of the synthesized films. When x-ray penetrates into a crystal sample, it is scattered by the periodically arranged atoms. These reflected x-rays come out from various atomic layers and interfere with each other. The diffraction pattern comes from the constructive interferences among them. The basis of x-ray diffraction is the Bragg's law which describes the condition for constructive interference between the scattered x-rays from atomic planes of a crystal. The Bragg's law is known as:

$$n\lambda = 2d \sin\theta \quad (2.12)$$

where n is the order of diffraction and is an integer, λ is the wavelength of the incident radiation and d is the spacing between adjacent planes, known as interplane spacing. (Feldman and Mayer 1986) Therefore, when λ is known, planes which scatter the incident radiation for diffractions can be defined based on the value of θ for first-order reflection ($n=1$).

The Bragg's law describes the condition and positions (angles) of diffracted beams but the intensities of diffraction peaks are correlated to the wave scattered by all the atoms in a unit cell of the measured material. The scattered wave of the unit cell is known as the structure factor (F_{hkl}) and can be described by the following equation: (Cullity 2001)

$$F_{hkl} = \sum_{n=1}^N f_n e^{2\pi i(hu_n + kv_n + lw_n)} \quad (2.13)$$

where f is the atomic scattering factor, u_n, v_n, w_n is fractional coordinates of atoms containing in the unit cell ($n=1,2,3\dots N$ for various atoms) and hkl is the Miller index of planes. When $F_{hkl}=0$, there is no reflections occur from the (hkl) plane so diffractions from the plane is not detectable. For Si (diamond structure), the coordinates of atoms in a unit cell are $(0\ 0\ 0)$, $(\frac{1}{2}\ \frac{1}{2}\ 0)$, $(\frac{1}{2}\ 0\ \frac{1}{2})$, $(0\ \frac{1}{2}\ \frac{1}{2})$, $(\frac{1}{4}\ \frac{3}{4}\ \frac{1}{4})$, $(\frac{3}{4}\ \frac{1}{4}\ \frac{1}{4})$, $(\frac{1}{4}\ \frac{1}{4}\ \frac{3}{4})$ and $(\frac{3}{4}\ \frac{3}{4}\ \frac{3}{4})$ so the structure factor $F_{hkl} =$

$f_{\text{Si}} * [1 + e^{\pi i(h+k)} + e^{\pi i(h+1)} + e^{\pi i(k+1)} + e^{\pi i(h+3k+1)/2} + e^{\pi i(3h+k+1)/2} + e^{\pi i(h+k+31)/2} + e^{\pi i(3h+3k+31)/2}]$. For the (001) and (002) planes, the factor equals to zero so that the first diffraction peak of Si along [001] direction is the (004) peak. However, epitaxial relationships are conventionally described using the base planes so the Si (001) plane is still used for alignment along the [001] direction.

In this work, synchrotron x-ray with photon energy of 8 keV (SSRL beamline 7-2) and a four-circle diffractometer were used to study the diffraction patterns. The four-circle diffractometer was used to define the thin-film structure and morphology with four motors, θ , 2θ , φ and χ , as shown in Figure 2.19. When the sample was oriented horizontally, specular θ - 2θ scans were performed to detect peaks corresponding to planes oriented parallel to the sample surface. Peak positions along the 2θ axis were directly correlated to the interplane spacing by Bragg's law. When the sample was oriented vertically, θ - 2θ scans also known as in-plane θ - 2θ scans resolve peaks related to planes perpendicular to the surface. In-plane scans with θ and 2θ fixed for particular peaks and varying φ axis allowed the study on symmetry of the peak and the capability of determining an epitaxial relationship between the film and the substrate. Diffraction peaks were then identified by referencing the Joint Committee on Powder Diffraction Standards (JCPDS) database. Figure 2.19 (a) shows the setup, a Si unit cell with the measured plane marked and specular scans of Si substrate and LiAlSiO₄ film on Si using a synchrotron source with a wavelength of 1.552 Å. The x-axis as q-spacing represents $2\pi/d$. By referring to the JCPDS database, epitaxial relationship of LiAlSiO₄ film on Si is identified as β -LiAlSiO₄ ($2\bar{0}20$) aligned with Si (001) and β -LiAlSiO₄ ($1\bar{2}10$) aligned with Si (100) with 90° symmetry.

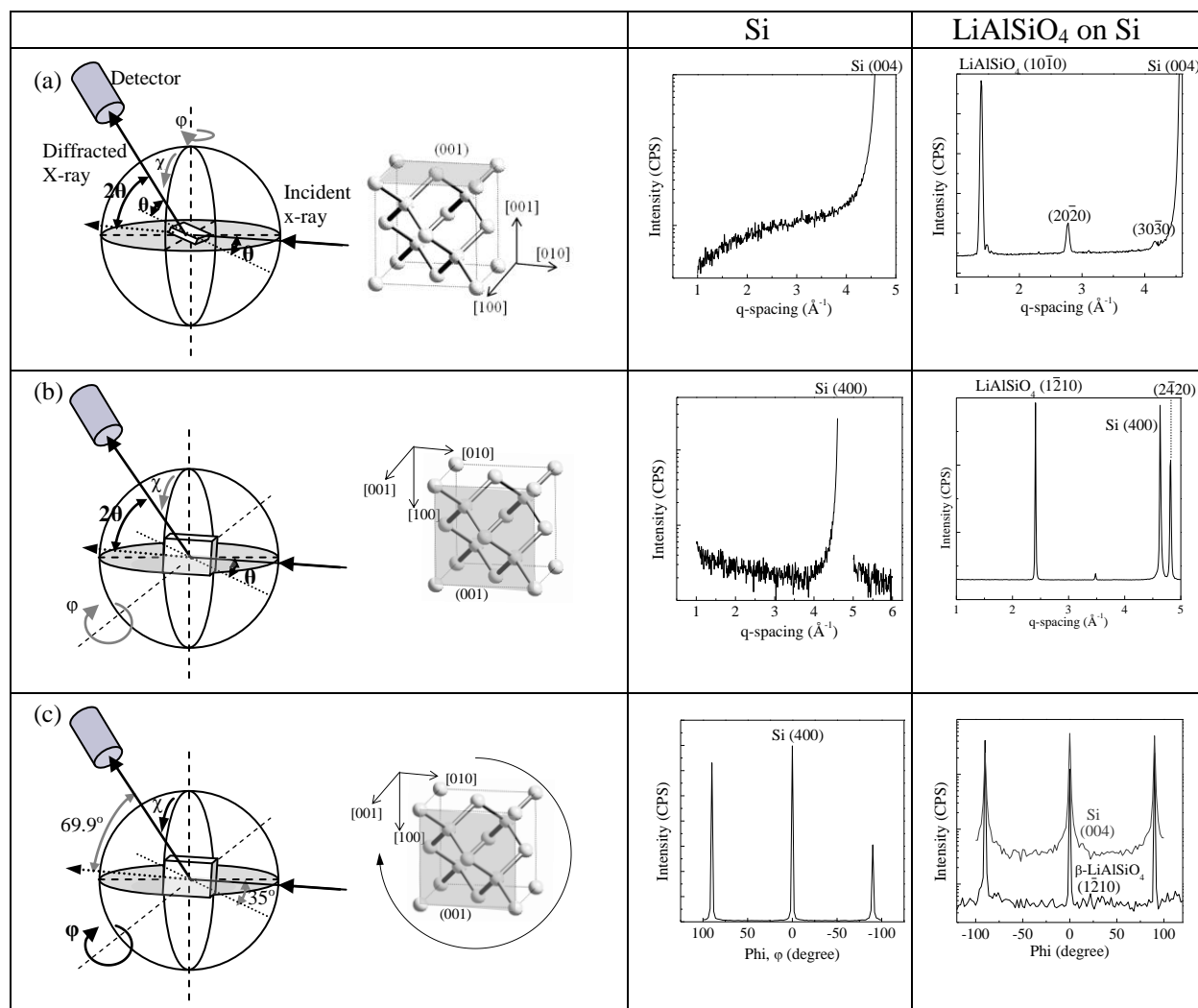


Figure 2.19. A schematic illustration of the synchrotron XRD setup with a four-circle diffractometer and the spectra for Si and LiAlSiO₄ on Si: (a) specular scan, (b) in-plane scan and (c) phi scan. The Si peaks are not completed for preventing the detector from saturation. (d) The angular position and d-spacing are compared with the JCPDS database. (e) A crystal model showing the interfacial epitaxial relationship of LiAlSiO₄ on Si.

2.2.5 High Resolution Transmission Electron Microscopy

Transmission electron microscopy (TEM) is an imaging technique like traditional microscope or light microscopy which can magnify small substances but the probe source is an electron beam instead of light. With electrons as the probe source, the resolution is controlled by the incident energy of electrons and has a value close to atomic size. Besides, electrons are smaller than atoms so that substances with sizes near atomic scales can be observed with a TEM system. The operating principles of TEM and high-resolution TEM (HRTEM) are the same; the only difference is that the incident energy of electrons in HRTEM is higher than that in TEM. According to the correlation between the electron wavelength and the incident energy, the electron beams of HRTEM can have smaller wavelength and obtain image with higher resolution:

$$\lambda = \frac{h}{(2mE)^{1/2}} \quad (2.14)$$

where λ is the electron wavelength, h is the Plank's constant ($=6.62 \times 10^{-34}$ Js), m is the electron mass ($=9.11 \times 10^{-31}$ kg), and E is the incident electron energy. The elemental composition of a sample in TEM technique can be determined by energy dispersive x-ray spectroscopy (EDX or EDS) and electron energy loss spectroscopy (EELS). (Goodhew, Humphreys et al. 2001) EDX is a technique providing local chemical analysis by measuring the energy of x-ray emitting by the measured sample. When the high-energy electron beam in TEM hit the sample, electrons in the lower energy states get excited and eject from the inner orbit shell with holes left. Electrons at higher energy levels then fill the holes and release energy in the form of x-ray. Because different elements have their unique atomic structure, the energy of released x-ray is different and can be used as signatures of elements. In light elements (atomic number < 4), electrons only

occupy in 1s and 2s levels and cannot generate x-ray, so they cannot be measured by EDX. (Goldstein, Newbury et al. 2003)

In this work, Titan TEM with an acceleration voltage of 300 kV ($\lambda=0.022 \text{ \AA}$) was used to study thin-film crystallinity, thickness as well as the conformality of thin-film coatings over nanowires or particles. Figure 2.20 (a) displays an HRTEM image taken on a Au/SiO₂ core-shell nanoparticle with LiAlSiO₄ coating for study the thickness of ALD films.

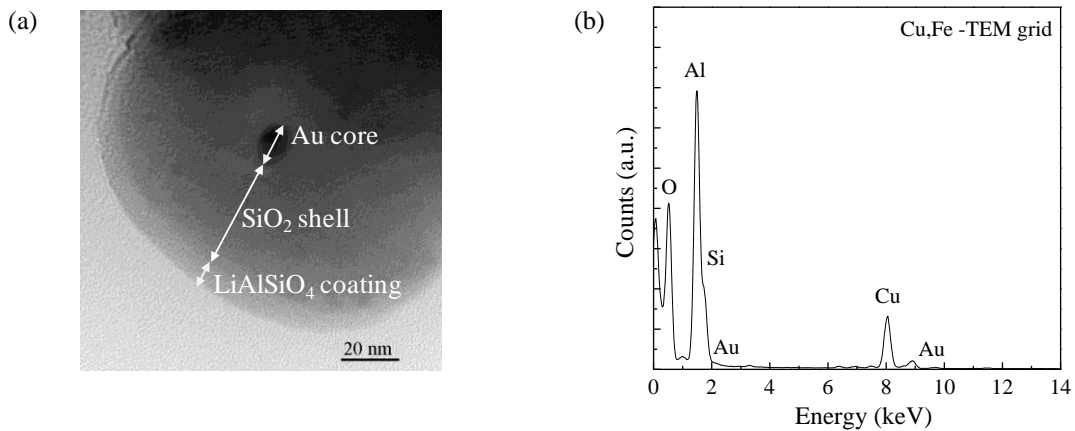


Figure 2.20. (a) An HRTEM image of $\sim 10 \text{ nm}$ LiAlSiO₄ over a Au/SiO₂ core-shell nanoparticle and (b) the corresponding EDX data to confirm the Si and Al presence.

In addition, selective area electron diffraction (SAED) provides diffraction patterns given by the scattered electrons which strike the sample at an appropriate Bragg's angle and interact with each other for constructive interference. A SEAD pattern from a single crystal is a series of arranged diffraction spots around the central bright spot which is from transmitted electrons. If a SEAD pattern is obtained from a polycrystalline sample, the pattern is of concentric rings instead of spots. For an amorphous structure, the pattern has a central sharp spot from transmitted electrons and a single broad ring. If the structure is single crystal or polycrystalline, by measuring the distance between the bright spots or rings, the interplane spacing can be defined by the Bragg's law. An SEAD image of an MBE synthesized AlGaN substrate is shown in

Figure 2.21 with spots originating from AlGa_N (0001) and (20 $\bar{2}$ 0) planes. Combining the Bragg's law, equation (2.12), with $r/L = \tan(2\theta_B)$ and assuming θ_B is small, the spacing can be calculated by:

$$d = \frac{nL\lambda}{r} \quad (2.15)$$

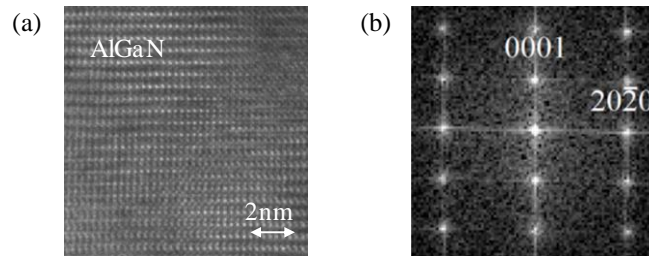


Figure 2.21. (a) An HRTEM cross-section image of AlGa_N and (b) the corresponding SEAD pattern showing the out-plane (0001) and in-plane (20 $\bar{2}$ 0) diffractions.

2.2.6 Inductively Coupled Plasma-Mass Spectrometry

Inductively coupled plasma-mass spectrometry (ICP-MS) is a technique for elemental determinations. Before the measurement, each sample was dissolved at 95 °C in 20% nitric acid (HNO₃) for 2 hours in a dust free environment for generating a ~1mL solution. Then 3 mL of 2% HNO₃ was used to extract the remaining sample and combined with the 1 mL solution prepared earlier. The prepared 4 mL solution was then injected as an aerosol into Agilent 7500ce ICP-MS equipment, which is composed of a high-temperature ICP source with a mass spectrometer. The ICP source generated an argon plasma which converts elements in the sample into ions. These ions are then separated by their mass to charge ratio and detected by the mass spectrometer. Because ions formed by the ICP discharge are typically positive ions, elements prefer to form negative ions are difficult to determine via ICP-MS. Therefore, the technique is

highly sensitive and capable of determining metal elements. Because Li cannot be detected easily by other techniques, ICP-MS was applied in this work to determine metal elements in synthesized films, especially the Li content.

2.2.7 Atomic Force Microscopy

Atomic force microscopy (AFM), one type of scanning probe microscopy (SPM), is used to analyze the surface morphology of synthesized films and substrates. Tapping mode AFM scans were applied using a VEECO Dimension 3100 system with n-type doped Si tapping-mode probes. To optimize the surface roughness sensitivity, adjustments of the distance between the probe and the sample surface were required while minimizing the force placed on the surface. During the operation, the probe on a cantilever oscillated at a frequency near its resonant frequency by a piezoelectric crystal and made contact with the sample surface in a short time. The probe deflection was sensed by position-sensitive detector over a relatively large distance through detecting reflection of a laser beam off the probe. In this way, a large angular deflection due to small movements of the cantilever and probe can be detected, resulting in a high sensitivity to the probe deflection. To maintain the oscillation amplitude, the voltage applied to the piezoelectric was modulated accordingly, completing the feedback loop. Changes in the oscillation amplitude can be recorded during the scans and translated into a topographic map. The surface roughness can then be evaluated by the root mean square (RMS) roughness, R_{rms} :

$$R_{\text{rms}} = \sqrt{\left(\frac{1}{n} \sum_{i=1}^n z_i^2\right)} \quad (2.16)$$

where n is the number of data points and z_i ($i=1-n$) are the heights. The AFM topographic map images are collected by the Nanoscope 6.12rl software, which calculates the RMS value

automatically for each scan. Figure 2.22 shows an AFM 3D image of a 130 Å AlN film on 4H-SiC with an RMS roughness of 7.64 Å.

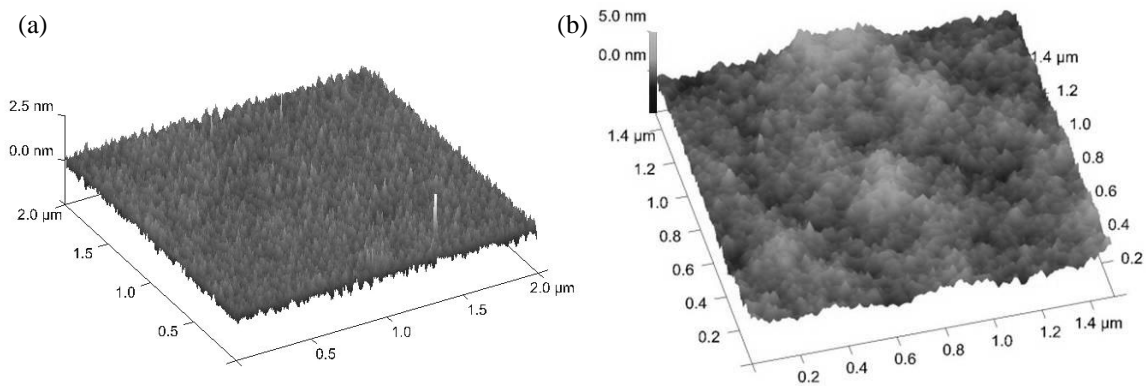


Figure 2.22. AFM images of (a) a clean 4H-SiC with an RMS roughness of 2.83 Å and (b) a 130 Å AlN film on 4H-SiC with an RMS roughness of 7.64 Å.

2.3 MOS-CAP Fabrication

In order to measure the electrical performance of dielectric films Al₂O₃ and AlN, metal-oxide-semiconductor (MOS) capacitors are made based on the process flow shown in Figure 2.23. SiC-based MOS capacitors are fabricated on an 8° off-axis n-type 4H-SiC substrate with an 8 μm SiC epitaxial layer (10¹⁵ cm⁻³ nitrogen doping). (Tanner, Perng et al. 2007) Evaporated 100 Å Ti/1000 Å Pt dots with 350 μm in diameters are deposited using a CHA 4.0 e-beam evaporator machine with a shadow mask as gate electrodes, and RF-sputtered 2000 Å Al deposited by CVC 601 machine is used as the back-side contact.

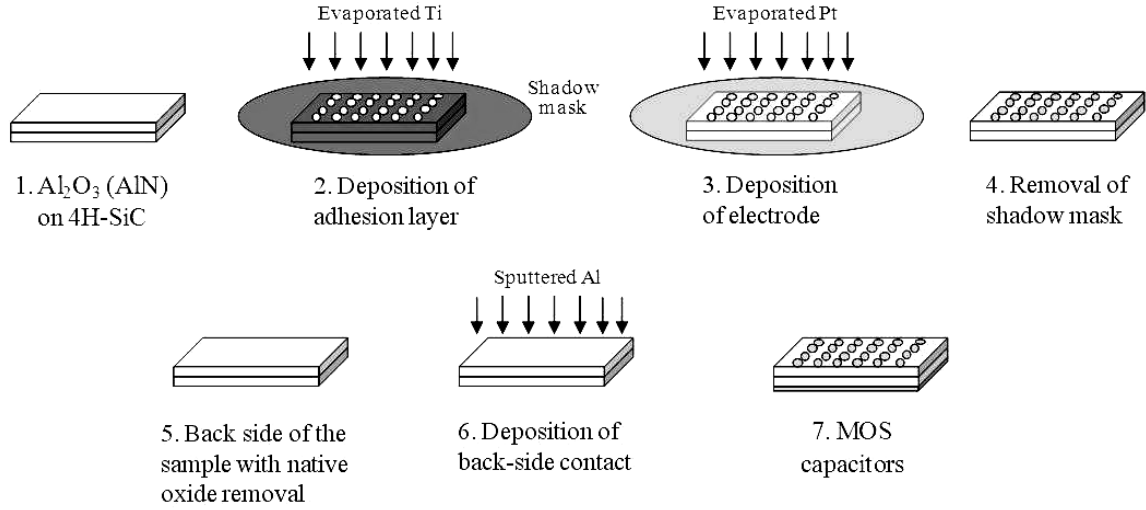


Figure 2.23. A process flow of the MOS capacitor device fabrication for characterizing the electrical performance of synthesized Al_2O_3 and AlN films on 4H-SiC.

2.3.1 Capacitance-Voltage Characteristic

The capacitance-voltage (C-V) measurement is performed by using a probe station connected to an HP 4284A precision LCR meter and acquiring the data via the Metric ICS software as the computer interface. The bias voltage is applied throughout the metal gate and the semiconductor layer with the dielectric layer between them so the device works as a MOS capacitor. By applying the bias voltage, the capacitance can be measured in various regions: accumulation, depletion, and inversion. The dielectric constant (κ) of Al_2O_3 and AlN can be extracted from the capacitance in accumulation region at a high frequency (1 MHz):

$$C_{\text{ox}} = \frac{\kappa \epsilon_0 A}{t} \quad (2.17)$$

where C_{ox} is the capacitance under accumulation, ϵ_0 is the permittivity of free space ($=8.85 \times 10^{-12}$ F/m), A is the area of the capacitor and t is the thickness of the dielectric. Figure 2.24 is a normalized C-V characteristic taken on a 268 Å Al_2O_3 film with a dielectric constant of 8.9.

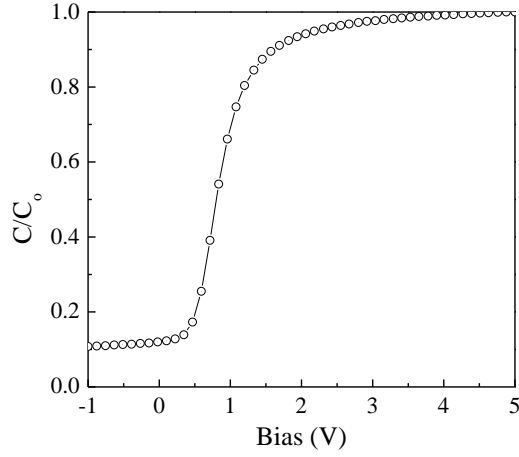


Figure 2.24. Normalized C-V characteristic measured from a 1000 Å Pt/100 Å Ti/268 Å Al₂O₃/n-type 4H-SiC MOS capacitor with 1000 Å Al as the back-side contact.

In an ideal case, when the voltage applied to gate is zero, the MOS is near the flat-band condition with the flat-band capacitance defined as:

$$\frac{1}{C_{fb}} = \frac{1}{C_{ox}} + \sqrt{\frac{kT}{\epsilon_{Si}q^2N_a}} \quad (2.18)$$

The flat-band voltage on the curve is the voltage when the capacitance equals the flat-band capacitance. In a real case, flat-band voltage is

$$\begin{aligned} V_{fb} &= \phi_m - \phi_s - \frac{Q_{ox}}{C_{ox}} \\ &= \phi_m - \left(\chi + \frac{E_g}{2q} + \frac{kT}{q} \ln \frac{N_D}{n_i} \right) - \frac{Q_{ox}}{C_{ox}} \end{aligned} \quad (2.19)$$

where ϕ_m is the work function of the metal gate, ϕ_s is the work function of the semiconductor, χ is the electron affinity of the semiconductor, k is the Boltzmann constant, q is the electron charge, N_D is doping concentration which is negative for n-type doping, n_i is the intrinsic carrier concentration and Q_{ox} is the total charge density in the oxide. (Sze and Ng 2007) Since work functions of the gate and the semiconductor substrate are known with given materials, the charge

density in an oxide can be extracted from the difference between the ideal and real flat-band voltages. The oxide charge includes mobile ions, fixed charge, interfacial traps, and some generated by radiation or stress.

2.3.2 Leakage-Voltage Characteristic

Leakage-voltage (I-V) measurement is accomplished by a probe station connected to an HP 4145 parameter analyzer. The Metric ICS software as the computer interface is used to define the parameters and collect the measurement results. This measurement is used to define the leakage current and the insulating quality of the ALD Al_2O_3 and AlN layers. When a positive bias is applied to the gate with an n-type semiconductor as the substrate, the electrons are attracted towards the dielectric/semiconductor interface. Therefore, the electron injection from the semiconductor through the dielectric to the gate can be measured as the leakage current when a positive bias is applied. This characteristic is normally shown in a graph of leakage current density (J) versus an electric field (E) across the dielectric. The leakage current density is calculated by normalizing the measured current by the device area. The electric field is defined as the applied voltage divided by the ALD film thicknesses. Figure 2.25 is a J-E curve of a 260 Å crystalline $\gamma\text{-Al}_2\text{O}_3$ film on 4H-SiC, showing a leakage current density of 10^{-3} A/cm² at 2.6 MV/cm.

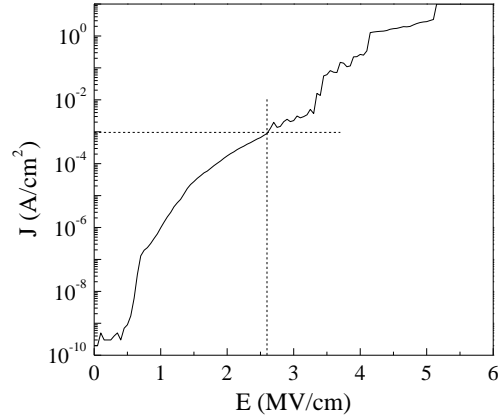


Figure 2.25. Leakage current density as a function of electric field across a 260 Å γ -Al₂O₃ film measured from an Al/260 Å γ -Al₂O₃/4H-SiC MOS capacitor. The dotted lines indicate that the leakage current density reached 10⁻³ A/cm² at 2.6 MV/cm.

The leakage current of synthesized films is correlated to defects in the material and at the interface and the energy barriers of valence and conduction bands at the interface. Various mechanisms for the charge conduction across the oxide can be categorized as ionic conduction, space-charge limited conduction, Fowler-Nordheim tunneling, Schottky emission and Poole-Frenkel emission. (Lamb 1967; Sze and Ng 2007)

2.4 Band Alignment

As mentioned in previous section, the leakage current is a function of energy band offsets at the dielectric/semiconductor interface and the quality of dielectric film and interface. Therefore, knowing the band offsets between the synthesized film and semiconductor substrate is one way to differentiate the cause of current leakage. In addition to the element compositions, XPS can also be used to define the valence band offset at the dielectric/semiconductor interface according to the valence band and core level spectra (Kraut, Grant et al. 1983; Waldrop and Grant 1996), as shown in Figure 2.26. When 4H-SiC is used as the substrate, the calculation of

the valence band offset (ΔE_V) can be performed based on the core level offset (ΔE_{CL}) and the valence band energies using core-level binding energies as the references. The maximum valence band energy of bulk SiC (E_V^{SiC}) is referenced to the Si 2p core-level binding energy (E_{CL}^{SiC}). The maximum valence band energy of the bulk dielectric ($E_V^{dielectric}$) is referenced to the core level energy ($E_{CL}^{dielectric}$). (Hashizume, Ootomo et al. 2003)

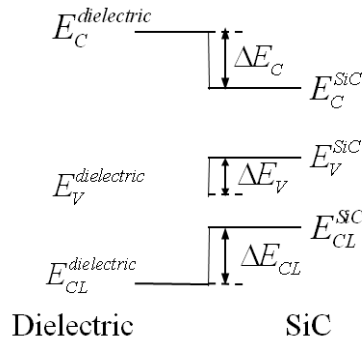


Figure 2.26. Schematic for determining the valence band offset at a dielectric/SiC interface by XPS spectra. (Waldrop and Grant 1996)

As a result, the valence band offset can be determined as:

$$\Delta E_V = (E_V^{SiC} - E_{CL}^{SiC}) - (E_V^{AIN} - E_{CL}^{AIN}) + \Delta E_{CL} \quad (2.20)$$

Since ΔE_V can be determined by XPS data, given the bandgaps (E_g) of SiC and dielectric, the conduction band offset (ΔE_C) can be calculated as:

$$\Delta E_C = E_g^{AIN} - E_g^{SiC} - \Delta E_V \quad (2.21)$$

The band alignment of amorphous Al_2O_3 films on 4H-SiC was performed using XPS spectra of a 4H-SiC substrate, a 200 Å Al_2O_3 film on 4H-SiC, and a 25 Å Al_2O_3 film on 4H-SiC, as shown in Figure 2.27. For the 4H-SiC sample, Si $2p_{3/2}$ peak is found at 100.40 eV with the valence band edge at 1.92 eV. For the thick Al_2O_3 film, the Al $2p_{3/2}$ peak is found at 74.30 eV

with the valence band edge at 3.33 eV. The positions of valence band edges are determined from linear extrapolation to the background. The ΔE_{CL} can be calculated from the position of the Al $2p_{3/2}$ peak (74.48 eV) and the Si $2p_{3/2}$ peak (100.40 eV) measured on the thin Al_2O_3 film sample. Using equation (2.20), the valence band offset is found to be 1.59 eV. With the bandgaps of 4H-SiC and Al_2O_3 , as listed in Table 1.1, the conduction band offset is found to be 2.15 eV.

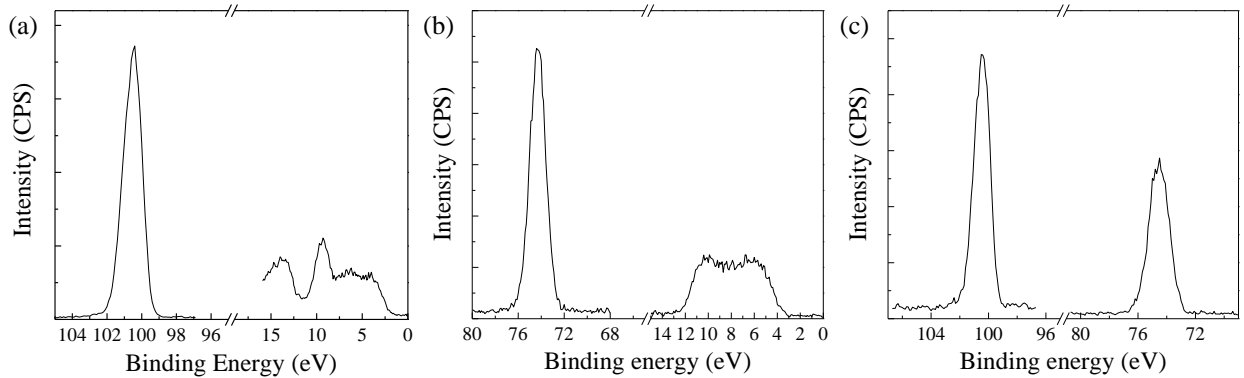


Figure 2.27. XPS spectra of (a) 4H-SiC, (b) a 200 Å Al_2O_3 film, and (c) a 25 Å Al_2O_3 film on 4H-SiC.

2.5 Hall Measurement

Hall Measurement is a widely used method to measure carrier density and mobility in semiconductors, especially for 2DEG in a heterostructure. (Ootomo, Hashizume et al. 2001; Derluyn, Boeykens et al. 2005; Liu, Chor et al. 2007) The basic principle of the Hall effect is the Lorentz force. When a current or an electron flow flowing along the direction which is perpendicular to a magnetic field, the Lorentz force may be induced by the interaction between the electric field and the applied magnetic field. The moving charges experience the force and move in response to it. For an AlGaN/GaN heterostructure, in which the carriers are electrons, if a current (I) flows towards the negative z -direction and a magnetic field (B) is along the positive

x-direction, electrons in response to the Lorentz force (F) drift toward the positive y-direction, resulting in an electric field and voltage across the material along the y-direction, as shown in Figure 2.28 (a). The voltage is known as Hall voltage (V_H). By measuring the Hall voltage and knowing the values of I and B , the sheet density (n_s) of the material can be determined based on the expression:

$$n_s = \frac{IB}{q|V_H|} \quad (2.22)$$

where q is the elementary charge ($=1.6 \times 10^{-19}$ c). (Solymar and Walsh 2004) If the sheet resistance (R_{sh}) of the sample is known, the Hall mobility can be determined as well based on the expression: (Derluyn, Boeykens et al. 2005)

$$\mu = \frac{|V_H|}{R_s IB} = \frac{1}{qn_s R_s} \quad (2.23)$$

The value of R_{sh} is conveniently obtained by the van der Pauw resistivity measurement, which is performed by providing a DC current along one edge of the sample and measuring the voltage across the opposite edge. Resistance values from different orientations ($R_{vertical}$ and $R_{horizontal}$) can be determined based on Ohm's law and R_{sh} can be calculated based on the van der Pauw formula:

$$\exp(-\pi R_{vertical} / R_s) + \exp(-\pi R_{horizontal} / R_s) = 1 \quad (2.24)$$

In this work, the measurement was performed using a Nanometrics Inc. HL5500PC system and 4 point probes to contact with $\sim 1 \text{ cm} \times 1 \text{ cm}$ square samples at 4 corner boundaries for studying the sheet resistance, carrier density and mobility of Al_2O_3 or AlN passivated AlGaN/GaN heterostructure samples. In order to provide Ohmic contacts for the probes, the four corners of each sample were covered by stainless steel washers during the Al-based thin-film deposition, as shown in Figure 2.28 (b).

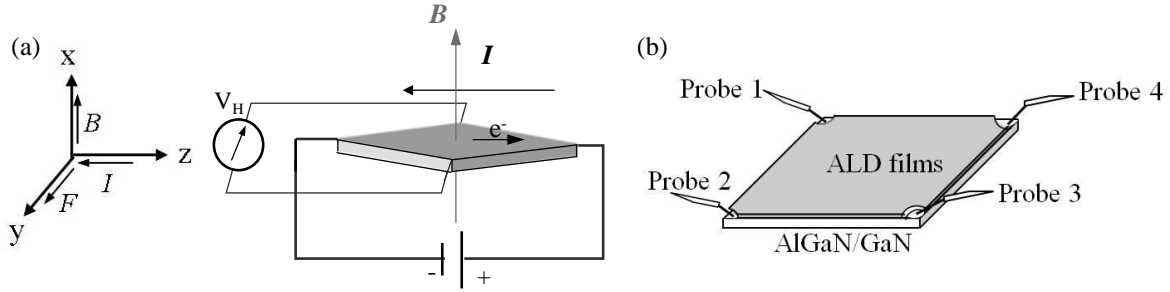


Figure 2.28. Schematic diagrams of the Hall measurement for determining the sheet resistance, carrier density and mobility of 2DEG in the AlGaIn/GaN heterostructure with surface passivated by ALD films: (a) the orientations of applied magnetic field, current and the induced Hall voltage (Solymar and Walsh 2004) and (b) the sample setup.

Before the measurement, the equipment checked the Ohmic contact of each probe on the sample by applying a potential of ~ 20 mV between any 2 probes. Once the Ohmic contacts were confirmed, sheet resistance was determined by van der Pauw method. Then, a current (I) of $91\mu\text{A}$ and a magnetic field (B) of 0.315 T were applied perpendicularly to each other on the measured sample to obtain the values of n_s and μ . Based on the technique principle, the values of R_s , n_s and μ are determined while the sample being measured is assumed to be perfect square-shapes. In order to avoid the measurement error from the sample geometry, one measurement is always involved data measured with different orientations of I , B and F . Table 2.4 shows the data collected from one measurement on a sample of 150 \AA ALD AlN on AlGaIn/GaN with the R_s , n_s and μ determined as $675.4 (\Omega/\text{sq})$, $-8.197 \times 10^{12} / \text{cm}^2$ and $1130 \text{ cm}^2/\text{V}\cdot\text{s}$, respectively.

Table 2.4. A set of data measured from 150 Å AlN thin-film passivated AlGaIn/GaN via the Hall measurement with an input DC current and a magnetic field of 91 μ A and 0.315 T, respectively.

Mesured voltage (V)	Symmetry	Factor	R_{sh} (Ω /sq)
$V_{43}= +1.841 \times 10^{-2}$, $V_{34}= -1.837 \times 10^{-2}$	1.90	0.97	675.3
$V_{41}= +9.707 \times 10^{-3}$, $V_{14}= -9.665 \times 10^{-3}$	1.90	0.97	675.3
$V_{21}= +1.840 \times 10^{-2}$, $V_{12}= -1.838 \times 10^{-2}$	1.90	0.97	675.5
$V_{23}= +9.704 \times 10^{-3}$, $V_{32}= -9.677 \times 10^{-3}$	1.90	0.97	675.5
Hall voltage, V_H (V)			
B \uparrow $V_{24}= -2.08 \times 10^{-3}$, $V_{42}= +2.09 \times 10^{-3}$	$V_{13}= -2.21 \times 10^{-3}$, $V_{31}= +2.28 \times 10^{-3}$		
B \downarrow $V_{24}= +2.20 \times 10^{-3}$, $V_{42}= -2.30 \times 10^{-3}$	$V_{13}= +2.17 \times 10^{-3}$, $V_{31}= -2.13 \times 10^{-3}$		
average $V_{24}= -2.17 \times 10^{-3}$		average $V_{13}= -2.18 \times 10^{-3}$	
$V_H= -2.18 \times 10^{-3}$ V			
$n_s= -8.197 \times 10^{12}$ /cm ²			
$\mu=1130$ cm ² /V-s			

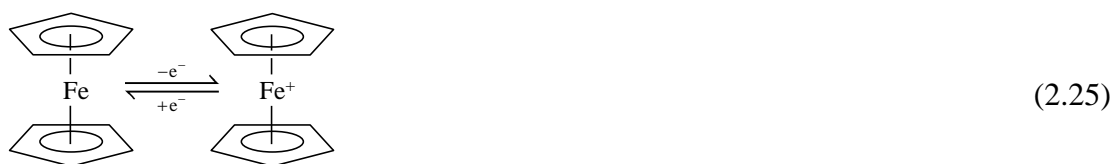
Because the symmetry of the sample being measured was critical for this technique, positioning of the four probes might also result in errors in the values of R_s , n_s and μ . In order to avoid the error, measurements were performed and repeated for three times after the sample was manually rotated by every 90°.

2.6 Electrolyte Characterization

For studying the electrical performance of synthesized LiAlSiO₄ films, ITO/quartz glass pieces (Prazisions Glas & Optik GmbH) were used as substrates for serving as a backside contact because of their electrical conductivity. Before growths, the ITO substrate was cleaned using acetone, isopropanol, and de-ionized water. Growths were performed with half of the substrate covered by a Si piece to block the deposition for easier access to the contact surface.

2.6.1 Cyclic Voltammetry Measurement

The cyclic voltammetry (CV) measurement is a type of potentiodynamic electrochemical measurement and is usually used to study the electrochemical properties of compound in a given solution. In the measurement, the potential, applied between the reference electrode and the working electrode, is swept from a positive to a negative potential and vice versa with a constant sweep rate while the current response at the electrode is measured between the working and the counter electrode. During a forward potential (positive to negative voltage) sweep, the current increases and demonstrate a peak as the potential reaches the reduction potential of the compound being analyzed. If the reaction is reversible, during the reversed potential sweep, the product formed in the reduction reaction will be reoxidized as its oxidation potential is reached and a current response corresponding to the oxidation will be detected. The oxidation peak has a reverse polarity from the reduction peak and shows a similar shape to the reduction peak. (Bard and Faulkner 2001) Therefore, the redox potential and electrochemical reaction rates of the compound can be measured using this technique. In this work, the technique is used to determine the presence of pin-holes in the LASO film by using the redox chemistry of ferrocene, bis-(η -cyclopentadienyl) iron (II), as a reference. Reduction/oxidation (redox) chemistry between ferrocene (FeCp_2)/ferricenium ion (FeCp_2^+), as shown in equation (2.25), is well-established and widely used in electrochemistry measurements. (Gritzner and Kuta 1984; Bond, McLennan et al. 1987) The formal potential of the redox couple in propylene carbonate (PC) is 0.27 V. (Sahami and Weaver 1981)



A 1mM ferrocene solution was prepared using anhydrous PC as the solvent and 100 mM tetrabutylammonium tetrafluoroborate (TBABF₄) as a supporting electrolyte to increase the ionic conductivity in the solution. Three electrodes, a working electrode (ITO), a counter electrode (Pt mesh) and a reference electrode (Pt mesh) were immersed in the solution with the other side connected to a VMP3 potentiostat (BioLogic, USA) to perform voltage sweeps, as shown in Figure 2.29 (a). For identifying whether there are pin-holes in LASO films, the LASO coated ITO samples were immersed into the solution to serve as the working electrode. During the voltammetric sweeps at a rate of 10 mV/s, the current response was measured to detect the redox reactions of ferrocene on the surface of ITO which was in contact with the solution. Whether the characteristic redox peaks of ferrocene is detected providing an indication that the molecule effectively penetrates the LASO film or not, further confirming the existence of pin-holes. Figure 2.29 (b) shows the current-voltage (I-V) response of a reversible ferrocene redox reaction on a clean ITO electrode. When sweeping to positive voltages, a distinctive peak that is attributed to the oxidation of FeCp₂ to FeCp₂⁺, while a sweep in the reverse direction produces a peak signifying the reduction of FeCp₂⁺ to FeCp₂.

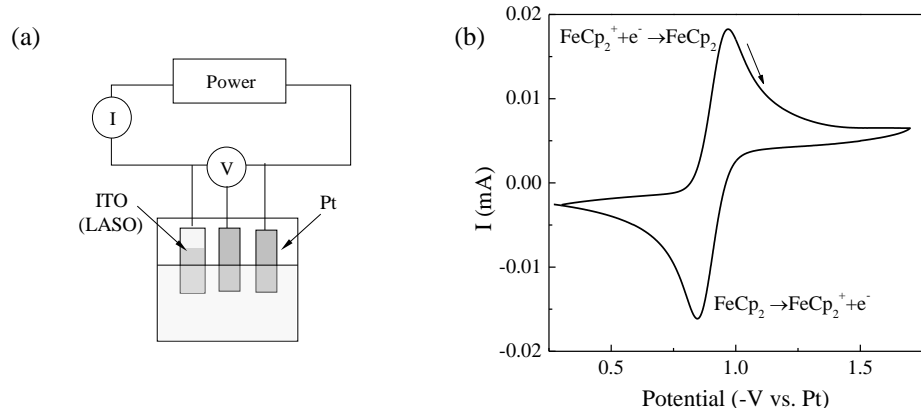


Figure 2.29. (a) Setup of the cyclic voltammetry measurement. (b) Characteristic IV curve measured on a clean ITO/quartz substrate in a solution of 1 mM Fc and 100 mM TBATFB in PC.

2.6.2 Impedance Measurement

Electrochemical impedance spectroscopy (EIS) is a powerful diagnostic tool for determining ionic conductivities of materials and normally measured using a small excitation signal, which can be expressed as a function of time:

$$V_t = V_0 \sin(\omega t) \quad (2.26)$$

where V_t is the potential at time t , V_0 is the amplitude of the signal, ω is the radial frequency ($=2\pi f$) and t is time. In a linear system, the response current signal is shifted in phase (Φ) due to the measured system and expressed as:

$$I_t = I_0 \sin(\omega t + \Phi) \quad (2.27)$$

Similar to Ohm's law, in which resistance (R) is the ratio between voltage (V) and current (I), the impedance of the system can be calculated as:

$$Z = \frac{V_t}{I_t} = \frac{V_0 e^{j\omega t}}{I_0 e^{j\omega t - \Phi}} = Z_0 e^{j\Phi} = Z_0 (\cos \Phi + j \sin \Phi) \quad (2.28)$$

The impedance is composed of a real part and an imaginary part. Common electrical elements and their impedance are summarized in Table 2.5.

Table 2.5. Basic electrical elements and their impedance.

Component	Current Vs. Voltage	Impedance
Resistor (R)	$V=IR$	$Z=R$
Inductor (L)	$V=LdI/dt$	$Z=j\omega L$
Capacitor (C)	$I=CdV/dt$	$Z=1/(j\omega C)$

The Nyquist plot is a widely used way to demonstrate the impedance of the material as a function of frequency. In which, the real part is plotted on the x-axis and the imaginary part is plot on the y-axis with each points representing impedance at one frequency. Figure 2.30 shows examples of Nyquist plots and their corresponding circuit models.

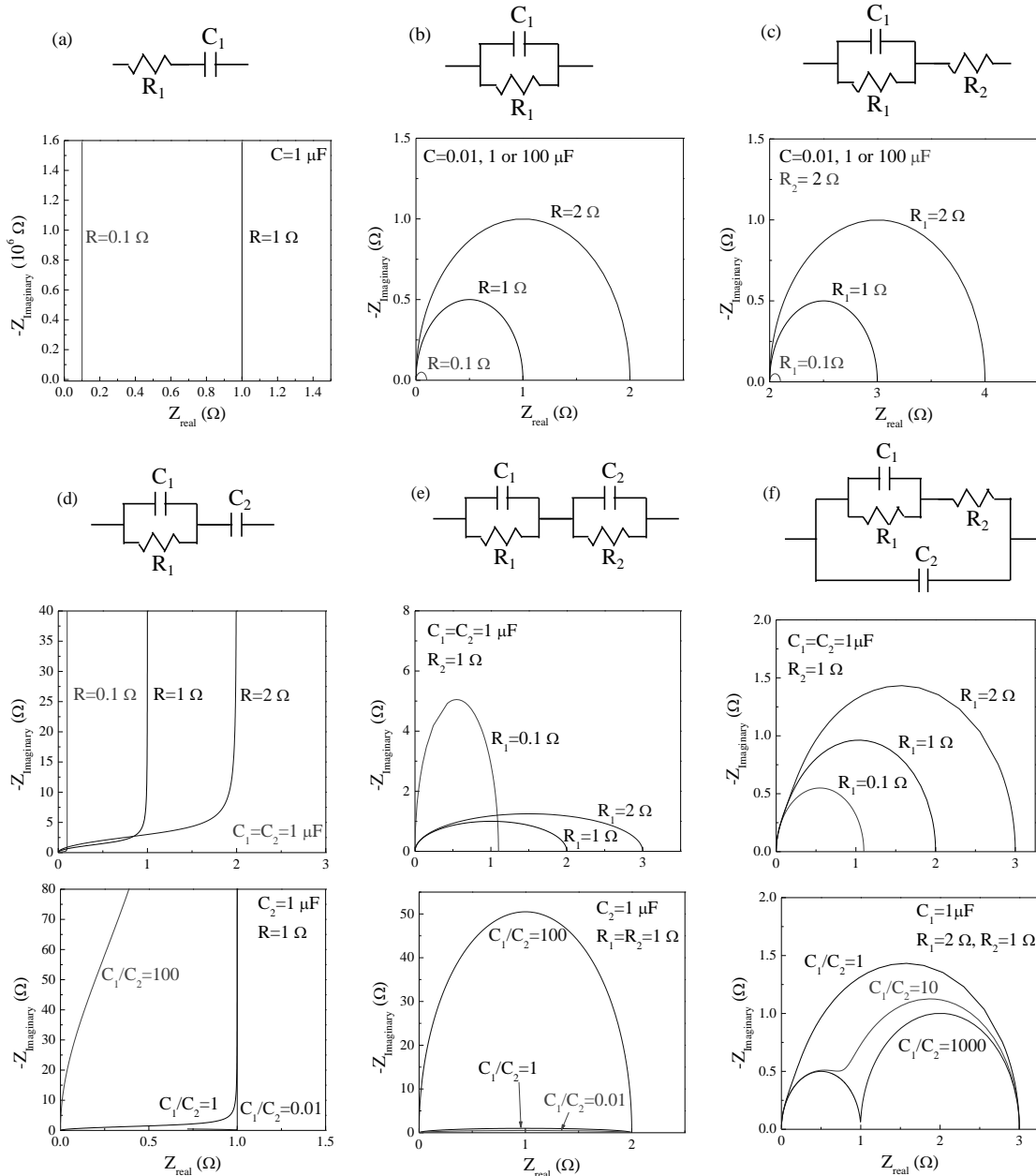


Figure 2.30. Nyquist plots of calculated impedance from various circuit models.

Impedance measurements were carried out on Li containing films deposited onto ITO substrates, serving as the back electrode for the measurements, with the setup shown in Figure 2.31. The top dot electrodes are $800 \mu\text{m}$ in diameters, comprised of a 10 nm adhesion layer of Ti followed by a 100 nm layer of Pt, deposited by e-beam evaporation with a shadow mask.

Tungsten probes, controlled by a Cascade Microtech probe station, were contacted to the ITO and Pt electrodes and connected to an HP 4284A LCR meter. A 13 mV root mean square (RMS) signal over a frequency range of 20 to 10^6 Hz was applied to the film with the impedance response collected.

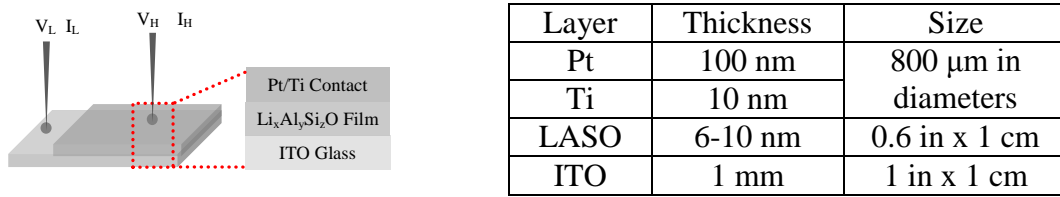


Figure 2.31. A schematic diagram of the setup for impedance measurements.

Equivalent circuit fittings of the measured data were carried out using ZView impedance analysis software (Scribner Associates). Figure 2.32 (a) shows impedance data measured from 10 nm $\text{Li}_x\text{Al}_y\text{O}$ (LAO) on ITO/quartz at various temperatures in a Nyquist plot. The results exhibited semicircle characteristics, equivalent to the impedance response of a resistor, representing ion transportation in the film, and a capacitor, representing the charge stored in the film since it works as a dielectric layer, in parallel. The response is commonly observed on ionic conductive thin-film materials, such as Li_2SO_3 (Furusawa, Kasahara et al. 2009) and LiAlSiO_4 (Shin-ichi, Satoshi et al. 2004) films. The measured data were fitted by equivalent circuits for resistance value of the resistor. The ionic conductivity (σ_{ion}) of the film was then calculated based on the equation:

$$\sigma_{\text{ion}} = t / (R_{\text{Bulk}} A) \quad (2.29)$$

where R_{Bulk} is the extrapolated DC resistance from the fitted circuit model, t is the film thickness and A is the area of the Pt electrode. Measurements at various temperatures were performed while the sample was placed on a hot plate to determine the dependence of ionic conductivities

on temperatures and further define the activation energy based on equation (1.20) or (1.21). The ionic conductivity of the film was determined from the circuit model shown in the inset and calculated as a function of temperature, as shown in Figure 2.32 (b).

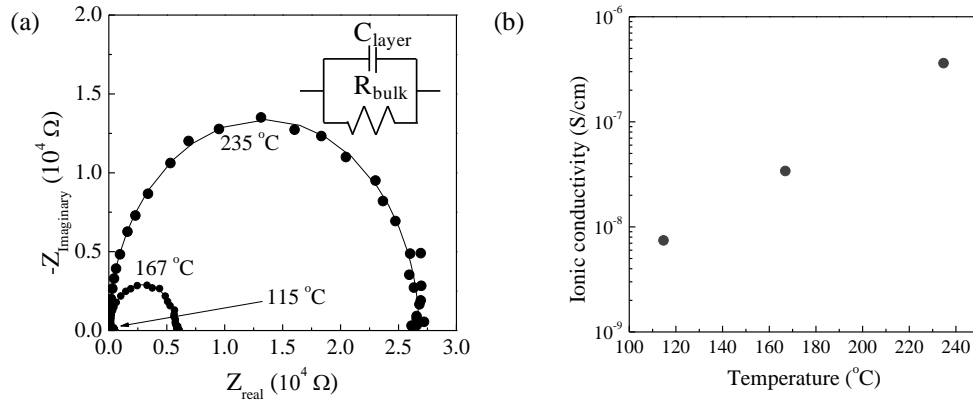
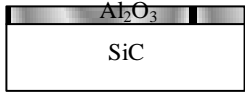
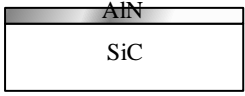
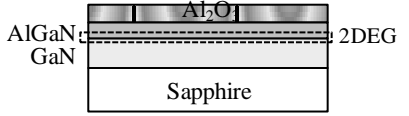
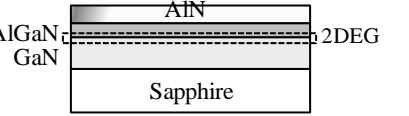


Figure 2.32. (a) Impedance data from a 10 nm $\text{Li}_x\text{Al}_y\text{O}$ film on ITO/quartz at various temperatures. The data were fitted (line) by the circuit shown in the inset. (b) Ionic conductivity as a function of temperature, as determined by the data in (a).

CHAPTER 3: BINARY Al-BASED MATERIALS FOR HIGH-POWER DEVICES

ALD growths of Al_2O_3 and AlN films were demonstrated on wide bandgap semiconductor 4H-SiC and AlGaIn/GaN substrates. Amorphous Al_2O_3 films were grown at 195 °C with a growth rate of 1 Å/cycle and 0.75 Å/cycle on 4H-SiC and AlGaIn/GaN, respectively. Epitaxial $\gamma\text{-Al}_2\text{O}_3$ films were formed on both 4H-SiC and AlGaIn/GaN heterostructures after post-deposition annealing. Due to the grain boundaries in crystalline films, amorphous Al_2O_3 demonstrated superior electrical properties for preventing the gate leakage to crystalline Al_2O_3 as a dielectric in SiC-based metal-insulating-semiconductor capacitors and passivating AlGaIn/GaN surface with an enhanced carrier density in the 2DEG. ALD AlN growths using TMA and NH_3 were realized with sufficient NH_3 flux and eliminated minute amount of moisture in NH_3 at a temperature window of 500-570 °C. Crystalline AlN films were grown at 540 °C with a growth rate of 1.5 Å/cycle. The ALD AlN films exhibited promising electrical performance, including a dielectric constant of 8.3, a leakage current density of 10^{-3} A/cm² at 4.3 MV/cm, and an increased carrier density on AlGaIn/GaN with a mobility of 1130 cm²/V-s. Among the three films, amorphous Al_2O_3 , $\gamma\text{-Al}_2\text{O}_3$ and AlN , the first one demonstrated the lowest gate leakage current while the second film showed the highest leakage current when they were applied on 4H-SiC. For surface-passivated AlGaIn/GaN, highest mobility of the 2DEG was obtained when AlN films were used. Table 3.1 shows a summary of the material systems studied in this chapter.

Table 3.1. Dielectric/wide bandgap semiconductor material systems studied in this work for high-power device applications.

	Al_2O_3	AlN
4H-SiC		
AlGaN/GaN		

3.1 Al_2O_3 on SiC

The growth of Al_2O_3 on 4H-SiC was studied and found to possess a deposition temperature window of 150-300 °C with a growth rate of 0.7-1.2 Å/cycle. Deposition at 195~200 °C provided amorphous stoichiometric Al_2O_3 films grown on 4H-SiC with a rate of ~1 Å/cycle. Band alignment of the as-deposited Al_2O_3 on 4H-SiC studied via XPS spectra, discussed in Section 2.4, demonstrated that the valence band offset was 1.59 eV and the conduction band offset was 2.15 eV, as shown in Figure 3.1.

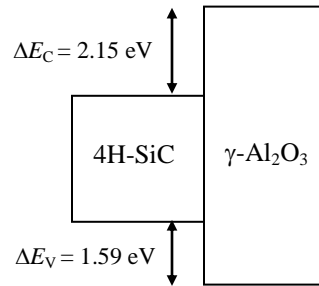


Figure 3.1. A schematic diagram of band alignment at the amorphous Al_2O_3 /4H-SiC interface determined by XPS analysis.

After post-deposition RTA in a N_2 ambient at 1000 °C, the film were crystallized with an epitaxial relationship of $\gamma\text{-Al}_2\text{O}_3$ (111) \parallel 4H-SiC (0001) and $\gamma\text{-Al}_2\text{O}_3$ ($1\bar{1}0$) \parallel 4H-SiC ($11\bar{2}0$) determined via XRD, as shown in Figure 3.2. (Tanner, Toney et al. 2007)

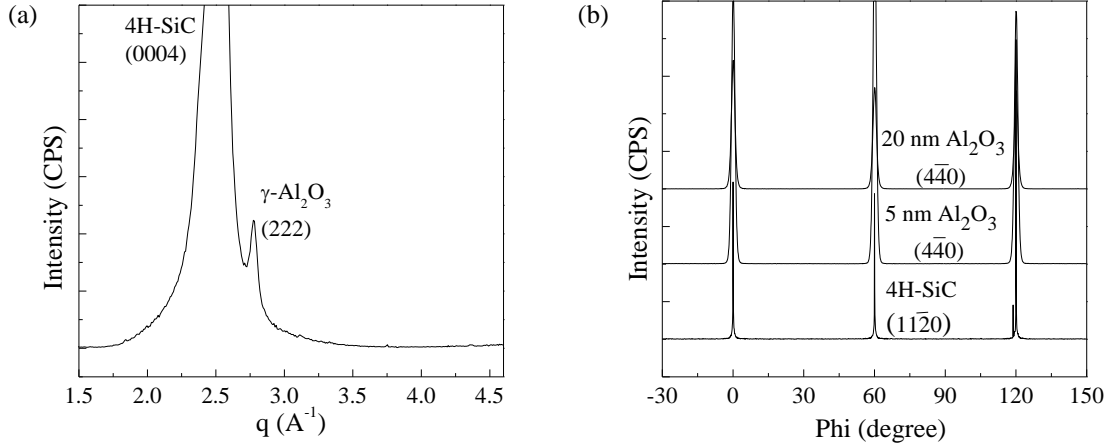


Figure 3.2. XRD spectra of $\gamma\text{-Al}_2\text{O}_3$ on 4H-SiC measured with a four-circle diffractometer: (a) specular scan of a 20 nm Al_2O_3 film and (b) in-plane phi scans on $\gamma\text{-Al}_2\text{O}_3$ films with two thicknesses in comparison with that of the substrate 4H-SiC. (Tanner, Toney et al. 2007)

In order to characterize electrical properties of the ALD Al_2O_3 films, metal-oxide-semiconductor (MOS) capacitors were made from an as-deposited 260 Å Al_2O_3 film and an crystallized 260 Å Al_2O_3 film on 4H-SiC (10^{15} cm^{-3} nitrogen doping) substrates based on the fabrication processing described in Section 2.3. Figure 3.3 (a) shows the normalized capacitance as a function of applied bias measured at 1 MHz on capacitors with the gate size of $1 \times 10^{-4} \text{ cm}^2$. A reasonably constant positive voltage shift of $\sim 1.3 \text{ V}$ relative to the ideal flat-band voltage was observed, suggesting a negative fixed charge density of $2\text{-}3 \times 10^{12} \text{ cm}^{-2}$. The dielectric constant of the film was determined as 9 using the accumulation capacitance and equation (2.17) in Section 2.3.1.

Leakage current-voltage (I-V) was then measured and displayed in the relationship between the electric field (E) and leakage current density (J). In Figure 3.3 (b), devices with crystalline dielectric film demonstrated lower leakage at low applied field, but the leakage current density dramatically increased when the field was larger than 0.5 MV/cm. At a lower electric field of 2.5 MV/cm, the leakage reached 10^{-3} A/cm². On the other hand, the leakage of devices with amorphous dielectric films reached 10^{-3} A/cm² at 8 MV/cm, suggesting the amorphous phase enable the device to work under high field with limited leakage. In contrast, the crystalline film could not prevent the leakage sufficiently due to charge conduction along the grain boundaries.

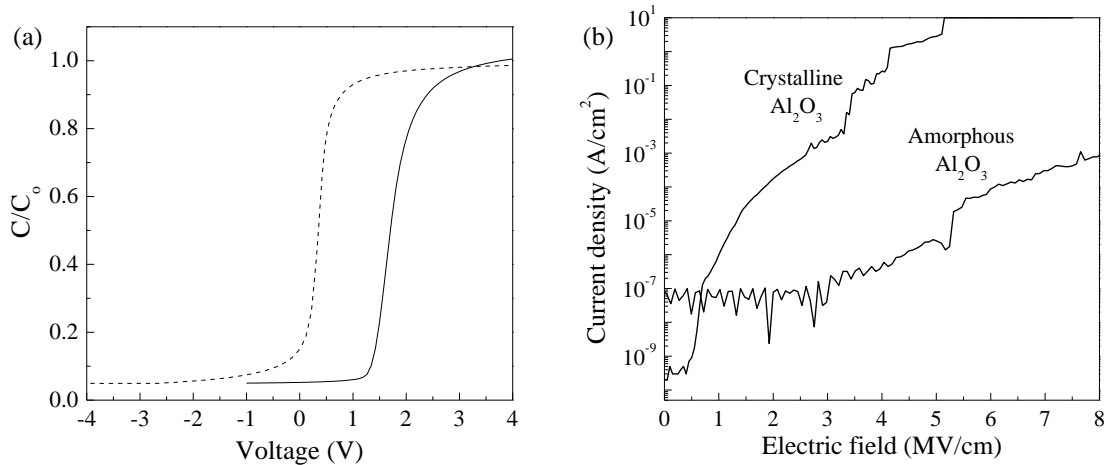


Figure 3.3. (a) Normalized current-voltage characteristic of MOS capacitors made from 260 Å as-deposited Al₂O₃ on epitaxial 4H-SiC with 1×10^{-4} cm² Al gate (solid line) in comparison with a calculated ideal curve (dash line). (b) Comparison of current leakage using crystalline and amorphous Al₂O₃ films as the gate dielectric. (Tanner, Perng et al. 2007)

Compared to the reported results of other gate dielectric materials on 4H-SiC, as summarized in Table 1.2, the results demonstrated an outstanding capability of the as-deposited Al₂O₃ film on preventing leakage. The material was then grown on AlGaN/GaN heterostructures

as surface passivation with its material and electrical characterization discussed in the next section.

3.2 Al₂O₃ on AlGaN/GaN

Al₂O₃ thin films were grown on AlGaN/GaN with various ALD cycles at 195 °C by alternatively introducing trimethylaluminum (TMA) and water vapor into the system. The thicknesses of synthesized films were determined by the integrated areas of peaks from the substrate and overlayer in XPS spectra described by equation (2.9) in Section 2.2.2. Due to the lack of optical model for the substrate, a good fit of the ψ and Δ curves could not be obtained using spectroscopic ellipsometry. In order to confirm the value of calculated thicknesses, a cross-section view of the film grown by 45 ALD cycles was studied via HRTEM imaging. In Figure 3.4, the film thickness is shown as a function of growth cycle. It is observed that the growth was well-controlled with a deposition rate of 0.75 Å/cycle as determined by the slope and no incubation time was required.

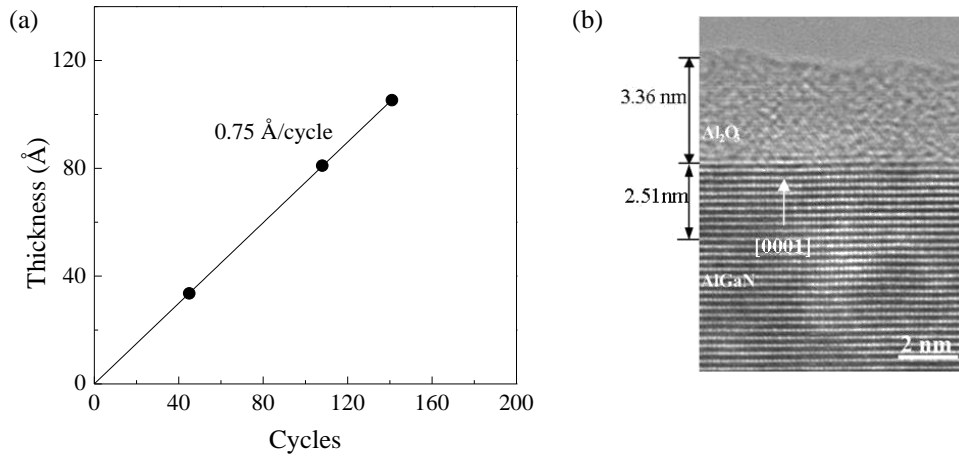


Figure 3.4. (a) Thickness of Al₂O₃ films as a function of ALD cycle at 195 °C on clean AlGaN/GaN with the deposition rate determined by the slope. (b) An HRTEM cross-section image of 3.36 nm Al₂O₃ grown via 45 ALD cycles on AlGaN to confirm the thickness calculated via XPS spectra.

With *ex-situ* XPS (monochromatic Al K α source), the stoichiometry of as-deposited Al₂O₃ film was analyzed. Spectra of 35 Å Al₂O₃ grown on AlGaN/GaN at 195 °C is shown in Figure 3.5. The O 1s peak was deconvoluted into two three peaks with the dominant O1s peak at 528.6 eV assigned to O-Al bonding. Because the measurements were performed *ex-situ*, the unassigned O peak and C content may be surface contamination from the ambient. The peak detected at Al 2p region was deconvoluted into two peaks with the peak at 72.2 eV assigned to Al-N bonding and the peak at 71.4 eV assigned to Al-O bonding. An Al to O ratio was then determined from the integrated intensity of peaks as ~0.64, suggesting a close to stoichiometric Al₂O₃ was synthesized. The near stoichiometry enables the synthesized amorphous Al₂O₃ film to be crystallized via rapid thermal annealing (RTA).

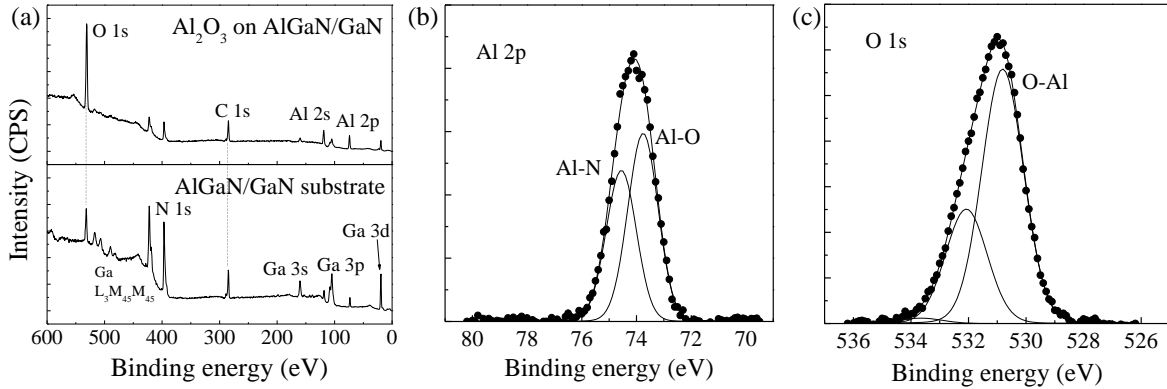


Figure 3.5. *Ex-situ* XPS spectra of 35 Å Al_2O_3 on AlGaIn/GaN: (a) survey in comparison with that of a clean AlGaIn/GaN substrate, (b) Al2p and (c) O1s.

Prior to RTA processing, the crystallinity of as-deposited films was studied to confirm that amorphous films were grown, like the cases on other substrates. During ALD Al_2O_3 thin-film growths on AlGaIn/GaN (0001), the surface structure was monitored by *in-situ* HREED. Figure 3.6 shows HREED patterns of Al_2O_3 film during a 45-cycle ALD growth. It confirmed that the deposited film was amorphous since no diffraction signatures were observed after 45 ALD cycles.



Figure 3.6. *In-situ* HREED patterns of Al_2O_3 /AlGaIn/GaN after 0, 3, 9, 11 and 45 ALD cycles at 195 °C.

Synthesized films with various thicknesses, 34-105 Å, were then annealed via *ex-situ* RTA at 1000 °C for 1 min to study the crystallization. In Figure 3.7, RHEED images of the annealed films are shown as a function of film thickness. The images indicate crystalline Al_2O_3

films were obtained after 1000 °C annealing for 1 minute. However, the crystallization of the thicker film was not fully completed since the RHEED pattern was more blurred compared to that of the 34 Å film.

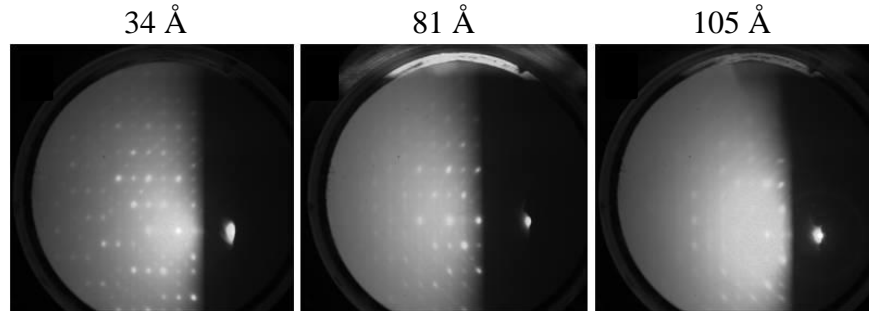


Figure 3.7. *Ex-situ* RHEED images of 34 Å, 81 Å and 105 Å Al₂O₃ films on AlGaIn/GaN after RTA in N₂ at 1000 °C for 1 min.

To investigate the structural and epitaxial properties of crystalline Al₂O₃ films on AlGaIn/GaN, XRD ($\lambda=1.549987$ Å) scans were performed on Al₂O₃ films of various thicknesses, 34-105 Å, along specular and in-plane directions, as shown in Figure 3.8. In the specular θ - 2θ scan of a 34Å film, the γ -Al₂O₃ (222) reflection was observed along with the reflection of AlGaIn/GaN (0002) plane and an intense peak corresponding to the α -Al₂O₃ (0006) reflection, originating from the sapphire substrate. It suggested that the growth direction of Al₂O₃ was [222], parallel to the [0001] direction of the AlGaIn/GaN/sapphire substrate. According to the position of the (222) reflection, the lattice spacing was 2.268 Å, slightly smaller than the value reported in JCPDS (56-0457), 2.2836 Å. The discrepancy indicates that the film was slightly compressed in the normal direction by 0.68%. For a 105 Å Al₂O₃ film, however, the peak of γ -Al₂O₃ (222) reflection was not detected, implied that the crystallization along the specular orientation was not well-arranged.

The phi scan of $\gamma\text{-Al}_2\text{O}_3$ ($4\bar{4}0$) in-plane reflection of the 34 Å film, as shown in Figure 3.8 (b), was compared to the scan of the off-peak background in log scale. The two scans are overlapping without detectable offsets, implying a well-aligned along the $[1\bar{1}0]$ direction. Besides, it showed that the peak for $\gamma\text{-Al}_2\text{O}_3$ ($4\bar{4}0$) repeats every 60° rather than 120° for three-fold symmetry, suggesting that the film adopted the hexagonal structural arrangement of the substrate. In contrast to the result found from the 34 Å film, the phi scan and detailed θ - 2θ scan of $\gamma\text{-Al}_2\text{O}_3$ ($4\bar{4}0$) reflection of the 105 Å film revealed a detectable difference from the off-peak background scan, showing a misalignment of the ($4\bar{4}0$) plane, as shown in Figure 3.8 (c) with the scan taken at $\phi=20^\circ$ as an off-peak background. The measurable offset found in 105 Å film suggested that thinner films demonstrated superior crystallinity. This result is corroborated by the RHEED analysis shown in Figure 3.7 where sharper diffraction patterns were found when the film was thinner.

The in-plane alignment of Al_2O_3 films to the AlGaIn/GaN substrate was studied by phi scans, as shown in Figure 3.8 (d). Due to the high intensity of AlGaIn ($20\bar{2}0$) reflection, the peak was used for the alignment. It is observed that $\gamma\text{-Al}_2\text{O}_3$ ($4\bar{4}0$) reflections of all the films are aligned and are 30° off to the substrate ($20\bar{2}0$) reflection. Because the angle between ($11\bar{2}0$) and ($20\bar{2}0$) planes is 30° for a hexagonal structure, the result suggested an alignment of the $\gamma\text{-Al}_2\text{O}_3$ ($4\bar{4}0$) and the AlGaIn ($11\bar{2}0$) planes. Therefore, the epitaxial relationship at the interface was determined as $\gamma\text{-Al}_2\text{O}_3$ (111) \parallel AlGaIn (0001) and $\gamma\text{-Al}_2\text{O}_3$ ($1\bar{1}0$) \parallel AlGaIn ($11\bar{2}0$), which is analogous to the epitaxial relationship of crystalline GaN and $\gamma\text{-Al}_2\text{O}_3$ stack on Si (111): GaN (0001) \parallel $\gamma\text{-Al}_2\text{O}_3$ (111) \parallel Si (111) and GaN ($11\bar{2}0$) \parallel $\gamma\text{-Al}_2\text{O}_3$ ($1\bar{1}0$) \parallel Si ($1\bar{1}0$) found by Wakahara et al. (Wakahara, Oishi et al. 2002). The lattice spacing of the $\gamma\text{-Al}_2\text{O}_3$ ($4\bar{4}0$) plane was determined to be ~ 1.401 Å for film thicknesses ranging from 34-105 Å and was slightly

larger than the value of 1.3984\AA reported in JCPDS (56-0457) for $\gamma\text{-Al}_2\text{O}_3$ ($\bar{4}\bar{4}0$) plane, suggesting that the film was expanded laterally to achieve lattice matching at the interface and confirming that the compression in the normal direction found from the specular scan was due to the lateral expansion.

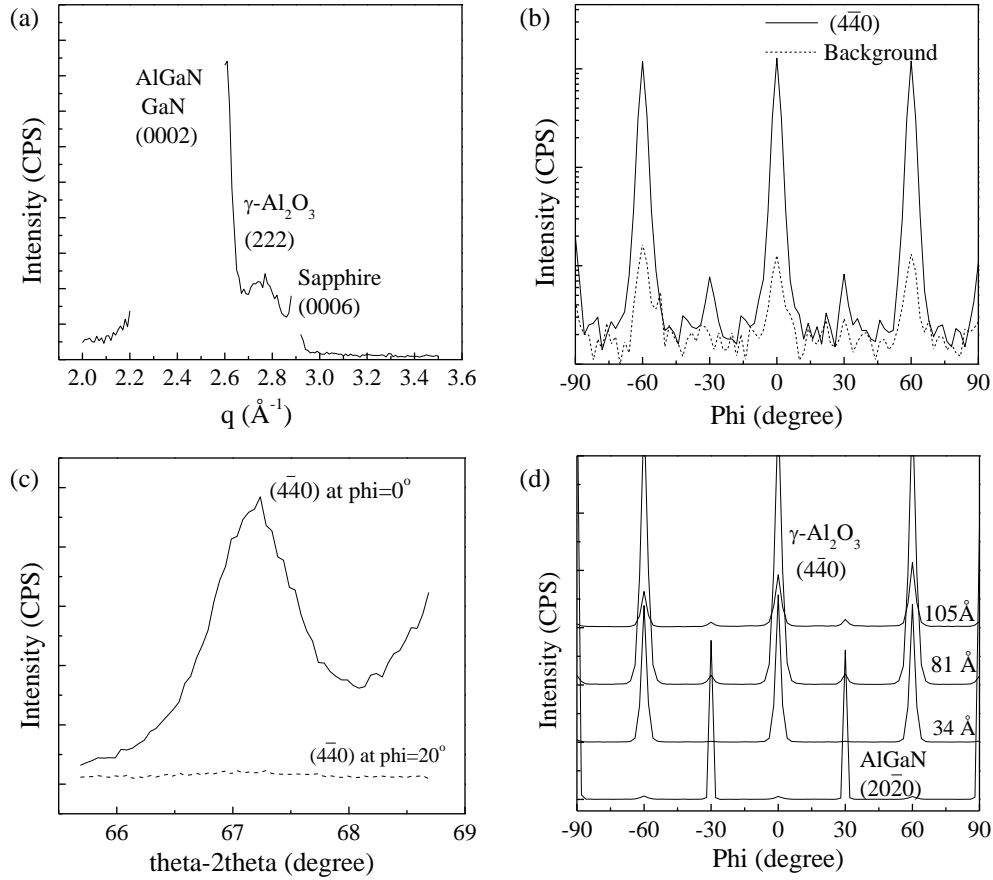


Figure 3.8. XRD spectra of a 34\AA $\gamma\text{-Al}_2\text{O}_3$ film on 275\AA $\text{Al}_{0.34}\text{Ga}_{0.66}\text{N}/5000\text{\AA}$ GaN/AlN nucleation/sapphire: (a) specular scan and (b) phi scan on the $\gamma\text{-Al}_2\text{O}_3$ ($\bar{4}\bar{4}0$) in-plane reflection in comparison with the off-peak phi scan, showing no measurable offset. The substrate peaks are incomplete because the scan was not performed over the peak to prevent the detector saturation. (c) In-plane radial scan on $\gamma\text{-Al}_2\text{O}_3$ ($\bar{4}\bar{4}0$) reflection of a 105\AA film in comparison with the off-peak scan at $\text{phi}=20^\circ$, showing a measurable offset. (d) Phi scans on $\gamma\text{-Al}_2\text{O}_3$ ($\bar{4}\bar{4}0$) in-plane reflection of films with various thicknesses in comparison with that of the substrate AlGaN ($20\bar{2}0$) reflection.

The epitaxial relationship of crystalline Al_2O_3 on AlGaN was studied by HRTEM imaging as well. As shown in Figure 3.9, diffraction patterns from HRTEM fast Fourier transformation (FFT) of an annealed 130 Å Al_2O_3 film revealed an epitaxial relationship of $\gamma\text{-Al}_2\text{O}_3$ (111) aligned with AlGaN (0001) and $\gamma\text{-Al}_2\text{O}_3$ ($1\bar{1}0$) with 30° rotation aligned with AlGaN ($10\bar{1}0$). This was in agreement with the result from XRD analysis. Schematics of AlGaN (0001) and $\gamma\text{-Al}_2\text{O}_3$ (111) planes and the interface alignment were built and shown in Figure 3.9 (d). Based on the coordinates, the in-plane $\gamma\text{-Al}_2\text{O}_3$ ($1\bar{1}0$) was aligned with AlGaN ($11\bar{2}0$), which is 30° to AlGaN ($10\bar{1}0$).

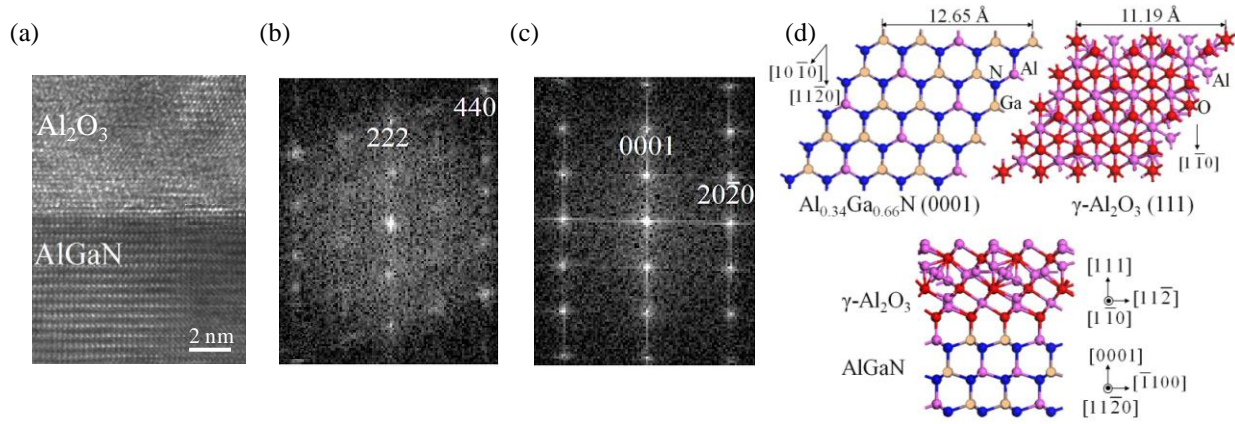


Figure 3.9. (a) An HRTEM image of a ~130 Å $\gamma\text{-Al}_2\text{O}_3$ film on $\text{Al}_{0.34}\text{Ga}_{0.66}\text{N}/5000\text{\AA}$ GaN/AlN/sapphire. The corresponding diffraction patterns generated from fast Fourier transformation (FFT) of (b) the $\gamma\text{-Al}_2\text{O}_3$ film and (c) AlGaN substrate. (d) Atomic arrangements on AlGaN (0001) and $\gamma\text{-Al}_2\text{O}_3$ (111) planes and a schematic showing the interface epitaxial alignment of $\gamma\text{-Al}_2\text{O}_3$ (111) || AlGaN (0001) and $\gamma\text{-Al}_2\text{O}_3$ ($1\bar{1}0$) || AlGaN ($11\bar{2}0$).

After the material characterization confirmed the high-quality Al_2O_3 thin-film growth on AlGaN/GaN, the electrical properties were studied. Due to the superior electrical performance found in Al_2O_3 amorphous phase on 4H-SiC for preventing leakage as shown in Section 3.1, as-

deposited Al₂O₃ films on AlGaN/GaN were studied via Hall measurement to assess their effect on the heterostructure.

In Figure 3.10, the measured parameters of 2DEG, such as carrier density, mobility and sheet resistance, are shown as a function of the thickness of ALD films. The data, shown for zero in Al₂O₃ thickness, were measured on clean AlGaN/GaN substrates. Similar to what has been reported in literature using surface passivation, such as HfO₂ (Liu, Chor et al. 2007) and SiO₂ (Arulkumaran, Egawa et al. 2005), the carrier density (n_s) was enhanced due to the passivated surface state with decreased mobility (μ_s) from increased interface roughness scattering as a result of higher carrier density confined at the AlGaN/GaN interface. Besides, it was found that the value of carrier density reached $\sim 8 \times 10^{12} \text{ cm}^{-2}$ after ALD films were applied regardless of the film thickness. It suggested that if a MOS-HEMT device structure were synthesized, using Al₂O₃ as the gate dielectric leads to a higher source-drain current and prevents the gate leakage but results in lower carrier mobility, degrading the advantage of using heterojunctions unless the device is operated at a high electric field for saturated carrier velocity.

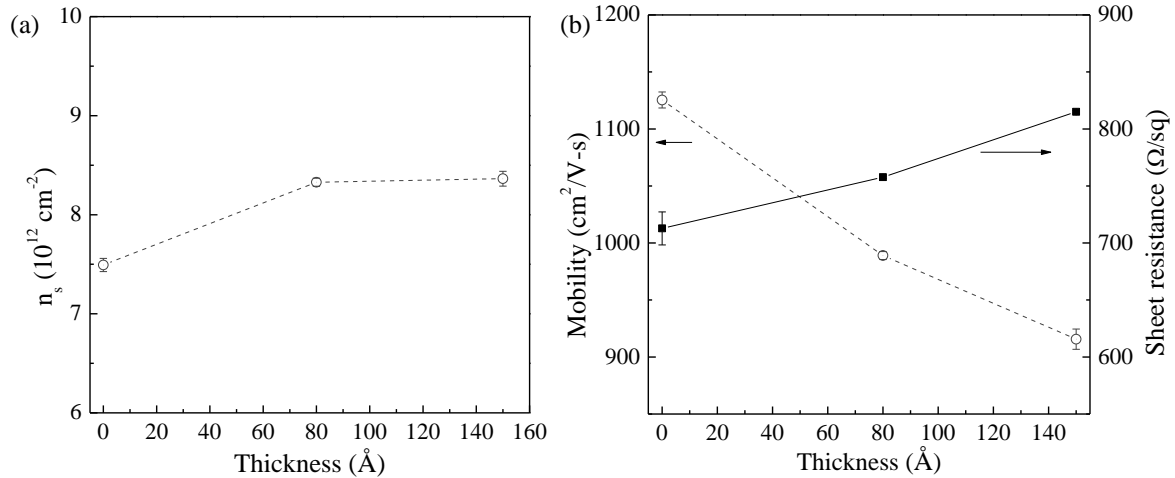


Figure 3.10. The effect of amorphous Al₂O₃ thickness on passivating the AlGaIn/GaN heterostructure: (a) sheet carrier density, and (b) carrier mobility (\circ) and sheet resistance (\blacksquare).

3.3 ALD of AlN

In contrast to Al₂O₃ growth using TMA and water, the ALD growth using TMA and ammonia is expected to have a much narrow window based on the surface chemistry studied by different research groups. (Mayer, Rogers et al. 1991; Liu, Bertolet et al. 1995) The ALD of AlN was first performed in a low vacuum system using thermal and radical enhanced processes to realize the required conditions for thermal ALD using the high vacuum chamber discussed in Section 2.1 with *in-situ* diagnosis techniques. An optimized deposition condition for AlN growths was then determined to synthesize AlN films for studying the material properties of ALD synthesized AlN.

3.3.1 Effect of NH₃ Dissociation and Flux

A vacuum hot-wall reactor with a chamber base pressure of 6×10^{-2} Torr was first used to study the required temperature for AlN thermal ALD growths. Growths were performed on both Si and 4H-SiC substrates at various wall temperatures of 350-380 °C with each deposition cycle composing of 5s TMA pulse, 60s pump-down, 40s NH₃ (99.99%) pulse and 240s pump-down. Figure 3.11 shows the N1s spectra of ALD AlN grown at various temperatures taken by *ex-situ* XPS. For the growths on SiC substrates, the N 1s peak was detected 360 °C, suggesting deposition temperatures ≥ 360 °C would be required for thermal AlN growth on SiC using TMA and NH₃. When the substrate was Si, higher temperatures ≥ 380 °C were required. This difference could attribute to the similar atomic arrangements and close lattice constants between AlN and SiC, making it easier to grown on SiC.

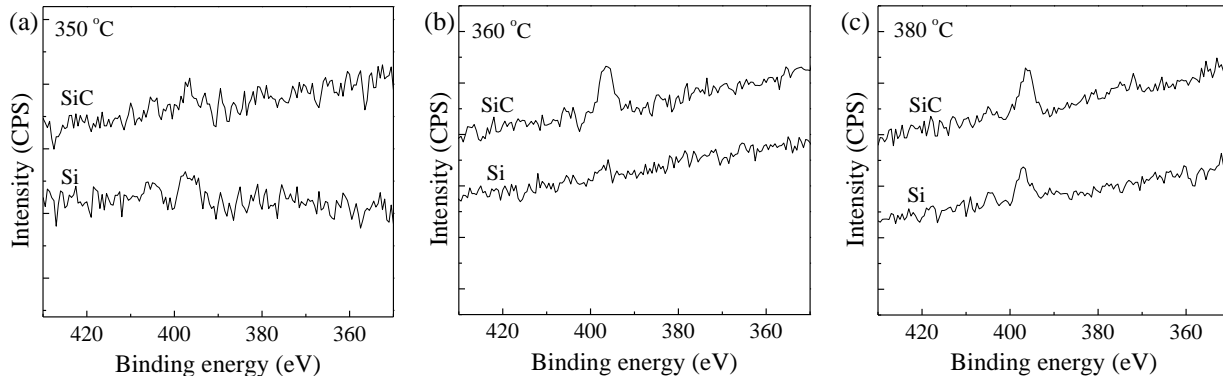


Figure 3.11. Identification of N in AlN on Si and SiC via XPS analysis as a function of deposition temperature. The films were grown at (a) 350, (b) 360 and (c) 380 °C using TMA and 99.99% NH₃ of 30 ALD cycles in a vacuum hot-wall reactor.

In order to confirm the higher deposition temperature compared that for Al₂O₃ growths (~200 °C) was required for AlN growths due to the NH₃ dissociate to generate the Al-N bonds, a nitrogen radical source was used to replace NH₃ for the growth. The radical enhanced growths

were performed at room temperature and 200 °C on Si with each growth cycle composing of a 5s TMA pulse, 60s pump-down, 30s N radical pulse and 60s pump-down. According to *ex-situ* XPS analysis, as shown in Figure 3.12, the N 1s peak was detected from both samples, confirming that deposition temperatures ≥ 380 °C found in thermal ALD were required for NH_3 to dissociate and perform the growth. From both of the films grown using radical N, high oxygen contents (55%) were found, suggesting a high vacuum deposition process might be demanded to reduce the amount of oxygen incorporation. Furthermore, higher Al and N contents with a lower C content was found from the film grown at 200 °C, implying that higher temperatures were required for high-quality nitride to grow.

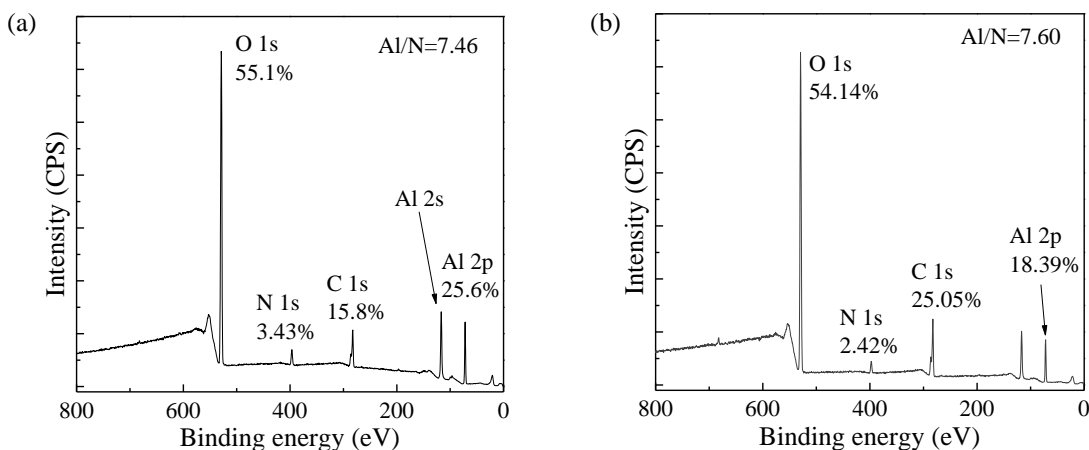


Figure 3.12. *Ex-situ* XPS spectra of AlN grown on Si using TMA and N radicals at substrate temperatures of (a) 200 °C and (b) 25 °C in a vacuum reactor.

With the same precursor pulses, depositions were performed on 4H-SiC at a substrate temperature of 340-390 °C using the high-vacuum chamber. Based on *ex-situ* XPS analysis, however, there was no N content detected from the deposited films. A high-temperature heating rope was then installed outside of the chamber wall to simulate the hot-wall reactor. Growths at a substrate temperature of 340-390 °C with a wall temperature of 300-330 °C were studied. A

summary of compositions analyzed via *ex-situ* XPS as a function of the deposition temperature is shown in Figure 3.13. N content was detected on films grown within the temperature range and found to increase with rising temperatures. High oxygen content (>25%) was detected on all of the samples but the value decreased with rising temperature as well as the Al content. Besides, when the temperature was increased, the intensities of Si and C were higher, suggesting the film was thinner. This implied aluminum oxide was grown with the nitride and the growth rate decreased at higher temperatures due to the reduced of the oxide growth. Partial oxygen content detected by the XPS could be from surface oxidation since the analysis was done after samples exposed to the ambient. Because the chamber volume was bigger than the hot-wall reactor, the results suggested that higher NH₃ flux to the sample surface was required. When the wall was heated as well, the temperature inside the chamber was around the wall temperature and was higher around the sample surface so that the injected NH₃ molecules during each pulse were heated up and possessed higher kinetic energy, resulting in an increased amount of NH₃ molecules transporting to the sample surface for the growth.

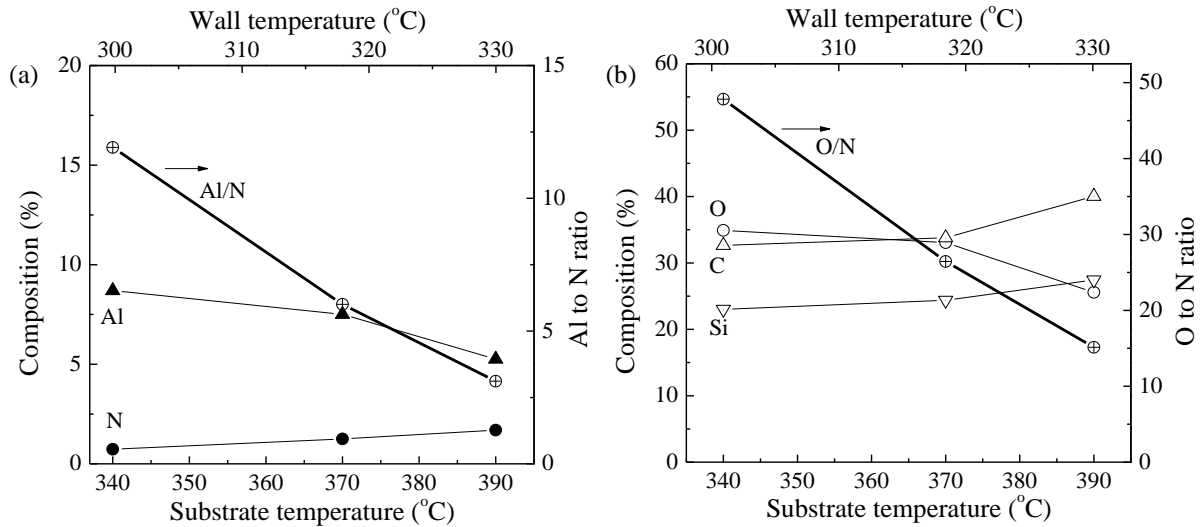


Figure 3.13. Composition of AlN on 4H-SiC, as determined by *ex-situ* XPS analysis, as a function of substrate and reactor wall temperatures using TMA and 99.99% NH₃ under high-vacuum.

To further confirm that higher NH₃ flux was required for the nitride growth, depositions performed at a substrate temperature of 500 °C with different NH₃ pulse conditions were studied using the high vacuum chamber, as shown in Figure 3.14. When a short pulse time of 5s for NH₃ was used, no N peak was detected with continuous pumping. When cyclic pumping was used, referring to that the chamber was isolated from pumps after the NH₃ pulse for 55s with a chamber pressure of ~2 Torr, followed by a pump-down process to $\sim 5 \times 10^{-5}$ Torr, N peak was detected by *ex-situ* XPS referring to 4% N. When a pulse time of 40s for NH₃ was used, which was used in this work, 4.5% N was detected. The results confirmed that a longer NH₃ pulse time for higher NH₃ flux was required, which was due to excess N source was necessary to maintain the preferential surface sites for Al incorporation to continue the growth. (Mayer, Rogers et al. 1991)

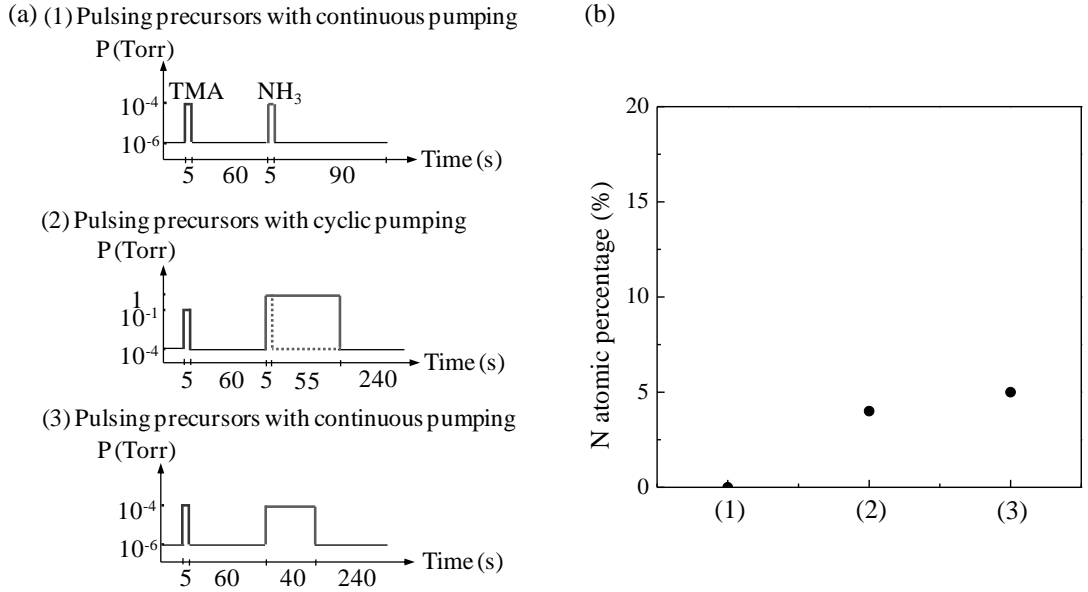


Figure 3.14. (a) Illustrations of deposition cycle sequences with different NH_3 pulse time under various operation pressure ranges and (b) corresponding N atomic percentage in the deposited films on 4H-SiC, as determined by *ex-situ* XPS analysis, via 100 deposition cycles using TMA and 99.99% NH_3 at a substrate temperature of 500 °C.

3.3.2 Effect of Moisture

Growths at substrate temperatures of 500-550 °C using the high-vacuum chamber were studied via *in-situ* XPS. Figure 3.15 shows the composition analysis from XPS spectra taken from samples with various deposition cycles at 540 °C. It shows that the Al, N and O contents increased as more deposition cycles were performed, suggesting the deposited film have oxygen incorporation in the growth. This might be due to the normally higher energy required for nitrides than oxides growth and suggest there was an oxygen source in the chamber or gas delivery system.

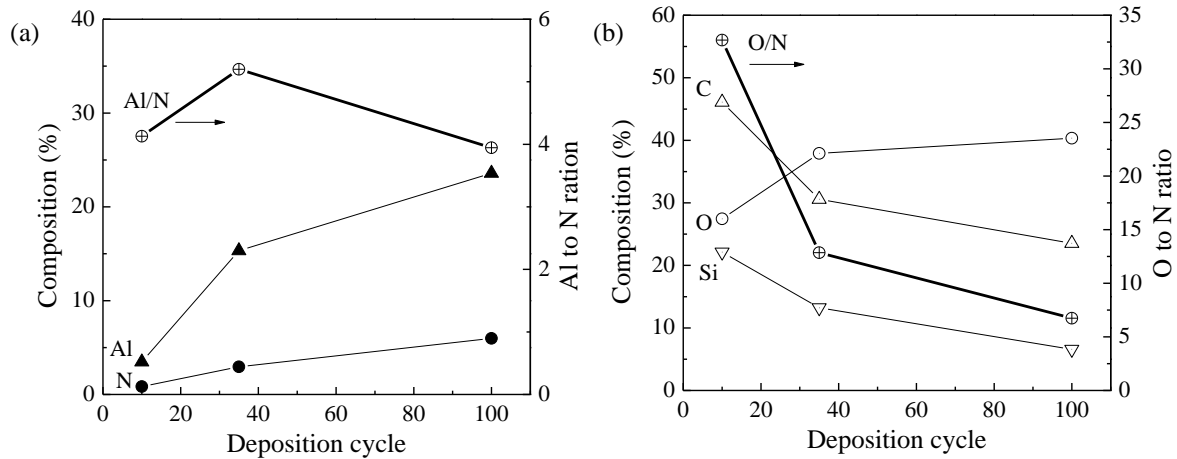


Figure 3.15. Composition of AlN on 4H-SiC, as determined by *in-situ* XPS analysis, as a function of ALD cycle using TMA and 99.99% NH₃ at a substrate temperature of 540 °C under high vacuum.

Three purity grades of NH₃, including 99.99% anhydrous and 99.99994% blue grade NH₃ and the blue grade NH₃ with moisture removal, were used to perform growths at 540 °C with the composition of deposited films studied via *in-situ* XPS, as shown in Figure 3.16. The result showed that O percentage decreased from 45% to 15% when the 99.99% NH₃ was substituted by purified NH₃ while Al percentage remains ~37%. Furthermore, the N content increased from 8% to 32%, which was higher than the O percentage and suggested that the moisture competed with NH₃ to perform oxide growths. Therefore, using high purity NH₃ with eliminated moisture was important for synthesizing high purity stoichiometric AlN thin films.

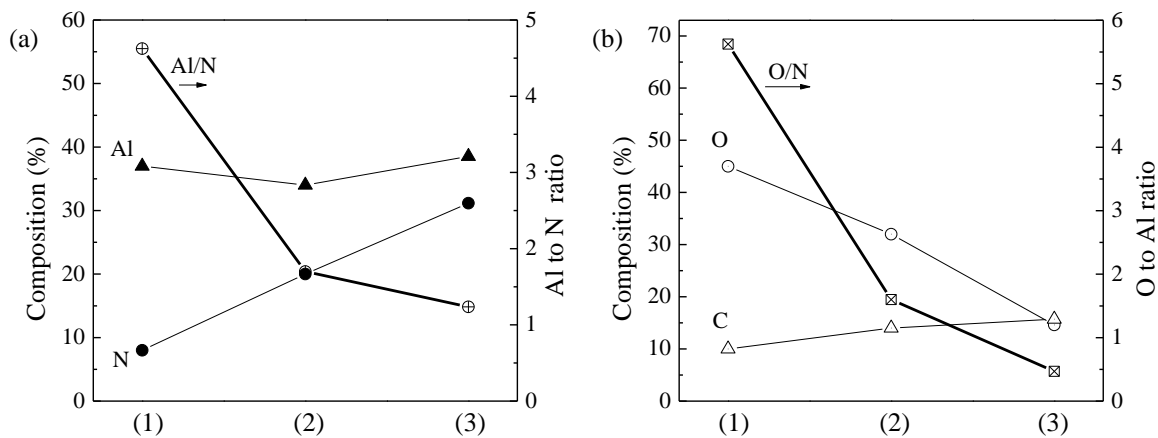


Figure 3.16. Composition of ~ 250 Å AlN on 4H-SiC, as determined by *in-situ* XPS analysis, as a function of NH₃ purity. The films were grown at a substrate temperature of 540 °C under high vacuum using TMA and (1) 99.99% NH₃, (2) 99.99994% NH₃ (blue grade) or (3) blue grade NH₃ with moisture removal.

3.3.3 Effect of Temp

The correlation of growth rates to deposition temperatures of AlN growths using blue-grade NH₃ and moisture removed (anhydrous) NH₃ was studied at a temperature range of 330-640 °C and was shown in Figure 3.17 (a). The growth rates were calculated from the film thickness deposited by a determined amount of cycles. It was found that with moisture presence, not only higher oxygen to nitrogen (O/N) ratios but also a different correlation of the growth rate to deposition temperatures were detected from growths performed with anhydrous NH₃. When there were moisture impurities in NH₃, the rate at studied temperatures were found to be 0.2-0.3 Å/cycle and independent of temperatures. Without the moisture, an ALD temperature window at 500-570 °C was observed with a growth rate of 1.4-1.7 Å/cycle. Furthermore, the rate increased at even higher temperatures and then decreased dramatically due to precursor decomposition. The results showed that moisture removal was critical since it competed with NH₃ to react with surface bonded TMA and further inhibited the nitride growth.

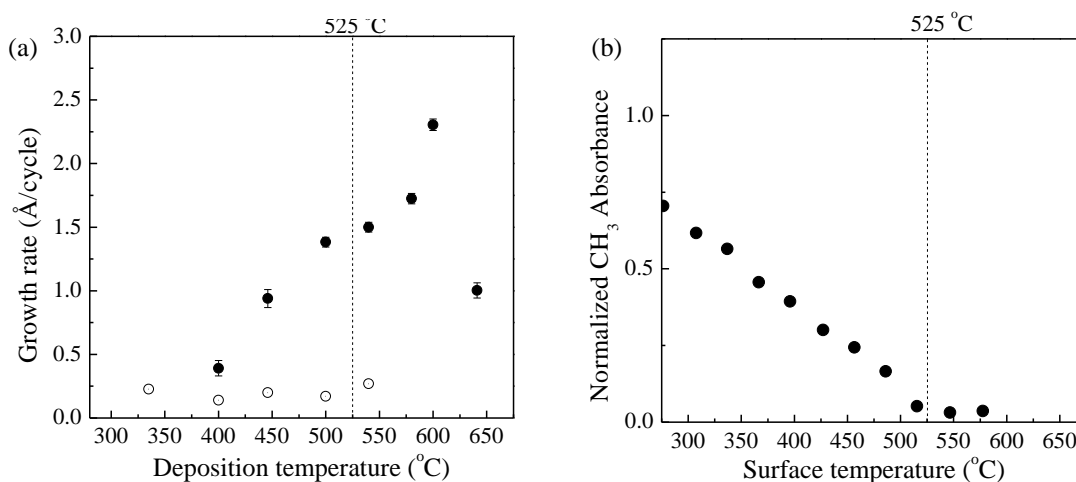


Figure 3.17. (a) AlN growth rate (Å/cycle) on 4H-SiC as a function of substrate temperature using TMA and blue grade NH₃, the latter with (●) and without (○) moisture removal. (b) Normalized integrated absorbance of C-H₃ stretching vibrations versus annealing temperature after a saturation TMA exposure at room temperature, adapted by (Dillon, Ott et al. 1995).

The growth rates of AlN using TMA and blue grade NH₃, with and without moisture removal, were found to possess distinctive dependence on the deposition temperature, as discussed in previous section. In order to study the mechanism systematically, composition of the films used for the growth rate study was then investigated by XPS *ex-situ*, as shown in Figure 3.18. In both cases, N contents increased at growth temperatures above 400 °C, confirming higher temperatures are required for NH₃ to react with -CH₃ ligands of surface bonded TMA to form Al-N bonding. (Puurunen, Lindblad et al. 2001) Thermodynamically, water is more reactive compared to NH₃ to react with TMA. (Xu, Chen et al. 2011) When temperature is high enough for NH₃ to react, the competition between the limited amount of moisture and NH₃ in this case could be kinetic. The N content in films grown with anhydrous NH₃ was higher than in films grown with moisture presence, showing the competition was eliminated.

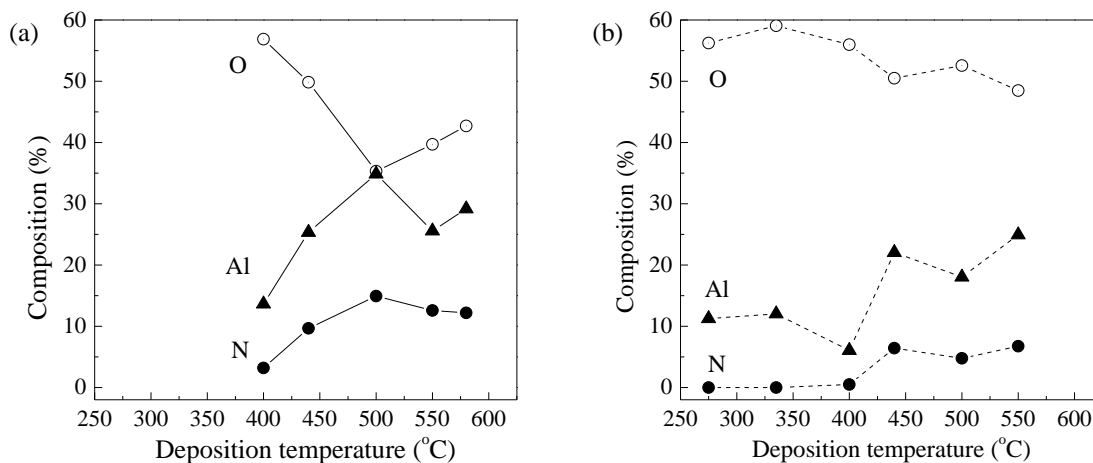


Figure 3.18. Composition of AlN on 4H-SiC, as determined by *ex-situ* XPS analysis, as a function of substrate temperature using TMA and blue grade NH₃, the latter (a) with and (b) without moisture removal.

Based on the factors discussed previously, ALD of AlN possesses a growth window of 500-570 °C with a growth rate of 1.4-1.7 Å/cycle. The following results are from AlN films grown using TMA and moisture removed blue grade NH₃ (anhydrous NH₃) at a substrate temperature of 540 °C under high vacuum.

3.4 AlN on 4H-SiC

The thicknesses of films grown on 4H-SiC via various numbers of deposition cycles at 540 °C were measured and shown as a function of deposition cycle in Figure 3.19. The thickness follows a linear relationship to deposition cycle with the growth rate determined from the slope as 1.51 Å/cycle. The intercept of fitted line on the x-axis suggests that an incubation period of ~100 cycles was required to initiate the growth. Compared to the ALD Al₂O₃ growth on AlGaN where no incubation time was found, it could be explained by the decomposition of TMA at temperatures >350 °C. According to the study on chemisorptions of TMA and NH₃ done by Bartram et al., the presence of methyl groups bonded to aluminum are required for the formation

of irreversible Al-N cross-linking network on the surface, which is necessary for ALD of AlN. (Bartram, Michalske et al. 1991) At the growth temperature of 540 °C, decomposition of TMA occurred and resulted in Al dangling bonds on the surface with less amounts of methyl groups for NH₃ to perform the growth. (Squire, Dulcey et al. 1985) Therefore, a long incubation period was required for ALD of AlN using the chemistry to initiate the growth with a constant rate.

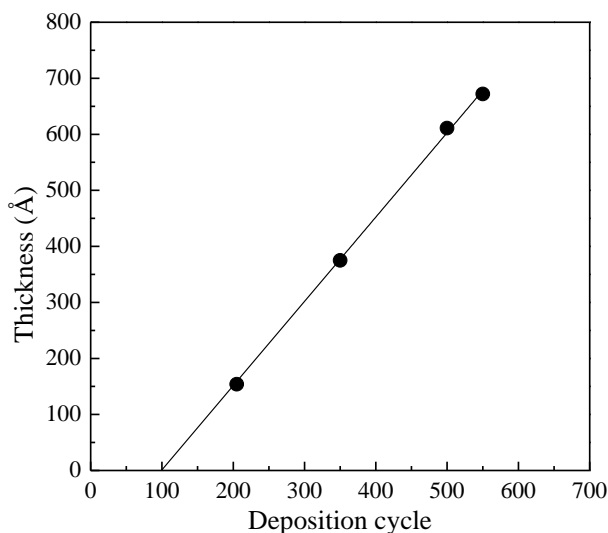


Figure 3.19. The thickness of AlN films on 4H-SiC measured via spectroscopic ellipsometry as a function of ALD deposition cycle using TMA and anhydrous NH₃ at a substrate temperature of 540 °C.

The composition of synthesized films was then analyzed via *in-situ* XPS. A XPS surface scan of 250 Å AlN thin film deposited on 4H-SiC at 540 °C is shown in Figure 3.20 (a). The C and Al contents in the synthesized film were found to be 15.7% and 38.5%, respectively, with the oxygen content of 14.6% and the N content of 31.2%. A high resolution scan on N1s peak spectrum is shown in Figure 3.20 (b) with the spectrum shifted using O 1s reference for O-Al-N at 530.4 eV. (Rosenberger, Baird et al. 2008) The N 1s peak was deconvoluted into two sub-peaks (FWHM: 1.76 eV) at binding energies of 395.6 and 397 eV with the integrated intensity as 87% and 13% of the total nitrogen intensity, respectively. Based on the results reported by

Rosenberger et al. on plasma source MBE synthesized AlN films (Rosenberger, Baird et al. 2008), the primary sub-peak was assigned to N-Al while the other one was referred to N-Al -O. It suggested the measured ~14.6% O was incorporated in the AlN growths. The Al to N ratio was found to be 1.2, suggesting close to stoichiometric AlN films with slightly higher Al content were synthesized.

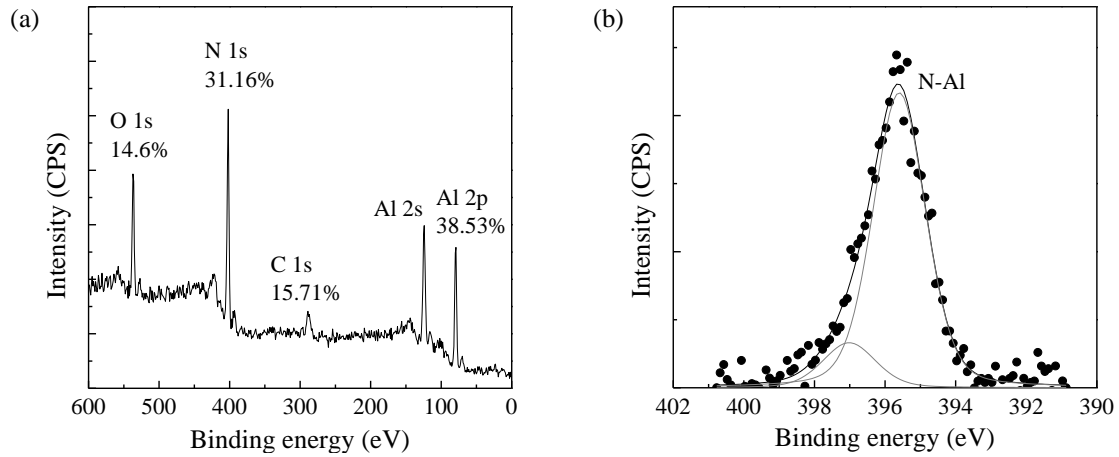


Figure 3.20. *In-situ* XPS spectra of 250 Å AlN on 4H-SiC, deposited using TMA and anhydrous NH₃ at a substrate temperature of 540 °C: (a) survey and (b) N 1s.

Surface structures of AlN films grown at 540 °C were studied by *in-situ* RHEED. The close to stoichiometric as-deposited AlN films were crystalline with the diffraction pattern shown in Figure 3.21 along $[11\bar{2}0]$ azimuth. The result suggested that crystalline films were deposited with preferred orientation in the $[0001]$ direction and the film grown on off-axis epi-SiC layer possessed better crystallinity. Elers et al. has demonstrated that at a deposition temperature of 500 °C, partial crystalline wurtzite AlN could be grown on glass substrates via ALD using aluminum trichloride (AlCl₃) and NH₃ at 500 °C. (Elers, Ritala et al. 1995) In this work, the 4H-SiC (0001) substrate provided a superior template compared to glass for wurtzite

AlN to grow, thus it is possible to deposit crystalline films at the deposition temperature of 540°C.

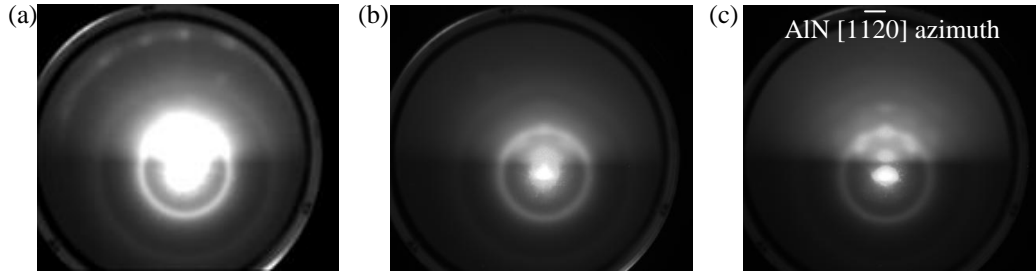


Figure 3.21. *In-situ* RHEED images of (a) 4H-SiC (0001) substrate, (b) 150 Å AlN on 4H-SiC (0001) and (c) 150 Å AlN on 8° off-axis epi-SiC (0001). The films were grown using TMA and anhydrous NH₃ at a substrate temperature of 540 °C.

The surface morphology of the AlN films was studied via AFM. In Figure 3.22, an AFM 3D image of an as-deposited 672 Å AlN film is shown with an RMS roughness of 7.67 Å. Considering the roughness of AlN films synthesized by other techniques, as described in Section 1.4.6, the value of the RMS roughness in this work is comparable to those achieved by MBE (3-14 Å). (Onojima, Kaido et al. 2005) It confirms the atomic-scaled controllability of ALD AlN.

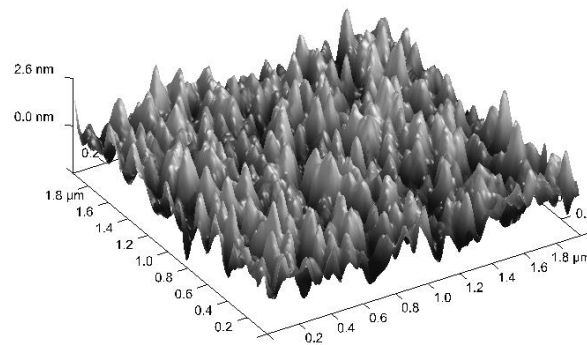


Figure 3.22. An AFM image (1.9 μm × 1.9 μm) of 672 Å AlN on 4H-SiC, deposited using TMA and anhydrous NH₃ at a substrate temperature of 540 °C, with an RMS roughness of 7.67 Å.

To characterize electrical properties of the synthesized ALD AlN films, metal insulator semiconductor (MIS) capacitors were made from an as-deposited 130 Å AlN on 4H-SiC (10^{15} cm⁻³ nitrogen doping) based on the fabrication processing described in Section 2.3. In Figure 3.23 (a), the normalized capacitance as a function of applied bias at 1 MHz is measured on capacitors with a Pt/Ti gate size of 9.62×10^{-4} cm². The dielectric constant of the film was determined based on the accumulation capacitance to be 8.3, which is comparable to the values reported in literature (8.5) (Onojima, Suda et al. 2002). I-V measurements showed that the leakage current density reached 10^{-3} A/cm² at an electric field of 4.3 MV/cm (Figure 3.23 (b)). Compared to the leakage current density of MBE synthesized AlN (327 Å) on 4H-SiC which reached 10^{-3} A/cm² at an electric field of ~ 3 MV/cm (Onojima, Suda et al. 2002), the ALD AlN film demonstrates better electrical performance on preventing the leakage at higher electric fields.

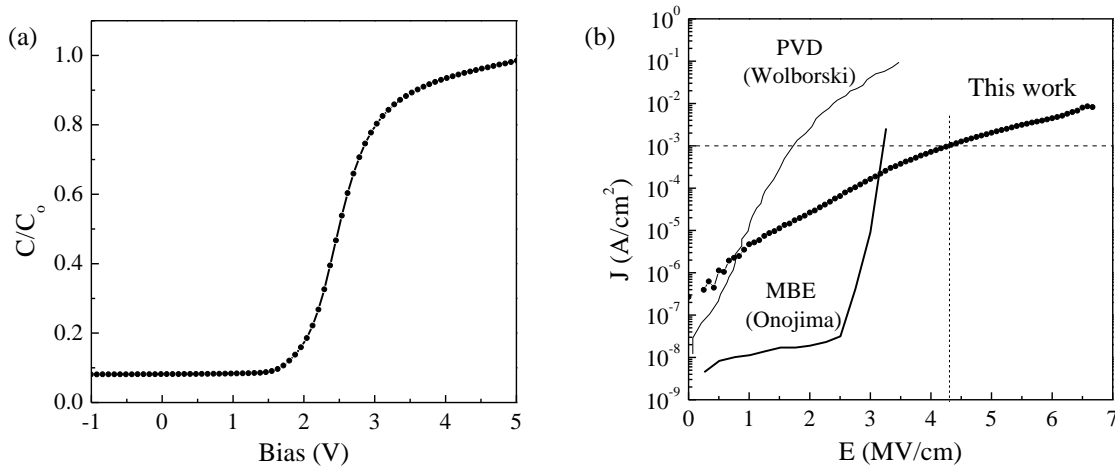


Figure 3.23. Electrical performance of MIS capacitors made from 130 Å as-deposited AlN on n-type 8° off-axis epitaxial 4H-SiC (0001) with 9.62×10^{-4} cm² Pt/Ti gate: (a) normalized current-voltage characteristic and (b) leakage current density as a function of applied electrical field in comparison with that of 1900 Å PVD AlN (Wolborski, Rosen et al. 2006) and 327 Å MBE AlN (Onojima, Suda et al. 2002) on SiC. The dotted lines indicate that the leakage current density reached 10^{-3} A/cm² at 4.3 MV/cm.

3.5 AlN on AlGaN/GaN

AlN thin films were grown on AlGaN/GaN at 540 °C with a growth rate of 1.5 Å/cycle. *Ex-situ* XPS spectrum of a 150 Å film, as shown in Figure 3.24, was studied and confirmed the deposition. Most of the carbon and oxygen contents found on the AlN film were from the ambient.

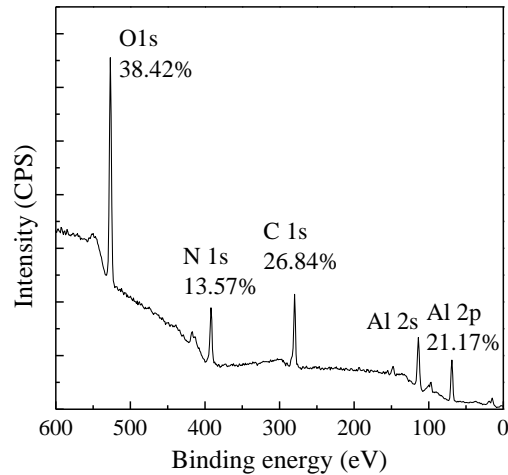


Figure 3.24. *Ex-situ* XPS survey spectrum of a 150 Å AlN film on AlGaN/GaN, deposited using TMA and anhydrous NH₃ at a substrate temperature of 540 °C.

The effect of AlN passivation on the heterostructure was studied via Hall measurements. In Figure 3.25, the measured parameters of 2DEG, such as carrier density, mobility and sheet resistance, are shown as functions of AlN thickness. Unlike Al₂O₃ on AlGaN/GaN, the carrier density (n_s) was enhanced with the mobility (μ_s) near to a constant of 1130 cm²/V-s. Besides, it was found that the value of carrier density increased with rising film thickness. The difference 2DEG properties of Al₂O₃ and AlN passivations suggested that the passivation mechanism of the two Al-based materials were dissimilar. Among the passivation materials studied on AlGaN/GaN, Si₃N₄ has demonstrated improvements in carrier density (41%), mobility (5%) and

the actual HEMT device performance as well. (Chen, Chen et al. 2008) The effect of Si_3N_4 passivation on the 2DEG is attributed to the reduced surface states and the tensile stress on the underneath AlGaIn layer, thereby increasing the sheet carrier density (n_s) due to additional piezoelectric polarization. This is analogous to the effect of AlN, which is a known piezoelectric material. Furthermore, its wurtzite crystal structure possesses spontaneous polarization, which could induce charges to accumulate at the interface as well. Therefore, additional 2DEG could be produced because of the polarization and stress from crystalline AlN and the interface between it and AlGaIn. Although the enhancements here in n_s (11%) and mobility are not comparable to the value reported on sputtered AlN (120nm) in Chen's work, as listed in Table 3.2, the thickness of AlN used here was much thinner, about 1/8 of the thickness used in that work. A thicker film can provide stronger piezoelectric and spontaneous polarizations and therefore the improvement in carrier density and mobility may be larger when a thicker AlN film is used. Besides, the crystalline properties of ALD AlN on AlGaIn/GaN were not studied in details to know how much strain was induced at the interface. For a high quality epitaxial AlN film synthesized by MBE on GaN, a small thickness of 35 Å is enough to generate 2DEG at the interface with a carrier mobility of 778 $\text{cm}^2/\text{V}\cdot\text{s}$ and a density of $\sim 2.7 \times 10^{13} \text{ cm}^{-2}$. However, a high growth temperature above 700 °C is required for synthesizing these high-quality epitaxial AlN films. (Chabak, Walker et al. 2011) Therefore, ALD AlN growth using TMA and NH_3 still enables AlN thin-film growths at lower temperatures and larger wafer processing even though the epitaxial quality of the synthesized ALD AlN films may not be as well-defined as that of MBE AlN films to provide comparable enhancements on the 2DEG properties of AlN coated AlGaIn/GaN.

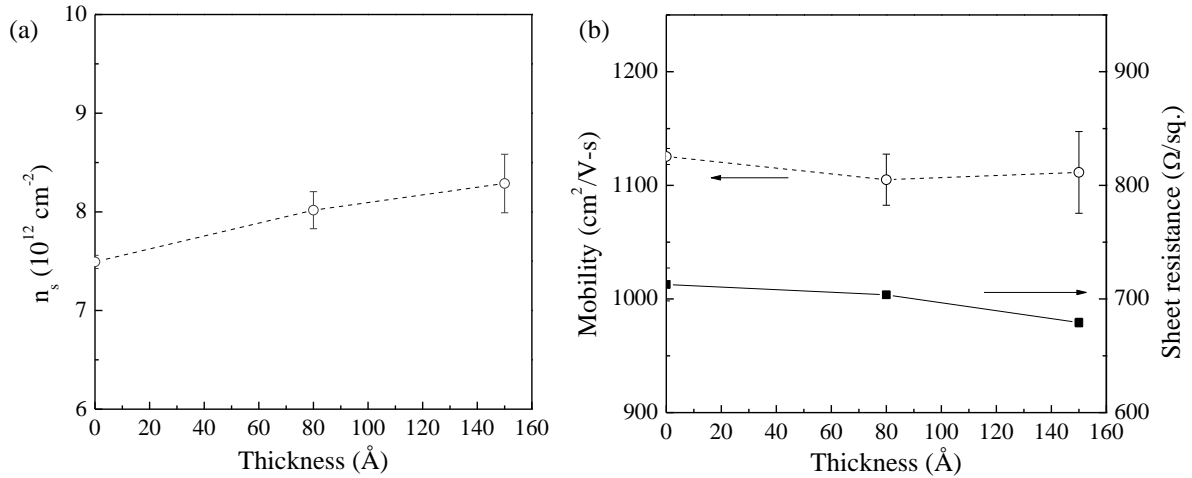


Figure 3.25. The effect of as-deposited AlN thickness on passivating the AlGaIn/GaN heterostructure: (a) sheet carrier density, and (b) carrier mobility ($-\circ-$) and sheet resistance ($-\blacksquare-$).

3.6 Summary

Surface reactions of TMA and NH_3 enable ALD of AlN at 500-570 $^\circ\text{C}$ with a growth rate of 1-1.5 $\text{\AA}/\text{cycle}$. However, the growth was highly sensitive to moisture. The minute amount of moisture in NH_3 has to be eliminated; otherwise, the temperature window for ALD could not be realized. Both binary Al-based material Al_2O_3 and AlN demonstrated dielectric properties and capabilities of preventing gate leakages and passivating the surface of a heterostructure. The electrical results of the two materials found in this work were summarized in Table 3.2 to compare with results reported in literature. It showed that Al_2O_3 was superior as a gate dielectric to minimize leakage on 4H-SiC due to its wider bandgap whereas AlN was superior as a passivation layer on AlGaIn/GaN to provide a higher carrier density and mobility. For AlGaIn/GaN MOS-HEMT fabrication, a thin layer of AlN as the interface to provide the separation between the top Al_2O_3 and underneath AlGaIn/GaN might be a potential setup for optimizing carrier density and mobility with the gate leakage current being eliminated efficiently.

Table 3.2. Electrical results of ALD Al₂O₃ and AlN films on two wide bandgap semiconductors, SiC and AlGaN/GaN, in comparison with the results reported in literature. (Onojima, Suda et al. 2002; Chen, Chen et al. 2008; Basu, Singh et al. 2010; Liu, Yang et al. 2011)

This work	Al ₂ O ₃	AlN
	$\kappa=9$	$\kappa=8.3$
4H-SiC	$J=10^{-3}$ A/cm ² at 8 MV/cm	$J=10^{-3}$ A/cm ² at 4.3 MV/cm
AlGaN/GaN	$n_s: 8.4 \times 10^{12}$ cm ⁻² (12% \uparrow) $\mu_s: 920$ cm ² /V-s (22% \downarrow)	$n_s: 8.3 \times 10^{12}$ cm ⁻² (11% \uparrow) $\mu_s: 1100$ cm ² /V-s (3% \downarrow)
Literature		
	$\kappa=10$	$\kappa=9.4$
4H-SiC	$J=10^{-3}$ A/cm ² at 8 MV/cm	$J=10^{-3}$ A/cm ² at 3.0 MV/cm
AlGaN/GaN	$n_s: 1.4 \times 10^{13}$ cm ⁻² (9% \uparrow) $\mu_s: 840$ cm ² /V-s (5% \downarrow)	$n_s: 1.1 \times 10^{13}$ cm ⁻² (29% \uparrow) $\mu_s: 1300$ cm ² /V-s (15% \uparrow)

Compared to state-of-the-art techniques for AlN thin-film synthesis (Onojima, Suda et al. 2002; Chen, Chen et al. 2008), the AlN ALD enabled a conformal AlN thin-film growth at lower temperatures with comparable electrical properties and a better interface quality on 4H-SiC with lower gate leakage at high electric fields. The passivation of AlN on AlGaN/GaN showed that the enhancements in n_s and μ_s were not comparable to the value reported on MBE or sputtered AlN, which could be due to the smaller thickness and poorer crystallinity of ALD AlN.

CHAPTER 4: IONIC CONDUCTIVE LiAlSiO_4 FILMS FOR ELECTROLYTES

Lithium aluminosilicate ALD thin-film growths were demonstrated via alternating ALD growths of the constituent oxides Li_2O , Al_2O_3 and SiO_2 . Precise controls of cation composition and thicknesses were achieved through well-controlled surface reactions during each precursor pulse cycles. Various compositions were achieved by changing the pulse cycle numbers, such as lithium alumina $\text{Li}_x\text{Al}_y\text{O}$ (LAO), lithium aluminosilicate $\text{Li}_x\text{Al}_y\text{Si}_z\text{O}$ (LASO) and stoichiometric LiAlSiO_4 . A growth rate of 20.6 Å per cycle sequence of 10(Al-O)-6(Li-O)-4(Si-O) was realized for LiAlSiO_4 growth at 290 °C. These as-deposited ALD films were amorphous, conformal over 3D Si or SiGe nanowires (NW), and pin-hole free, as confirmed by electrochemical testing of LiAlSiO_4 on indium tin oxide in ferrocene. The ionic conductivity at room temperature and the activation energy for Li transport of ALD LASO films were in the range of 10^{-9} - 10^{-7} S/cm and 0.46-0.89 eV, respectively, and both were correlated to the composition of the film. After rapid thermal annealing at 900 °C, ALD films crystallized with the epitaxial relation of LiAlSiO_4 to silicon, a potential anode material in Li-ion battery, found to be $\beta\text{-LiAlSiO}_4$ ($1\bar{2}10$) || Si (100) and $\beta\text{-LiAlSiO}_4$ ($10\bar{1}0$) || Si (001). The LiAlSiO_4 coating on SnO_2 NWs demonstrated the formation of Sn particles could be suppressed due to the fast Li ion transport in the coating, making it promising to build NW based batteries.

4.1 ALD of LiAlSiO_4

LiAlSiO_4 is one type of $\text{Li}_2\text{O-Al}_2\text{O}_3\text{-SiO}_2$ ($\text{Li}_x\text{Al}_y\text{Si}_z\text{O}$, LASO) composites, which was conventionally prepared via high temperature sintering of the solid precursors. (Johnson, Biefeld

et al. 1976) To synthesize the solid oxide composite thin films, ALD growths of constituent oxides Li_2O , Al_2O_3 and SiO_2 were initially demonstrated separately with various deposition cycles on Si via ALD at 290°C . In Figure 4.1, thickness of synthesized oxide films are shown as a function of deposition cycles. The thickness of each oxide film follows a linear relationship to deposition cycle and showing growth rates of 0.86, 1.08 and $2.14 \text{ \AA}/\text{cycle}$ for Li_2O , Al_2O_3 and SiO_2 , respectively. The constant growth rates suggest the growths are well-controlled and confirm ALD growths at 290°C .

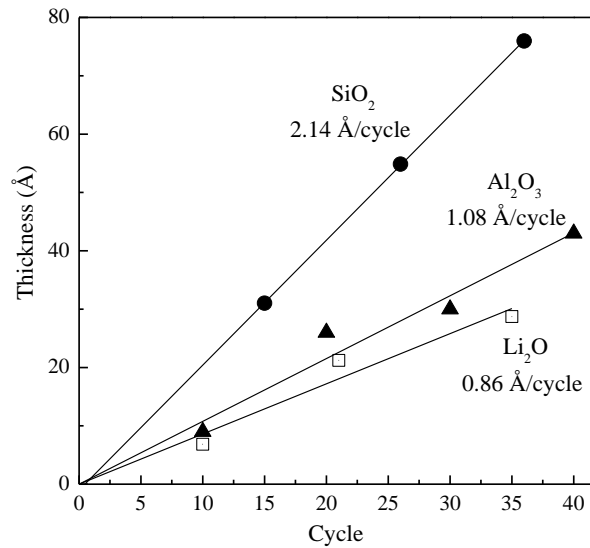


Figure 4.1. The thickness of Li_2O (-□-), Al_2O_3 (-▲-) and SiO_2 (-●-) films grown on Si at 290°C as a function of ALD deposition cycle. The thickness of Li_2O was calculated from Si signal attenuation from XPS spectra while the thicknesses of Al_2O_3 and SiO_2 were determined via spectroscopic ellipsometry.

The three ALD growths were then performed to synthesize $\text{Li}_x\text{Al}_y\text{Si}_z\text{O}$ (LASO) thin films with the deposition sequence of one global cycle as $b(\text{Al-O})-a(\text{Li-O})-c(\text{Si-O})$ with a , b , c representing the number of ALD cycles for Li_2O , Al_2O_3 and SiO_2 growths, respectively. Since each constituent oxide growth showed controllability in thickness, the thickness of LASO films grown with a given global cycle sequence was supposed to follow a linear relationship to the

global cycle number. In Figure 4.2, the thickness of LiAlSiO_4 films prepared with a deposition cycle sequence of 10(Al-O)-6(Li-O)-4(Si-O) is shown as a function of the global cycle number. It confirms that the film thickness follows a linear relationship to the number of global cycle with a growth rate of $20.6 \text{ \AA}/(\text{global cycle})$.

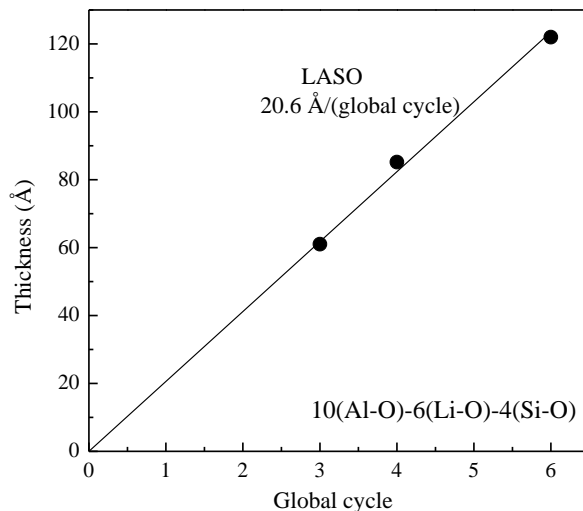


Figure 4.2. The thickness of LiAlSiO_4 films grown on SiO_2/Au nanoparticles at 290°C as a function of global cycle which composed of 10(Al-O)-6(Li-O)-4(Si-O). The film thickness was determined by HRTEM imaging.

To study compositional control of LASO ALD growths, samples prepared with various combinations of local cycle numbers a , b and c were studied with one global cycle, $b(\text{Al-O})-a(\text{Li-O})-c(\text{Si-O})$, set to be 20 local cycles ($a+b+c=20$). In order to avoid the possible overlapping of Si signals from LASO films and the Si substrate, Ge substrate was used for this analysis. In Figure 4.3 (a), UPS spectra of LASO films deposited with 5 global cycles on Ge are shown. The atomic percentage of each metal element (noted as x , y and z) was calculated based on the spectra to study the ALD controllability in cation atomic composition, especially Li contents. In Figure 4.3 (b), the calculated Li atomic percentage is shown as a function of the ratio of ALD cycle numbers for Li_2O to the total ALD cycle numbers in one global sequence, $a/(a+b+c)$. The

curve followed a general trend that the atomic percentage increased with rising cycle ratios, suggesting the number of local cycle a, b and c plays a role in adjusting composition of synthesized films. The cause of having the data points distributed within a band as opposed to a line could be due to the incubation time since the cycles required for the three constituent oxides to grow on each other was not considered in the graph.

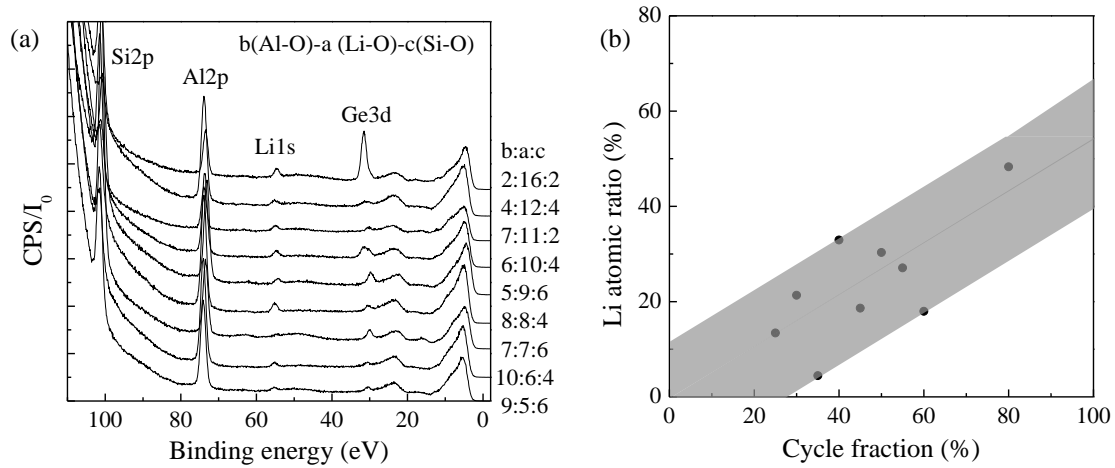


Figure 4.3. (a) UPS spectra of $\text{Li}_x\text{Al}_y\text{Si}_z\text{O}$ on Ge deposited via 5 global cycles of b(Al-O)-a(Li-O)-c(Si-O). (b) Calculated Li contents from the UPS spectra as a function of (Li-O) deposition cycle fraction ($a/(a+b+c)$).

4.2 Conformality of $\text{Li}_x\text{Al}_y\text{Si}_z\text{O}$ Coating

LASO films were deposited over vapor-liquid-solid synthesized Si and SiGe NWs on Si substrates using the 2(Al-O)-2(Li-O)-2(Si-O) sequence. Coated NWs were sonicated off from the Si substrate with DI water for characterizations by HRTEM. The coatings on measured NWs were found to be conformal with a thickness of $\sim 8\text{nm}$. In Figure 4.4 (a), a HRTEM image of a LASO coated SiGe NW is shown in comparison with that of a bare NW are shown as an example. The conformal coating over Si NWs was also confirmed by HRTEM and EDX, as shown in Figure 4.4 (b) and (c).

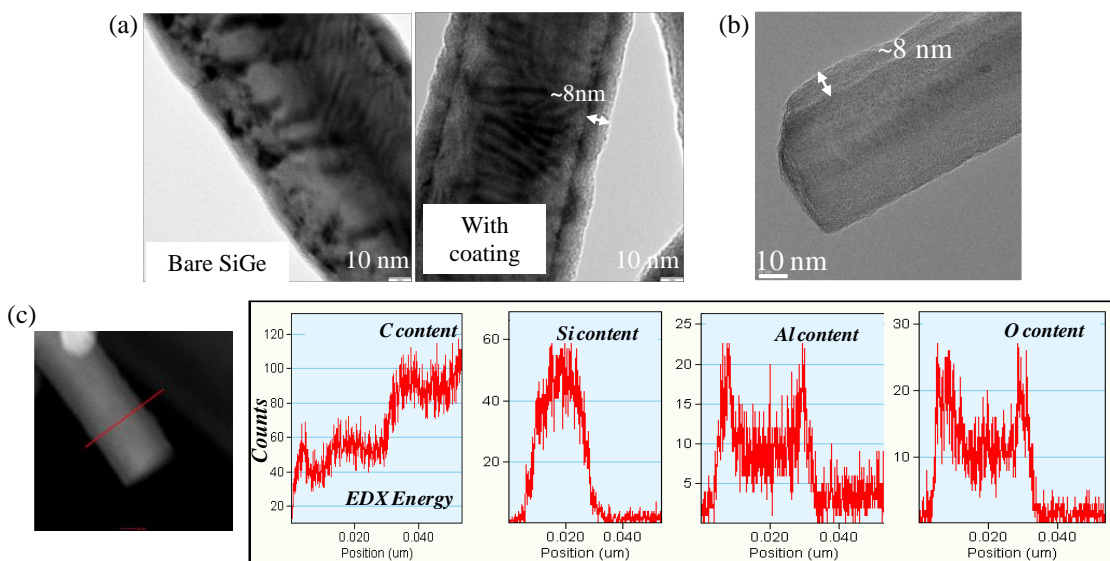


Figure 4.4. HRTEM images of conformal ~8 nm LASO coatings, deposited via the 2(Al-O)-2(Li-O)-2(Si-O) deposition sequence, over (a) SiGe and (b) Si nanowires. (c) A scanning TEM (STEM) image of the coated Si nanowires in (b) and the corresponding EDX analysis along the cross-section, confirming the presence of Si, Al and O in the coating.

The LASO coating over CVD synthesized higher aspect ratio Si NWs using the 10(Al-O)-6(Li-O)-4(Si-O) sequence was studied as well and shown in Figure 4.5. The SEM image (Figure 4.5 (a)) shows the clean Si nanowires with a height of ~50 μm and a diameter of ~75 nm grown vertically on a Si substrate. These nanowires were then coated with a layer of LASO and sonicated off from the Si substrate for HRTEM imaging. HRTEM image of a coated NW is shown in Figure 4.5 (b). It is observed that the coating is conformal and amorphous with the analysis EDX (Figure 4.5 (c)) confirming the presence of Al. Due to the limitation of the EDX, ICP-MS was applied and confirmed the existence of Li, as shown in Figure 4.5 (d). A higher Al content was found in a clean Si piece might due to measurement contamination. Since the Al content was detected via EDX, this analysis was mainly for showing the presence of Li.

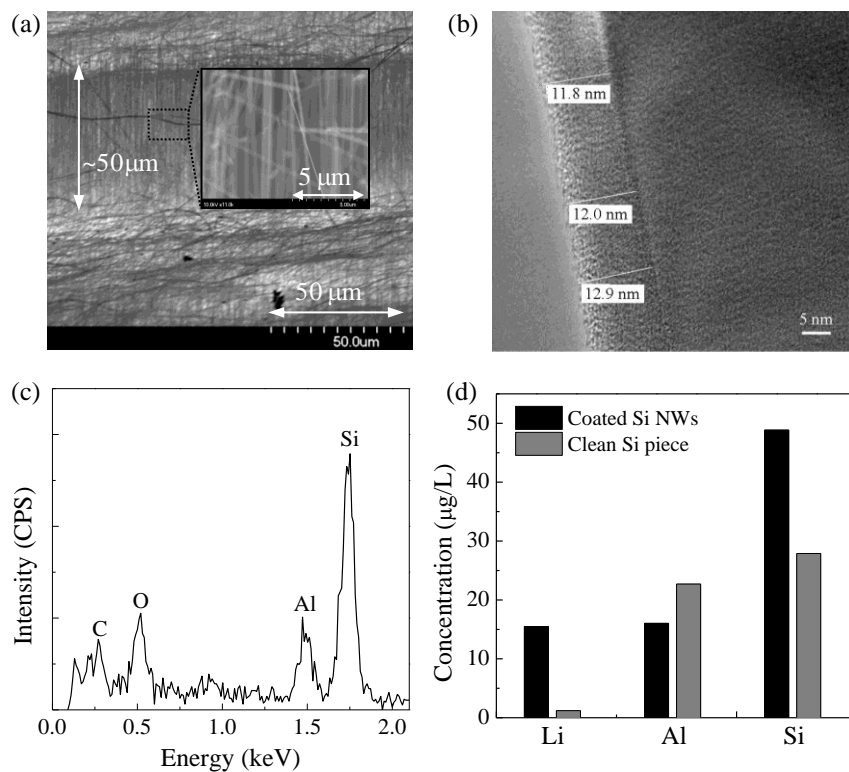


Figure 4.5. (a) An SEM image of a clean CVD synthesized Si NWs on Si substrate. (b) An HRTEM image of one of the Si NWs after LASO deposition of 6 global cycles of the 10(Al-O)-6(Li-O)-4(Si-O) sequence. (c) The corresponding EDX data confirmed the Si and Al presence and (d) the corresponding ICP-MS data confirmed the Li presence.

The results presented previously have demonstrated the LASO ALD enabled conformal thin-film coatings on high aspect ratio features with controls of thickness and cation composition. To serve as electrolyte materials or electrode coatings, these synthesized LASO films need to be pin-hole free, able to block current leakages and provide ionic conductivity.

4.3 Electrochemistry Characteristic

To assess the quality of LASO films for preventing potential electrical shorts between the anode and cathode as electrolyte materials, 6 nm and 10 nm LASO films were grown on ITO with half side masked using the 10(Al-O)-6(Li-O)-4(Si-O) sequence. The LASO coated ITO

sides were then immersed into ferrocene solution for cyclic voltammetry measurements. In Figure 4.6, the current responses measured by cyclic voltammetry of a bare ITO electrode (dash line) and a 6 nm LASO coated ITO electrode (solid line) are shown as a function of applied potential. If the ALD coating was not conformal and possessing pin-holes, electrons generated or lost during the reduction/oxidation of ferrocene due to potential changes on the ITO electrode would occur and result in a current response, as found on the bare ITO electrode. However, it is observed that the characteristic peaks of ferrocene were completely suppressed by neither 6 nm nor 10 nm (not shown but the response was identical to that of the 6 nm film) thick LASO film, indicating that there was no ferrocene oxidation or reduction. The small area of current-potential loop measured on LASO coated ITO was due to accumulated charges on the electrode surface induced by the applied potential, known as a double layer capacitor, confirming the electrical insulation of LASO thin films. The measurement confirmed that conformal and pin-hole free coverage of electrically insulating LASO films on ITO was achieved by ALD.

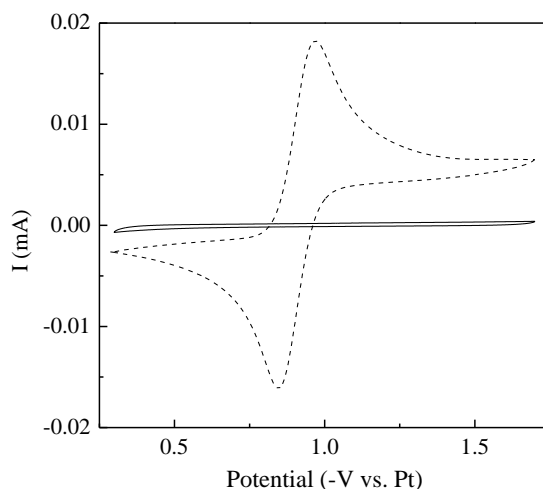


Figure 4.6. Cyclic voltammetry characteristics of a clean ITO (dash line) and 6 nm LiAlSiO_4 coated ITO (solid line) in a solution of 1 mM ferrocene and 100 mM TBATFB in anhydrous PC.

4.4 Ionic Conductivity

Impedance measurements of LASO films on ITO substrates were performed to assess their ionic conductivity. In Figure 4.7 (a), impedance performances of as-deposited LASO films prepared with 5 global cycles of b(Al-O)-a(Li-O)-c(Si-O) sequences are shown in Nyquist plots. Ionic conductivities were interpreted based on the circuit model discussed in Section 2.6.2 and are shown in Figure 4.7 (b) as a function of Li contents, as measured by UPS analysis. It is found that deposited LASO films were ionic conductive, with conductivities in a range of 10^{-9} to 10^{-7} S/cm and correlated to the Li content in the film.

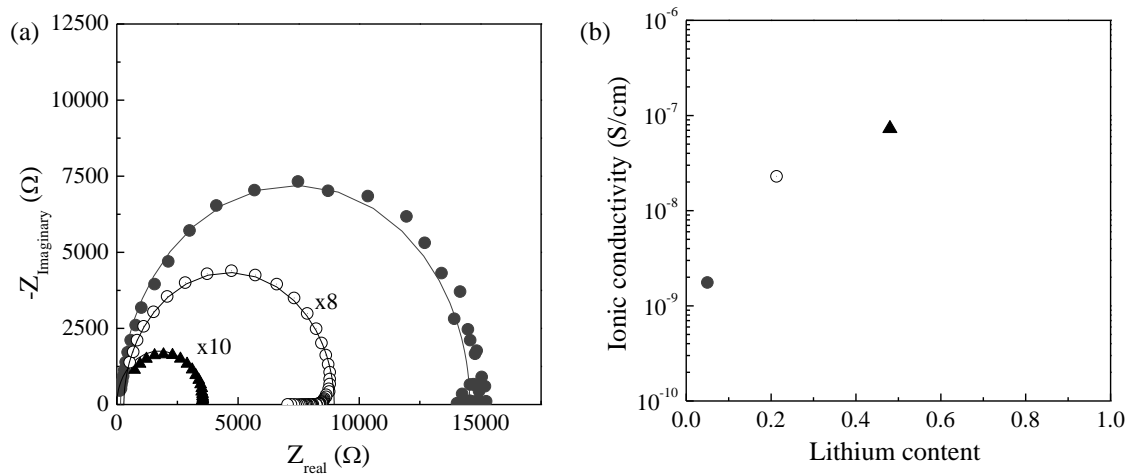


Figure 4.7. (a) Nyquist plots of impedance data (symbols) of as-deposited LASO films prepared via 5 global cycles of b(Al-O)-a(Li-O)-c(Si-O), where b:a:c=2:16:2 (\blacktriangle), 10:6:4 (\circ) and 16:2:2 (\bullet), and the fittings (lines) for interpreting the ionic conductivity. (b) The corresponding ionic conductivity as a function of Li content.

For solid thin-film electrolytes, the ionic conductivity is usually lower than their bulk states due to the limited site for ion hopping. For example, an ionic conductivity of 1.1×10^{-5} S/cm was found in $(\text{Li}_{0.5}\text{La}_{0.5})\text{TiO}_3$ thin-films (Ahn and Yoon 2004) while the bulk possesses an ionic conductivity of $\sim 10^{-3}$ S/cm as listed in Table 1.8. Therefore, the ionic conductivity of LASO was lower than that of bulk LiAlSiO_4 , 10^{-5} S/cm, could be explained. In addition, the

measured LASO films were amorphous in which the ion transport path was not well-defined; this could result in a lower ionic conductivity as well. Although ionic conductivity of these ALD LASO films are lower than the values reported on other thin-film electrolytes, such as LiSiPON ($\sigma_{\text{ion}}=8.8\times 10^{-6}$ S/cm) and $(\text{Li}_{0.5}\text{La}_{0.5})\text{TiO}_3$, a ionic conductivity higher than 10^{-8} S/cm may be sufficient to serve as electrolytes thin-films with a thickness $<15\text{nm}$ for batteries to provide 1 J/mm^3 , the storage in current battery technology (Warneke, Last et al. 2001). Therefore, these ALD synthesized LASO films have demonstrated their potential as electrolytes in a 3D micro-battery.

In Figure 4.8, ionic conductivities of LASO films prepared by the 10(Al-O)-6(Li-O)-4(Si-O) sequence are shown as a function of film thickness. It indicates that the ionic conductivity decreased with rising film thicknesses, similar to the results reported previously on PLD synthesized LiAlSiO_4 films with thicknesses in a range of 7.5-1200 nm (Shin-ichi, Satoshi et al. 2004) and which could be attributed to an increased number of charge carriers at the interface as space charges resulting in a higher ionic conductivity.

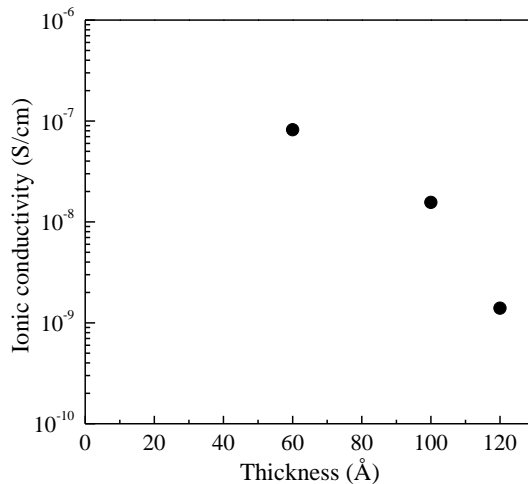


Figure 4.8. Ionic conductivity as a function of film thicknesses with the films prepared via the 10(Al-O)-6(Li-O)-4(Si-O) sequence.

To confirm the measured ionic conductivity was from Li transport not due to electrical leakage, which could potentially result in a higher conductivity electrically with decreasing film thicknesses, ionic conductivity as a function of temperature was then measured on this LASO film with a thickness of 10 nm. In Figure 4.9, the ionic conductivity of an as-deposited LASO film prepared with 5 cycles of the 10(Al-O)-6(Li-O)-4(Si-O) sequence is shown as a function of temperature, in comparison with that of LAO deposited by the 10(Al-O)-6(Li-O)-4(Al-O) sequence in which the SiO₂ was replaced by Al₂O₃. The sequences were chosen to maintain the local cycle fraction of Li₂O for the same amount of Li contents in the two films to study the effect of Si content on the activation energy. Based on equation (1.20), the activation energy of LASO and LAO were found to be 0.89 and 0.46 eV, respectively, which are in good agreement with values reported for bulk LiAlSiO₄ (Nagel and Bohm 1982) and bulk Li β-Al₂O₃ (Briant and Farrington 1981), confirming that charge transport in the ALD films arises from Li⁺ conduction. The lower activation energy of bulk Li_{4.4}Al_{0.4}Si_{0.6}O₄ and Li β-Al₂O₃ compared to stoichiometric LiAlSiO₄ may be explained by the crystal structures which defined the energy barrier for Li hopping. Here the ALD films were amorphous but also demonstrated that LASO possesses a higher activation energy compared to LAO, showing the cation compositions, which affect the bonding environment of each atom in the material, plays an important role to the Li transport.

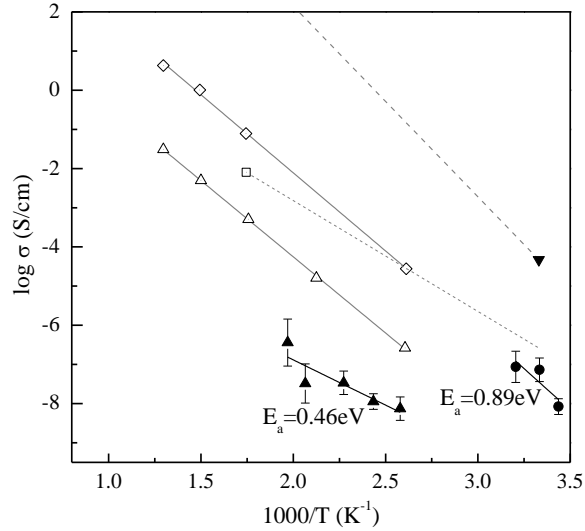


Figure 4.9. Ion conductivity of LASO and LAO films prepared via 5 cycles of the 10(Al-O)-6(Li-O)-4(Si-O) (-●-) and 10(Al-O)-6(Li-O)-4(Al-O) (-▲-) sequences, respectively, as a function of temperature in comparison with data reported in literature of single crystal β -LiAlSiO₄(\perp c) (- Δ -) (Nagel and Bohm 1982), β -LiAlSiO₄(//c) (\diamond) (Nagel and Bohm 1982), LiAlSiO₄ (-▼-) (Thangadurai and Weppner 2002) and Li_{4.4}Al_{0.4}Si_{0.6}O₄ (-□-) (Thangadurai and Weppner 2002).

Although the as-deposited amorphous ALD LASO thin films met the criteria for micro-battery electrolyte, the advantage of using LASO thin films as electrolytes may be even more promising if 1D ionic conductor β -LiAlSiO₄ thin films is realized. Post-deposition annealing was then performed on these synthesized LASO films to study the thermal stability and crystallinity for synthesizing β -LiAlSiO₄.

4.5 Controlled Crystallization of LiAlSiO₄

Theoretically, epitaxial films can be engineered via ALD followed by post-deposition thermal treatments if the stoichiometry is achieved. In other words, if a single crystalline film of LiAlSiO₄ is formed, it can serve as additional evidence on the composition controllability of ALD. In order to choose among possible annealing treatments to crystallize LASO films, their

thermal stabilities were studied on silicon wafer pieces, chosen because of its high thermal stability and ease access. Thin films prepared via 5 global cycles of b(Al-O)-a(Li-O)-c(Si-O) sequences were analyzed by UPS with *in-situ* annealing. Samples are mapped in Figure 4.10 (a) based on the different a, b and c in one global cycle, b(Al-O)-a(Li-O)-c(Si-O), used to deposit them. In Figure 4.10 (b), cation compositions of these measured LASO films are shown in a phase diagram measured after annealing at various temperatures. It is observed that higher annealing temperatures result in decreases in the Li content. On some samples, element Li was not even detected after 900 °C annealing. This was possibly due to the intercalation of Li into Si substrate since Si possesses high Li intercalation capacity, 4200 mAhg⁻¹, and is known as a promising viable anode material for Li-ion battery. (Chan, Peng et al. 2008)

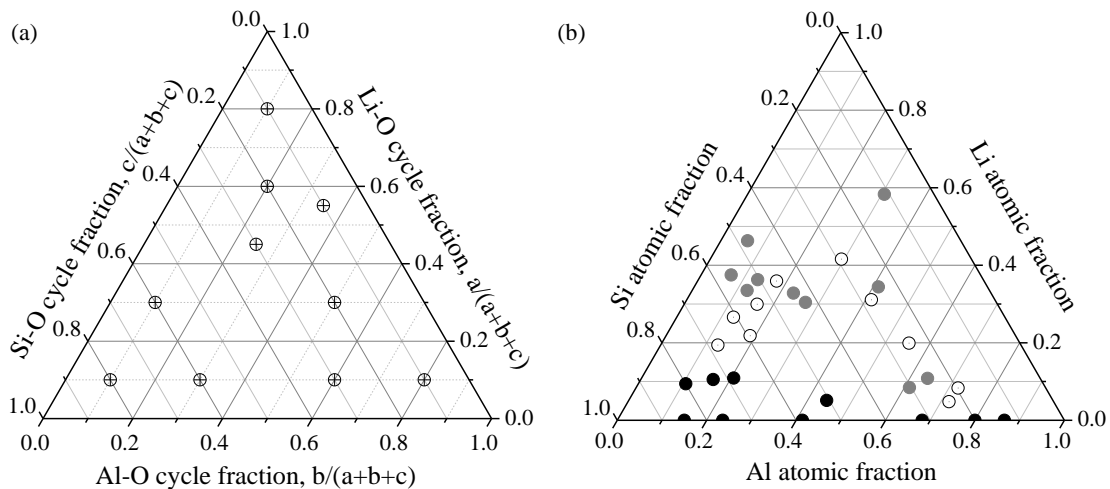


Figure 4.10. (a) A deposition cycle map of LASO films on Si prepared by 5 global cycles of b(Al-O)-a(Li-O)-c(Si-O). (b) The corresponding compositional map, as determined by synchrotron UPS analysis, showing the cation contents varied with *in-situ* annealing temperatures: as-deposited (●), 500 °C (○), and 900 °C (●).

Due to the Li intercalation issue, RTA was chosen to crystallize the films for reduced thermal budgets. In Figure 4.11 (a), specular XRD θ - 2θ scans of a 10 nm LASO film prepared via the cycle sequence of 10(Al-O)-6(Li-O)-4(Si-O) on Si (001) after RTA at various

temperatures. It indicates that as-deposited LASO film was amorphous, in agreement with the HRTEM result on coated Si NWs shown previously. Upon annealing, the film remained amorphous at 500 °C but crystallized at 900 °C. This result corroborated the crystallization temperature found on β -LiAlSiO₄ thin films synthesized by PLD. (Shin-ichi, Satoshi et al. 2004) Peaks in the specular scan were identified as reflections of β -LiAlSiO₄ (10 $\bar{1}$ 0) and (20 $\bar{2}$ 0) planes along with Si (004). The d-space of the two planes was calculated as 2.27 Å and 4.52 Å, respectively. The value for the β -LiAlSiO₄ (20 $\bar{2}$ 0) plane was less than the literature value of 4.55 Å (JCPDS 01-077-0158), indicating that the film was slightly compressed in the normal direction (0.66%) and suggesting that the film was expanded laterally to maintain the volume. Figure 4.11 (d) shows the corresponding UPS spectra of the film confirming the presence of all three cations after annealing at temperature up to 900 °C.

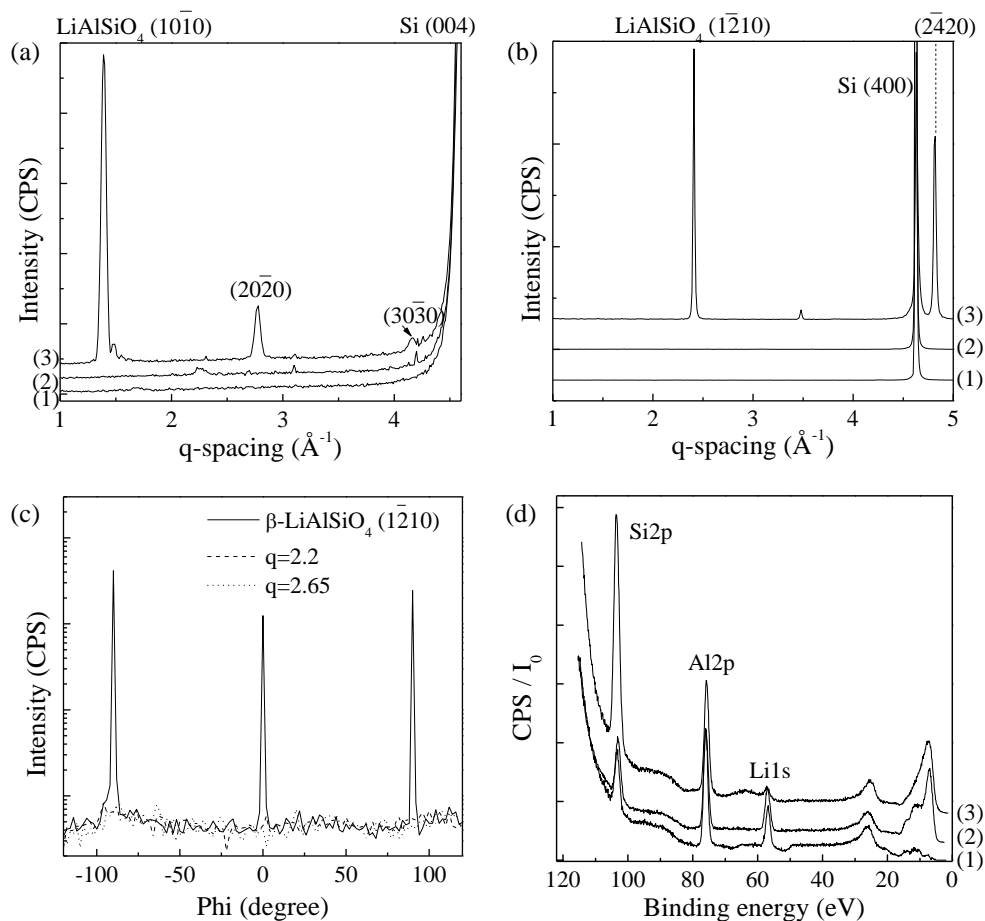


Figure 4.11. XRD spectra of 10 nm LiAlSiO_4 on Si (001) after post-deposition RTA at various temperatures, (1) as-deposited, (2) 500 °C and (3) 900 °C, for 90 seconds in N_2 : (a) specular scans, (b) in-plane scans and (c) phi scan of 900 °C annealed film. (d) The corresponding UPS spectra to confirm the presence of cations, especially Li. Thin films were prepared using the 10(Al-O)-6(Li-O)-4(Si-O) sequence.

Other than specular scans, in-plane radial scans were also performed, shown in Figure 4.11 (b), to provide LASO crystallinity and its epitaxial relationship to Si. Peaks were found at $q = 2.4$ and 4.8 \AA^{-1} and identified as $\beta\text{-LiAlSiO}_4$ ($1\bar{2}10$) and ($2\bar{4}20$) reflections, respectively, along with Si (400) reflection. A phi (-120° to 120°) scan on the position for $\beta\text{-LiAlSiO}_4$ ($1\bar{2}10$) was performed and is shown in Figure 4.11 (c). The results revealed that the plane possessed a four-fold symmetry that repeated every 90° , rather than 60° for six-fold symmetry, suggesting the $\beta\text{-LiAlSiO}_4$ film adopted the cubit arrangement of the Si substrate. The epitaxial relationship of

the crystalline LiAlSiO_4 to Si was $\beta\text{-LiAlSiO}_4 (1\bar{2}10) \parallel \text{Si} (100)$ and $\beta\text{-LiAlSiO}_4 (10\bar{1}0) \parallel \text{Si} (001)$.

When the stoichiometry of LiAlSiO_4 was not achieved, poor crystallinity of annealed films was found, as shown in Figure 4.12 for XRD spectra taken from LASO films prepared by various b(Al-O)-a(Li-O)-c(Si-O) sequences after RTA at 900 °C. The spectra shows that the film prepared by the 10(Al-O)-6(Li-O)-4(Si-O) sequence demonstrated the best crystalline quality since its as-deposited composition was closest to the LiAlSiO_4 stoichiometry. The film prepared using the 12(Al-O)-4(Li-O)-4(Si-O) sequence remained amorphous after annealing, confirming that the crystallinity was highly correlated to the film composition. The fact that the initially amorphous LASO films could be annealed into crystalline LiAlSiO_4 confirmed the compositional control attainable with ALD.

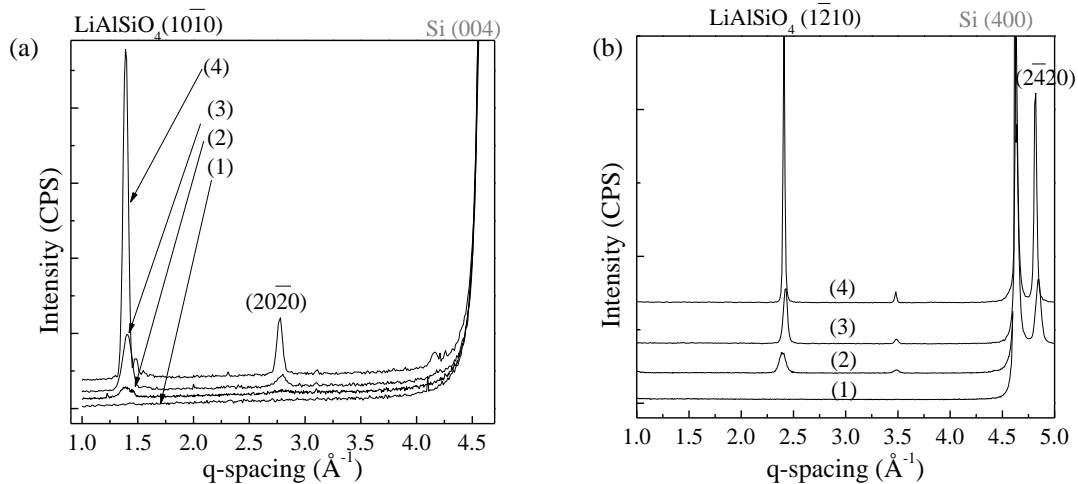


Figure 4.12. XRD spectra of LASO on Si (001) after post-deposition RTA at 900 °C: (a) specular scan and (b) in-plane scan. The films were grown by 5 global cycles of b(Al-O)-a(Li-O)-c(Si-O), where b:a:c = (1) 12:4:4, (2) 7:11:2, (3) 5:9:6 and (4) 10:6:4.

According to the epitaxial relationship found from XRD measurements, Figure 4.13 is an illustration to aid visualization of the alignment between these two materials at the interface. In

this case, Li channel was parallel to the sample surface, instead of perpendicular to the surface, because the substrate Si (001) was used. The cubic arrangement of Si substrate surface provided the template for epitaxial β -LiAlSiO₄ to form with a growth direction of $[10\bar{1}0]$, showing that the potential to control the orientation of the Li channel by adjusting the substrate orientation is possible and promising for achieving fast ion conduction for the electrolyte in a solid-state battery.

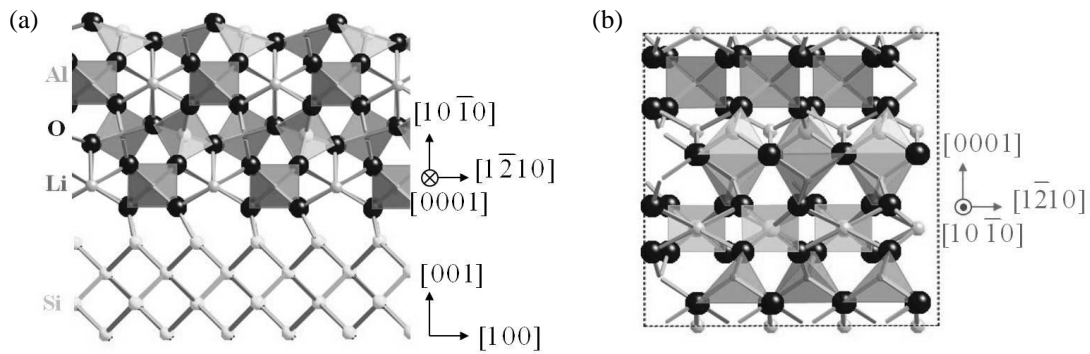


Figure 4.13. Crystal models showing the interfacial epitaxial relationship of β -LiAlSiO₄ on a Si (001) substrate: (a) side-view and (b) top-view.

4.6 Effect on SnO₂ NW Electrode

After characterizing the properties of synthesized LASO films, the amorphous LiAlSiO₄ was applied over SnO₂ NWs using the 10(Al-O)-6(Si-O)-4(Li-O) sequence to study its application in SnO₂ NW batteries and the effect on the formation of Sn NPs. The coated NWs were sonicated off using DI water for studying their lithiation process using *in-situ* HRTEM. Figure 4.14 (a) shows a cross-section image of a uniform and amorphous LiAlSiO₄ film (60 Å) coated SnO₂ surface. During lithiation at a high rate of 20 A/cm² (10 nm/s), it shows that the Li ionic conductive LASO film enhanced the formation of uniform Li₁₃Sn₅ alloy and suppressed the

formation of metallic Sn NPs, as shown in Figure 4.14 (b) and confirmed by SEAD, as shown in Figure 4.14 (c-d). It showed that the ionic conductive LiAlSiO_4 could be applied on the SnO_2 NW surface to change the reaction kinetics for suppressing the formation of Sn NPs. However, the LASO_4 coating cracked after lithiation due to volumetric expansion of the Li inserted NW anode. Furthermore, the highly Li^+ -conductive electrolyte coatings, which was LiAlSiO_4 in this case, resulted in shrinking of the NW surfaces during the delithiation process due to the faster Li transport and the formation of Sn crystals. (Zhang, Liu et al. 2012) The results emphasized the effect of engineering coatings of various materials over the NW surface on modifying the electrochemical reaction kinetics to suppress the hazardous Sn whiskers or NPs formation in a Li-ion battery. It suggested that using a direct electrolyte coating on SnO_2 NWs without other modifications might not be sufficient to electrically insulate the electrodes. Therefore, surface modifications on SnO_2 or different anodes with reduced volumetric expansions are required for applying the ALD LASO electrolyte to build a working 3D microbattery.

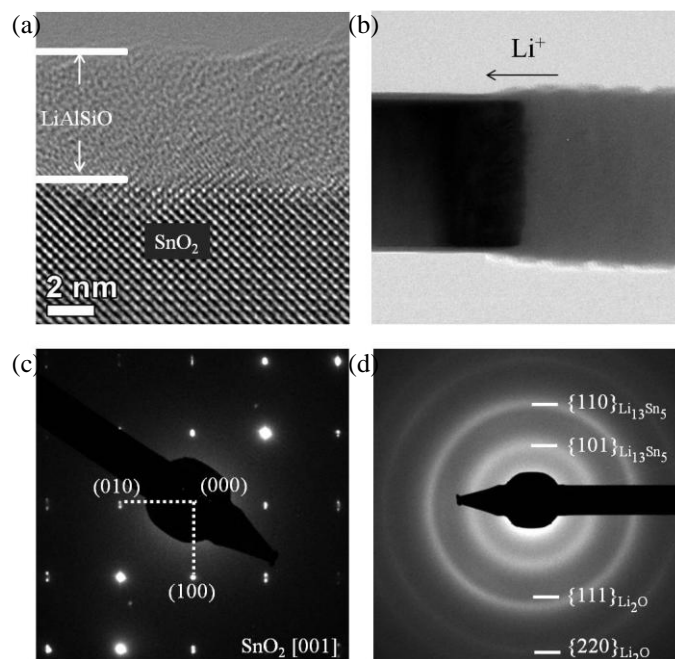


Figure 4.14. *In-situ* HRTEM cross-section images of a 6nm amorphous LiAlSiO_4 coated SnO_2 nanowire: (a) before and (b) during the lithiation process. SEAD patterns of the nanowire during the lithiation process: (c) unreacted site showing diffractions of SnO_2 and (d) lithium incorporated site showing diffractions of $\text{Li}_{13}\text{Sn}_5$. (Zhang, Liu et al. 2012)

4.7 Summary

The miniaturization of Li-ion batteries has drawn attentions for their outstanding performance in portable electronics and on-chip power applications. To realize this potential, an ultra-thin and highly conformal electrolyte layer is needed to coat the 3D electrode array. Furthermore, undesired chemical reactions on the surface of or in the electrodes during the charge-discharge cycling can reduce battery capacity and the long-term reliability of current battery technology. The use of solid electrolytes can effectively suppress the formation of undesired products, such as SEI layer and metallic Sn NPs during the lithiation process of a SnO_2 NW, and achieve the requirements of electrolytes for microbatteries (conformal, pin-hole free and ultra-thin). In this work, ionic conductive LiAlSiO_4 (LASO) ultra-thin films were

synthesized via ALD by alternating the growths of constituent oxides, Li_2O , Al_2O_3 and SiO_2 , with controls of the thickness and stoichiometry. The as-deposited amorphous films were applied on non-planar and even on high aspect ratio surfaces conformally without any pin-holes. The metal oxide framework formed by Al_2O_3 and SiO_2 made the ternary composites electrical insulating which effectively blocked the redox reaction of ferrocene on an indium tin oxide surface during voltage sweeps. Their ionic conductivities providing by the mobile Li transport were correlated to the Li content and could be easily enhanced by elevated temperatures based on activation energies, which were related to the cation composition of the films. The crystalline phase, 1D ionic conductor $\beta\text{-LiAlSiO}_4$, was realized via post-deposition rapid thermal annealing when the stoichiometry was achieved in the as-deposited films.

The application of the amorphous LiAlSiO_4 film on SnO_2 NWs showed that the material possessed a high ionic conductivity, which changed the reaction kinetic and further suppress the formation of metallic Sn NPs. Although surface modifications on electrodes might be required to build a working 3D microbattery using NW electrodes, the ALD synthesized composites demonstrated the capability to serve as electrolytes for high aspect ratio electrodes, which was known to be the critical part for building 3D microbatteries.

CHAPTER 5: SUMMARY AND FUTURE WORK

Al-based materials, Al_2O_3 , AlN and LiAlSiO_4 possess material properties suitable for dielectrics in SiC- and GaN-based high-power devices or electrolytes in Li-ion microbatteries, making it attractive to synthesize these materials at lower deposition temperatures with controls in film thicknesses, cation compositions and surface conformality over high aspect ratio features using ALD.

Al_2O_3 and AlN thin films were grown using pulses of TMA/ H_2O and TMA/ NH_3 , respectively, in a high-vacuum reactor to achieve a high quality interface on SiC and AlGaN/GaN heterostructures. The growth rate of ALD Al_2O_3 at 0.75-1 Å/cycle was realized at 195-200 °C on the two substrates with no incubation time. The as-deposited films were amorphous and crystallized into $\gamma\text{-Al}_2\text{O}_3$ after RTA at 1000 °C with epitaxial relationships to both substrates of $\gamma\text{-Al}_2\text{O}_3$ (111) || 4H-SiC (0001) or AlGaN (0001) and $\gamma\text{-Al}_2\text{O}_3$ ($1\bar{1}0$) || 4H-SiC ($11\bar{2}0$) or AlGaN ($11\bar{2}0$). Due to grain boundaries, crystallized Al_2O_3 films demonstrated a higher gate leakage current (10^{-3} A/cm² at 2.5 MV/cm) compared to amorphous Al_2O_3 films (10^{-3} A/cm² at 8 MV/cm). ALD growth of AlN was realized and found to be sensitive to three parameters: NH_3 dissociation/flux, moisture, which competed with and inhibited nitride growth, and deposition temperature. A growth rate of AlN at 1.5 Å/cycle was obtained at 540 °C with an incubation period of ~100 deposition cycles due to the limited amount of $-\text{CH}_3$ ligands on the surface for NH_3 to react. As-deposited AlN films were crystalline with RHEED showing the pattern of w-AlN [$11\bar{2}0$] azimuth, suggesting that the growth direction was [0001]. The electrical properties of ALD AlN films were promising, including a dielectric constant of 8.3 and a leakage current density of 10^{-3} A/cm² at 4.3 MV/cm, which were comparable to those of MBE

synthesized AlN, confirming the ability and feasibility of ALD to synthesize crystalline AlN at a relatively lower temperature compared to convention techniques, such as MBE and MOCVD. ALD Al₂O₃ demonstrated a superior ability on minimizing the leakage compared to ALD AlN while AlN has a small lattice mismatch to SiC for smaller interface state density, making it promising to use a dielectric stack of AlN/Al₂O₃ on 4H-SiC for enhanced device performance by providing an improved interface and eliminated gate leakage current. While serving as surface passivation layers on AlGaIn/GaN heterojunctions, both binary Al-based materials, Al₂O₃ and AlN, demonstrated the capability of passivating the heterostructure surface but ALD AlN passivation yielded a higher carrier mobility. In order to optimize the 2DEG properties, the Al-based dielectric/AlGaIn interface properties are necessary to be studied to understand the mechanism of surface passivations, including interface roughness, strain and crystallinity using techniques of x-ray reflectivity, XRD and TEM. MIS-HEMTs should be made with the two materials as the gate dielectric to assess their effects on the current collapse, dispersion and leakage current for actual applications in high-power devices. Even though the ALD AlN demonstrated promising capability of passivating the surface, the improvement in 2DEG properties were not comparable to the value reported on sputtered or MBE AlN passivated AlGaIn/GaN, suggesting that the epitaxial quality of ALD AlN were not as good as those films. The crystalline properties of as-deposited and annealed AlN should be studied for exploring the potential of engineering high quality epitaxial AlN on SiC by post-deposition RTA treatments. In order to reduce the carbon incorporation and the precursor decomposition for high purity ALD AlN, other Al-precursors could be examined for a wider growth temperature window.

Ionic conductive LiAlSiO₄ (LASO) ultra-thin films were synthesized by alternating the growths of constituent oxides, Li₂O, Al₂O₃ and SiO₂, using pulses of LTB/H₂O, TMA/H₂O and

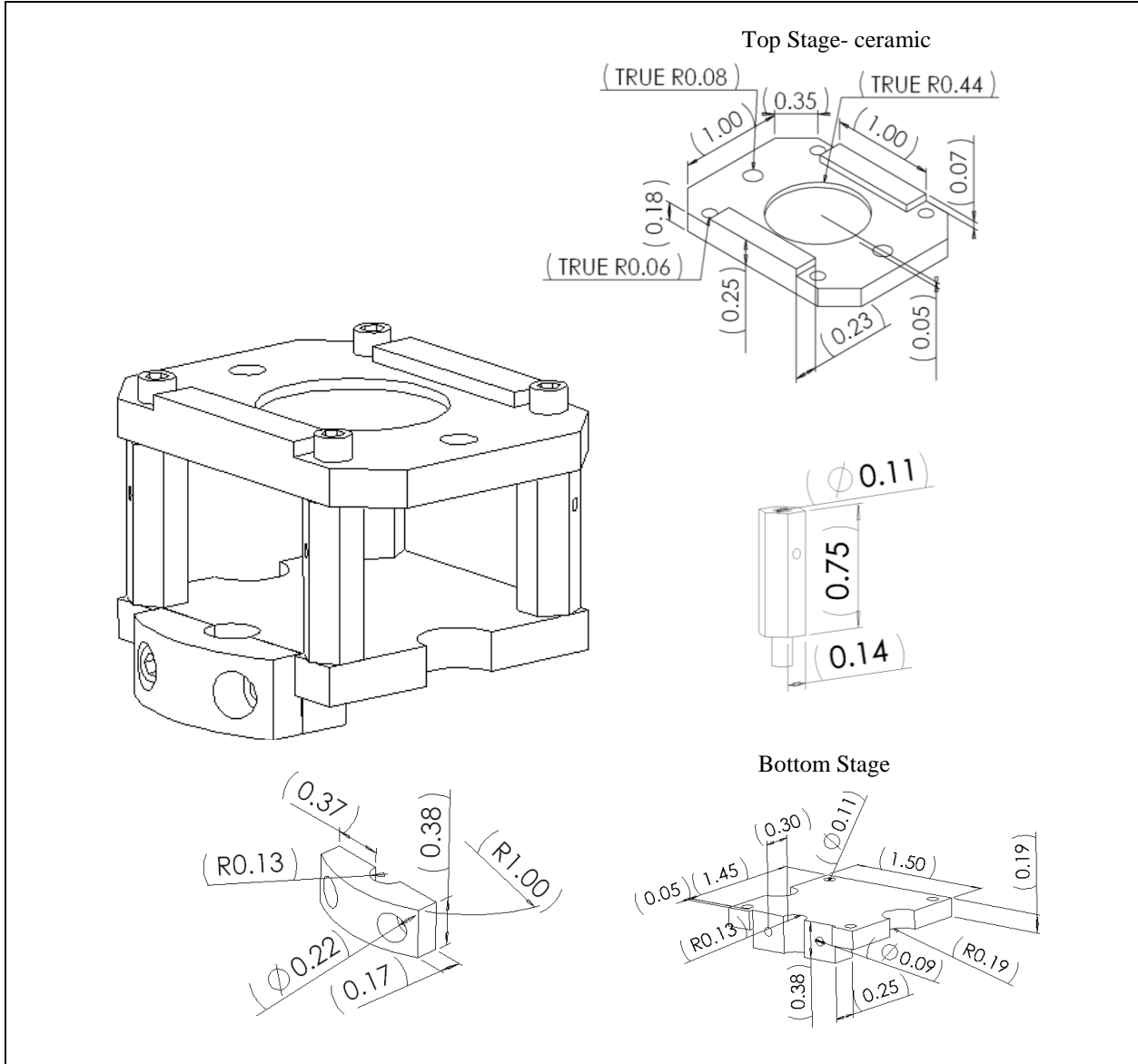
TEOS/H₂O, respectively in a hot-wall reactor. Stoichiometric LiAlSiO₄ was realized at a growth rate of ~20.6 Å per global cycle sequence of 10(Al-O)-6(Li-O)-4(Si-O) at 290°C. As-deposited films were amorphous, conformal over 3D Si/Ge nanowires, and pin-hole free, as confirmed by electrochemical testing of LiSiAlO₄ on indium tin oxide in ferrocene. Ionic conductivities of Li_xAl_ySi_zO composites providing by the mobile Li transport were in the range of 10⁻⁹-10⁻⁷ S/cm and correlated to the Li content. The Li transport can be improved at elevated temperatures based on activation energies, which were related to the cation composition of the films and in a range of 0.34-0.98 eV. As-deposited LiAlSiO₄ films on Si (001) crystallized after RTA at 900 °C with an epitaxial relationship of β-LiAlSiO₄ (1 $\bar{2}$ 10) || Si (100) and β-LiAlSiO₄ (10 $\bar{1}$ 0) || Si (001), proving that ALD of Li_xAl_ySi_zO films possessed the capability to tune the stoichiometry. The ALD synthesized composites demonstrated the capacity to serve as electrolytes for high aspect ratio electrodes, which was known to be the critical part for building 3D microbatteries. In order to find a precise correlation of the local cycle ratios to the cation composition, the incubation period for one oxide to grow on the other should be quantified. On the other hand, the ALD films were so thin that it is possible to damage the film by probes while the impedance response was measured through Pt/Ti contacts using the probe station. Although the issue could be avoided by using hanging mercury drop electrodes (HMDE), impedance measurements at various temperatures cannot be performed for determining the activation energy due to the toxicity of mercury vapor. Therefore, another measurement setup, such as conductive AFM using AC input signal, may be one of the solutions. (O'Hayre, Lee et al. 2004) Because a temperature of 900 °C was required to crystallize the LiAlSiO₄ films while the backside contact ITO could not remain its electrical conductivity after this high temperature thermal treatment, another substrate, such as highly doped Si or poly-Si, should be used for characterizing

electrochemical properties of the crystalline films. The application of the amorphous LiAlSiO_4 film on SnO_2 NWs showed that the material possessed a high ionic conductivity, which changed the reaction kinetic and further suppressed the formation of metallic Sn NPs. However, the LiAlSiO_4 coating cracked after lithiation due to volumetric expansion of the Li inserted NW anode. In addition, the highly Li^+ -conductive LiAlSiO_4 coatings resulted in shrinking of the NW surfaces during the delithiation process and the formation of Sn crystals. It suggested that using a direct electrolyte coating on SnO_2 NWs without other modifications might not be sufficient to electrically insulate the electrodes since the volumetric expansion and Sn formation may be the issues. Therefore, surface modifications on SnO_2 , such as carbon coatings, or different anode materials, such as porous Si or graphite, to reduce volumetric expansion and eliminate Sn particle formation are required for applying the ALD LASO_4 electrolyte to build a working 3D microbattery. The bandgap energy diagram of LASO should be studied and compare with that of potential electrodes, such as Si or graphite and LiCoO_x . As shown in Figure 1.13, the conduction band edge of LASO (similar to the LUMO of an organic liquid electrolyte) should be higher than the Fermi level energy of the anode while the valence band edge of LASO (similar to the HOMO of an liquid electrolyte) should be higher than the Fermi level energy of the cathode to avoid chemical reactions in the electrolyte during battery charge/discharge cycles for a long-term reliability. The studies can be done through computational simulation using first principle calculation or experimental measurements, such as XPS/UPS. Other than electrolytes, the thin ALD LASO films can also be studied as surface modification layers to eliminate the formation of solid electrolyte interface (SEI).

APPENDICES

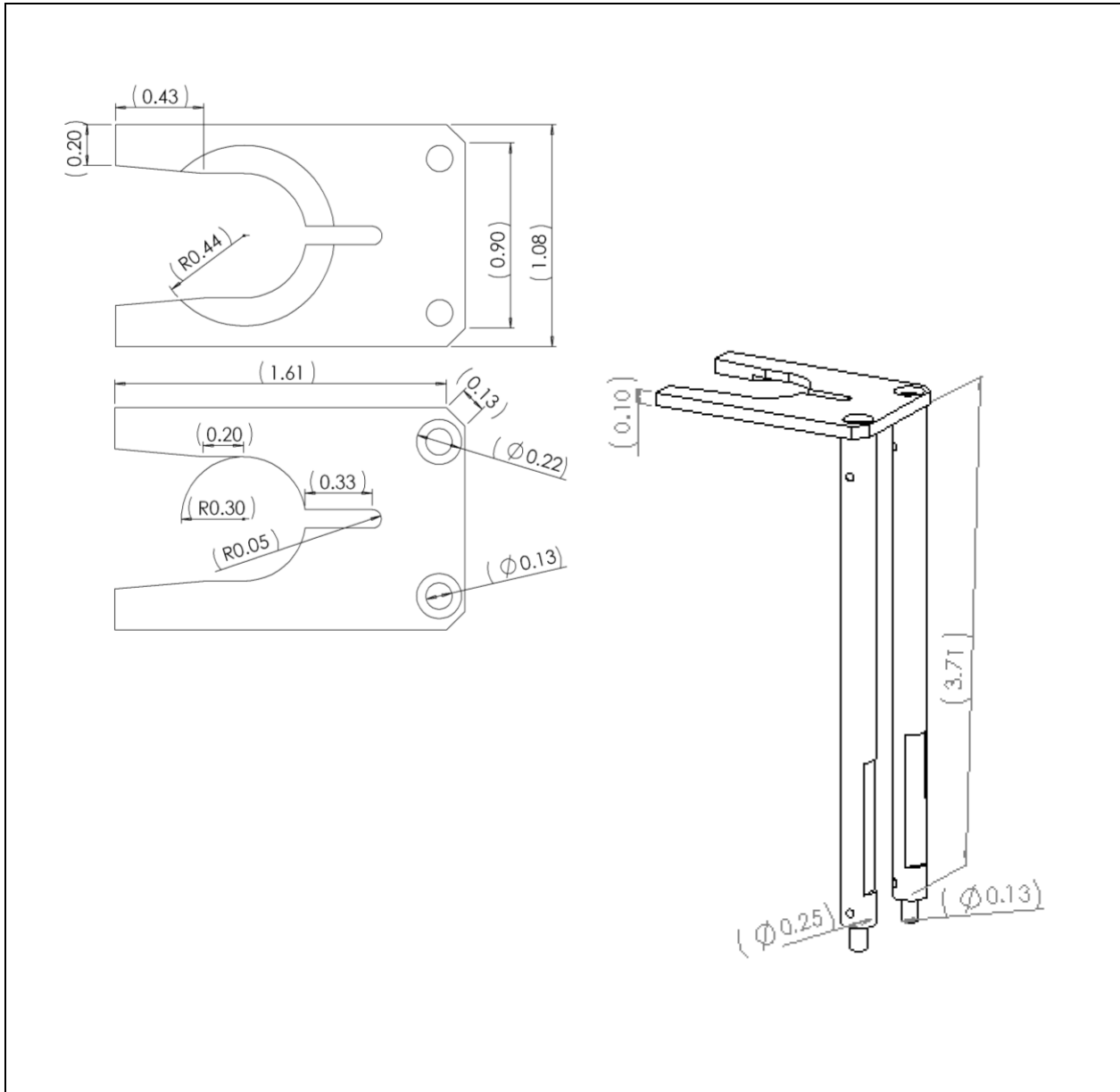
APPENDIX A: Design of ALD Reactor for Al₂O₃ and AlN Growth

A.1. Heating Station for High-vacuum ALD Chamber



University of California, Los Angeles, Department of Chemical and Biomolecular Engineering						
Part	Heating Station	Material	Ceramic-top stage/Stainless steel (316)			
Filename	HEATER LIFT ASM	Scale	No	Unit	inch	Quantity 1
Designer	Ya-Chuan Perng	Date				
Revised by		Date				
Contractor	Transfer Eng.	Date	3/8/2010			
Comments		Tolerance	+/- .0001			

A.2. Receiving Fork for High-vacuum ALD Chamber

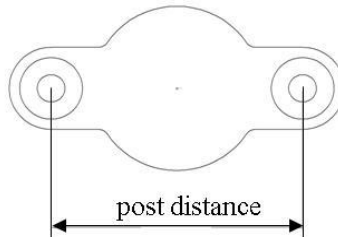


University of California, Los Angeles, Department of Chemical and Biomolecular Engineering							
Part	Heating Station	Material	Stainless steel (316)				
Filename	HEATER LIFT ASM	Scale	No	Unit	inch	Quantity	1
Designer	Ya-Chuan Perng	Date					
Revised by		Date					
Contractor	Transfer Eng.	Date	3/8/2010				
Comments		Tolerance	+/- .0001				

A.3. Sample Stage and Heater Temperature Calibration

The sample heating station design uses a ceramic resistive heater (Momentive Boralectric Heater, HT-03), shown in Table A.1, to heat a molybdenum holder on which the sample is mounted. Power is supplied to the heater through two electrical contacts using two molybdenum nuts and one rod on each side to hold the heater onto the top heating stage made of ceramics. Copper wires are attached to the rods underneath the top heating stage by nuts. The other ends of the wires are connected to an electrical feedthrough wrapped with Kapton tapes to prevent electrical shortage. The feedthrough connections on the ambient side are electrical connectors to hold wires connected to a three-prong plug, through which power is supplied by a voltage transformer. By varying the input voltage, the temperature of the sample can be controlled and was calibrated by measuring temperatures using a k-type thermocouple mounted on the Mo holder surface with a screw and a thermocouple mounted on the heater, as shown in Figure A.1. Both temperatures are read through thermocouple feedthroughs and their change as functions of input voltage are measured, as shown in Figure A.2.

Table A.1. Schematic and specifications of the ceramic heater, boralectric heater HT-03.



Heater diameter (mm)	Length (mm)	Post distance (mm)	Contact diameter (mm)	Hole diameter (mm)	Watts	Volts	Ohms	Current max (A)
25.4	51.8	38.1	9.5	4	300	40	9-15	10

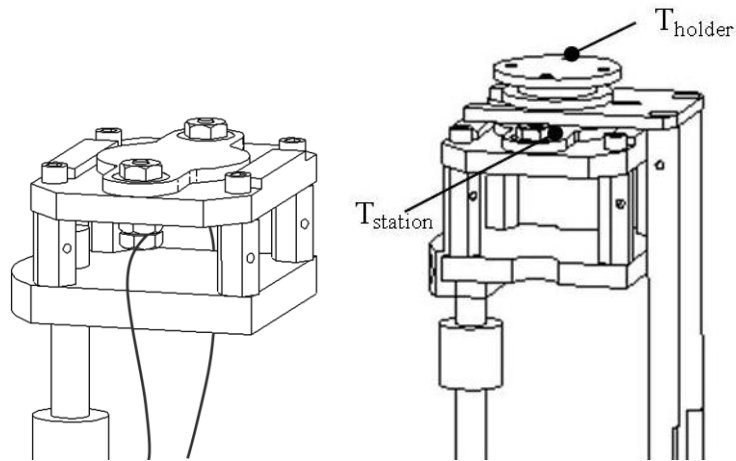


Figure A.1. Assembly of the sample heating stage and setup of temperature calibration.

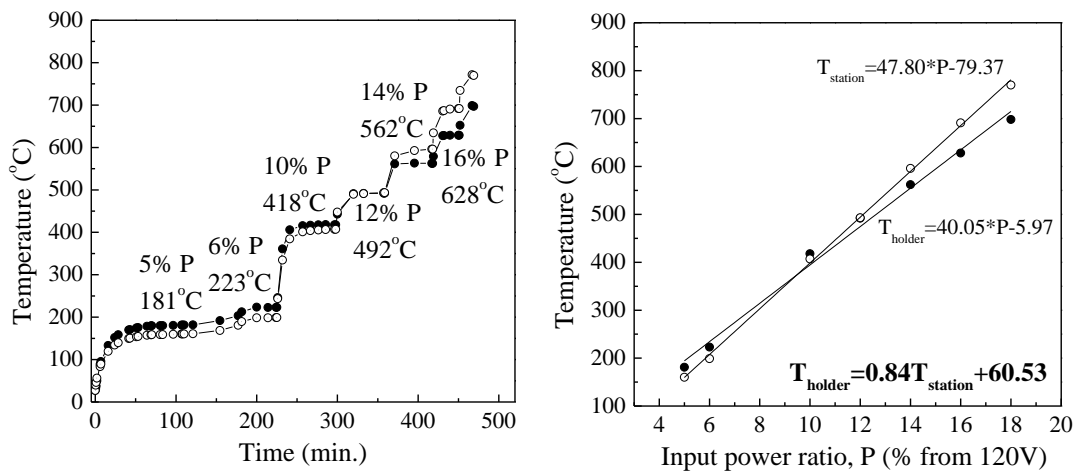


Figure A.2. Sample holder (-●-) and heater (-○-) temperatures as function of input heater power.

A.4. Automation of Deposition Process

The LabVIEW 8.2 program may be updated to include interlocks and additional controls. The technical support (phone) provided by National Instruments is very useful in translating process steps into code. The current program has a ten-step sequence, as shown in Figure A.3, that is looped N times, where N is the desired number of global ALD cycles. Steps 1-5 is for TMA deposition with N_2 purge that can be looped A times, where A is the desired number of TMA cycles. Steps 6-10 are for NH_3 deposition with N_2 purge that can be looped B times, where B is the desired number of NH_3 cycles. The user can also specify a *Wait Time* to delay the deposition process after selecting *Run*, which may be used to allow the sample to heat to the operating temperature prior to deposition without further intervention from the user. On the Control Panel, the user inputs N , the length of the pulses and evacuation steps, and the voltage to be supplied to the MFCs for each pulse step. Upon selecting *Run*, the process will run for the specified number of cycles and then the automated valves and MFCs will remain closed. At the conclusion of the process, the user is required to manually close the valves on the precursor bubbler and purge the gas lines to remove any remaining vapor, as detailed in the Operating Procedure in Section C.6 and C.7. Then the sample heater and gas line heaters should be manually turned off, though this step may be easily automated if desired.

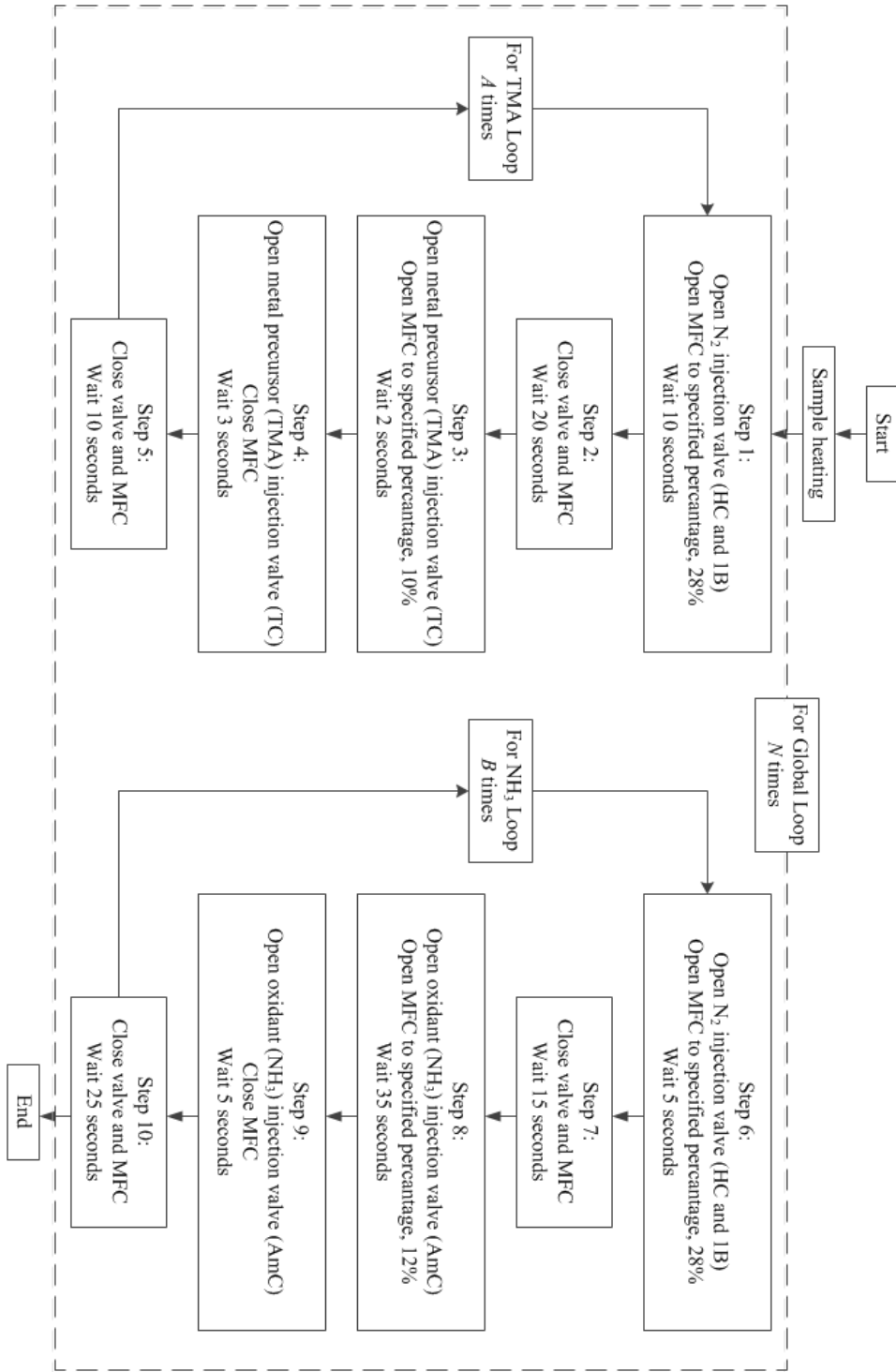
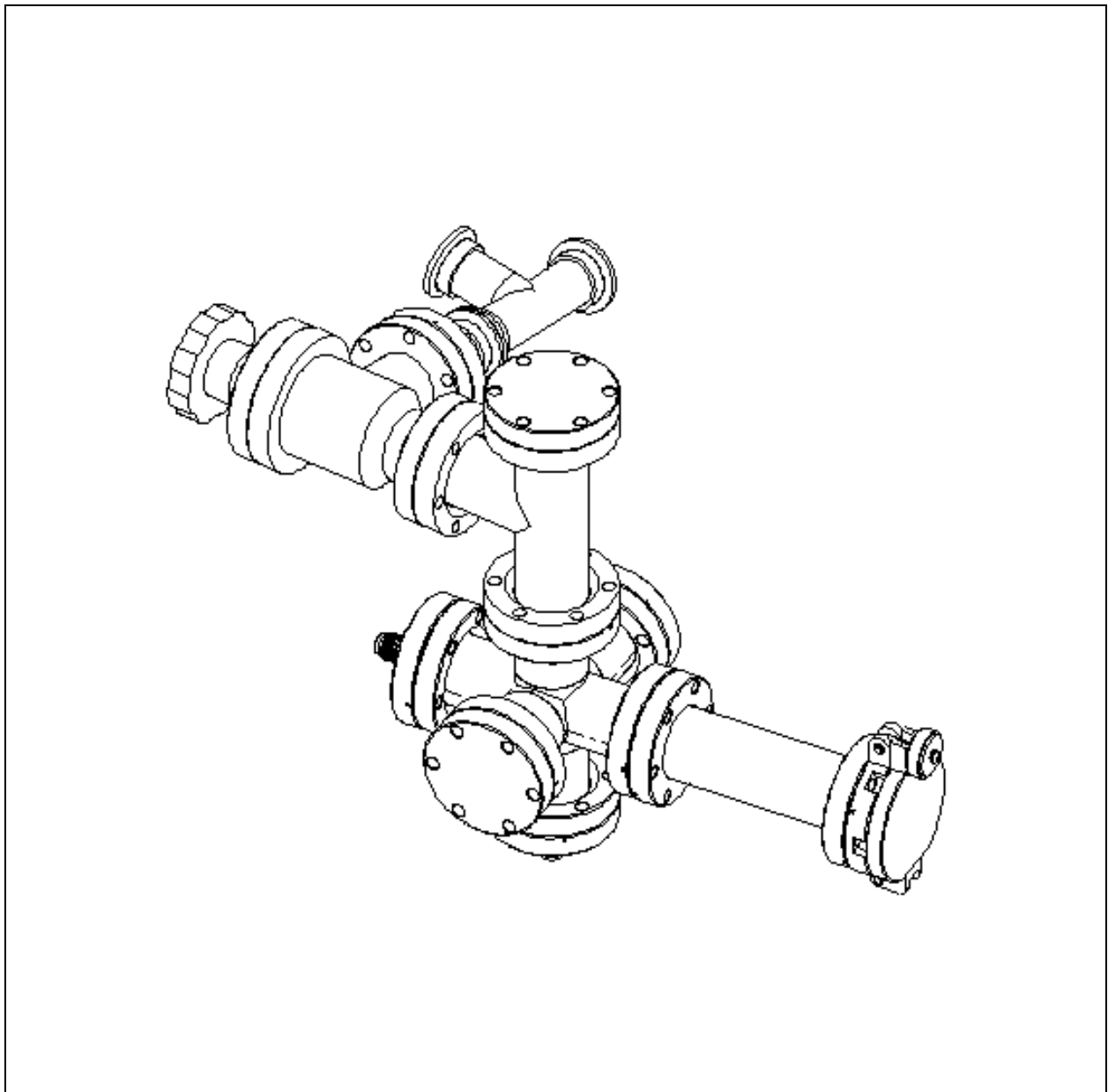


Figure A.3. A flow schematic of Labview program for AlN deposition under high-vacuum with N_2 purging.

APPENDIX B: Design of ALD Reactor for LiAlSiO₄ Growth

B.1. Isometric View of Low-vacuum ALD Reactor



University of California, Los Angeles, Department of Chemical and Biomolecular Engineering							
Part	HW ALD Reactor	Material	Stainless steel (316)				
Filename	Li Chamber 120322	Scale	No	Unit	inch	Quantity	1
Designer	Ya-Chuan Perng	Date	2/5/2009				
Revised by		Date					
Contractor		Date					
Comments	All parts were from MDC or NC		Tolerance	+/- .0001			

B.2. Sample Heating Design

A hot-wall reactor is designed using a 2 3/4" CF 6-way cross and a heater on the ambient side to heat up the sample to the desired deposition temperature of 290 °C in 2 hours (can be ranges). An insulation material (superwool 607 blanket) is required to cover the heater to prevent heat loss to the ambient and to maintain the outside temperature is < 50 °C for safety issue. In order to build the reactor, we need to select a heater with required power to heat up the chamber and an insulation material with a required thickness.

- **Assumption:**

1. The air temperature (T_∞) is 300 K.
2. The reactor is made of a stainless steel tube with an inner radius of r_1 , outer radius of r_2 and a length of L . Heater is applied outside of the stainless steel tube and evenly supplies a heating rate of q to heat up the reactor. An insulation wrap is applied outside of the heater with a thickness of (r_3-r_2) .
3. Temperature controller controls the temperature outside of the S.S. wall (T_3).
4. T_c is the chamber wall temperature, including T_2 and T_3

- **Heat transfer of the reactor in a cylinder coordination:**

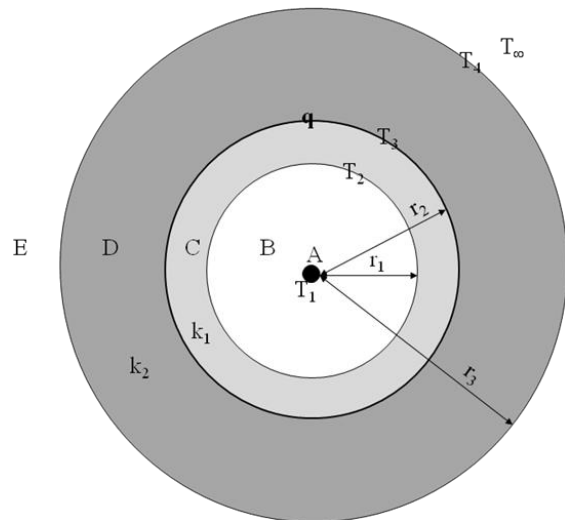
(A) Sample: $\rho C_p V \frac{\partial T_1}{\partial t} = \sigma \varepsilon A (T_2^4 - T_1^4)$

(B) Vacuum: $q_r = \sigma \varepsilon A (T_2^4 - T_1^4)$

(C) Reactor wall: $k_1 \left[\frac{1}{r} \frac{\partial}{\partial r} \left(r \frac{\partial T}{\partial r} \right) \right] = \rho C_p \frac{\partial T}{\partial t}$

(D) Insulation: $k_2 \left[\frac{1}{r} \frac{\partial}{\partial r} \left(r \frac{\partial T}{\partial r} \right) \right] = \rho C_p \frac{\partial T}{\partial t}$

(E) Air: $q_a = hA(T_4 - T_\infty)$



- **Properties:**

T_3 is 563 K (290 °C) during the deposition, controlled by a temperature controller (Omega CN 9000A).

$$r_1=0.685''=0.0174\text{m}, r_2=0.75''=0.0191\text{m}$$

$$L\sim 5''=0.127\text{m}$$

$$h_{\text{air}}= 20 \text{ W/m}^2\text{-K}$$

$$\rho_{\text{superwool}}=128 \text{ kg/m}^3; C_{p,\text{superwool}}=1050 \text{ J/kg-K}; k_{\text{superwool}}=0.13 \text{ W/m-K}$$

$$\rho_{\text{s.s.}}=8000 \text{ kg/m}^3; C_{p,\text{s.s.}}=500 \text{ J/kg-K}; k_{\text{s.s.}}=20 \text{ W/m-K}$$

$$\rho_{\text{Si}}=2300 \text{ kg/m}^3; C_{p,\text{Si}}=714 \text{ J/kg-K}; \epsilon_{\text{Si}} \text{ (emissivity of si surface)} =0.6; V_{\text{Si}}=1\text{cm}\times 1\text{cm}\times 400\mu\text{m}$$

$$\sigma \text{ (Stefan-Boltzmann constant)}=5.67\times 10^{-8}\text{W/m}^2\text{-K}^4$$

- **To calculate the power of heater and the time required to heat up samples:**

<Step 1> Calculate how long it takes to heat up the chamber to 290 °C if there is no heat loss outside:

$$\rho_{\text{s.s.}} \cdot C_{p,\text{s.s.}} \cdot V_{\text{chamber}} \frac{dT_c}{dt} = q \Rightarrow \int_{300}^{563} 99.03dT_c = q \int_0^t dt \Rightarrow 26044.2 = qt$$

Figure B.1 shows the relationship between heater power and time required for the chamber to be heated up to desire temperature, which is less than 1.4 hours if the heater power is larger than 5W.

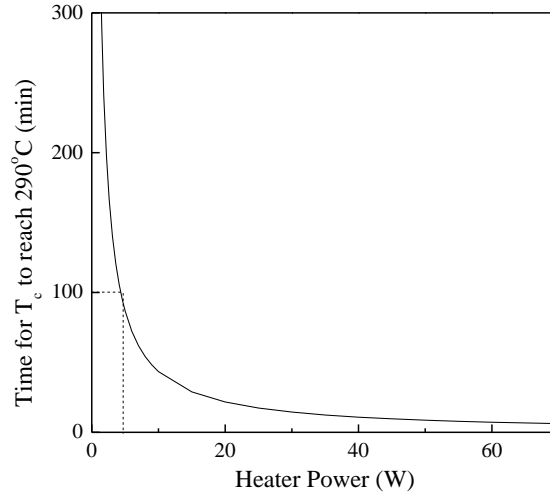


Figure B.1. Time needed for the chamber wall to be heated up to 290 °C as function of the heater power.

<Step 2> Calculate sample temperature (use small object approximation) when chamber wall (T_2) is at 290 °C ($T_2=563\text{K}$):

$$\begin{aligned} \rho C_p V \frac{dT_{Si}}{dt} &= \sigma \varepsilon A (T_2^4 - T_{Si}^4) \Rightarrow \rho_{Si} C_{p,Si} V_{Si} \frac{dT_{Si}}{(T_2^4 - T_{Si}^4)} = \sigma \varepsilon_{Si} A dt \\ \Rightarrow \int_{300}^T \frac{dT_{Si}}{563^4 - T_{Si}^4} &= \int_0^t 1.118 \times 10^{-10} dt \\ \Rightarrow \frac{1}{4(563)^3} [-\ln(563 - T_{Si}) + \ln(563 + T_{Si}) + 2 \tan^{-1}(\frac{T_{Si}}{563})] \Big|_{300}^T &= 1.118 \times 10^{-10} t \end{aligned}$$

Figure B.2 shows the time required for the sample to be heated up to the deposition temperature is ~1.67 minutes when chamber wall is at 290 °C.

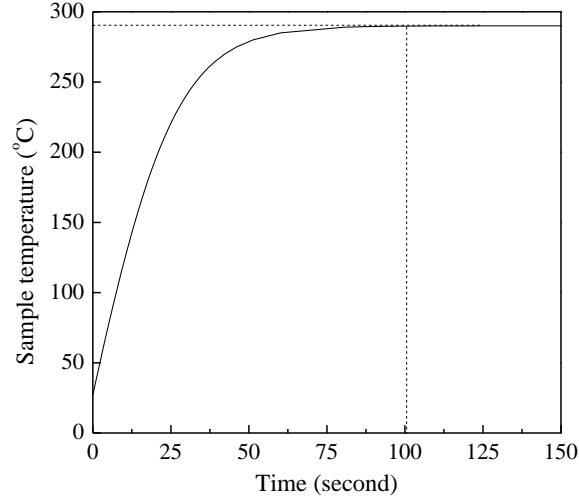


Figure B.2. Time needed for the Si sample inside a 290 °C chamber to be heated up to 290 °C.

Therefore, it takes 1 hour and 28 minutes to heat up the sample if the heater power is 5 W. The heat-up time can be shortened if the heater power is higher, as shown in Figure B.1.

- **To calculate the required thickness of the insulation material to eliminate the heat loss and lower the ambient temperature to $\leq 50^\circ\text{C}$:**

<Step 1> Calculate the heat loss as a function of insulator thickness (d_{is}) at steady state:

Only heat loss to the outside so $k_2\left[\frac{1}{r}\frac{\partial}{\partial r}\left(r\frac{\partial T_D}{\partial r}\right)\right]=0$, $T_D=T_4$ and $q_a = hA(T_4 - T_\infty)$. The

heat loss can be calculated using the following equation and show in Figure B.3 (a).

$$q = \frac{T_3 - T_\infty}{\frac{\ln(r_3/r_2)}{2\pi k_2 L} + \frac{1}{h(2\pi r_3)L}} = \frac{T_3 - T_\infty}{\frac{\ln[(r_2 + d_{is})/r_2]}{2\pi k_2 L} + \frac{1}{h[2\pi(r_2 + d_{is})]L}}$$

<Step 2> Calculate the outside temperature, T_4

$$T_4 = T_\infty + \frac{T_3 - T_\infty}{\frac{\ln[(r_2 + d_{is})/r_2]}{2\pi k_2 L} + \frac{1}{h[2\pi(r_2 + d_{is})]L}} \times \frac{1}{h[2\pi(r_2 + d_{is})]L}$$

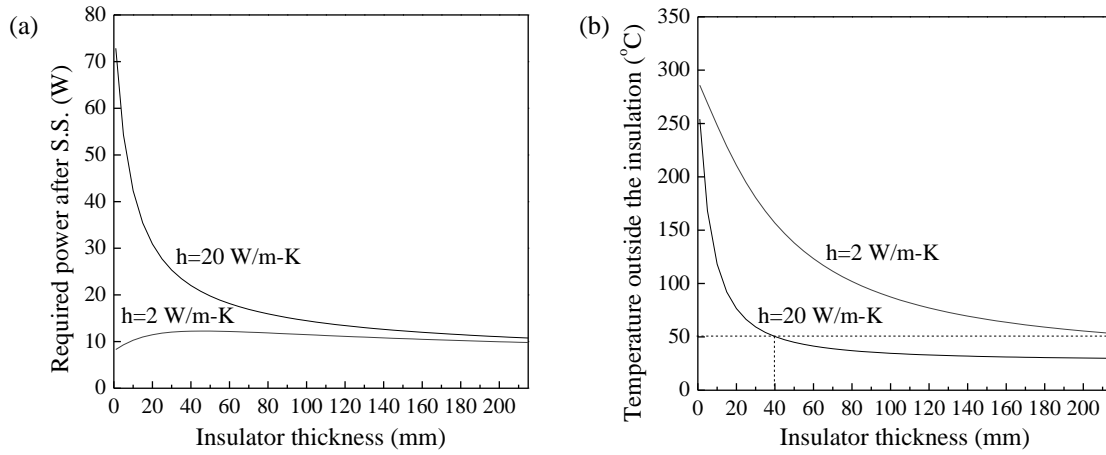


Figure B. 3. (a) Required heating power to compensate the heat loss and (b) the temperature outside of the insulation material as function of insulator thickness.

Therefore, thicker than 40 mm insulation blanket is required to decrease the outside temperature to be lower than 50°C.

APPENDIX C: Operating Procedure for AlN Growths in High-vacuum ALD System

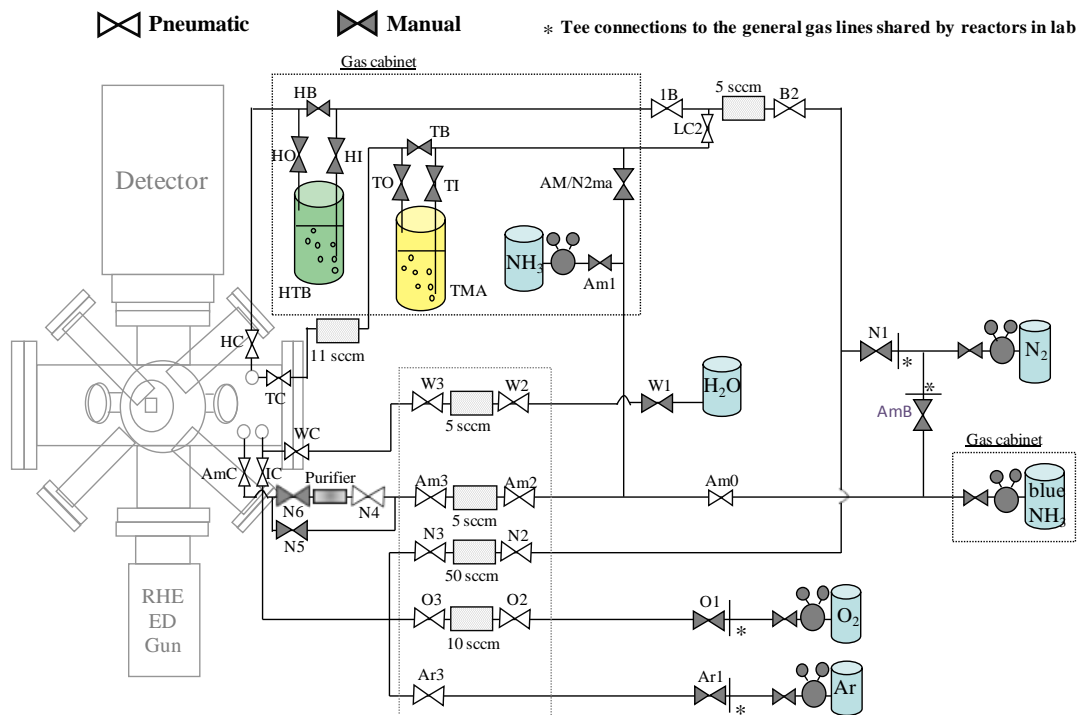


Figure C.1. A schematic on the layout of gas lines to the high-vacuum reactor for high quality Al_2O_3 and AlN thin-film growths.

Table C.1. Vapor pressures of chemicals used in this work.

Chemical	Vapor pressure	Source temperature	Gas line temperature
Water	17.5 mm Hg (20°C)	RT	60 °C
NH_3	6658 mm Hg (21°C)	RT	RT
TMA	9 mm Hg (20°C)	RT	60 °C
HTB	0.5 mm Hg (50°C)	RT	60 °C

C. 1. To Vent the Chamber

1. Make sure the gate valve between chamber and Transfer Tube is closed.
2. Close the gate valve between the RHEED gun and the RHEED turbopump (TP).
3. Heat the chamber for more than 5 min at 80 °C to bake out.

4. Turn off the cold cathode gauge and then close the pneumatic gate valve between the main TP and chamber.
5. Make sure the chamber is isolated from pumps.
6. Then open N2, N3 and IC valves with the N₂ MFC setting at 20% until the pressure is almost to atmosphere pressure (look at Pirani gauge). Then, close the valves and MFC.

C. 2. To Pump the Chamber from Atmosphere

Start with all In-line Valves, Gate Valves, and Gas Line Valves closed. Chamber turbo and mechanical pumps are turned off.

1. Make sure the backing valve to the TP is closed and then turn on the mechanical pump for the chamber. Open the In-line Roughing Valve to the chamber. Pressure should spike and then drop quickly to ~ 100 mTorr on the TC gauge (indicating chamber has been rough pumped). The Pirani gauge (PG1) should read a similar pressure.
2. Wait for the pressure to be $\sim 4 \times 10^{-2}$ Torr (it takes about 5 min from atmosphere to base pressure).
3. Close the In-line Roughing Valve to isolate the chamber from the MP.
4. Open the Backing Valve to the Chamber Turbo Pump to pump the turbo with the MP.
5. [If the TP is on during the venting, this step can be skipped]
 - Do not turn on the Turbo Pump until it is pumped down to ~ 60 mTorr by the MP.
 - Make sure cooling water is running to the Turbo Pump.
 - Check the TP is at 60 mTorr (TC gauge).
 - Press the “Pumping Unit” button on the Chamber TP Controller to start running the TP. Wait ~ 10 min until it winds up to full speed as indicated by controller.
6. Make sure the Chamber Pressure has not raised above $\sim 6 \times 10^{-2}$ Torr (Pirani gauge). If it has, close the Backing Valve and **then** open the Roughing Valve to repump the chamber by MP (maximum 5 minutes). Then close Roughing Valve and open Backing Valve.
7. Open the Pneumatic Gate Valve between the TP and chamber. There should be a loud compressed air sound as it opens.

8. Wait for 1min, turn on cold cathode gauge and monitor chamber pressure (cold cathode gauge can only be on when pressure is $\leq 10^{-4}$ Torr). Bake the chamber for overnight at ~ 80 °C to reach base pressure of $< 5 \times 10^{-8}$ Torr.

C.3. To Pump the RHEED Gun (required to perform RHEED measurement)

1. Make sure the gate valve between RHEED gun and TP is closed.
2. [If the MP and TP are running during the venting, this step can be skipped]
 - Turn on the MP connected to the RHEED TP.
 - Open the foreline Valve between the RHEED MP and TP to evacuate the TP.
 - Check that the pressure on the TC gauge is < 30 mTorr.
 - Make sure cooling water is running to the TP.
 - Turn on the TP. Wait 10 minutes for it to ramp up to full speed.
3. Turn on the Ion gauge by pressing IG2 bottom on the Gauge Controller and wait until the pressure is ≤ 1 order higher than the chamber pressure. (Pressure has to be $\leq 5 \times 10^{-6}$ Torr for the interlock).
4. Carefully and very slowly open the gate valve between the pump and the RHEED gun (Screw loosens easily).

C.4. To Load a Sample Using the Loadlock

Vent Loadlock:

1. Make sure the pneumatic gate valve between Loadlock and Transfer Tube is closed.
2. Turn off the Ion Gauge measuring the Loadlock pressure.
3. Close the pneumatic gate valve between the Loadlock and its Turbo Pump.
4. *The LL should now be completely isolated.*
5. Unlock the load lock door, so when the chamber is fully vented the door will open. Open the vent valve and wait for the chamber to vent fully. Vent slowly, $\frac{1}{4}$ turn of the knob every 5 minutes.
6. Close vent valve.

Load Sample into LL and Pumpdown:

1. Open the LL door and insert sample block onto rotating plate. Make sure that the two screws on sample holder faces load lock window and slightly to the right of the center for fork to pick up sample holder.
2. Close LL Door.
3. Close foreline valve of TP to isolate TP and close the foreline valve to isolate TransferTube (TT) TP as well.
4. Open roughing valve to Chamber.
5. Wait until TC gauge reads base pressure of the MP (≤ 5 mTorr).
6. Close roughing valve.
7. Open foreline valves of LL TP and TT TP.
8. Open the pneumatic gate valve between TP and LL to pump down LL by TP.
9. Wait 10 minutes and then turn on Ion Gauge. (Ion gauge can only be on when pressure is $\leq 10^{-4}$ Torr.)
10. Wait until LL pressure reaches minimum 2 orders of magnitude above the TT pressure.

Transfer from LL to TT:

1. Check TT pressure to make sure it is in 10^{-8} Torr. Open LL-TT gate valve. Check TT pressure again to make sure it doesn't change much (by one order of magnitude).
2. Close LL-Turbo valve (to protect TP in case samples drop).
3. Bring TT arm into the LL.
4. Transfer block to TT arm.
5. Retract arm into TT completely. Place sample holder onto the cart.
6. Close LL-TT valve.
7. Open LL-Turbo valve.

Transfer from TT to ALD Chamber:

1. ALD chamber should be $\leq 1 \times 10^{-7}$ Torr (Cold cathode gauge) with the heating station lowered.
2. Pick up sample holder from cart with arm.

3. Open ALD-TT valve (manual).
4. Bring arm into ALD chamber.
5. Slide the sample onto the receiving fork and raise the arm to get the holder into the cutoff space on the bottom of the receiving fork. Then raise the stage until the bottom of the sample is held by the stage.
6. Retract arm into TT slowly while making sure the holder is sitting in the chamber.
7. After the arm is fully retracted, close ALD-TT gate valve (should hear clicks before it is fully closed).
8. Use flashlight to make sure that the knobs on the stage heater do not touch the receiving fork otherwise will short-circuit the chamber. Also check the heater resistivity (should be 11.0Ω).
9. If doing RHEED, the heating stage needs to be lowered so the sample holder can be measured with a height slightly lower.

C.5. Manual AlN Deposition

The chamber should be at base pressure $\leq 5 \times 10^{-8}$ Torr with all gas line valves closed.

1. Use flashlight to look to make sure that the knobs on the stage heater are not touching the receiving fork.
2. Check the resistivity of the stage heater, which should be 11Ω. If slightly higher, check the plastic tube connections. If way higher, something may be wrong with the stage, such as the wire connects are loosed.
3. Slowly ramp up the heating to the sample stage, increase 2-3% each time, to reach the desired temperature (based on the temperature calibration) as monitored using the thermocouple feedthrough. Record temperature and pressure in log book with each ramping.
4. Heat the TMA line to 50-60°C (set-point is 2.2) during the last temperature ramping. Check temperature with thermometer probe.
5. Wait 20 minutes at the final heating temperature until stabilized.
6. Set Nitrogen MFC to 28%. Check that all other MFCs start at 0%.
7. Open necessary valves while waiting for sample temperature to stabilize.

- Manually open the regulator (blue and silver) for NH₃ cylinder in the gas cabinet by the wall in dry lab.
 - Open TO on bubbler for TMA in gas cabinet under the MFC controllers.
 - Open the pneumatic valves Am0, Am2, Am3, N4, 1B and B2 and manual valves N6 and HB.
8. Open HC valve on chamber.
 9. Wait 10 seconds for N₂ purging. Check chamber pressure and flow rate on MFC controller.
 10. Close HC valve on chamber.
 11. Wait 20 seconds for pumpdown.
 12. Dial up TMA MFC to 10%.
 13. Open TC valve on chamber to pulse TMA in.
 14. Wait 5 seconds. Check chamber pressure and flow rate on MFC controller.
 15. Dial down TMA MFC to 0 and close TC valve on chamber.
 16. Wait 10 seconds for pumpdown.
 17. Open HC valve on chamber.
 18. Wait 5 seconds for N₂ purging. Check chamber pressure and flow rate on MFC controller.
 19. Close HC valve on chamber.
 20. Wait 15 seconds for pumpdown.
 21. Dial up NH₃ MFC to 12%.
 22. Open AmC valve on chamber to pulse NH₃ in.
 23. Wait 40 seconds. Check chamber pressure and flow rate on MFC controller.
 24. Dial down NH₃ MFC to 0 and close AmC valve on chamber.
 25. Wait 25 seconds for pumpdown.
- Repeat Steps #8-25 for desired number of cycles.
26. Close the regulator (blue and silver) for NH₃ cylinder in the gas cabinet by the wall. Close TO on bubbler for TMA in gas cabinet under the MFC controllers. Close the pneumatic valves Am0, AM2, AM3, N4, 1B and B2 and manual valves N6 and HB.
 27. Turn off stage heater.
 28. Turn off heater on TMA precursor line.

29. After the temperature is ≤ 70 °C, lower sample stage in order to transfer sample holder to the cart in transfer tube.

Go to Section C.7 to pump down the lines after finishing depositions.

C.6. Automated AlN Deposition

The chamber should be at base pressure $\leq 5 \times 10^{-8}$ Torr with all gas line valves closed.

1. Use flashlight to look to make sure that the knobs on the stage heater are not touching the receiving the fork.
2. Check the resistivity of the stage heater, which should be 11 Ω . If slightly higher, check the plastic tube connections. If way higher, something may be wrong with the stage, such as the wire connects are loosed.
3. Slowly ramp up the heating to the sample stage, increase 2-3% each time, to reach the desired temperature (based on the temperature calibration) as monitored using the thermocouple feedthrough. Record temperature and pressure in log book with each ramping.
4. Heat the TMA precursor line to 50-60°C during the last temperature ramping. Check temperature with thermometer by hand.
5. Wait 20 minutes at the final heating temperature until stabilized.
6. Turn MFC controller to Auto Flow setting while waiting for sample temperature to stabilize.
7. Open necessary valves while waiting for sample temperature to stabilize.
 - Manually open the regulator (blue and silver) for NH₃ cylinder in the gas cabinet by the wall in dry lab.
 - Open TO on bubbler for TMA in gas cabinet under the MFC controllers.
 - Open the pneumatic valves Am0, Am2, Am3, N4 and B2 and manual valves N6 and HB.
8. Open the LabVIEW 8.2 file on the PC for AlN deposition (filename: combined-AlN-heater_N2purging).
 - Check the voltage and channel settings for the MFCs.
 - Check the timing (in milliseconds) for each step.

- Enter the number of cycles.
9. Press Start in the Labview program.
 10. [This step is due to the fact that there is a delay in the beginning and can be skipped]
Stop the program during the pumpdown of Nitrogen at the beginning. The light for the Nitrogen valves (1B and HC) will turn on and then off, when it turns off stop the program.
 11. Reset the settings for each step.
 12. Press Start in the Labview program again.
 13. Check that the process starts and proceeds correctly based on the timing and the chamber pressure.
 14. Before the last run starts, close the regulator (blue and silver) for the NH₃ cylinder in the gas cabinet. Close TO on bubbler for TMA in gas cabinet under the MFC controllers. Close the pneumatic valves Am0.
 15. After the deposition is finished (stop automatically), turn off the stage heater and the heater for the TMA line.
 16. Close the pneumatic valves AM2, AM3, N4 and B2 and the manual valve N6.
 17. After the temperature is $\leq 70^{\circ}\text{C}$, lower sample stage in order to transfer sample holder to the car in transfer tube.
- Go to Section C.7 to pump down the lines after finishing depositions.

C.7. To Pump Down Gas Lines After the Deposition

Pump out TMA Gas Line: (Begin with all valves closed)

1. Turn on heating to TMA precursor line to 50-60°C. Check temperature with thermometer by hand.
2. Open TC valve on chamber.
3. Dial up TMA MFC to 50% slowly, making sure the chamber pressures does not go above 8×10^{-4} Torr.
4. Wait for the line to pump down to $< 2 \times 10^{-6}$ Torr.
5. Dial down TMA MFC to 0%.
6. Close TC valve on chamber.

7. Turn off heating to TMA precursor line.

Pump out NH₃ Gas Line: (Begin with all valves closed)

1. Open AmC valve on chamber.
2. Dial up NH₃ MFC to 20% slowly, making sure the chamber pressures does not go above 8×10^{-4} Torr.
3. Open pneumatic valve Am3 and manual valve N5.
4. Wait for the line to pump down to $< 5 \times 10^{-6}$ Torr.
5. Close pneumatic valve Am3 and open Am2 for 30 seconds.
6. Open valve Am3 and close valve Am2.

Repeat Steps #4-6 for 3 times.

7. Leave valves Am3, Am2, AmC and N5 open until the line is pumped down to $< 2 \times 10^{-6}$ Torr.
8. Close valves Am3, Am2, AmC, and N5.

This completes pumping down the line up to valve Am0. If pumping down all the way to the NH₃ cylinder is needed, continue with the following:

9. Dial down NH₃ MFC to 10%
10. Open pneumatic valves Am0, Am2, Am3 and AmC and manual valve N5.
11. Wait for the line to pump down to $< 2 \times 10^{-6}$ Torr (takes overnight)
12. Close AmC valve on chamber.
13. Close Am3, Am2, and Am0 pneumatic valves and N5 manual valve.

Double-check all valves are closed and all the heaters are off.

APPENDIX D: Operating Procedure for LiAlSiO_4 Growths in Low-vacuum Hot-wall ALD System

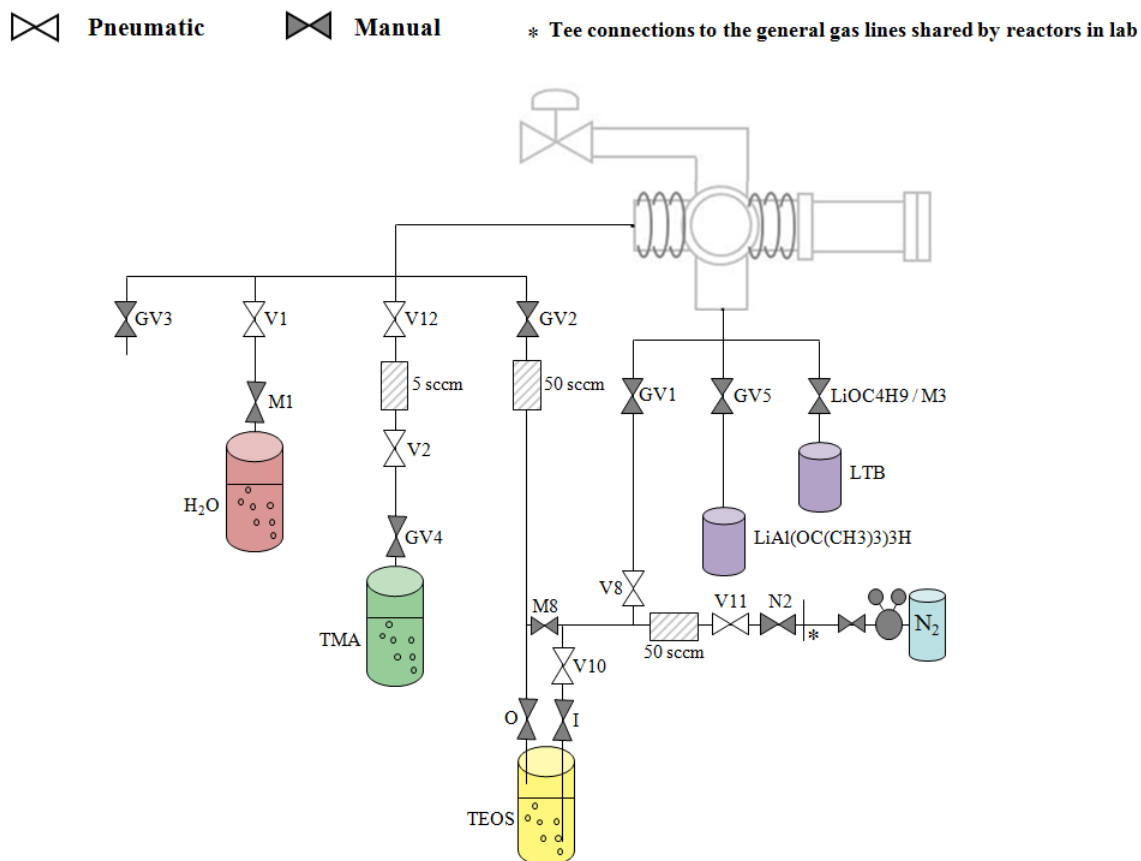


Figure D.1. A schematic on the layout of gas lines to the hot wall reactor for LASO thin-film growths.

D. 1. To Vent the Chamber

1. Make sure all the valves are closed and isolate the chamber by closing the roughing valve to MP.
2. Untighten the chamber door.
3. Flow nitrogen by setting N_2 MFC (Channel 4) to 10-15%.
4. Open pneumatic valves V11 and V8.
5. Open GV1 slowly and purge chamber with nitrogen for 5 minutes.
6. Close GV1, V11, and V8. (Note: should not overpressurize chamber because small the nitrogen flow rate, and this is to coat the chamber wall with nitrogen.)

7. Vent the reactor by slowly opening GV3 until the door opens. (Note: keep a hand in front of the door before it opens in order to catch it, otherwise it may hit the metal frame and get damaged.)
8. After venting, close GV3 to the chamber.

D. 2. To Load the Sample and Pump the Chamber from Atmosphere

1. Open the door of chamber and load the sample into the chamber. Make sure the sample is placed in the center of the reactor.
2. Close the door and tighten the knob.
3. Open the roughing valve and pump the chamber pressure to the base pressure (60-70 mTorr).
4. Perform “Nitrogen Purge” (*) during the pumpdown to reduce moisture in the chamber. (At least 3 times)
 - Set channel 4 of MFC controller to 10-15%.
 - Open V8.
 - Open V11 for 2 seconds, and then close V11.
 - Open fully GV1. Pressure will go up to 300-400 mTorr then wait till it goes down to base pressure so line is pumped down.
 - Close GV1.
 - Once base pressure is reached, repeat the procedure.
5. Close pneumatic valves V11, V8 and GV1, and ramp down N₂ MFC to 0%.

D. 3. Manual Deposition Process

Heat up chamber and required gas lines. (Note: Li precursor (LTB) line takes time to heat up so do it while heating up the chamber)

1. Heat the chamber to 290°C by increasing the temperature set-point every 25 minutes to prevent overshooting/heating of controller.

- Plug in white cord (controller) and black power strip (heating wire). To change the set point, hold down the “*” button and hold “SP1” for increasing or “SP2” for decreasing temperature.
 - Set the temperature controller to 80-100°C.
 - Raise the temperature to 150-180°C
 - Raise the temperature to 220°C
 - Raise the temperature to 290°C and wait for 40 minutes to start the deposition (Note: The controller is reading the wall of chamber, so need to wait more minutes for inside chamber to heat up. The door window temperature will be at ~50-60°C when chamber at 290°C).
2. Heat the gas lines:
- LTB (155-160°C): (Takes 1-2 hours) ramp up the transformer (black square box) for heating power to 20%, and then (30 minutes later) increase to 28% – has thermometer controller to check and give readout of temperature.
 - TMA and Water (50-60 °C): (Takes ~10 minutes) plug in heating cords for the lines to the power strip connected to a transformer (gray) and set the transformer to 30%.
 - TEOS (50-60 °C): (Takes ~10 minutes) set the transformer (black square box) for the heating power to 9%.



3. For Li-O growth, record the temperature for LTB in experimental log book.
For Al-O growth, open GV4 and set TMA MFC (channel 2) to 3%.

For Si-O growth, open the bubbler inlet and outlet valves (O and I manual valve inside cabinet) **simultaneously**, open V11 and set MFC channel 3 and 4 (carrier gas N₂) to 3%. For LiAlSiO₄, alternate cycles of Al oxide (b cycles for each global cycle), Li oxide (a cycles for each global cycle), and Si oxide (c cycles for each global cycle). Deposit total of # global cycles. (Note: Aluminum deposit first because have good surface adhesion, Silicon deposit as last layer because lithium easily reacts with CO₂ in atmosphere to form Li₂CO₃.) For stoichiometric LASO, a:b:c=6:10:4.

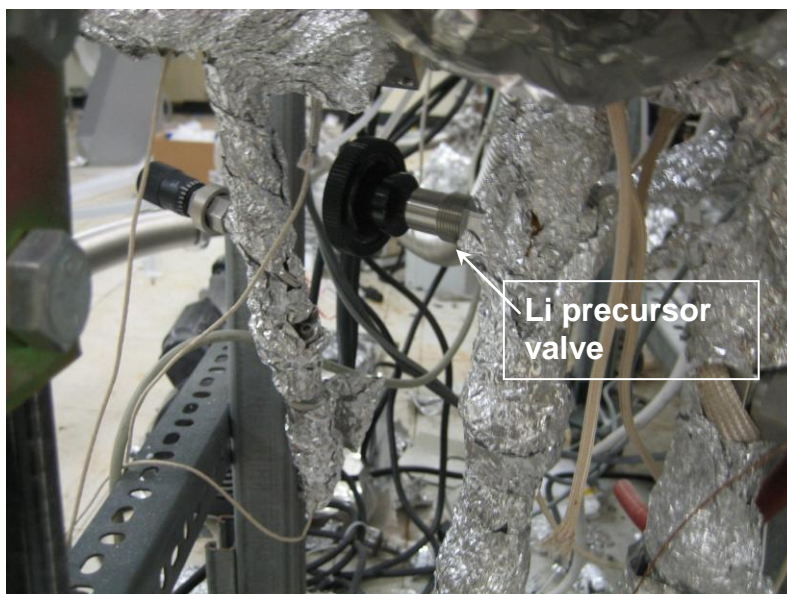
The procedures listed below are only for one cycle each! (Note: pump down time can be extended if need be, but cannot extend pulse time.)

4. Al₂O₃ Deposition: (repeats for b cycles)

- Open the pneumatic valves V2 and V12 for 5 seconds. Watch the chamber pressure change, which should increase to ~100 mTorr.
- Close V12 and then close V2.
- Wait for 45 seconds for pumpdown. Make sure chamber goes back to base pressure. Before the pumpdown time of 45 seconds are up, open water manual valve M1 to setting of 10.
- Open valve V1 for 5 seconds. Watch the chamber pressure, which should increase to 100-200 mTorr, but make sure it does not go above 200 mTorr. (Note: water does not have MFC so vapor pressure can be high.)
- Close pneumatic valve V1 and then close manual M1 for water.
- Pump down for 45 seconds till base pressure has been reached. (Note: if chamber has not reached the base pressure after pump down time of 60 seconds, then do a “Nitrogen Purge” (Step *) by pulsing nitrogen in for 10 seconds.)

5. Li₂O Deposition: (repeats for a cycles)

- Slightly open the valve LiOC4H9/M3 for 10 seconds to pulse LTB. Pressure will increase by 5-10 mTorr.



- Close valve LiOC₄H₉/M3.
- Wait for 60 seconds for pumpdown. Make sure chamber goes back to base pressure. Before the pump down time of 60 seconds are up, open water valve M1 to setting of 10.
- Open valve V1 for 10 seconds. Watch the pressure, which should increase to 100-200 mTorr, but make sure it does not go above 200 mTorr. (Note: water does not have MFC so vapor pressure can be high.)
- Close V1 and then close manual valve M1 for water.
- Pump down for 60 seconds till base pressure has been reached. (Note: if chamber has not reached the base pressure after pump down time of 60 seconds, then do a “Nitrogen Purge” (Step *) by pulsing nitrogen in for 10 seconds.)

6. SiO₂ Deposition: (repeats for c cycles)

(Note: if nitrogen purge was used in previous deposition, need to reset the MFC channel 4 to 3% before beginning deposition.)

- Open valve V10 and then half way open the manual valve GV2 for 20 seconds. Pressure will increase to 200 mTorr.
- Close manual valve GV2 and then close V10.

- Wait for 60 seconds to pump down. Make sure chamber goes back to base pressure. Before the pump down time of 60 seconds are up, open water valve M1 to setting of 10.
- Open valve V1 for 15 seconds. Watch the pressure, which should increase to 100-200 mTorr, but make sure it does not go above 200 mTorr. (Note: water does not have MFC so vapor pressure can be high.)
- Close V1 and then close manual valve M1 for water.
- Pump down for 60 seconds till base pressure has been reached. (Note: if chamber has not reached the base pressure after pump down time of 60 seconds, then do a “Nitrogen Purge” (Step *) by pulsing nitrogen in for 10 seconds.)

Repeats Steps #4-6 based on the required numbers of the global cycle.

7. Close all MFC and valves.
8. Turn off all the heating for chamber, water, and precursor containers.
9. Wait for the chamber to cool down to at least 50°C or lower. (This will take about ~2 hours roughly and will take ~1 hour to cool down to ~80°C.)

D. 4. To unload the sample

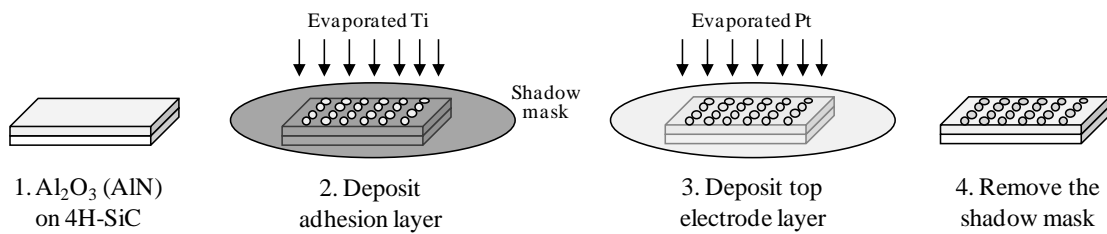
1. Do Nitrogen Purge Step (* in Section D.2) 3 times.
2. Repeat D.1.
3. Open the chamber to unload the sample.

If not loading sample in a short time, pump down the chamber (do not need to do nitrogen purge if there is no sample).

APPENDIX E: MOS Capacitor Fabrication Process

1. Gate Deposition with Shadow Mask: (Same as the contact for impedance measurement)

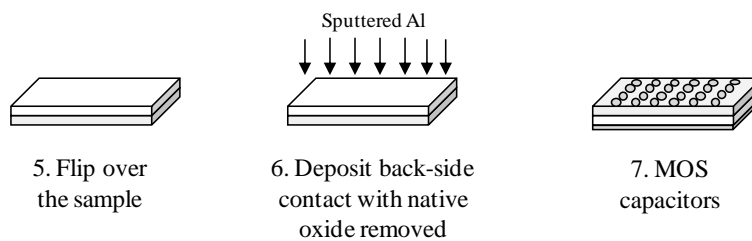
Using CHA 4.0 E-beam evaporator to deposit 100 Å Ti (2 Å/s) and 1000 Å Pt (1 Å/s). (~2 hours)



2. Backside Aluminum Sputtering:

Scratch backside with scribe to remove oxide.

CVC 601 sputtering of 2000 Å aluminum. Bias of 230 V to remove residual native oxide.



APPENDIX F1: Parts and Services for the ALD System

Vendor	Catalog #	Description
Nor-Cal	Custom	Custom vacuum chamber and part manufacturing
Transfer Engineering	Custom	Custom heating station and receiving fork
Momentive Performance Materials	HT-03	1-inch diameter ceramic heater (stage), accessories
ESPI	Specify dimensions	Molybdenum (raw material, can be machined by the machine shop)
Parker	PS2982B53P	15mm Solenoid Kit
Parker	PSFTN0N10NP	Parker valve assembly (10-station) - Air Manifold
S&S Fluid Power	PS298305P	15mm 3-pin DIN 43650C Quick Connect (18-inch cord)
National Instruments	USB-9481 PCI-6722	Relay Module Analog Output Board
Celerity	955-034-0005	MFC controller Auto cable
Laminar Technologies		MFCs (rebuilt)
Huntington	VF-187-A	Mini rotary-linear motion feedthrough
Larson	n/a	Quartz window (6" CF flange)
MDC	463000	Sealed-off glass tube (1 1/3" CF)
Process Materials	URS-100	MFC controller (surplus)
Sigma-Aldrich	59777-50G	TMA ($\geq 99.9999\%$)
	663301	TMA (97%) with precursor host
	445541-5G	HTB (99.99%)
	333859-25ML	TEOS (99.999%)
	339261-800mL	Hydrofluoric acid, 48wt% in water
Strem Chemicals	03-0780-25g	LTB (98%)
Airgas	G2659751	50lb, Ammonia, Grade Ultima 6N4 (99.99994%)
Entegris	CE35KFSK4R	Hydride gas purifier (NH ₃)
Thermal Ceramics	Superwool 607	Insulation blanket for hot-wall reactors
Gelest	zBUB-S-0150	Bubblers
Staib Instruments	RS-64	RHEED screen and gun
K-Space Associates	KSA-400	RHEED detector
<hr/>		
Vendor	Service	
Machine shop	Stands for HV-ALD chamber	
Cree, Inc.	SiC wafer, CMP finish	
NovaSiC	Chemical mechanical polishing of SiC wafers	
American Precision	SiC wafer dicing	

Dicing		
Phosphor Solutions		RHEED screen cleaning
Collaborator	Company/school	Project
Vincent Gambin	Northrop Grumman	AlGaIn/GaN wafer and Hall measurements
Stephen Sadow	University of South Florida	Epitaxial SiC growth for device fabrication
Kang Wang	UCLA	Shadow mask for device fabrication (contact: Caifu Zeng) Characterization for piezoelectric materials (contact: Tao Wu)
Sarah Tolbert	UCLA	Porous nanowires for half cell fabrication (contact:)
Alec Talin	Sandia National Laboratory	Single nanowire battery

APPENDIX F2: NH₃ purifier (Entegris 35KF)

The purifier is a SK (hydride) series and made of electropolished 316L stainless steel housing. The materials in the purifier are 60-80% manganese dioxide (MnO₂) and 20-40% inorganic oxide. The handling and potential hazards can be found from MSDS (8004351). The purifier was installed in the NH₃ gas line vertically and close to the reactor, with a bypass gas line. When no depositions are running, the valves on both of the inlet and outlet should be closed to protect the purifier. Do not pump down the NH₃ gas line through the purifier, instead use the bypass gas line. The temperature of the purifier should always be <80 °C.

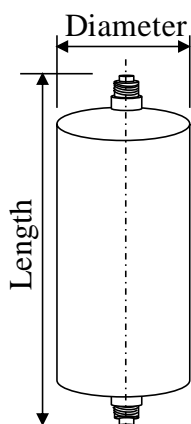


Table F.2. Physical specifications of the 35KF purifier.

Length (mm)	Diameter (mm)	Approx. weight (kg)	Bed volume (cc)
84	38	0.3	39
Max. flow rate (SLPM)	Max. operating pressure (psig)	Max. differential pressure (psid)	Pressure drop (psid)
1	250	200	0.5

APPENDIX F3: Superwool 607 blanket

The materials of the insulation include 60-70 % silica (SiO_2), 25-35% calcium oxide (CaO), 4-7% magnesium oxide (MgO) and minor zirconia (ZrO_2) and alumina (Al_2O_3). When people are handling the insulation material, gloves and masks should be applied to avoid touching or breathing the particles. The thermal conductivity of the material is a function of temperature, as listed in Table F.3.

Table F.3. Thermal conductivity of the insulation material.

Mean temperature ($^{\circ}\text{C}/^{\circ}\text{F}$)	Thermal conductivity ($\text{W}/\text{m}\cdot\text{K}$)
260/500	0.06
538/1000	0.13
816/1500	0.22
982/1800	0.28

APPENDIX G: Troubleshooting

G.1 High Resistance of Sample Heater

The sample heater resistance should be 11.0 Ω . If the heater resistance is $>14 \Omega$, as measured across the feedthrough connections outside vacuum, the heater will not heat up efficiently. It is likely that the electrical connections to the heater inside vacuum have become loose.

1. Visually inspect the heater for loose power connections.
2. Vent the chamber and take out the stage.
3. Tighten the connections between the stranded copper wires and the molybdenum (Mo) nuts attached to the tantalum rods.
4. Tighten the Mo nuts onto the electrical pads on top of the heater.
5. Replace spacers if broken or cracked.
6. Check resistance between the two leads on the power cable.
7. If it is still too high, repeat.
8. If it is still too high, pull on the copper wires to check whether they have come slightly loose from the electrical feedthrough connections (which cannot be easily accessed due to the flange geometry. If this is the case, take out the feedthrough and re-attach the wires.
9. When the desired resistance (11.0 Ω) is achieved and determined to be stable, replace the stage on the chamber. Pump down and bake the chamber until the chamber pressure reaches high 10^{-8} Torr, which usually takes several days.

G.2 RHEED Gun Interfered by Solenoid

The RHEED beam will be affected by magnetic field and electrical field. When solenoid is near the beam, the direction is affected and changes. In order to avoid this situation, make sure there is no solenoid or electricity near the RHEED beam.

G.3 Air Leaks from Wobble Stick or Glass Window Seal

Wobble sticks (VG, ZWS20) used for LL/R2P2/ALD sample transfer are fragile at the bellows, where the vacuum seal may be damaged easily if the bellows are not moved gently during sample transfer, venting or pump-down process. If there is a leak around the bellows, a pressure increase can be detected via cold cathode or ion gauge when the wobble stick is lifted up (the bellows are stretched). The seal between a view port (glass or quartz) and the CF flange frame is generated by glues, which may be damaged by high temperature (>200 °C) heating. Therefore, when baking or heating the reactors, especially high-vacuum systems, the temperature of the wall should always be monitored and maintained below the limit. In order to identify the leak, IPA can be gently spread on the seal part with chamber pressure being monitored for an increase in pressure.

G.4 Failure of Pneumatic Gate Valves

A pneumatic gate valve is normally opened or closed by a switch or buttons, which control the flow of compressed air. When the valve cannot be controlled by the switch or buttons, it could be due to the failure of the solenoid or the spring of the valve itself. If the problem is from the solenoid, the flow of compressed air can be changed manually to open or close the gate valve. There are usually two compressed air lines between the solenoid and gate valve. When one of the lines has higher pressure than the other, the gate valve will be either open or close. If the solenoid is broken, which means it cannot switch the pressure difference between the two lines, the two lines can be manually switched to provide positive or negative pressure difference to the gate valve. If the gate valve itself is broken, the body part could potentially be replaced without disconnecting the whole gate valve (contact the vendor for replacement).

G.5 Failure of Turbo Pumps

When a turbo pump (TP) stops running (rotation speed <full speed), isolate the chamber and power it off. If the mechanic pump is still running, close the backing valve after waiting for

10 minutes (wait until the TP is fully winded down). If the mechanic pump is off as well, close the backing valve right away. Then, check whether cooling water is running. Find another TP control (the same model) to check whether the problem is from the control or the pump itself. If it is the pump, remove it from the reactor and check the blades for damages. Contact the Duniway Stockroom Corp. for a rebuild service or trading it in for a rebuilt one (same as the controller).

BIBLIOGRAPHY

- Adam, T., J. Kolodzey, et al. (2001). "The electrical properties of MIS capacitors with AlN gate dielectrics." Applied Surface Science **175**: 428-435.
- Afanas'ev, V. V., A. Stesmans, et al. (2003). "Mechanisms responsible for improvement of 4H-SiC/SiO₂ interface properties by nitridation." Applied Physics Letters **82**(4): 568-570.
- Agarwal, A., S. Seshadri, et al. (1997). "Temperature dependence of Fowler-Nordheim current in 6H- and 4H-SiC MOS capacitors." IEEE Electron Device Letters **18**(12): 592-594.
- Ahn, J. K. and S. G. Yoon (2004). "Characteristics of perovskite (Li_{0.5}La_{0.5})TiO₃ solid electrolyte thin films grown by pulsed laser deposition for rechargeable lithium microbattery." Electrochimica Acta **50**(2-3): 371-374.
- Arulkumar, S., T. Egawa, et al. (2005). "Studies of electron beam evaporated SiO₂/AlGaIn/GaN metal-oxide-semiconductor high-electron-mobility transistors." Japanese Journal Of Applied Physics Part 2-Letters & Express Letters **44**(24-27): L812-L815.
- Balachander, K., S. Arulkumar, et al. (2005). "A comparison on the electrical characteristics of SiO₂, SiON and SiN as the gate insulators for the fabrication of AlGaIn/GaN metal-oxide/insulator-semiconductor high-electron mobility-transistors." Japanese Journal Of Applied Physics Part 1-Regular Papers Brief Communications & Review Papers **44**(7A): 4911-4913.
- Bard, A. J. and L. R. Faulkner (2001). Electrochemical Methods: Fundamentals and Applications. New York, USA, John Wiley & Sons, Inc.
- Barin, I., O. Knacke, et al. (1973). Thermochemical Properties of Inorganic Substances. Berlin, Germany, Springer-Verlag.
- Bartram, M. E., T. A. Michalske, et al. (1991). "Chemisorption of trimethylaluminum and ammonia on silica - mechanisms for the formation of Al-N Bonds and the elimination of methyl-groups bonded to aluminum." Chemistry Of Materials **3**(5): 953-960.
- Bass, M. (1994). Devices, Measurements and Properties. New York, USA, McGraw-Hill, Inc.
- Basu, S., P. K. Singh, et al. (2010). "Effects of short-term DC-bias-induced stress on n-GaN/AlGaIn/GaN MOSHEMTs with liquid-phase-deposited Al₂O₃ as a gate dielectric." IEEE Transactions On Electron Devices **57**(11): 2978-2987.
- Bates, J. B., N. J. Dudney, et al. (2000). "Thin-film lithium and lithium-ion batteries." Solid State Ionics **135**(1-4): 33-45.
- Battye, F. L., J. G. Jenkin, et al. (1974). "Photoelectron determination of attenuation of low-energy electrons in Al₂O₃." Physical Review B **9**(7): 2887-2893.
- Bechstedt, F. and K. Hubner (1981). "Mean free-path of photo-electrons in silicon and silicon-oxides." Physica Status Solidi A-Applied Research **67**(2): 517-526.
- Belonoshko, A. B., R. Ahuja, et al. (2000). "Mechanism for the kappa-Al₂O₃ to the alpha-Al₂O₃ transition and the stability of kappa-Al₂O₃ under volume expansion." Physical Review B **61**(5): 3131-3134.
- Biefeld, R. M., G. E. Pike, et al. (1977). "Percolative ionic-conduction in LiAlSiO₄ glass-ceramic system." Physical Review B **15**(12): 5912-5920.
- Binari, S. C., K. Ikossi, et al. (2001). "Trapping effects and microwave power performance in AlGaIn/GaN HEMTs." IEEE Transactions On Electron Devices **48**(3): 465-471.

- Bond, A. M., E. A. McLennan, et al. (1987). "Assessment of conditions under which the oxidation of ferrocene can be used as a standard voltammetric reference process in aqueous-media." Analytical Chemistry **59**(24): 2853-2860.
- Braun, W. (1999). Applied RHEED: Reflection High-Energy Electron Diffraction During Crystal Growth. Berlin, Germany, Springer-Verlag.
- Briant, J. L. and G. C. Farrington (1981). "Ionic conductivity in lithium and lithium-sodium beta alumina." Journal Of The Electrochemical Society **128**(9): 1830-1834.
- Briggs, D. (1977). Handbook of X-Ray and Ultraviolet Photoelectron Spectroscopy. London, Philadelphia, Rhein, Heyden.
- Briggs, D. and M. P. Seah (1990). Practical Surface Analysis. New York, John Wiley & Sons, Inc.
- Bruce, P. G. (1995). Solid State Electrochemistry. Cambridge, Cambridge University Press.
- Buttari, D., S. Heikman, et al. (2002). Digital etching for highly reproducible low damage gate recessing on AlGaIn/GaN HEMTs. Lester Eastman Conference On High Performance Devices.
- Cairns, E. J. (2004). Battery Overview. Chapter B. Encyclopedia of Energy. New York, Elsevier.
- Chabak, K. D., D. E. Walker, Jr., et al. (2011). "High-performance AlN/GaN HEMTs on sapphire substrate with an oxidized gate insulator." IEEE Electron Device Letters **32**(12): 1677-1679.
- Chan, C. K., H. L. Peng, et al. (2008). "High-performance lithium battery anodes using silicon nanowires." Nature Nanotechnology **3**(1): 31-35.
- Chan, C. K., X. F. Zhang, et al. (2008). "High capacity Li ion battery anodes using Ge nanowires." Nano Letters **8**(1): 307-309.
- Chang, Y. C., Y. J. Lee, et al. (2007). "MBE grown high kappa dielectrics Ga₂O₃(Gd₂O₃) on GaN." Journal Of Crystal Growth **301**: 390-393.
- Chao, C., L. Xingzhao, et al. (2011). "Fabrication of enhancement-mode AlGaIn/GaN MISHEMTs by using fluorinated Al₂O₃ as gate dielectrics." IEEE Electron Device Letters **32**(10).
- Chen, C., D. J. Chen, et al. (2008). "Effects of an AlN passivation layer on the microstructure and electronic properties of AlGaIn/GaN heterostructures." Applied Physics A-Materials Science & Processing **90**(3): 447-449.
- Cho, D. H., M. Shimizu, et al. (2002). "AlN/AlGaIn/GaN metal insulator semiconductor heterostructure field effect transistor." Japanese Journal Of Applied Physics Part 1- Regular Papers Short Notes & Review Papers **41**(7A): 4481-4483.
- Cimalla, V., J. Pezoldt, et al. (2007). "Group III nitride and SiC based MEMS and NEMS: materials properties, technology and applications." Journal Of Physics D-Applied physics **40**: 6386-6434.
- Claudel, A., E. Blanquet, et al. (2009). "Thermodynamic and experimental investigations on the growth of thick aluminum nitride layers by high temperature CVD." Journal Of Crystal Growth **311**(13): 3371-3379.
- Cleveland, E. R., P. Banerjee, et al. (2010). "Profile evolution for conformal atomic layer deposition over nanotopography." ACS Nano **4**(8): 4637-4644.
- Cros, A., N. Garro, et al. (2007). "Raman scattering as a tool for the evaluation of strain in GaN/AlN quantum dots: The effect of capping." Physical Review B **76**.
- Cullity, B. D. (2001). Elements of X-Ray Diffraction. Upper Saddle River, NJ, Addison-Wesley Publishing Company, Inc.

- Derluyn, J., S. Boeykens, et al. (2005). "Improvement of AlGaIn/GaN high electron mobility transistor structures by in situ deposition of a Si₃N₄ surface layer." Journal Of Applied Physics **98**(5): 054501.
- Dillon, A. C., A. W. Ott, et al. (1995). "Surface chemistry of Al₂O₃ deposition using Al(CH₃)₃ and H₂O in a binary reaction sequence." Surface Science **322**(1-3): 230-242.
- Elers, K.-E., M. Ritala, et al. (1995). "Atomic layer epitaxy growth of AlN thin films." Journal De Physique II **5**: C5-1021-C5-1027.
- Engelmark, F., G. F. Iriarte, et al. (2001). "Structural and electroacoustic studies of AlN thin films during low temperature radio frequency sputter deposition." Journal Of Vacuum Science & Technology A-Vacuum Surfaces And Films **19**(5): 2664-2669.
- Feldman, L. C. and J. W. Mayer (1986). Fundamentals of Surface and Thin Film Analysis. Upper Saddle River, NJ, P T R Prentice-Hall, Inc.
- Furusawa, S.-i., A. Kamiyama, et al. (2008). "Fabrication and ionic conductivity of amorphous lithium meta-silicate thin film." Solid State Ionics **179**(15-16): 536-542.
- Furusawa, S.-i., T. Kasahara, et al. (2009). "Fabrication and ionic conductivity of Li₂SiO₃ thin film." Solid State Ionics **180**(6-8): 649-653.
- George, S. M. (2010). "Atomic layer deposition: an overview." Chemical Reviews **110**(1): 111-131.
- Gil, B. (1998). Group III Nitride Semiconductor Compounds-Physics and Application. New York, Oxford University Press Inc.
- Gila, B. P., F. Ren, et al. (2004). "Novel insulators for gate dielectrics and surface passivation of GaN-based electronic devices." Materials Science & Engineering R-Reports **44**(6): 151-184.
- Goldstein, J., D. E. Newbury, et al. (2003). Scanning Electron Microscopy and X-ray Microanalysis. New York, USA, Plenum Press.
- Goodenough, J. B. and K. Youngsik (2011). "Challenges for rechargeable batteries." Journal Of Power Sources **196**(16): 6688-6694.
- Goodhew, P. J., J. Humphreys, et al. (2001). Electron Microscopy and Analysis. New York, NY, Taylor & Francis.
- Gosset, L. G., J. F. Damlencourt, et al. (2002). "Interface and material characterization of thin Al₂O₃ layers deposited by ALD using TMA/H₂O." Journal Of Non-Crystalline Solids **303**(1): 17-23.
- Green, B. M., K. K. Chu, et al. (2000). "The effect of surface passivation on the microwave characteristics of undoped AlGaIn/GaN HEMTs." IEEE Electron Device Letters **21**(6): 268-270.
- Gritzner, G. and J. Kuta (1984). "Recommendations on reporting electrode-potentials in nonaqueous solvents (recommendations 1983)." Pure And Applied Chemistry **56**(4): 461-466.
- Groner, M. D., S. M. George, et al. (2006). "Gas diffusion barriers on polymers using Al₂O₃ atomic layer deposition." Applied Physics Letters **88**(5).
- Guha, S., N. A. Bojarczuk, et al. (2002). "Lattice-matched, epitaxial, silicon-insulating lanthanum yttrium oxide heterostructures." Applied Physics Letters **80**(5): 766-768.
- Hasegawa, H., T. Inagaki, et al. (2003). "Mechanisms of current collapse and gate leakage currents in AlGaIn/GaN heterostructure field effect transistors." Journal Of Vacuum Science & Technology B **21**(4): 1844-1855.

- Hashizume, T., S. Ootomo, et al. (2003). "Surface passivation of GaN and GaN/AlGaN heterostructures by dielectric films and its application to insulated-gate heterostructure transistors." Journal Of Vacuum Science & Technology B **21**(4): 1828-1838.
- Hashizume, T., S. Ootomo, et al. (2001). "Chemistry and electrical properties of surfaces of GaN and GaN/AlGaN heterostructures." Journal Of Vacuum Science & Technology B **19**(4): 1675-1681.
- Hesse, K. F. (1985). "Crystal structures of natural and synthetic alpha-eucryptite, LiAlSiO₄." Zeitschrift Fur Kristallographie **172**(1-2): 147-151.
- Hill, J. M., D. G. Royce, et al. (1976). "Properties of oxidized silicon as determined by angular-dependent x-ray photoelectron spectroscopy." Chemical Physics Letters **44**(2): 225-231.
- Horio, K., H. Takayanagi, et al. (2006). "Analysis of buffer-trapping effects on current collapse of GaN FETs." Physica Status Solidi C(6).
- Horn, K. R. V. (1967). Aluminum, Prepared by Engineers, Scientists, and Metallurgists of Aluminum Company of America. Metals Park, American Society for Metals.
- Huang, J. Y., L. Zhong, et al. (2010). "In situ observation of the electrochemical lithiation of a single SnO₂ nanowire electrode." Science **330**: 1515-1520.
- Hummel, F. A. (1951). "Thermal expansion properties of some synthetic lithia minerals." Journal Of The American Ceramic Society **34**(8): 235-239.
- Husson, E. and Y. Repelin (1996). "Structural studies of transition aluminas. Theta alumina." European Journal Of Solid State Inorganic Chemistry **33**: 1223-1231.
- Hwang, C.-M., C.-H. Lim, et al. (2011). "Evaluation of Si/Ge multi-layered negative film electrodes using magnetron sputtering for rechargeable lithium ion batteries." Thin Solid Films **519**(7): 2332-2338.
- Ishizawa, N., T. Miyata, et al. (1980). "A structural investigation of alpha-Al₂O₃ at 2170 K." Acta Crystallographica B **36**: 228-230.
- Jeon, C. M. and J. L. Lee (2005). "Effects of tensile stress induced by silicon nitride passivation on electrical characteristics of AlGaIn/GaN heterostructure field-effect transistors." Applied Physics Letters **86**(17).
- Johnson, R. T., R. M. Biefeld, et al. (1976). "Ionic conductivity in solid electrolytes based on lithium aluminosilicate glass and glass-ceramic." Journal Of The Electrochemical Society **123**(5): 680-687.
- Johnson, R. T., B. Morosin, et al. (1975). "Ionic conductivity in LiAlSiO₄." Physics Letters A **54**(5): 403-404.
- Jung, Y. S., A. S. Cavanagh, et al. (2010). "Enhanced stability of LiCoO₂ cathodes in lithium-ion batteries using surface modification by atomic layer deposition." Journal Of The Electrochemical Society **157**(1): A75-A81.
- Kakanakova-Georgieva, A., P. O. A. Persson, et al. (2004). "Sublimation epitaxy of AlN on SiC: growth morphology and structural features." Journal Of Crystal Growth **273**(1-2): 161-166.
- Kemerley, R. T., H. B. Wallace, et al. (2002). "Impact of wide bandgap microwave devices on DoD systems." Proceedings Of The IEEE **90**(6): 1059-1064.
- Kiehne, H. A. (2003). Battery Technology Handbook. New York, Marcel Dekker Inc.
- Kihara, K. (1990). "An x-ray study of the temperature dependence of the quartz structure." European Journal Of Mineralogy **2**: 63-77.
- Kim, H., R. M. Thompson, et al. (2003). "Effects of SiN passivation and high-electric field on AlGaIn-GaN HFET degradation." IEEE Electron Device Letters **24**(7): 421-423.

- King, S. W., E. P. Carlson, et al. (1999). "X-ray photoelectron spectroscopy analysis of GaN/(0001)AlN and AlN/(0001)GaN growth mechanisms." Journal Of Applied Physics **86**(10): 5584-5593.
- Kraut, E. A., R. W. Grant, et al. (1983). "Semiconductor core-level to valence-band maximum binding-energy differences: Precise determination by x-ray photoelectron spectroscopy." Physical Review B **28**(4): 1965-1977.
- Lamb, D. R. (1967). Electrical Conduction Mechanisms in Thin Insulating Films. London, Methuen.
- Lammert, H., M. Kunow, et al. (2003). "Complete identification of alkali sites in ion conducting lithium silicate glasses: A computer study of ion dynamics." Physical Review Letters **90**(21).
- Lee, B., S.-Y. Park, et al. (2008). "Conformal Al₂O₃ dielectric layer deposited by atomic layer deposition for graphene-based nanoelectronics." Applied Physics Letters **92**(20).
- Lee, C.-K., E. Cho, et al. (2007). "Comparative study of electronic structures and dielectric properties of alumina polymorphs by first-principles methods." Physical Review B **76**(24).
- Lee, K.-K., G. Namkoong, et al. (2007). "III-nitrides growth and AlGaIn/GaN hetero structures on ferroelectric materials." Materials Science And Engineering B-Solid State Materials For Advanced Technology **140**(3): 203-211.
- Li, C.-T. (1968). "The crystal structure of LiAlSi₂O₆ III (high-quartz solid solution)." Zeitschrift Fur Kristallographie **127**(S): 327-348.
- Li, W. Q. and S. H. Garofalini (2004). "Molecular dynamics simulation of lithium diffusion in Li₂O-Al₂O₃-SiO₂ glasses." Solid State Ionics **166**(3-4): 365-373.
- Liu, C., E. F. Chor, et al. (2007). "Enhanced device performance of AlGaIn/GaN HEMTs using HfO₂ high-k dielectric for surface passivation and gate oxide." Semiconductor Science And Technology **22**(5): 522-527.
- Liu, H., D. C. Bertolet, et al. (1995). "Reactions of trimethylaluminum and ammonia on alumina at 600 K - surface chemical aspects of AlN thin-film growth." Surface Science **340**(1-2): 88-100.
- Liu, L., Y.-T. Yang, et al. (2011). "The electrical characteristics of a 4H-silicon carbide metal-insulator-semiconductor structure with Al₂O₃ as the gate dielectric." Chinese Physics B **20**(12).
- Lizarraga, R., E. Holmstroem, et al. (2011). "Structural characterization of amorphous alumina and its polymorphs from first-principles XPS and NMR calculations." Physical Review B **83**(9).
- Loewenstein, W. (1954). "The distribution of aluminum in the tetrahedra of silicates and aluminates." American Mineralogist **39**(1-2): 92-96.
- London, D. and D. M. Burt (1982). "Chemical models for lithium aluminosilicate stabilities in pegmatites and granites." American Mineralogist **67**(5-6): 494-509.
- Long, J. W., B. Dunn, et al. (2004). "Three-dimensional battery architectures." Chemical Reviews **104**(10): 4463-4492.
- Lu, W., V. Kumar, et al. (2003). "DC, RF, and, microwave noise performance of AlGaIn-GaN field effect transistors dependence of aluminum concentration." IEEE Transactions On Electron Devices **50**(4): 1069-1074.
- Luo, B., J. W. Johnson, et al. (2002). "Influence of MgO and Sc₂O₃ passivation on AlGaIn/GaN high-electron-mobility transistors." Applied Physics Letters **80**(9): 1661-1663.

- Luo, B., R. Mehandru, et al. (2002). "Comparison of surface passivation films for reduction of current collapse in AlGaIn/GaN high electron mobility transistors." Journal Of The Electrochemical Society **149**(11): G613-G619.
- Maeda, N., M. Hiroki, et al. (2007). "Systematic study of insulator deposition effect (Si_3N_4 , SiO_2 , AlN, and Al_2O_3) on electrical properties in AlGaIn/GaN heterostructures." Japanese Journal Of Applied Physics Part 1-Regular Papers Brief Communications & Review Papers **46**(2): 547-554.
- Mahapatra, R., A. K. Chakraborty, et al. (2007). "Effects of interface engineering for HfO_2 gate dielectric stack on 4H-SiC." Journal Of Applied Physics **102**(2).
- Marso, M., G. Heidelberger, et al. (2006). "Origin of improved RF performance of AlGaIn/GaN MOSHFETs compared to HFETs." IEEE Transactions On Electron Devices **53**(7): 1517-1523.
- Mayer, T. M., J. W. Rogers, et al. (1991). "Mechanism of nucleation and atomic layer growth of AlN on Si." Chemistry Of Materials **3**(4): 641-646.
- Mehandru, R., B. Luo, et al. (2003). "AlGaIn/GaN metal-oxide-semiconductor high electron mobility transistors using Sc_2O_3 as the gate oxide and surface passivation." Applied Physics Letters **82**(15): 2530-2532.
- Messier, D. R. and P. Wong (1971). "Epitaxial growth of Al_2O_3 on Al_2O_3 substrates by chemical vapor deposition." Journal Of The Electrochemical Society **118**(5): 772-&.
- Mishra, U. K., P. Parikh, et al. (2002). "AlGaIn/GaN HEMTs - An overview of device operation and applications." Proceedings Of The IEEE **90**(6): 1022-1031.
- Mishra, U. K., L. Shen, et al. (2008). "GaN-based RF power devices and amplifiers." Proceedings Of The IEEE **96**(2): 287-305.
- Morkoc, H. (2008). Handbook of Nitride Semiconductors and Devices: Materials Properties, Physics and Growth. Weinheim, Germany, WILEY-VCH Verlag GmbH & Co. KGaA.
- Morkoc, H., R. Cingolani, et al. (1999). "Polarization effects in nitride semiconductor device structures and performance of modulation doped field effect transistors." Solid-State Electronics **43**(10): 1909-1927.
- Morkoc, H., S. Strite, et al. (1994). "Large-band-gap SiC, III-V nitride, and II-VI ZnSe-based semiconductor device technologies." Journal Of Applied Physics **76**(3): 1363-1398.
- Myers, R. L., Y. Shishkin, et al. (2005). "High growth rates ($> 30 \mu\text{m}/\text{h}$) of 4H-SiC epitaxial layers using a horizontal hot-wall CVD reactor." Journal Of Crystal Growth **285**: 486-490.
- Nagel, W. and H. Bohm (1982). "Ionic conductivity studies on LiAlSiO_4 - SiO_2 solid solutions of the high quartz type." Solid State Communications **42**(9): 625-631.
- Needham, S. A., G. X. Wang, et al. (2007). "Synthesis and electrochemical performance of doped LiCoO_2 materials." Journal Of Power Sources **174**(2): 828-831.
- Nie, X., E. I. Meletis, et al. (2002). "Abrasive wear/corrosion properties and TEM analysis of Al_2O_3 coatings fabricated using plasma electrolysis." Surface & Coatings Technology **149**(2-3): 245-251.
- Nishi, Y. (2001). "Lithium ion secondary batteries; past 10 years and the future." Journal of Power Sources **100**(1-2): 101.
- Norby, P. (1990). "Thermal transformation of zeolite Li-A(BW). The crystal structure of gamma-eucryptite, a polymorph of LiAlSiO_4 ." Zeolites **10**(3): 193-199.
- Notten, P. H. L., F. Roozeboom, et al. (2007). "3-D integrated all-solid-state rechargeable batteries." Advanced Materials **19**(24): 4564-4567.

- O'Hayre, R., M. Lee, et al. (2004). "Ionic and electronic impedance imaging using atomic force microscopy." Journal Of Applied Physics **95**(12): 8382-8392.
- Ohta, A., H. Koshina, et al. (1995). "Relationship between carbonaceous materials and electrolyte in secondary lithium-ion batteries." Journal Of Power Sources **54**(1): 6-10.
- Ollivier, B., R. Retoux, et al. (1997). "Crystal structure of kappa-alumina: an x-ray powder diffraction, TEM and NMR study." Journal Of Materials Chemistry **7**(6): 1049-1056.
- Onojima, N., J. Kaido, et al. (2005). "Molecular-beam epitaxy of AlN on off-oriented SiC and demonstration of MISFET using AlN/SiC interface." Physica Status Solidi C **7**: 2643-6.
- Onojima, N., J. Suda, et al. (2002). "Growth of AlN (1 1 2bar 0) on 6H-SiC (1 1 2bar 0) by molecular-beam epitaxy." Japanese Journal Of Applied Physics Part 2-Letters **41**(12A): L1348-L1350.
- Onojima, N., J. Suda, et al. (2002). "Molecular-beam epitaxial growth of insulating AlN on surface-controlled 6H-SiC substrate by HCl gas etching." Applied Physics Letters **80**(1): 76-78.
- Ootomo, S., T. Hashizume, et al. (2001). "Surface passivation of AlGaIn/GaN heterostructures using an ultrathin Al₂O₃ layer." Physica Status Solidi A-Applied Research **188**(1): 371-374.
- Ostling, M., R. Ghandi, et al. (2011). "SiC power devices - present status, applications and future perspective." 2011 23rd International Symposium On Power Semiconductor Devices & ICs (ISPSD).
- Ott, A. W., J. W. Klaus, et al. (1997). "Al₂O₃ thin film growth on Si(100) using binary reaction sequence chemistry." Thin Solid Films **292**(1-2): 135-144.
- Paglia, G., A. L. Rohl, et al. (2005). "Determination of the structure of gamma-alumina from interatomic potential and first-principles calculations: The requirement of significant numbers of nonspinel positions to achieve an accurate structural model." Physical Review B **71**(22).
- Park, M.-S., S.-H. Hyun, et al. (2008). "Performance evaluation of printed LiCoO₂ cathodes with PVDF-HFP gel electrolyte for lithium ion microbatteries." Electrochimica Acta **53**(17): 5523-5527.
- Pillars, W. W. and D. R. Peacor (1973). "Crystal structure of beta eucryptite as a function of temperature." American Mineralogist **58**(7-8): 681-690.
- Ponce, F. A., B. S. Krusor, et al. (1995). "Microstructure of GaN epitaxy on SiC using AlN buffer layers." Applied Physics Letters **67**(3): 410-412.
- Posadas, A., F. J. Walker, et al. (2008). "Epitaxial MgO as an alternative gate dielectric for SiC transistor applications." Applied Physics Letters **92**(23).
- Powell, C. J., A. Jablonski, et al. (2005). "NIST databases with electron elastic-scattering cross sections, inelastic mean free paths, and effective attenuation lengths." Surface And Interface Analysis **37**(11): 1068-1071.
- Puurunen, R. L., M. Lindblad, et al. (2001). "Successive reactions of gaseous trimethylaluminium and ammonia on porous alumina." Physical Chemistry Chemical Physics **3**(6): 1093-1102.
- Raistrick, I. D., C. Ho, et al. (1976). "Ionic conductivity of some lithium silicates and aluminosilicates." Journal Of The Electrochemical Society **123**(10): 1469-1476.
- Ren, Z., K. Sun, et al. (2009). "Polymer electrolytes based on poly(vinylidene fluoride-co-hexafluoropropylene) with crosslinked poly(ethylene glycol) for lithium batteries." Solid State Ionics, Diffusion & Reactions **180**(9-10).

- Robertson, J. and B. Falabretti (2006). "Band offsets of high k gate oxides on III-V semiconductors." Journal Of Applied Physics **100**(1).
- Rosenberger, L., R. Baird, et al. (2008). "XPS analysis of aluminum nitride films deposited by plasma source molecular beam epitaxy." Surface And Interface Analysis **40**(9): 1254-1261.
- Roy, R. and E. F. Osborn (1949). "The system lithium metasilicate spodumene silica." Journal Of The American Chemical Society **71**(6): 2086-2095.
- Ruzmetov, D., V. P. Oleshko, et al. (2012). "Electrolyte stability determines scaling limits for solid-state 3D Li ion batteries." Nano Letters **12**(1): 505-511.
- Sahami, S. and M. J. Weaver (1981). "Deficiencies of the ferricinium-ferrocene redox couple for estimating transfer energies of single ions." Journal Of Solution Chemistry **10**(3): 199-208.
- Saib, S., N. Bouarissa, et al. (2008). "Structural and dielectric properties of AlN under pressure." Physica B-Condensed Matter **403**(21-22): 4059-4062.
- Sartbaeva, A., S. A. T. Redfern, et al. (2004). "A neutron diffraction and Rietveld analysis of cooperative Li motion in beta-eucryptite." Journal Of Physics: Condensed Matter **16**: 5267-5278.
- Shi, Z., L. Lu, et al. (2003). "Solid state thin film lithium microbatteries." Advanced Materials For Micro- And Nano-Systems (AMMNS).
- Shin-ichi, F., S. Satoshi, et al. (2004). "Preparation and ionic conductivity of beta-LiAlSiO₄ thin film." Solid State Ionics **167**(3-4): 325-329.
- Sierra-Sastre, Y., S. Choi, et al. (2008). "Vertical growth of Ge nanowires from biotemplated Au nanoparticle catalysts." Journal Of The American Chemical Society **130**(32): 10488-+.
- Singh, J. (2003). Electronic and Optoelectronic Properties of Semiconductor Structures. Cambridge, UK, Cambridge University Press.
- Singh, R. (2006). "Reliability and performance limitations in SiC power devices." Microelectronics Reliability **46**(5-6): 713-730.
- Singh, R. and A. R. Hefner (2004). "Reliability of SiC MOS devices." Solid-State Electronics **48**(10-11): 1717-1720.
- Soltay, L. G. and G. S. Henderson (2005). "The structure of lithium-containing silicate and germanate glasses." Canadian Mineralogist **43**: 1643-1651.
- Solymer, L. and D. Walsh (2004). Electrical Properties of Materials. New York, Oxford University Press Inc.
- Squire, D. W., C. S. Dulcey, et al. (1985). "Mechanistic studies of the decomposition of trimethylaluminum on heated surfaces." Journal Of Vacuum Science & Technology B **3**(5): 1513-1519.
- Stebbins, J. F. and Z. Xu (1997). "NMR evidence for excess non-bridging oxygen in an aluminosilicate glass." Nature **390**(6655): 60-62.
- Stevens, K. S., M. Kinniburgh, et al. (1995). "Demonstration of a silicon field-effect transistor using AlN as the gate dielectric." Applied Physics Letters **66**(23): 3179-3181.
- Stoklas, R., D. Gregusova, et al. (2011). "Performance of AlGaN/GaN metal-insulator-semiconductor heterostructure field-effect transistors with AlN gate insulator prepared by reactive magnetron sputtering." Journal Of Vacuum Science & Technology B **29**(1).
- Strite, S. and H. Morkoc (1992). "GaN, AlN, and InN: A review." Journal Of Vacuum Science & Technology B **10**(4): 1237-1266.

- Sze, S. M. and K. K. Ng (2007). Physics of Semiconductor Devices. Hoboken, NJ, John Wiley & Sons., Inc.
- Tanner, C. M., Y. C. Perng, et al. (2007). "Electrical performance of Al₂O₃ gate dielectric films deposited by atomic layer deposition on 4H-SiC." Applied Physics Letters **91**(20): 203510.
- Tanner, C. M., M. F. Toney, et al. (2007). "Engineering epitaxial gamma-Al₂O₃ gate dielectric films on 4H-SiC." Journal Of Applied Physics **102**(10).
- Tarascon, J. M. and M. Armand (2001). "Issues and challenges facing rechargeable lithium batteries." Nature **414**(6861): 359-367.
- Taube, A., S. Gieraltowska, et al. (2011). "Electronic properties of thin HfO₂ films fabricated by atomic layer deposition on 4H-SiC." Acta Physica Polonica A **119**(5): 696-698.
- Taur, Y. and T. H. Ning (1998). Fundamentals of Modern VLSI Devices. New York, Cambridge University Press.
- Thangadurai, V. and W. Weppner (2002). "Solid state lithium ion conductors: design considerations by thermodynamic approach." Ionics **8**: 281.
- Thokchom, J. S. and B. Kumar (2010). "The effects of crystallization parameters on the ionic conductivity of a lithium aluminum germanium phosphate glass-ceramic." Journal Of Power Sources **195**(9): 2870-2876.
- Thomas, C., L. Vivier, et al. (1997). "Deuterium tracer studies on hydrotreating catalysts - Isotopic exchange between hydrogen and hydrogen sulfide on sulfided NiMo/Al₂O₃." Journal Of Catalysis **167**(1): 1-11.
- Uchiyama, H., E. Hosono, et al. (2008). "A nanoscale meshed electrode of single-crystalline SnO for lithium-ion rechargeable batteries." Electrochemistry Communications **10**(1).
- Usman, M., A. Hallen, et al. (2011). "Toward the understanding of stacked Al-based high-k dielectrics for passivation of 4H-SiC devices." Journal Of The Electrochemical Society **158**(1): H75-H79.
- Van, T. T. and J. P. Chang (2005). "Radical-enhanced atomic layer deposition of Y₂O₃ via a beta-diketonate precursor and O radicals." Surface Science **596**(1-3): 1-11.
- Wakahara, A., H. Oishi, et al. (2002). "Organometallic vapor phase epitaxy of GaN on Si(111) with a gamma-Al₂O₃(111) epitaxial intermediate layer." Journal Of Crystal Growth **236**(1-3): 21-25.
- Wakihara, M. (2001). "Recent developments in lithium ion batteries." Materials Science & Engineering R-Reports **33**(4): 109-134.
- Waldrop, J. R. and R. W. Grant (1996). "Measurement of AlN/GaN (0001) heterojunction band offsets by x-ray photoemission spectroscopy." Applied Physics Letters **68**(20): 2879-2881.
- Wallace, R. M. and G. D. Wilk (2003). "High-kappa dielectric materials for microelectronics." Critical Reviews In Solid State And Materials Sciences **28**(4): 231-285.
- Warneke, B., M. Last, et al. (2001). "Smart Dust: Communicating with a cubic-millimeter computer." Computer **34**(1): 44-51.
- Warneke, B. A. and K. S. J. Pister (2004). "An ultra-low energy microcontroller for Smart Dust wireless sensor networks." 2004 IEEE International Solid-State Circuits Conference (IEEE Cat. No.04CH37519).
- Wartena, R., A. E. Curtright, et al. (2004). "Li-ion microbatteries generated by a laser direct-write method." Journal Of Power Sources **126**(1-2): 193-202.

- Weitzel, C. E., J. W. Palmour, et al. (1996). "Silicon carbide high-power devices." IEEE Transactions On Electron Devices **43**(10): 1732-1741.
- Willander, M., M. Friesel, et al. (2006). "Silicon carbide and diamond for high temperature device applications." Journal Of Materials Science-Materials In Electronics **17**(1): 1-25.
- Winter, J. K. and S. Ghose (1979). "Thermal expansion and high temperature crystal chemistry of the Al₂SiO₅ polymorphs." American Mineralogist **64**: 573-586.
- Wolborski, M., D. Rosen, et al. (2006). "Aluminum nitride deposition on 4H-SiC by means of physical vapor deposition." Thin Solid Films **515**(2): 456-459.
- Xi, Y. A., K. X. Chen, et al. (2006). "Very high quality AlN grown on (0001) sapphire by metal-organic vapor phase epitaxy." Applied Physics Letters **89**(10).
- Xu, Y., L. Chen, et al. (2011). "Initial reaction mechanism of H-passivated Ge surface passivation by atomic layer deposition of Al₂O₃ and AlN." Thin Solid Films **519**(18): 6000-6003.
- Yeh, J. J. and I. Lindau (1985). "Atomic subshell photoionization cross-sections and asymmetry parameters: $1 \leq Z \leq 103$." Atomic Data And Nuclear Data Tables **32**(1): 1-155.
- Yoder, M. N. (1996). "Wide bandgap semiconductor materials and devices." IEEE Transactions On Electron Devices **43**(10): 1633-1636.
- Zhang, L. Q., X. H. Liu, et al. (2012). "Direct observation of Sn crystal growth during the lithiation and delithiation process of SnO₂ nanowires." Micron: doi:10.1016/j.micron.2012.01.016.
- Zhou, R.-S. and R. L. Snyder (1991). "Structures and transformation mechanisms of the eta, gamma and theta transition aluminas." Acta Crystallographica B **47**: 617-630.